Nucleolar distribution of the HIV-1 nucleocapsid protein investigated by the super-resolution microscopy

Oleksandr Glushonkov

UNIVERSITÉ DE STRASBOURG

ÉCOLE DOCTORALE DES SCIENCES DE LA VIE ET DE LA SANTÉ

UMR CNRS 7021 Laboratoire de Bioimagerie et Pathologies

THÈSE présentée par :

Oleksandr GLUSHONKOV

soutenue le : **06 avril 2018**

pour obtenir le grade de : **Docteur de l'Université de Strasbourg**

Discipline/ Spécialité : Sciences du vivant/ Biophysique

Imagerie de fluorescence à haute résolution : étude de la localisation nucléolaire de la nucléocapside du VIH

THÈSE dirigée par :

M. DIDIER Pascal	Professeur, Université de Strasbourg

RAPPORTEURS :

M. SLIWA Michel	Chargé de recherches, Université de Lille
M. FAVARD Cyril	Ingénieur de recherches, Institut de Recherche en Infectiologie de Montpellier

AUTRES MEMBRES DU JURY :

WEISS Etienne	Professeur, Université de Strasbourg

INVITÉE:

RÉAL Eléonore	Maitre de conférences, Université de Strasbourg

Table of contents

Acknowledgements

I would like to express my gratitude to everyone who became a part of my life during these last four years. I am grateful for their help with my master and PhD projects and will always cherish the memories made during our amazing travels and social events.

I am greatly thankful to my supervisor Prof. Pascal Didier for teaching me microscopy techniques and sharing his vast knowledge, for his guidance to all my queries and fruitful discussions of the results. I admire his tips and tricks on troubleshooting different problems related to an optical setup or a process of image acquisition; he has magical skills to resolve all of them within a couple of minutes what I have already witnessed many times. I appreciate his significant help during the writing of this manuscript.

I am grateful to the director of our laboratory Prof. Yves Mély for giving me the opportunity to do my master in the University of Strasbourg and to continue the project during this PhD.

I would like to thank the members of jury Dr. Cyril Favard, Dr. Michel Sliwa, Prof. Etienne Weiss and Dr. Eléonore Réal for accepting the proposal to evaluate my research work. Their comments and correction will improve the quality of the manuscript.

A special note of thanks to Dr. Eléonore Réal and Dr. Emmanuel Boutant for teaching me multiple biological assays, for their help with biology-related problems and discussions of the results. I appreciate their efforts and time devoted for correcting the thesis. Thanks, Manu, for your suggestions to efficiently use Twitter to follow scientific news and developments in the field of super-resolution microscopy.

I am thankful to Prof. Maxime Lehmann and his PhD student Elisabeth Silva for their collaboration. In addition, his constant efforts to organize and support the Journal club meetings help many PhD and master students to prepare for their defenses.

I would like to thank permanent members of the lab: Dr. Julien Godet, Dr. Frederic Przybilla and Dr. Ludovic Richert for the help with plugins/macros/scripts writing; Dr. Nicolas Humbert for the preparation of the NC peptide; Dr. Denis Dujardin for his help with the microinjection experiments; Dr. Halina Anton, Dr. Christian Boudier, Dr. Andrey Klymchenko, Dr. Mayeul Collot, Dr. Andreas Reisch and Dr. Youri Arntz for their support, scientific discussions and helpful suggestions.

Many thanks to my PhD and Postdoc colleges: Dr. Lesia Kovalenko (for reviewing the HIV part of the thesis), Dr. Vasyl Kilin, Dr. Marianna Sholokh, Dr. Kateryna Trofymchuk and Dr. Iryna Lysova who helped me to establish myself in Strasbourg during the early stage of my master studies; Dr. Manuel Pires, Dr. Sarwat Zgheib, Tanveer Ahmad and Waseem Ashraf for teaching me to work in a cell culture lab, to do transfection, immunofluorescent labeling and western blot experiments and providing useful tips and lifehacks that are not written in published protocols; Dr. Bohdan Andreiuk, Nina Melnychuk, Tkhe Kyong Fam, Oleksii Dukhno, Taras Sych, Dr. Liliyana Zaayter, Dr. Redouane Bouchaala, Anne Runser, Doriane Heimburger, Faisal Nadeem and Dr. Yosuke Niko for their help in the lab and for sharing good moments outside of the lab (cinema, restaurants, bowling etc.).

Many thanks to my friend Rajhans Sharma, who has been always there when I needed help, that includes bringing me to the hospital when I broke my hand and providing me food during the nights of thesis writing. His company made the PhD life much better during tough times.

I would like to thank Dr. Guy Duportail, Marlyse Wernert, Ingrid Barthel, Melanie Muser and Geraldine Schverer for their help with diverse administrative procedures and paper work. Thanks, Guy, for showing me the election process in France.

I am immensely grateful to all my family members and especially my parents for their support, love and encouragements through all my life. I wish to express my gratitude to Maïté and her family who introduced me to the French culture, supported me all along the thesis writing and allowed me to work during the Christmas holidays.

I am thankful to French ministry of science and education for the financial support.

Thank you very much!
Sasha

Abstract

During this experimental thesis work, we investigated the nuclear and nucleolar localization of the nucleocapsid protein (NC) of HIV-1. Previous studies performed in our laboratory evidenced a strong accumulation of NC in the subnuclear structure called nucleolus. Playing role in multiple cellular processes, nucleolus is often targeted by viruses to promote their replication. Electron microscopy revealed three components within the nucleolus (fibrillar centers, dense fibrillar component and granular component) associated to specific steps of the ribosome biogenesis. Based on this "compartment ~ functions" relation, we decided to characterize precisely the distribution of NC in all three nucleolar components to understand better the reason of nucleolar targeting by NC during the replication cycle. The background to this field will be given in the Introduction, where mentioned above processes are discussed in more details.

Significant part of the project was focused on the development of a high-resolution optical microscopy approach in our laboratory. Among different existent techniques, we selected the localization-based microscopy PALM/STORM, because of its high lateral resolution and the simplicity of implementation. While it is quite straightforward to perform single color experiments, it becomes much more challenging in multi-color imaging. Different factors as sample drift, chromatic aberration, optical and chemical properties of fluorescent probes need to be considered. These problems and solutions to them are summarized in the first part of the Results sections and in the Scientific Reports publication.

After the optimization of imaging protocols, the NC-mEos2 fusion protein overexpressed in HeLa cells was visualized simultaneously with immunolabeled nucleolar markers. The use of high-resolution fluorescence microscopy enabled us to resolve for the first time the three nucleolar compartments and to demonstrate the preferential localization of NC in the granular compartment of nucleolus. Finally, preliminary experiments performed with living cells showed that NC is actively transported in the nucleus and therefore may interact directly with nucleolar proteins.

Chapter 1. Introduction

1.1. HIV-1

1.1.1. General information

Human immunodeficiency virus type 1 (HIV-1) was first isolated from a culture derived from a lymph node biopsy at the Institute Pasteur (Paris) in 1983 [1]. Shortly after, the relation between HIV infection and acquired immunodeficiency syndrome (AIDS) has been established. The virus targets preferably CD4+ helper T-cells [2,3] of the immune system that coordinate the immune response of the organism to pathogens like viruses, bacteria and fungi. The virus uses these cells and their proteins for replication. At the end of HIV life cycle, newly produced particles leave the host cell, destroy the membrane and as a result the cell itself. Without treatment, the viral load increases [2,3] and the number of immune cells decreases. Untreated HIV replication causes progressive CD4+ T cell loss and a wide range of immunological abnormalities, leading to an increased risk of infectious complications. With a weak immune system, all the infections that normally should have been eliminated, can now easily progress without any resistance.

Since its discovery, HIV-1 has been the subject of intense investigation and is believed to be one of the most well-studied viruses [4]. Sequence comparisons suggest that both HIV-1 and HIV-2 are the result of cross-species transmissions [5]. The virus most closely related to HIV-1 is the simian immunodeficiency virus (SIV). Surveys of African apes identified that *Pan troglodytes troglodytes* is a primary reservoir for HIV-1 (groups M, N) [6,7] and *Sooty mangabey (Cercocebus atys)* – for HIV-2 [8,9]. The SIV has been probably transmitted to humans when they hunted these animals for meat, and then in a new host the virus evolved to HIV. Using statistical approaches applied to HIV-1 sequence data from central Africa, it was estimated that the time of first infections was at the beginning of the twentieth century (1920s Kinshasa, now the Democratic Republic of Congo) [10] and then virus started to spread across Africa and later the whole world. Location and dating estimates were validated using the earliest HIV-1 archival sample, also from Kinshasa [10]. In 2017, according to the data and estimation provided by UNAIDS (Joint United Nations Programme on HIV/AIDS), around 37 million people live with HIV, 1.8 million has been infected in 2016 and 1.0 million AIDS-related deaths have been registered the same year [11].

Progress in understanding of the virus structure, replication cycle, infection pathway and pathogenesis, helped scientists to develop the antiretroviral (ARV) drugs that are able to decrease the viral load, suppress the virus replication, and decrease the probability of

transmission from individuals receiving the treatment to their non-infected partners [12]. Thanks to these developments, AIDS-related deaths started, and till now continue, to decline. Global scale-up of antiretroviral therapy (ART) has been the primary contributor to a 48% decline in deaths from AIDS-related causes, from a peak of 1.9 million in 2005 to 1.0 million in 2016 [11]. Collectively, the world receives high marks for its HIV/AIDS efforts from the Joint United Nations Program on HIV/AIDS (UNAIDS) in Geneva, Switzerland. It notes in Ending AIDS [13] that 19.5 million of the estimated 36.7 million people living with the virus now receive lifesaving antiretroviral drugs. This is the first time in history that more than half of the infected people are being treated.

Unfortunately, the existent antiretroviral therapies are not able to eliminate the virus completely, but only minimize the negative effects and extend the life expectance. The problem with these therapies is related to the virus mutation and to the development of drug resistance [14]. HIV-1 exhibits high genetic diversity because of its high rates of recombination and mutation, rapid turnover rates, and the persistent nature of the virus [14,15]. The high rate of HIV-1 evolution enables the virus to elude the body's immune control and better resist to drug therapy. When a person is treated with multiple drugs that target simultaneously several viral proteins (e.g. protease inhibitors together with reverse transcriptase inhibitors) the rate at which resistance can develop is greatly reduced, making treatment more effective in a long term. However, the antiretroviral therapy is not curative; if drugs are stopped, the virus rebounds within weeks [12]. In addition to T helper cells, HIV-1 can also infect the other cell types (memory CD4+ T cells, naive CD4+ T cells, monocyte and macrophage lineage), among which are long-lived cells and self-renewal cells [16,17]. Once HIV DNA is integrated into the host chromatin, the virus has the capacity to reinitiate rounds of replication as long as the cell persists. ART can prevent new cells from becoming infected, but these drugs cannot eliminate infection once the viral DNA is successfully integrated into its target cell. This reservoir is also the source of virus return among effectively treated individuals who interrupt or stop ART. Limitation of ART drugs is that they must be taken by patient each day. Prolonged treatment is associated with drug toxicities and a risk of viral resistance. Thus, the HIV research community must continue to explore novel therapeutic strategies, including those that target steps in the viral replication cycle that are not disrupted by currently available drugs.

1.1.2. Viral genome

Human immunodeficiency virus (HIV) is classified within lentivirinae – a subfamily of retroviridae viruses with RNA-encoded genetic information, that utilize host DNA genomes to proliferate via reverse transcription and chromosomal integration.

The HIV-1 genome is encoded by an ~9-kb RNA. Two copies of unspliced gRNAs are found as a non-covalent dimer in the mature viral particles. The HIV-1 genome encodes nine open reading frames (Figure 1). Three major genes encode the Gag, Pol, and Env polyproteins, which are subsequently proteolyzed into individual proteins common to all retroviruses. [18] The four proteins contained in Gag (matrix (MA), capsid (CA), nucleocapsid (NC), and p6) and the two contained in Env (surface (SU or gp120) and transmembrane (TM or gp41)) are structural components that build the virion's core and outer membrane envelope. The three proteins contained in Pol (protease (PR), reverse transcriptase (RT) and integrase (IN)) provide essential enzymatic functions and are also encapsulated within the particle. HIV-1 encodes six additional proteins, often called accessory proteins. Three of them (Vif, Vpr, and Nef) are found in the viral particle. Two other accessory proteins, Tat and Rev, provide essential gene regulatory functions, and the last protein, Vpu, indirectly assists in assembly of the virion [18,19].

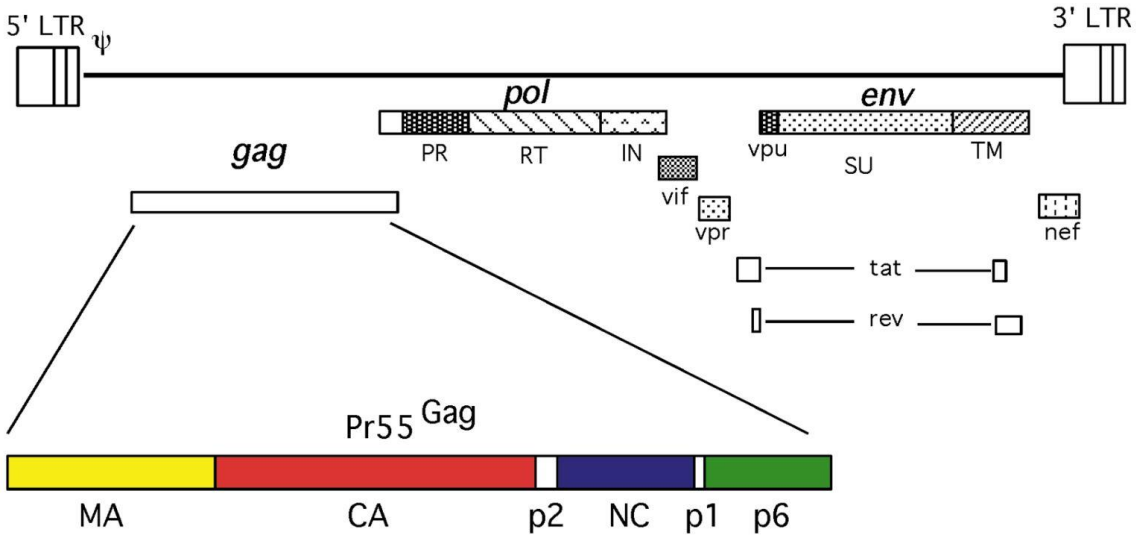

Figure 1. Organization of HIV-1 genome Adapted from (Freed E., 1998) [20].

The coding regions are adjoined with two non-coding sequences, 5′-UTR and 3′-UTR. The 5′-UTR of the HIV-1 genomic RNA (gRNA) is a highly structured region that contains a number of folded RNA elements (Figure 2): the transactivation response element (TAR), which serves as the binding site for the viral Tat protein and the positive transcription elongation factor b (P-TEFb) complex; the polyadenylation site; the primer-binding site (PBS), which

binds a molecule of tRNA(Lys3) so that it is packaged into virions and can prime the initiation of reverse transcription; and Ψ site, which is composed of four stem-loops SL (SL1 – SL4), among which the dimer initiation signal (DIS), which contributes to RNA dimerization; the major splice donor (SD); and *gag* start codon AUG [21,22].

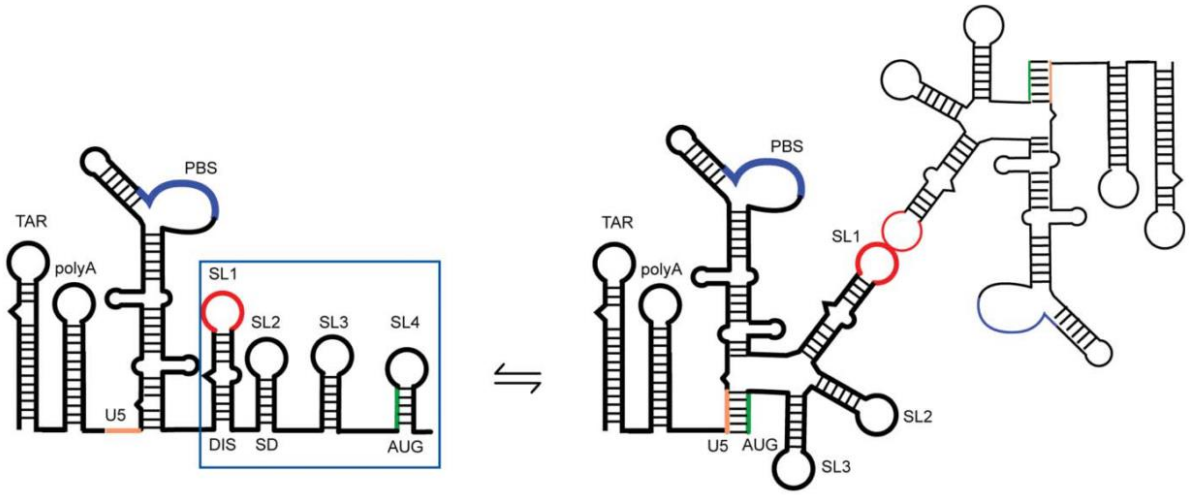

Figure 2. Schematic representation of the first 615 nucleotides at the 5′-end of HIV-1 gRNA. The Psi region (SL1-SL4) is highlighted with a blue square. Two different secondary structure conformations are demonstrated in the figure: one facilitates the translation (left) whereas the second favors the dimerization and genome packaging (right), showing U5-AUG interaction. Adapted from (Bernacchi et al., 2017) [23].

The 5′-UTR region plays a crucial role along the viral lifecycle and is the most conserved gRNA part. The selective packaging of gRNA is based on cis-acting elements located in the 5′ untranslated region (UTR) of the gRNA. The NC domain of Gag polyprotein promotes gRNA incorporation into viral particles and displays a strong preference for Psi-containing RNAs. Moreover, each structural element in Psi was previously found to behave as an independent binding site for the mature NCp7. Two different secondary structure conformations were suggested for 5′-UTR region: one which facilitates the translation and another one which favors the dimerization and genome packaging [24] (Figure 2).

1.1.3. The structure of viral particle

The HIV virion is approximately 100 nm in diameter, composed of two copies of 35S single-stranded RNA [25] embedded together with RT, IN, and PR within the protein clusters of NC, CA, and MA. All viral components are enclosed within a lipid/lipoprotein membrane, derived from the membrane of the host cell, flanked by TM and SU proteins (Figure 3). Exposed surface glycoproteins (SU, gp120) are anchored to the virus via interactions with the transmembrane protein (TM, gp41). These envelope proteins initiate an infection through the interaction with CD4 receptors and chemokine co-receptors expressed on the host cell membrane surfaces [3,26].

The matrix shell comprising approximately 2000 copies of the matrix protein (MA, p17) lines the inner surface of the viral membrane. In the center of viral particle there is a conical core composed of the same 2000 copies of the capsid protein (CA, p24). It encapsidates two copies of the unspliced viral genome, stabilized as a ribonucleoprotein complex with the nucleocapsid protein (NC, p7), and three essential virally encoded enzymes: protease (PR), reverse transcriptase (RT) and integrase (IN). Some of the accessory proteins, Nef, Vif and Vpr, are also packaged to the HIV particles, while the other three, Rev, Tat and Vpu, are found and function within the host cell.[27]. Proper assembly of capsid cores as well as uncoating or disassembly (i.e. removal of the CA shell and release of the ribonucleoprotein complex) are both critical for formation of a functional reverse transcription complex (RTC).

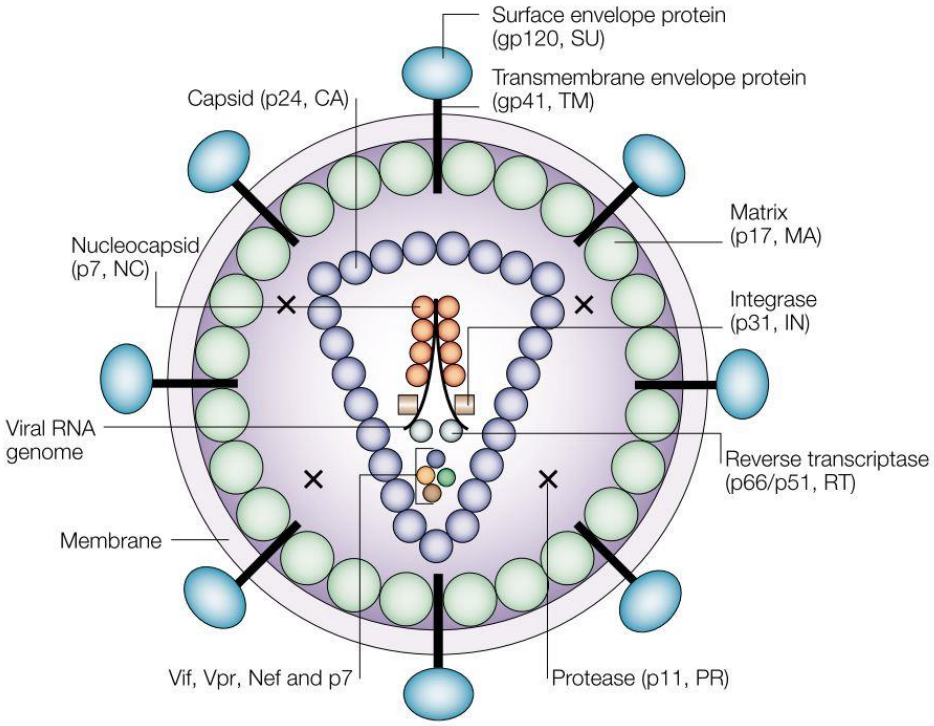

Figure 3. Schematic representation of the HIV-1 virion organization. Adapted from (Robinson, H. L., 2002) [28].

In the immature particle, Gag molecules are packed in a radial manner. Following the release of individual Gag domains by the viral protease, the CA proteins reassemble to form the conical capsid core. The organization of CA in the mature HIV-1 capsid core is well defined. An early study correctly proposed that the capsid core assembles with fullerene-like geometry, such that CA forms predominantly hexameric rings to generate a lattice that is closed off at both ends by the inclusion of pentamers: seven at the wide end and five at the narrow end [29,30].

1.1.4. Viral proteins

Structural proteins: MA, CA, NC, p6

MA (132 amino acids (aa)) is the N-terminal component of the Gag polyprotein and is important for the attachment of Gag and GagPol polyproteins to the plasma membrane prior to viral assembly. Two parts of MA are involved in membrane targeting: N-terminal myristate group that inserts into the lipid membrane, and basic residues located within the first 50 amino acids that interact with phospholipid head groups. In addition to targeting Gag and GagPol to the membrane, MA also favors the incorporation of Env glycoproteins with long cytoplasmic tails into viral particles [31,32].

CA (231 aa) forms the core of the virus particle, with ∼2000 copies per virion. The C-terminal domain (residues 152–231) functions primarily in assembly and is important for CA dimerization and Gag oligomerization [21,29].

NC (55 aa) is a small, basic, nucleic acid binding protein with one or two zinc-binding domains or zinc fingers (ZFs), each containing the metal-ion binding motif CX2CX4 HX4 C, more commonly referred to as CCHC motif. The NC protein of HIV-1 has two zinc fingers, which are connected by a short flexible basic peptide linker. The amino acid composition of the two fingers is similar, though not identical [33]. Moreover, their biological activities and biochemical properties are not equivalent and both fingers are required for virus replication [34]. NC has two unique aromatic amino acid residues, F16 and W37, in each ZF motif. It has previously been shown that these aromatic residues and linker region are important for the nucleic acid chaperone activity of NC, including dimerization of the gRNA [35,36].

The primary function of NC is to bind specifically to the packaging signal and deliver full-length viral RNAs into the assembling virion. NC is a basic protein that also binds single-stranded nucleic acids nonspecifically, leading to coating of the genomic RNA that presumably protects it from nucleases and compacts it within the core. Chaperone-like functions of NC enhance other nucleic acid-dependent steps in the life cycle; for example, by promoting annealing of the tRNA(Lys3) primer, melting of RNA secondary structures, or DNA strand exchange reactions during reverse transcription or by stimulating integration [37,38]. In addition, Zhang and Crumpacker showed that NC nuclear localization plays an important role in inducing HIV-1 early mRNA expression and contributes to the rapid viral replication that occurs during HIV-1 infection [39]; NC also induces the degradation of Tat protein via the proteasome pathway [40].

The **p6** comprises the C-terminal 51 amino acids of Gag and is important for incorporation of Vpr during viral assembly. The p6 domain recruits the endosomal sorting complex required for transport (ESCRT) apparatus, which catalyzes the membrane fission step to complete the budding process [21].

Viral enzymes: PR, RT, IN

PR (99 aa) cleaves the Gag and GagPol polyproteins to produce the mature infectious viral particle. PR functions as a dimer and is a part of Pol, so PR activity initially depends on the concentration of GagPol and the rate of autoprocessing. The final stoichiometries are determined largely by the amount of GagPol produced by ribosomal frameshifting and incorporated into the virion (~5–10% of Gag). Cleavage efficiencies of PR can vary substantially among sites, thereby influencing the order of appearance of different processed proteins [19].

RT is a heterodimer containing a 560 aa subunit (p66) and a 440 aa subunit (p51) both derived from the Pol polyprotein. The protein is responsible for the process of reverse transcription, when viral genome is transformed into duplex DNA in order to be integrated in the host chromosome during integration step. RT catalyzes both RNA-dependent and DNA-dependent DNA polymerization reactions and contains an RNase H domain that cleaves the RNA portion of RNA-DNA hybrids generated during the reaction [41].

IN (288 aa) catalyzes a series of reactions to integrate the viral genome into a host chromosome. In the first step, IN removes two 3′ nucleotides from each strand of the linear viral DNA, leaving overhanging CAOH ends. In the second step, the processed 3′ ends are covalently joined to the 5′ ends of the target host DNA. In the third step, which probably involves additional cellular enzymes, unpaired nucleotides at the viral 5′ ends are removed and the ends are joined to the target site 3′ ends, generating an integrated provirus flanked by five base-pair direct repeats of the target site DNA [42].

Envelope proteins: SU (gp120) and TM (gp 41)

Viral entry is initiated by the binding of the **SU (gp120)** glycoprotein (515 aa), located on the viral membrane surface, to the specific cell surface receptors. The major receptor for HIV-1 is CD4, an immunoglobulin (Ig)-like protein expressed on the surface of a subset of T cells and primary macrophages. The SU-CD4 interaction is not sufficient for HIV-1 entry. Instead, a group of chemokine receptors that mobilize intracellular calcium and induce leukocyte chemotaxis serves as essential viral coreceptors [43].

TM (gp41) is a 345 aa protein located in the viral membrane. The protein mediates fusion between the viral and cellular membranes following receptor binding. An N-terminal hydrophobic glycine-rich "fusion" peptide has been predicted to initiate fusion, and a transmembrane region is important both for fusion and for anchoring Env in the viral membrane [43].

Accessory proteins: Tat, Rev, Vif, Vpr, Nef, Vpu

Tat (86-101 aa) enhances the processivity of transcribing polymerases, and under some conditions may also enhance the rate of transcription initiation. Tat increases production of viral mRNAs ~100-fold and consequently is essential for viral replication. In the absence of Tat, polymerases generally do not transcribe beyond a few hundred nucleotides, though they do not appear to terminate at specific sites. Unlike typical transcriptional activators, Tat does not bind to a DNA site but rather to an RNA hairpin known as TAR (trans-activating response element), located at the 5′ end of the nascent viral transcripts [44].

Rev (116 aa) is required to export unspliced RNAs that contain a Rev-responsive element (RRE) in the Env coding region. Rev contains a leucine-rich nuclear export signal (NES) that allows it to shuttle between the nucleus and cytoplasm [45].

Vif is a 192 aa protein that is important for the production of highly infectious mature virions. Vif mutant viruses show markedly reduced levels of viral DNA synthesis and produce highly unstable replication intermediates, suggesting that Vif functions before or during DNA synthesis. The viral infectivity factor (Vif) is essential for the productive infection and dissemination of HIV-1 in non-permissive cells (such as CD4+ T lymphocytes and macrophages, the natural cell targets of the virus), containing the cellular anti-HIV defense cytosine deaminases APOBEC3 (A3G and A3F). Vif neutralizes the antiviral activities of the APOBEC3G/F by diverse mechanisms including their degradation through the ubiquitin/proteasome pathway and their translational inhibition. In addition, Vif appears to be an active partner of the late steps of viral replication by interacting with Gag, reverse transcriptase and genomic RNA [46].

Vpr is a small basic protein (14 kDa) of 96 amino acids. It is the only viral auxiliary protein specifically incorporated into virus particles through direct interaction with the Gag precursor, indicating that this presence in the core of the mature virions is mainly required for optimal establishment of the early steps of the virus life cycle in the newly infected cell. In spite of its small size, a plethora of effects and functions have been attributed to Vpr, including

induction of cell cycle arrest and apoptosis, modulation of the fidelity of reverse transcription, nuclear import of viral DNA in macrophages and other non-dividing cells, and transcriptional modulation of viral and host cell genes [47].

Vpu (81 aa) promotes degradation of CD4, when the receptor interacts with the newly synthesized Env glycoproteins (gp160) in the endoplasmic reticulum, thus allowing Env transport to the cell surface for assembly into viral particles [48].

Nef is a 206 aa N-terminally myristoylated protein that, like Vpu, reduces the levels of cellular CD4. Nef facilitates the routing of CD4 from the cell surface and Golgi apparatus to lysosomes, resulting in receptor degradation and preventing inappropriate interactions with Env. By downregulating CD4, Nef may enhance Env incorporation into virions, promote particle release, and possibly affect CD4+ T-cell signaling pathways [49,50,51].

1.1.5. Virus life cycle

The HIV-1 replication cycle (Figure 4) is a complex process that is regulated by both viral and cellular proteins and can be divided into early and late phases. The early phase starts when the virus binds to cell surface receptors and is followed by the cell entry; uncoating of the viral capsid; reverse transcription of the viral RNA to DNA; nuclear import of viral DNA; and terminates when the proviral DNA integrates into the host genome [26,41,42]. The late phase refers to the events that occur from gene expression to the release and maturation of new virions, and includes the transcription of viral genes; export of the viral RNAs from the nucleus to the cytoplasm; translation of viral RNAs to produce the Gag polyprotein precursor (also known as Pr55Gag), the GagPol polyprotein precursor, the viral envelope glycoproteins (Env glycoproteins), and the regulatory and accessory viral proteins; trafficking of Gag and GagPol precursors and of the Env glycoproteins to the plasma membrane; assembly of the Gag and GagPol polyproteins at the plasma membrane; encapsidation of the viral RNA genome by the assembling Gag lattice; incorporation of the viral Env glycoproteins; budding off of the new virions from the infected cell; and particle maturation [21,29].

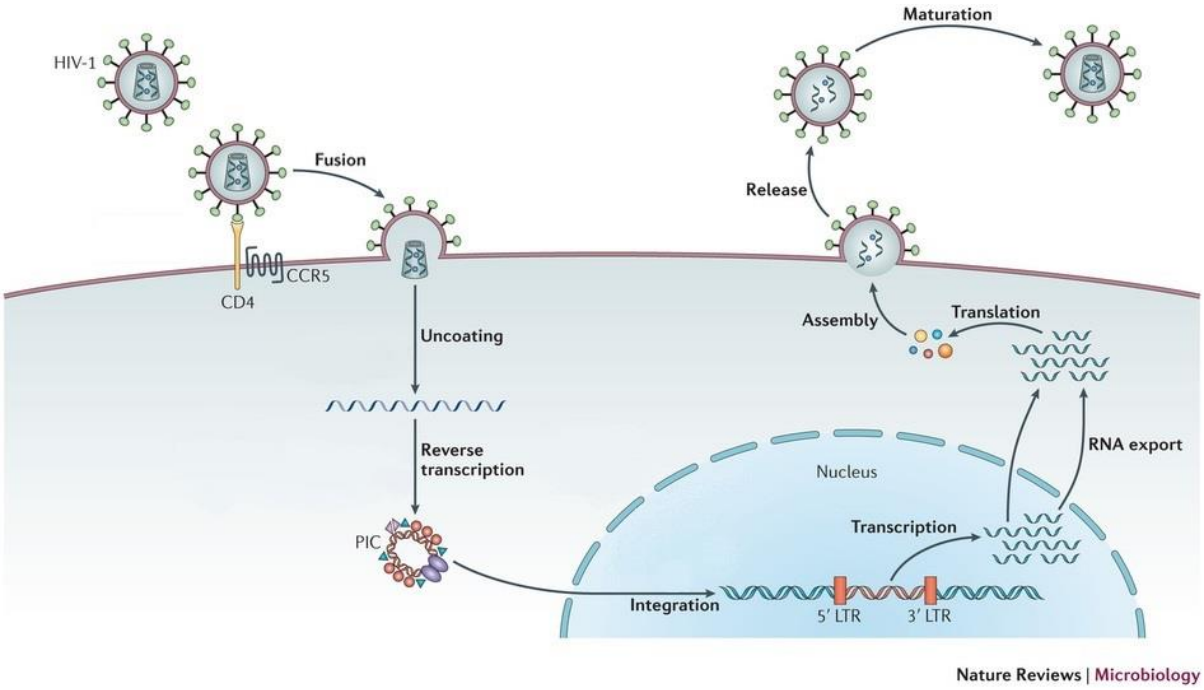

Figure 4. HIV replication cycle. Adapted from (Barré-Sinoussi et al., 2013) [4].

Infection and entry

HIV-1 attacks different cells of immune system that expresses CD4 receptor on their surfaces, for example T lymphocytes, monocytes, macrophages and dendritic cells. The infection process begins when the surface (SU) envelope (Env) glycoprotein gp120 binds CD4. This binding triggers a conformational change in gp120 that enhances its affinity for a secondary receptor, or "coreceptor". The major physiologically relevant coreceptors for HIV-1 are β-chemokine receptor type 5 (CCR5) and α-chemokine receptor type 4 (CXCR4). Upon binding of gp120 to the coreceptor, further conformational changes in both gp120 and gp41 trigger a membrane fusion reaction that delivers the viral core into the cytoplasm. HIV-1 can enter a host cell through two different mechanisms: either direct, pH-independent fusion with the plasma membrane (PM) or clathrin-mediated endocytosis followed by low-pH fusion with the endosomal membrane [26,43].

Reverse transcription

Reverse transcription is an essential step in retroviral replication. It consists of a complex series of biochemical reactions that culminate in synthesis of a linear double-stranded (ds) DNA copy of the single-stranded (ss) viral RNA (vRNA) that is ultimately integrated into the host genome. This process, which is catalyzed by the virus-encoded reverse transcriptase (RT) enzyme, is an early postentry event that occurs in the cytoplasm of infected cells. Although there are viral and cellular factors that assist during the reverse transcription the two

enzymatic activities that are necessary and sufficient to carry out this process are present in RT. These are DNA polymerases that can copy either RNA or DNA template, and RNase H that degrades RNA if, and only if, it is a part of RNA-DNA duplex [41].

Like many other DNA polymerases, RT needs both a primer and a template. Genomic RNA is plus-stranded (the genome and the messages are copied from the same DNA strand), and the primer for the synthesis of the first DNA strand (the minus strand) is a host tRNA(Lys3) which is annealed to a complementary PBS sequence at the 5′ end of the viral RNA. It would appear, based on *in-vitro* experiments, that the addition of the first few nucleotides is slow and difficult. DNA synthesis speeds up considerably once the first five to six deoxyribonucleotides have been added to the 3′ end of the tRNA primer [52,53]. DNA synthesis creates an RNA–DNA duplex, and the vRNA sequence that has been already copied start to be degraded by the RNase H. When the minus-strand DNA synthesis nears the 5′ end of the genomic RNA, the U5 and R regions are copied and -ssDNA is transferred to the 3′ end of the genome to continue the elongation. Meanwhile, the synthesis of +ssDNA is initiated by the PPT region located next to U3 and propagates in the opposite to -ssDNA sense till the primer tRNA(Lys3) is copied. After this, RNase H removes the primer and the rest of initial vRNA. The 3′ end of the plus-strand DNA contains 18 nucleotides copied from the tRNA primer, which are complementary to 18 nucleotides at the 3′ end of the minus-strand DNA that were copied from the PBS. These two complementary sequences anneal, and DNA synthesis extends both the minus and plus strands to the ends of both templates. After the viral DNA is synthesized by reverse transcription in the cytoplasm, it stably associates with IN and other proteins as a high-molecular-weight nucleoprotein complex or pre-integration complex (PIC) that is later transported to the nucleus for subsequent integration.

Integration to host genome

To carry out the integration, PICs must cross the nuclear membrane. Several nuclear pore proteins appear to be important not only for nuclear localization but also for efficient integration after nuclear entry. In the nucleus, the covalent attachment of the proviral DNA copy to the host cell DNA is catalyzed by the virus encoded IN protein. Integration occurs precisely at the termini of the viral DNA, but integration can take place at many locations in the host genome. Most positions in chromosomal DNA can serve as integration acceptor sites, but there are distinct regional preferences that differ among groups of retroviruses. Some of these preferences appear to involve chromatin-associated factors that also interact with IN.

However, the viral DNA can also undergo several circularization reactions that do not support subsequent replication and represent dead ends for the virus. The integrated viral DNA, known as the provirus, serves as the template for the synthesis of viral RNAs, which are transported to the cytoplasm [42].

Expression of viral gene and proteins

After synthesis in the nucleus, HIV-1 RNAs are transported to the cytoplasm, where they undergo two main processes: translation into viral proteins and packaging into newly assembled virus particles. A large number of viral mRNA species are synthesized, some of which are multiply spliced before nuclear export; others are exported in a partially spliced or unspliced form. The host cell transcriptional machinery produces doubly spliced HIV transcripts for the expression of regulatory proteins – Tat and Rev. Then the Rev protein mediates the nuclear export of intron-containing viral RNAs (unspliced or singly spliced) by binding to a highly structured cis-acting RNA element known as the Rev-responsive element (RRE). The full-length RNA serves as a messenger (mRNA) to direct the translation of the 55 kDa Gag polyprotein precursor. At the same time, the 160 kDa GagPol polyprotein, which contains the viral enzymes protease, reverse transcriptase and integrase, is also expressed at ~5% of the level of Gag, owing to a programmed ribosomal frameshifting event during Gag translation [54,55].

Assembly

The path to the virus assembly begins with translocation of Gag and GagPol to the assembly site – the plasma membrane (PM). Intracellular trafficking of Gag and its binding to the membrane is mediated by a membrane-binding domain, which comprises of the covalently attached myristic acid linked to the N-terminus of MA and the highly basic patch of residues that forms a positively charged surface at the "top" of the folded MA domain. One of the primary functions of the basic patch is to bind the PM phosphoinositide phosphatidylinositol-4,5-bisphosphate (PtdIns(4,5)P2), which plays a major role in directing Gag to the PM [21].

During its trafficking to the plasma membrane, or after its arrival there, Gag interacts with dimeric viral RNA, and in the same time it begins to multimerize. Retroviral NC domains direct the packaging of viral genomic RNA by binding to the packaging signal, often referred to as the ψ-element, that is located near the 5′ end of the genomic RNA in the 5′ untranslated region (UTR). As in the case for other retroviruses, two copies of full-length viral RNA are packaged into HIV-1 virions. The presence of two copies of genomic RNA in each particle

provides the opportunity for recombination during reverse transcription and may also allow reverse transcription to proceed if one RNA copy is damaged [56].

Virus assembly proceeds at the plasma membrane, where the Gag protein and the full-length genomic RNA assemble into the nascent, immature virus particle together with the GagPol precursor. Although the Gag–RNA contacts help to nucleate the assembly, the main viral determinant that drives Gag multimerizetion is the CA domain [57]. The assembling particle incorporates Env glycoproteins. Env incorporation could, in theory, take place through several non-mutually exclusive mechanisms: a passive process; co-targeting of Gag and Env to a common site on the plasma membrane (for example, a lipid raft-type microdomain); direct recruitment of Env by Gag; and indirect recruitment of Env by Gag via a host cell bridging protein [43]. Genetic data support a central role for the MA domain of Gag and the gp41 cytoplasmic tail of Env in Env glycoprotein incorporation and suggest direct or indirect interactions between Env and MA. In the immature particle, Gag molecules are aligned and packed radially, with the MA domain bound to the inner leaflet of the viral membrane and the C terminus of Gag oriented towards the center of the particle [58].

Release and maturation

When the new immature viral particle is formed, Gag then recruits the endosomal sorting complex required for transport (ESCRT) machinery via a direct association between the PTAP motif in p6 and the tumor susceptibility gene 101 (TSG101) subunit of ESCRT-I. Gag also engages in direct binding with the ESCRT-associated factor ALG2-interacting protein X (ALIX), primarily through the YPXL motif in p6. As the budding process proceeds, the ESCRT-III and vacuolar protein sorting 4 (VPS4) complexes are recruited and drive the membrane scission reaction that leads to the particle release [21].

When expressed alone, Gag is competent to drive the assembly and release of non-infectious, immature virus-like particles (VLPs). Particle infectivity requires the proteolytic activity of the viral protease, which is expressed and brought into virions as part of the GagPol precursor. Concomitant with the virus release, the viral protease cleaves a number of sites in both Gag and GagPol polyproteins to trigger the virus maturation. PR cleavage leads to the core condensation and the generation of a mature, infectious virion which is now capable of initiating a new round of infection. Protease-mediated Gag and GagPol processing is accompanied by a major change in virion morphology (Figure 5). In the immature particle, Gag

molecules are packed in a radial manner. Following liberation of the individual Gag domains by the viral protease, the CA protein reassembles to form the conical capsid core [19].

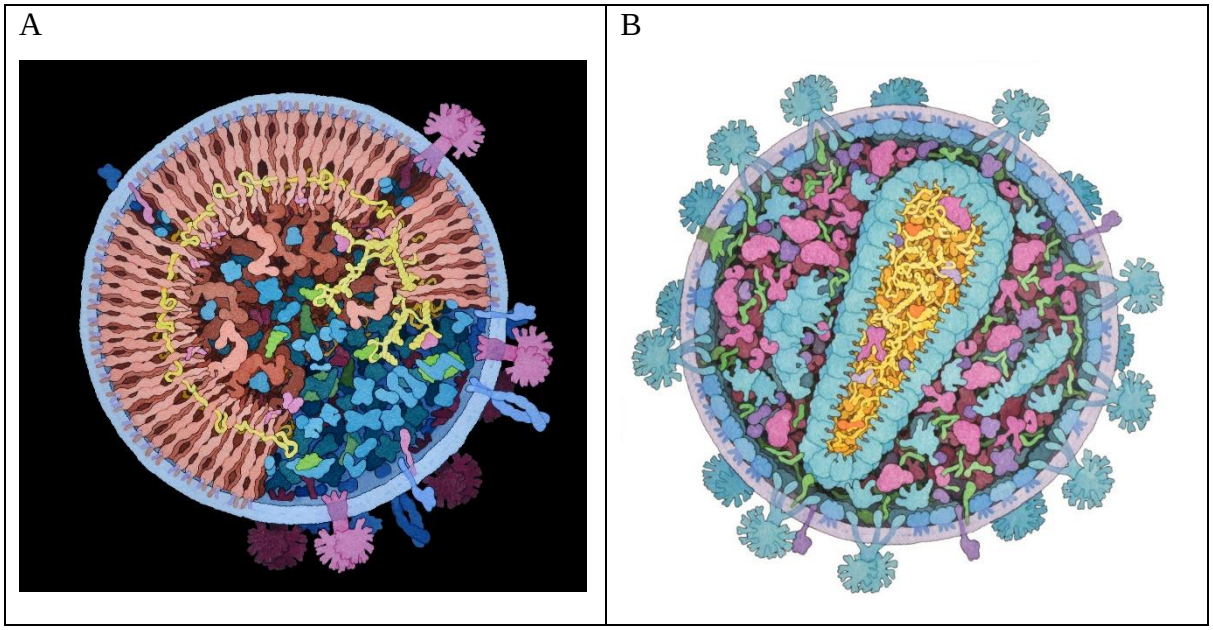

Figure 5. Structure of immature (A) and mature (B) HIV-1 particles. Adapted from David S. Goodsell [59].

The released and mature viral particles is now ready to infect new cells and re-initiate the virus replication cycle by binding to the CD4 receptor on the cell's surface.

1.1.6. Nucleocapsid protein (NC)

Viral nucleocapsid protein (NC) has highly conserved structure among different viral strains; it plays a key role in the early and late stages of the virus life cycle, and therefore might be a good target for the development of new inhibitors [60]. Indeed, the mature form of the nucleocapsid protein NCp7 shows chaperone activities on HIV-1 RNA and DNA, it remodels nucleic acid structures so that the most thermodynamically stable conformations are formed. This activity is essential for virus replication and has a critical role in mediating highly specific and efficient reverse transcription. As a part of Gag polyprotein, NC domain recognizes the packaging signal sequence in the full length vRNA genome, dimerizes and encapsidates it into the viral particle. In addition, it was already shown that a point mutation of NC leads to noninfectious virus, what makes it an interesting object for investigations [60].

Several studies demonstrate the importance of NC during the integration step. For example, Thomas et al. [61] found that the quantities of viral DNA (vDNA) observed with viruses containing either the nucleocapsid His23Cys or His44Cys mutations were significantly lower than those observed in infections with virus containing wild-type NC. In-depth kinetic studies showed that both mutations caused sever defects in integration, but minimally perturbs the

reverse transcription. This suggests that the principal reason for the replication defectiveness of these mutant viruses is impairment of integration [61]. In addition, the effect of NC on 3′ processing of viral DNA by integrase and integrase-mediated strand-transfer has been also determined by multiple research groups [33,37,62].

NC functions throughout the virus replication cycle; as a result, research aimed at blocking NC function has been underway for many years. Much of this effort has been aimed at developing compounds that eject zinc from the NC zinc fingers. A limitation of this approach has been toxicity arising from a lack of specificity for retroviral NC versus host protein zinc-fingers. For the development of new inhibitors, the knowledge of NC functions and interactions with other viral and host proteins during the replication cycle is essential.

1.1.7. Nuclear and nucleolar localization of NC

A model was recently proposed (Mirambeau G. and Lyonnais S.) in which due to its lower affinity to dsDNA as compared to ssDNA and vRNA, a large fraction of NCp7 is released in the cytoplasm during the process of reverse transcription, so that only a small fraction of NCp7 remains associated with the PIC [63,64]. Indeed, multiple studies have demonstrated the cytoplasmic and nuclear localization of NC with different strategies and techniques of determination [39,65].

Infection with wild type

Gallay et al. examined the subcellular distribution of various HIV proteins during the early steps of the virus life cycle (Figure 6A). To this end, CD4+ HeLa-derived P4-2 cells were acutely infected with the wild type HIV-1; cellular extract was fractioned into membranes, cytosol and nucleus at 1 h and 8 h postinfection; finally, fractions were analyzed by immunoprecipitation and western blot tests. The results show that at 1 h postinfection, NC was detected in the cytosol, whereas at 8 h postinfection, approximately half of NC had migrated to the nucleus [65]. In another study, Zhang and Crumpacker [39] examined the time course of virion NC nuclear localization by using immunofluorescent staining with a monoclonal antibody specific to NC (Figure 6B and 6C). The virion NC appeared in the cytoplasm at 4 h postinfection; at 10 h – in the nucleus; at 18 h - accumulated predominantly in the nucleus; and at 32 h – the protein was found in both the nucleus and the cytoplasm. This pattern of NC nuclear localization was observed in both human lymphatic cell line H9 cells and in peripheral blood mononuclear cell (PBMC) acutely infected with HIV-1_{IIIB}.

More recent studies revealed the *nucleolar* localization of NC protein [66,67]. However, it is worth to note that the number of NC copies in cells was much higher because of transfection and overexpression (see the following section).

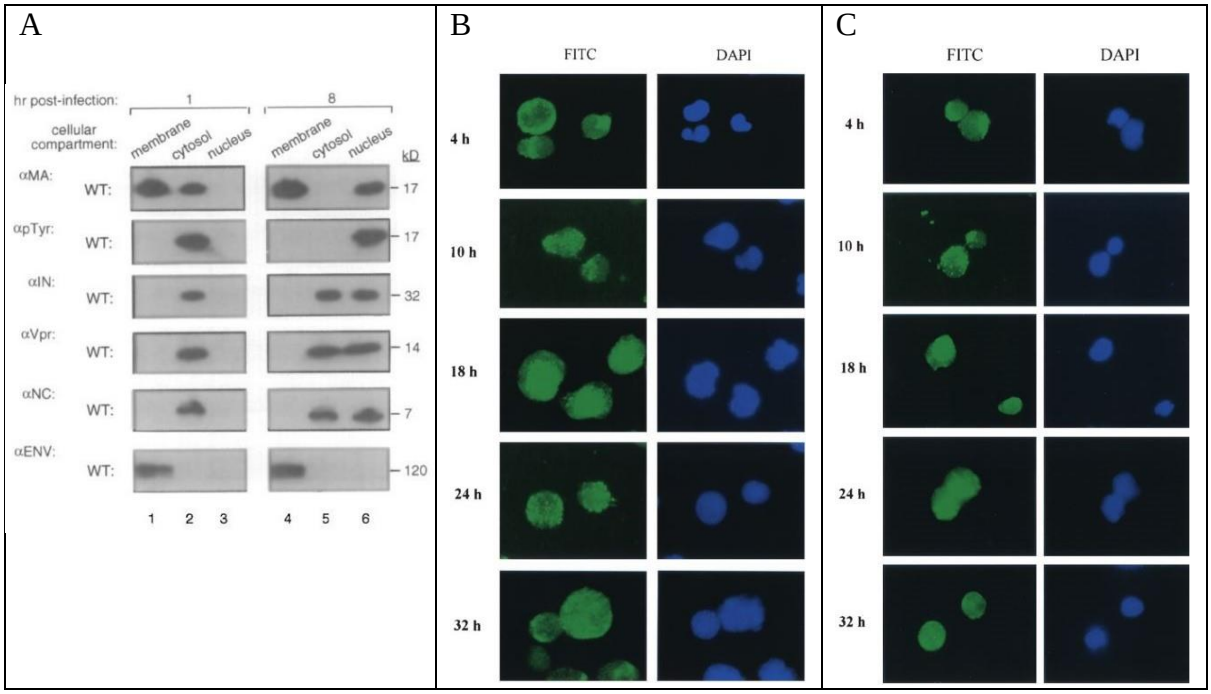

*Figure 6. Nuclear localization of NC in cells infected with wild-type HIV-1. (A) Extracts of **P4-2** cells infected with wild-type HIV-1. Immunoprecipitation followed by western blot shows the nuclear localization of NC protein at 8 hours after infection. Adapted from (Gallay et al., 1995)* [65]*. (B and C) Immunostaining of NC with fluorescein isothiocyanate (FITC) in **H9** cells (B) and in **PBMC** cells (C) acutely infected with HIV-1_{IIIB}. Adapted from (Zhang and Crumpacker, 2002)* [39].

Transfection with plasmid constructs

Yu et al. examined the subcellular localization of overexpressed HIV-1 NC protein in HeLa cells, detected by @NC antibody (Figure 7A). They found that the mature form of NC localizes throughout the entire cell, including nucleus and nucleolus. To confirm the nuclear localization ability of NC and exclude any cell-specific effects or problems with immunofluorescence, including non-specific or false-positive staining, the following control experiments were performed: examination of cytoplasmic and nuclear fractionates of 293T cells transfected with the same plasmid; the localization of an EGFP-fused NC (NC-EGFP) in HeLa and MT-4 (human CD4 T cell line) cells. As observed in the immunofluorescence study, fractionation studies confirmed that NC protein could be localized to both nucleus and nucleolus. Furthermore, the subcellular distribution pattern of NC-EGFP also showed localization in cytoplasm, nucleus and nucleolus as untagged NC protein. The same results were also reported by Anton et al. HeLa cells transfected with eGFP-labeled NCp7 revealed mainly the cytoplasmic and the nucleolar localization of the protein (Figure 7B). In the nucleolus, NC binds to cellular RNAs, and notably to ribosomal RNAs which are the most

abundant. The binding of NCp7 to ribosomes was further substantiated by the intracellular co-diffusion of NCp7 with the ribosomal protein 26, a component of the large ribosomal subunit. Finally, gradient centrifugation experiments demonstrated a direct association of NCp7 with purified 80S ribosomes [66]. In both studies, the nuclear and nucleolar localization of transfected NC was observed in the absence of any expressed viral gRNA. Therefore, the presence of viral gRNA is not a pre-requisite for the observed localization of NC.

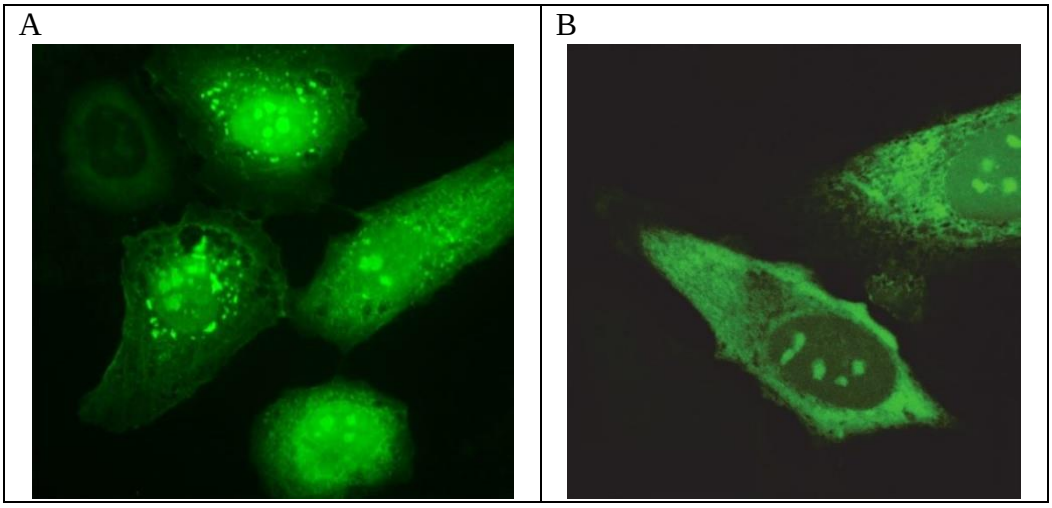

Figure 7. Nucleolar localization of overexpressed NC in HeLa cells. (A) Immunofluorescence of NC-transfected HeLa cells (rabbit polyclonal anti-NC custom antibody, abfrontier, Korea). Adapted from (Yu et al., 2016) [67]. (B) Cellular localization of overexpressed NC protein in HeLa cells transiently transfected with NCp7-eGFP construct. Adapted from (Anton et al., 2015) [66].

NC protein has a nucleolar localization signal (NoLS) in its sequence. Using YFP fusions of HIV-1 NC and mutants, Lochmann et al. demonstrated that two regions are responsible for protein's nucleolar localization: aa 10-11 (R10/K11) and aa 32-34 (R32/K33/K34) [68]. However, Yu et al. did not find any evidence to support the role of N-terminus (aa 10-11) in nucleolar targeting, and suggested that a linker region is sufficient to drive this localization [67] (Figure 8).

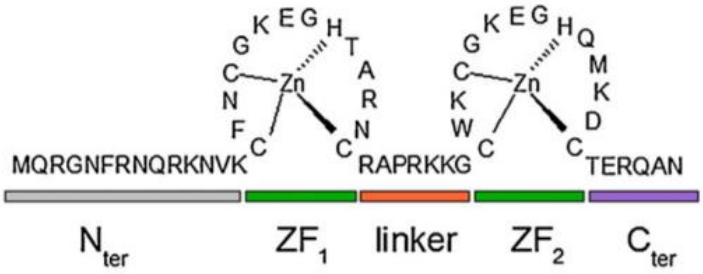

Figure 8. The sequence of NC protein. Adapted from (Godet et al.) [69]

Although there are many evidences of the nucleolar localization of NC protein, it is still not clear why NCp7 localizes in this subnuclear compartment – is it due to the chaperoning role of NCp7 in vDNA integration, passive diffusion due to the high affinity to cellular RNAs

or an interaction with nucleolar and/or ribosomal proteins? And what is the role of NCp7 in the nucleolus?

1.2. Nucleolus

1.2.1. Structure and functions

The nucleolus, a large nuclear domain, is the ribosome factory of the cells. Ribosomal RNAs are synthesized, processed and assembled with ribosomal proteins in the nucleolus, and the ribosome subunits are then transported to the cytoplasm [70]. In dividing eukaryotic cells, the nucleoli assemble at the end of mitosis; they remain functionally active throughout the interphase, and disassemble at the beginning of mitosis [71]. Each cell possesses at least one nucleolus with a shape reflecting its activity or differentiation state. Indeed, the size of the nucleolus depends on the level of ribosome production. In dividing cells, ribosome production is high, and the size of the nucleolus varies from 0.5 to 7 μm in diameter (Figure 9A).

The molecular processes occurring in the nucleolus determine its structural organization. By using electron microscopy (EM), three basic "building blocks" were found in higher eukaryotes: the fibrillar center (FC), partly or entirely surrounded by the dense fibrillar component (DFC), and both of them are embedded in the granular component (GC), mainly composed of granules of 15–20 nm in diameter [70] (Figure 9B).

Ribosome biogenesis is a multistep process that starts with the transcription of ribosomal genes (rDNA) by RNA polymerase I (pol I) at the border between FC and DFC. The newly synthesized pre-rRNA transcripts are then processed by specific nucleolar proteins and modified by the small nucleolar ribonucleoproteins - snoRNPs (methylation and pseudouridylation). The 47S pre-rRNA undergoes a series of cleavages ultimately resulting in 18S, 5.8S and 28S rRNAs. These steps take place in DFC, and followed by the association of rRNA with ribosomal proteins in GC in order to form small (40S) and large (60S) ribosome subunits. [70,72]

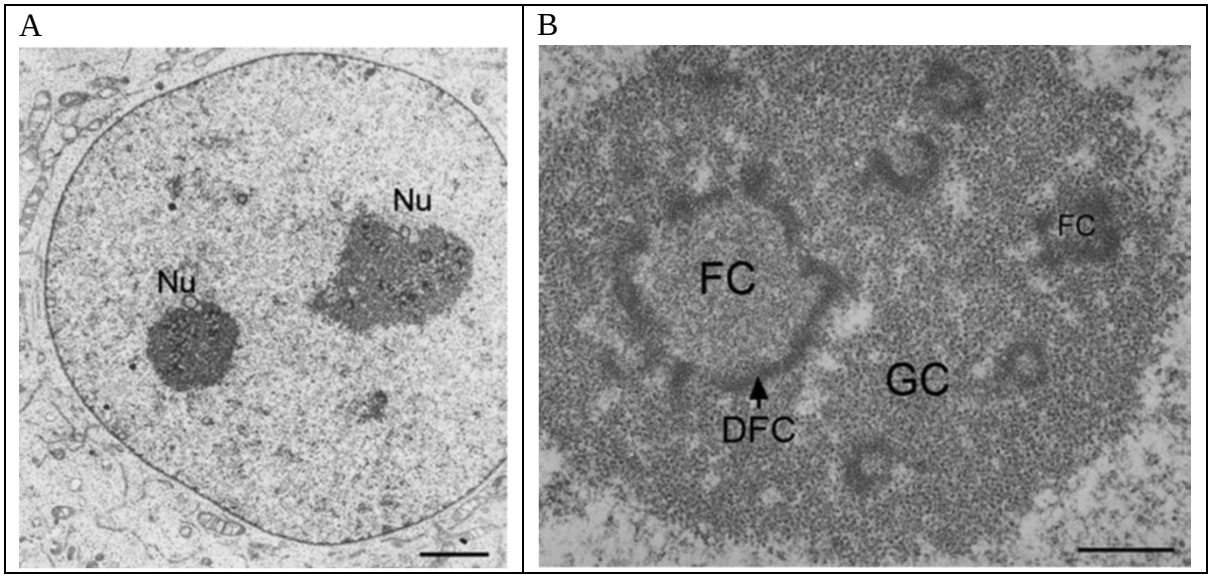

Figure 9. Electron microscopy images of nucleolus. (A) Nuclear organization of human HeLa cell. Two nucleoli (Nu) of 3 µm and 7 µm in diameter are visible in the nucleus. Scale bar: 3 µm. Adapted from (Olson, 2011) [71]. (B) Nucleolar organization in a HeLa nucleus. Three distinct sub-domains of nucleolus are well resolved by transmission electron microscopy (TEM): fibrillar centers (FCs), dense fibrillar component (DFC) and granular component (GC). Scale bar: 1 µm. Adapted from (Olson, 2011) [71].

In nucleoli, the vectorial distribution of machineries correlates with different processing steps. For example, RPA43 - the largest subunit of RNA-polymerase-I - takes part in rDNA transcription and localizes in FCs; fibrillarin that participates in the early stages of rRNA processing, localizes in DFC along with the U3 snoRNA[73]; whereas the protein B23 (NPM) that is involved in the intermediate or later stages of ribosome biogenesis has been localized to GC. These findings have led to assigning specific functions to specific compartments of the nucleolus. Therefore, particular steps of the ribosome production can be identified by specific markers and consequently localized by fluorescence microscopy, offering another way of revealing the organization of the nucleolus (Figure 10).

Several proteomic analyses have identified over 700 human proteins that stably co-purify with isolated nucleoli. Classification of molecular functions of nucleolar proteins shows that approximately 30% have a function that is related to the production of ribosome subunits. However, the diverse identities and functions of many of the other nucleolar proteins are consistent with additional processes that occur within the nucleolus. This includes many pre-mRNA processing factors and proteins that are involved in cell-cycle control as well as DNA replication and repair.

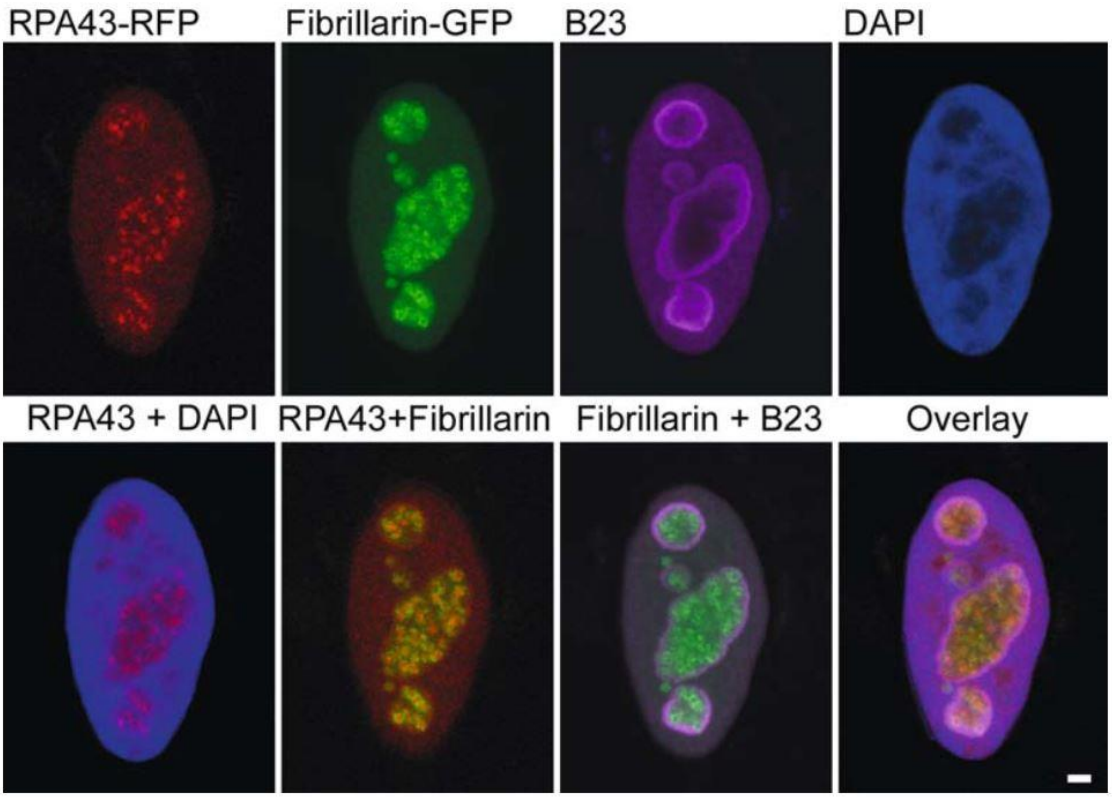

Figure 10. Organization of the HeLa cell nucleolus. Labeled RNA-polymerase-I-recruiting subunit (RPA43), fibrillarin (Fib) and nucleophosmin (NPM or B23) proteins were used as markers of FCs, DFC and GC components of the nucleolus respectively. Scale bar: 2µm. Adapted from (Olson and Dundr, 2005) [74].

Nucleoli respond to changes in cellular growth rate and metabolic activity, which indicates that they constantly receive and respond to signaling events. One important reason for the regulation of nucleolar activity is the crucial need for the cell to maintain a sufficient number of ribosome subunits to support protein-synthesis levels during cell growth and division. Considering that the key role of the nucleolus is to ensure that the cell receives enough ribosomes, it is not surprising that its activity is tightly regulated. In addition, recent data indicate that nucleoli are also involved in coordinating and regulating cell-cycle-control events (for example by sequestration of specific proteins [75]) and stress responses [76].

1.2.2. Targeting by viruses

Nucleolus is known to be targeted by many different viruses in order to promote their replication [77,78]. In addition to the production of ribosomal particles, nucleolus plays role in other cellular processes like regulation of mitosis, cell growth and proliferation or stress response [79]. The multifunctional role of the nucleolus and nucleolar proteins can be used by different virus in order to control cellular transcription and cell division, facilitate the virus transcription and up-regulate the translation of virus-encoded proteins [80,81,82,83,84].

Over 100 viral proteins of more than 50 distinct viruses have been reported to localize in nucleoli. Some viruses change nucleolar architecture, re-localize nucleolar proteins, and recruit them to virus replication centers [80,81]. Other viruses, such as poliovirus, arterivirus, and HIV-1, exploit nontraditional nucleolar functions and alter the cell cycle to enhance virus replication [83,85,86]. The nucleolar localization of viral proteins has been functionally linked to viral ribonucleoprotein complex formation, viral RNA export, genome packaging, genome replication, capsid assembly, and pathogenesis.

A number of factors can determine whether a protein localizes to the nucleolus. Soluble proteins of less than 40–60 kDa can diffuse passively into the nucleoplasm through the nuclear pore complex and could in principle diffuse in and out of the nucleolar compartment. Non-specific RNA binding proteins that diffuse into the nucleus may therefore be expected to become concentrated in the nucleolus because a large amount of rRNA is present. As for large proteins, their transport through the nuclear pore is an active process requiring ATP and nuclear localization signals (NLSs), which also make up (in part) nucleolar localization signals (NoLS) [84,76].

Among retroviruses, both viral proteins and unspliced viral RNAs interact with nucleoli and nucleolar proteins. The nucleolus plays a key role in the function of the HIV-1 Rev protein, which mediates the nuclear export of unspliced viral RNA. The nucleolus is the site of Rev dimerization, which is required for its activity [87]. Rev localizes to the nucleolus through its interaction with the cellular protein B23 [88]. When unspliced HIV-1 RNA containing the Rev response element (RRE) RNA binds to Rev, B23 is displaced, and Rev moves into the cytoplasm. B23 may also serve as a shuttle for the import of HIV Rev from the cytoplasm into the nucleus or nucleolus to allow further rounds of export of RRE-containing viral RNAs [88]. Furthermore, linking a ribozyme to a small nucleolar RNA results in strong decrease of HIV-1 replication, suggesting that the ribozyme cleaves HIV-1 RNA as it traffics through the nucleolus [89] and supporting the important role played by the nucleolus in HIV-1 biology. Moreover, the HIV-1 protein Tat that plays role in transcription and synthesis of vRNA also localizes to nucleolus.

1.3. Imaging techniques

Imaging techniques are perfectly suited to study the cellular distribution of a protein. Among the variety of techniques, with their strengths and weaknesses, it is necessary to select the one that fits best to the assigned (particular) task. Optical microscopy is one of the most powerful and versatile diagnostic tools in modern cell biology. Whereas the bright-field microscopy (e.g. phase contrast, DIC), using a transmitted through the sample white light, can show the cellular morphology (shape and biggest organelles) without much of details, the fluorescence microscopy together with highly specific fluorescent labeling methods reveal much more information about the cellular structure and proteins localizations. Unfortunately, even with perfect lenses, optimal alignment, and large numerical apertures, the optical resolution of light microscopy is limited by diffraction to approximately half of the wavelength of the light used. Several super-resolution techniques have been developed in the past two decades in order to overcome this limit. Using nonlinear effects, specific dyes and buffers, and algorithms for data analysis, they demonstrate a resolution up to few nanometers. Although the near-field scanning optical microscopy (**NSOM**) [90,91] bypasses the diffraction limit and provides the resolution in the 20 nm range [92], it can be used only for surface studies. Therefore, we will further concentrate on the far-field microscopy techniques, where the working distance between the object plane and the front lens of the optical system is at least several hundred wavelengths.

1.3.1. Far-field nanoscopy

The development of laser technology in combination with novel optical and photophysical approaches, highly sensitive and fast detection systems, and computer-based evaluation procedures have made it possible to radically overcome the Abbe limit of conventional far-field fluorescence microscopy. Imaging techniques that show improvement in optical resolution can be divided into three groups: employing the point spread function (PSF) modification, structured illumination or random switching schemes of single emitters.

In light microscopy, an object may be considered as an arrangement of a number of point sources at given spatial positions (x, y, z) absorbing, emitting, or scattering light. The ultimate goal of light microscopic structure analysis is to identify the point sources and to determine their positions as precisely as possible. Because of the diffraction of light on a circular aperture, the light emitted by such point sources is represented in the focal plane by a Bessel function of a first kind or Airy disk (Figure 11A). This instrument response function,

better known as a point spread function (PSF), is a characteristic of each individual microscope. The obtained image is a result of a convolution of a real distribution of single emitters with the PSF of the microscope. The resolution of the microscope system is usually determined by the minimal distance between two objects that still can be resolved. Rayleigh criterion says that two point-sources with the same emission wavelength and lifetime can be resolved when the first diffraction minimum of one source coincides with the maximum of another (Figure 11B). Knowing the position of the first minimum of a Bessel function showed in Figure 11, we can determine the minimal resolvable distance:

$$d_{min} = \frac{0.61\lambda}{NA}$$

where λ – wavelength used, $NA = n \sin \alpha$ – numerical aperture (here n – refractive index, α – half of an aperture angle).

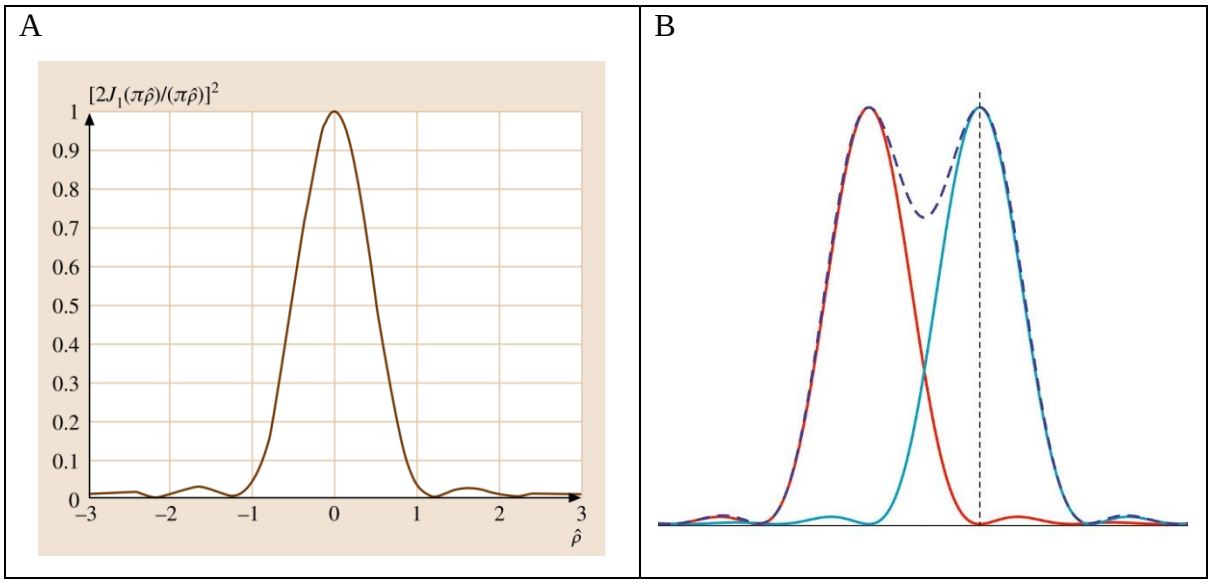

Figure 11. (A) Normalized intensity distribution in the focal plane of a lens. The function $[2J_1(\pi\hat{\rho})/(\pi\hat{\rho})]^2$ is shown, where $J_1(\pi\hat{\rho})$ is a Bessel function of the first kind and $\hat{\rho} = 2n\rho a/(\lambda f)$ (n – refractive index, ρ – distance in polar coordinates, a – radius of a circular aperture, λ – wavelength, f – focal length). Adopted from (Haglund, 2012) [93].(B) The Rayleigh criterion. Two point-sources can be resolved when the first diffraction minimum of one source coincides with the maximum of another.

The basic idea in Abbe/Rayleigh theory of optical resolution is the assumption that all point sources are registered simultaneously. However, the image of the object (i.e. the information about positions of point emitters) can be obtained in another way. Instead of simultaneous excitation and detection of all fluorescent elements of the object, it is possible to reconstruct the image in the sequential manner, point by point (or step by step). This is the principle of two super-resolution techniques: focused scanning nanoscopy and localization microscopy.

1.3.2. PSF modification (STED, GSD)

The idea of scanning nanoscopy relies on the fact that the positional information is obtained from the mechanics of the system (e.g. piezoelectrical stage or galvo-mirror) and thus significantly increases the resolution, because the last does not depend on the illumination wavelength. But this will work only if we can decrease the diameter of the emitting spot (FWHM of PSF) defined by Abbe limit: $D_{min} = \frac{\lambda}{2n \sin \alpha} = \frac{\lambda}{2NA}$. Straightforward way to do it is changing one of the parameters in the formula: wavelength or numerical aperture. If we are talking about fluorescence microscopy and visible light, λ in this case is limited by 400 nm. In case of **electron microscopy** however, where a beam of accelerated electrons is used, the wavelength can be 10^5 times shorter giving a typical resolution of hundreds of picometers. Despite of this incredible resolution, the electron microscopy has several disadvantages compared to the fluorescence microscopy:

- electron microscopes are expensive to build and maintain;
- the samples largely have to be viewed in vacuum, as the molecules that make up air would scatter the electrons;
- the need for extremely thin sections of the specimens, typically about 100 nanometers;
- inability to work with living cells.

Creating these thin sections for biological and materials specimens is technically very challenging. Biological tissue specimens are chemically fixed, dehydrated and embedded in a polymer resin to stabilize them sufficiently to allow ultrathin sectioning. Sections of biological specimens, organic polymers and similar materials may require staining with heavy atom labels in order to achieve the required image contrast. These processes may result in artifacts, but these can usually be identified by comparing the results obtained by using radically different specimen preparation methods.

Let's now look at the second parameters – numerical aperture (NA). Since in practical light microscopy, the maximum refractive index n is typically around 1.5, one would have to increase the full aperture angle to change the size of PSF. This is the way the **4Pi microscopy** works. By placing two objectives in front of each other we can extend the aperture angle 2α beyond 180º; the coherent light is focused from all sides (sterical angle 4π) by constructive interference [94]. Although this technique allows to increase the axial resolution up to 75 nm [95,96], the optical resolution in the lateral direction was improved only marginally.

The first successful concept to achieve a lateral optical resolution far below 100 nm in a far-field arrangement was the **stimulated emission depletion (STED) microscopy** [97]. This method is based on the scanning of an object with a focused laser beam. The increase in resolution is achieved by using an appropriately shaped second beam of a red-shifted wavelength λ_{STED} (STED beam) (Figure 12A). The donut-shaped beam produces an illumination pattern around the excitation beam that induces the stimulated emission of excited molecules from the lowest S_1 state to the highest S_0 state (Figure 12B). Employment of this nonlinear effect results in a decrease of the detected spot size (D_{fl}) which is now much smaller than the diffraction limit ($D_{fl} << D_{min}$). Nowadays, the STED microscopy concept on modern setups gives a resolution of 15-20 nm in the lateral plane [98].

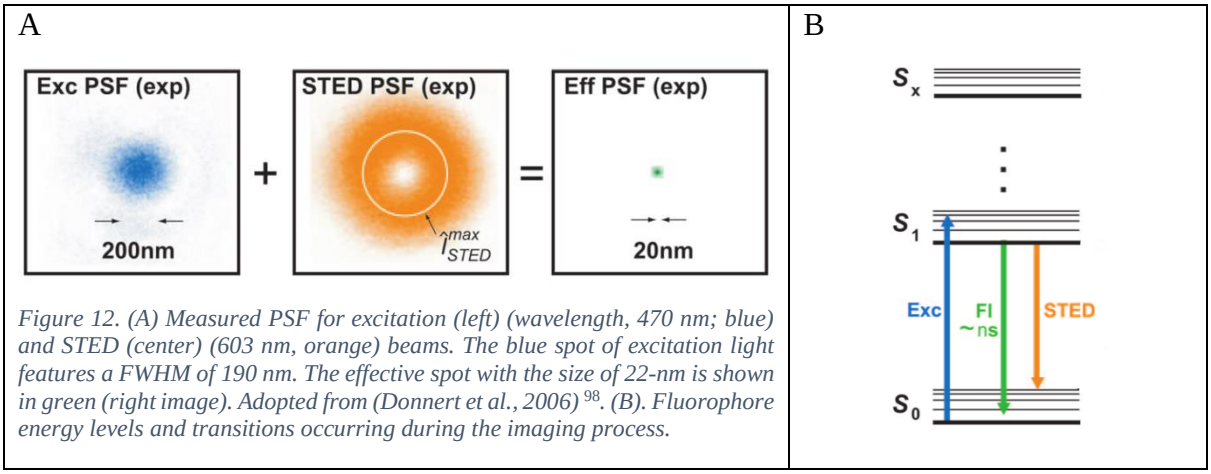

Figure 12. (A) Measured PSF for excitation (left) (wavelength, 470 nm; blue) and STED (center) (603 nm, orange) beams. The blue spot of excitation light features a FWHM of 190 nm. The effective spot with the size of 22-nm is shown in green (right image). Adopted from (Donnert et al., 2006) [98]. (B). Fluorophore energy levels and transitions occurring during the imaging process.

Another technique, called **ground-state depletion (GSD) microscopy**, is using the same principle as in STED, but instead of the depletion of the excited state S1, the ground state S_0 is depleted [99]. In this case the density of molecules in the ground state is greatly diminished in the region around the excitation beam. This in achieved by high laser power excitation ($I_{depl} \geq 10$ MW/cm^2 [99]) with the same wavelength, in order to make as many "S_0=>S_1=>S_0" cycles as possible and populate the triplet state. The intersystem crossing (ISC) is a forbidden transition (because of the spin change and selection rules) and the probability to populate it is very low, but if we increase the number of cycles between S_0 and S_1 states we also increase the chance to populate the triplet T_1 state. Again, because the ISC is forbidden, the lifetime of the molecule in the T_1 state is in a range of microseconds whereas the lifetime in the S_1 state is about few nanoseconds. When the ground state is depleted there are no molecules that can be excited to S_1 which later can emit a photon during the relaxation to the ground state. Only the center of the illuminated region, under low illumination intensities, is not depleted and can emit

photons. With a ground state depletion technique we can achieve the resolution up to 15 nm [99], and with a lower laser power ($I_{depl} \approx 10^2$ kW/cm^2) of GSD beam – 50 nm [100].

The mentioned above scanning nanoscopy techniques have been generalized under the acronym **RESOLFT** - reversible saturable optical linear fluorescence transitions. The general formula for resolution of these method [101]: $D_{min} \approx \frac{\lambda}{2n*\sin\alpha\sqrt{1+\xi}}$, where $\xi = \frac{P}{P_{sat}}$ – the saturation factor given by the applied power P driving the reversible transition between fluorescent and non-fluorescent states; P_{sat} – saturation power that classifies the magnitude of the power necessary to attain 50% of the according transition. The higher the saturation factor becomes, the more the optical resolution is improved.

1.3.3. Structured illumination (SIM)

Structured illumination microscopy (SIM) is a wide-field method that illuminates the sample with a series of spatially modulated patterns of high frequency. This pattern is typically generated by a laser light passing through a movable optical grating and projected via the objective onto the sample [102], or it can be also created by the interference of two or more laser beams [103]. Applying this illumination to the fluorescent sample, containing fine structures, results in the signals multiplication and appearance of Moiré fringes (Figure 14a). These fringes are coarser than the original patterns and thus can be observed in the microscope, even if the structure we are looking at is too fine to be resolved. Knowing the illumination pattern, the information about the sample can be extracted from the recorded Moiré fringes [102].

To understand better the principle and achievable resolution of the SIM technique, it is useful to look at the process of image formation in both real and frequency (Fourier) spaces. In the widefield fluorescence microscopy, labels distributed within the sample (ρ) get excited by the illumination light (I) and then emit photons during the process of relaxation. Before being detected on the camera, the signal is blurred because of the diffraction phenomenon. The mathematical representation of this process can be described by the following formula:

$$g = PSF \otimes (\rho \cdot I)$$

where g is the formed image, and the convolution with a PSF describes blurring caused by the diffraction. Before talking about the equivalent operation in Fourier space, I will briefly present what this space is.

With the help of Fourier transform, every object can be uniquely described as a sum of sinusoidal functions, where each has four characteristic parameters: direction of propagation,

frequency, amplitude and phase. Higher spatial frequencies represent fine object details and lower frequencies – coarse details (Figure 13). As the PSF specifies the microscope resolutions in real space, the optical transfer function (OTF) does it in Fourier space; it describes how well each spatial frequency gets transferred by the optical system (Figure 13, right panel). During the image formation, multiplication by the OTF acts like a low pass filter:

$$FT[g] = OTF \cdot (FT[\rho] \otimes FT[I])$$

Only frequencies smaller than Abbe cut-off frequency ($k_{max} = \frac{1}{\Lambda_{min}} = \frac{2NA}{\lambda}$) are detectable [104].

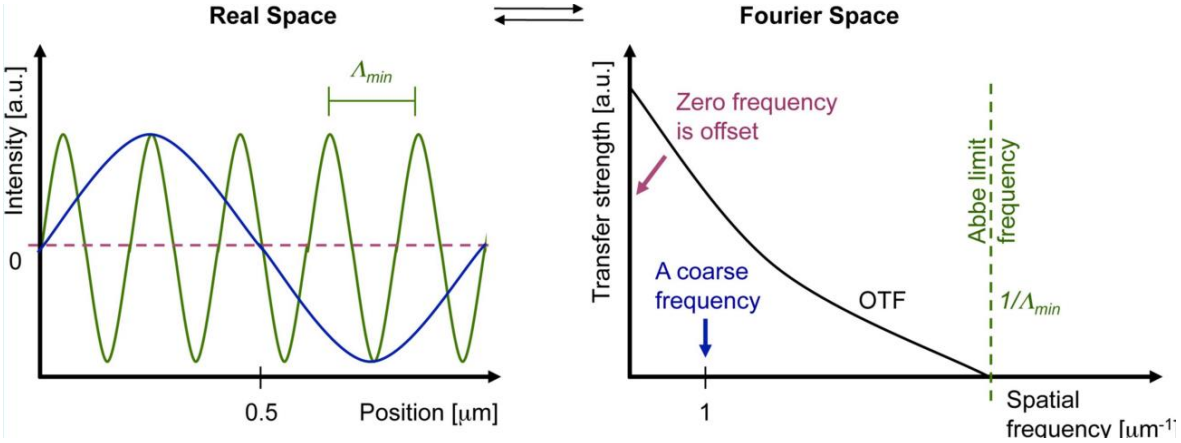

Figure 13. The diffraction (Abbe) limit. Adopted from (Schermelleh et al., 2010) [104].

In the two-dimensional case, all *sin* functions from Fourier transform can be graphically represented as a picture, where the position of each pixel encodes the wave frequency and propagation direction, and the pixel value – amplitude and phase of this wave. Now, when we consider the propagation direction, the optical transfer function is represented as a circle with the radius of $1/\Lambda_{min}$ (see Figure 14b). The information lying outside of this circle cannot be detected during the conventional imaging. In contrast to homogeneous illumination, where the Fourier transform of the illumination pattern ($FT[I]$) results only in one point with a zero frequency, the spatially varying illumination of SIM gives additional non-zero frequencies in Fourier space. In case of sinusoidal illumination (interference of multiple laser beams), the Fourier transform gives only two non-zero points, $+k_{ex}$ and $-k_{ex}$ (Figure 14c), which after the convolution with a Fourier transform of the fluorescence emitters distribution results in the appearance of two additional circles (Figure 14d): Moiré fringes ($\rho \cdot I$) in the frequency space $FT[\rho] \otimes FT[I] = R(k) \otimes I(k_{ex}) \dashrightarrow R(k - k_{ex})\ and\ R(k - k_{ex})$. The observable region now contains a new information that originates in two offset regions and that was not accessible with a conventional imaging.

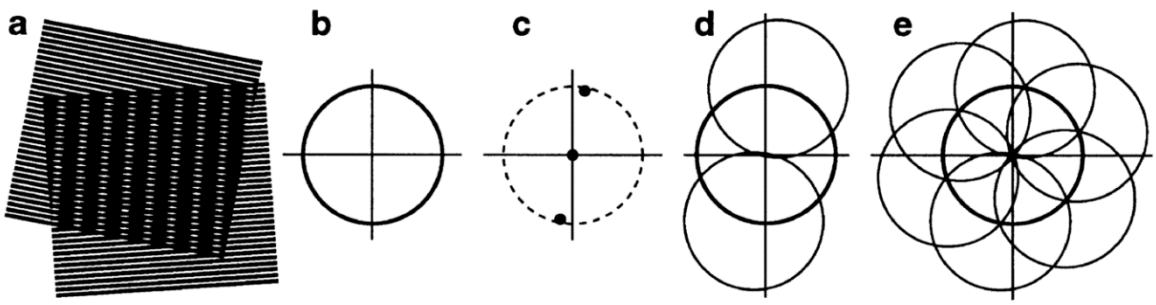

Figure 14. Moiré fringes and principle of SIM. Adopted from (Gustafsson, 2002) [102]

Computational techniques are applied to remove the information about the striped pattern and extract the image of a structure with improved resolution from the sum of three contributions. The coefficients by which three circles are added together depend on the phase of the illumination pattern. By recording three or more images of the sample with phase-shifted illumination, the three components can be unmixed, and the information restored to its proper position. Additional images with different illumination orientation are needed to achieve the isotropic resolution improvement (Figure 14e).

Because the periodicity of illumination pattern is also limited by diffraction, the highest resolution improvement that can be obtained with the linear SIM is a factor of two in comparison to the conventional microscopy. Short acquisition time, low irradiation intensity and no specific requirements to the fluorescent labels are the most attractive features of the structured illumination microscopy. They make this super-resolution technique a suitable tool for the imaging of living cells, as it was shown on the examples of mitochondria, tubulin, and kinesin dynamics [105,106].

It is worth mentioning that even this new resolution limit can be pushed further (< 50 nm) using the nonlinear response of the fluorescence emission rate to the change in excitation intensity [107]. This nonlinearity can be achieved by the saturation of the excited state (saturated SIM or SSIM) and leads to the appearance of harmonics in the illumination pattern (nk_{ex}). Higher harmonics lead to higher resolution, but there are practical limitations to this scheme, like signal to noise ratio and labels photostability.

1.3.4. Localization microscopy

Previously discussed approaches require a built of complex laser optical systems, a use of high laser power, or sophisticated algorithms for data analysis. On the other hand, the **single-molecule localization microscopy** is much easier to implement and gives the best resolution compared to described above super-resolution techniques. Indeed, a standard widefield setup

with a high numerical aperture objective and sensitive camera can be used to achieve a ten-fold increase in resolution. The idea is to temporally separate the emission of single fluorophores (scanning in time), and then localize each one of them individually by fitting the diffraction pattern with a 2D gaussian function (Figure 15). To achieve the temporal separation, the majority of fluorescent molecules is transferred to the dark state, and only a small fraction of them can return to the bright state, stochastically or controlled with a laser of specific wavelength. If the probability of activation is sufficiently low, the detected fluorophores localized far enough from each other, so there is only one emitter detected in a diffraction limited area. The dark state can be a long lived non-emissive state of the same molecule like in direct stochastic optical reconstruction microscopy (**dSTORM**), or a different form of this molecule (e.g. cys-, trans- isomers; different spectral signature) as it is used in photoactivable localization microscopy (**PALM**). The emission of molecules residing in the ON state is readout by the camera, processed in order to obtains *x* and *y* coordinates of the center of fit, and then this procedure is repeated again. Usually thousands of frames are recorded to obtain a reconstructed image of a sample.

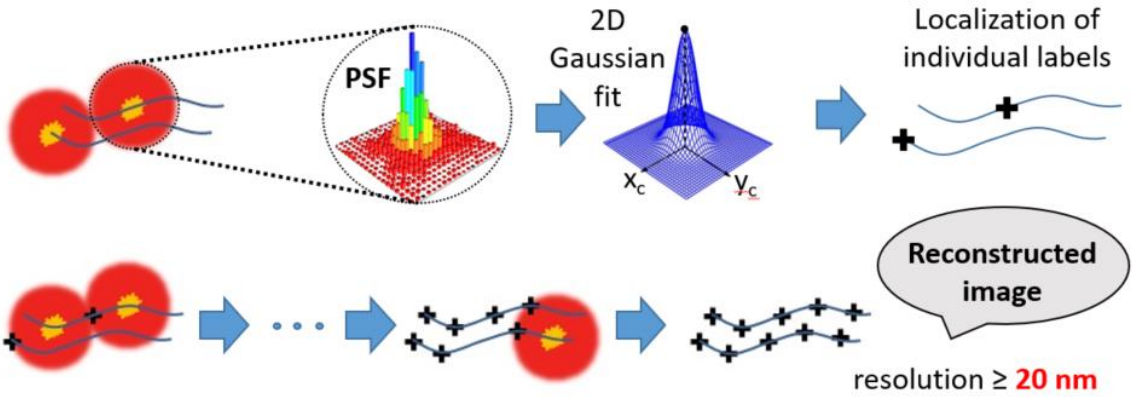

Figure 15. The working principle of single-molecule localization microscopy techniques.

Each collected photon in the image gives the position of the fluorescent label with a position error which equals to the standard deviation of the fit. Every detected photon is a new measurement of the position, so in this case the localization coordinates will be given as an average of the positions of all detected photons. The localization precision depends on the number of detected photons and is given by the common statistical formula for the standard error of the mean:

$$< (\Delta x)^2 > = \frac{s^2}{N},$$

where Δx – error in localization, s – standard deviation of the point spread function, N – number of collected photons. Now, if we include an error related to the pixilation noise, uncertainty of where exactly the photon arrived to the pixel of a finite size a, and the background noise b, uncertainty of whether the photon arrived from the fluorescent label, the given formula will be modified [108]:

$$< (\Delta x)^2 > = \frac{s^2 + a^2/12}{N} + \frac{8\pi s^4 b^2}{a^2 N^2}$$

To summarize, the localization microscopy technique requires very bright fluorescent emitters that can transfer between their fluorescent and non-fluorescent states. The time that particle resides in the dark state should be much longer than the one it spends in the bright state, in order to avoid artifacts related to the detection of several particles within the same diffraction region.

Labels

The concept of transition between fluorescent and non-fluorescent states of a molecule is common for all localization microscopy techniques, however they exploit different types of emitters with different mechanisms of blinking. The most common switchers are photoactivable fluorescent proteins (PA-FPs), used in PALM, and standard organic fluorophores (dSTORM). Both of them have strengths and limitations and differ on several important points.

Fluorescent proteins are genetically fused to the protein of interest, whereas organic fluorophores usually require an antibody for targeting, which unlike the protein fusion results in a non-specific binding. On the other hand, organic fluorophores with antibodies can label endogenous proteins at concentrations much lower than overexpressed protein fusion. These labels also differ in size. While the size of synthetic dyes is in a range of few nanometers, its complex with an antibody (15-30 nm depending on the number of antibodies) is much bigger than a photoactivable fluorescent protein (4 nm) (Figure 16). Although the smallest resolvable distance between two point emitters is dictated by the localization precision of the individual point sources, the effective resolution of a continuous structure must take into account the density of localized fluorescent labels [109]. According to the Nyquist-Shannon sampling theorem, the distance between two neighboring fluorophores must be at least twice smaller than the desired resolution [110]. Therefore, the smaller size of fluorescent proteins is beneficial

for higher density of labeling and consequently for a higher achievable resolution (if not considering the photon budget of these probes).

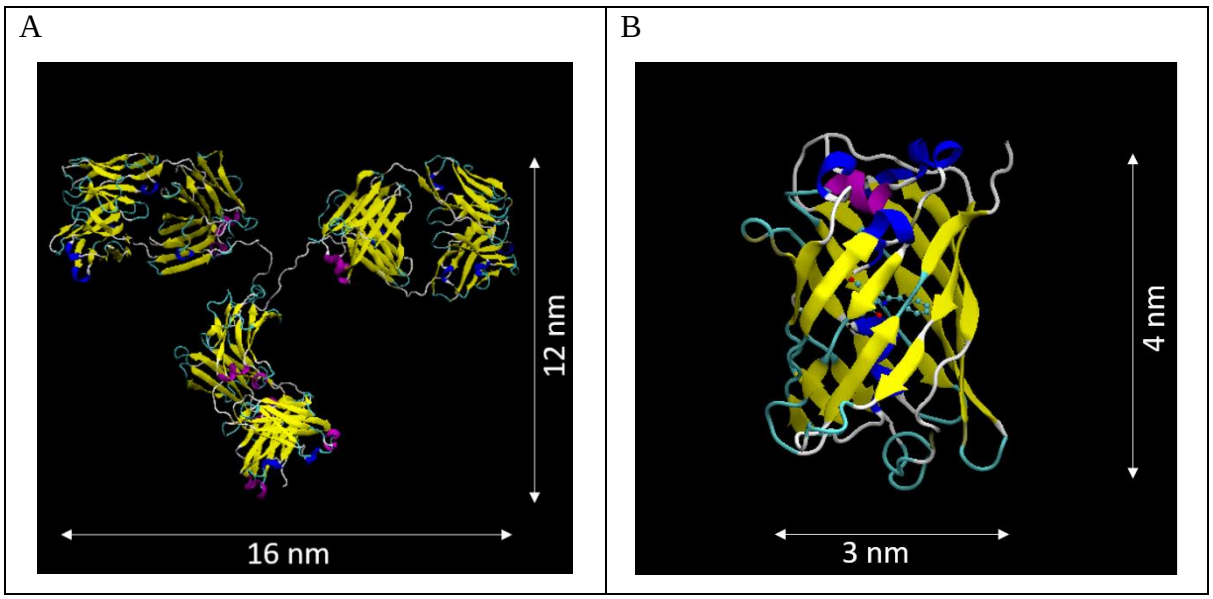

Figure 16. The size of (A) Immunoglobulin (1igt, protein data bank) and (B) enhanced green fluorescent protein eGFP (4eul, protein data bank).

On the contrary, PA FPs display lower photostability and brightness than standard organic fluorophores. The number of detectable photons for PA-FPs is typically a few hundred photons before they bleach, whereas synthetic fluorophores can emit more than 1,000 photons per cycle. This number, as it was discussed previously, has a direct impact on the localization precision, and thus on the final resolution.

The mechanism of switching

PAFPs can be divided into three groups according to their photochemical properties, two with irreversible photoconversion and one with reversible switching of fluorescent proteins [111,112]. The PA-GFP protein, derivative of GFP from *Aequoria victoria*, and the PA-mCherry protein, from *Discosoma sp.*, represent the first group and demonstrate the irreversible photoconversion from the neutral (protonated) to anionic (deprotonated) form of the chromophore, preceded by decarboxylation of the Glu222 residue. In the neutral state these proteins are non-fluorescent or demonstrate very low emission intensity (for PA-GFP when excited with 488 nm laser). However, the irradiation with UV light (405 nm) leads to the conversion of FP to its anionic form (Figure 17 left panel). Fluorescent proteins of the second group (e.g. mEos2 [113]) can change their absorption and emission spectra upon UV irradiation. In this case the backbone cleavage in the His65 residue leads to the formation of a new double bond and increase in the length of conjugation, thus changing the spectral signature of a

fluorescent protein (Figure 17 middle panel). Proteins of the third group (e.g. KFP and Dronpa) are capable of the reversible photoconversion between the dark and bright states. The proposed mechanism of this switching is a UV-induced *trans*-to-*cis* isomerization followed by chromophore deprotonation (Figure 17 right panel).

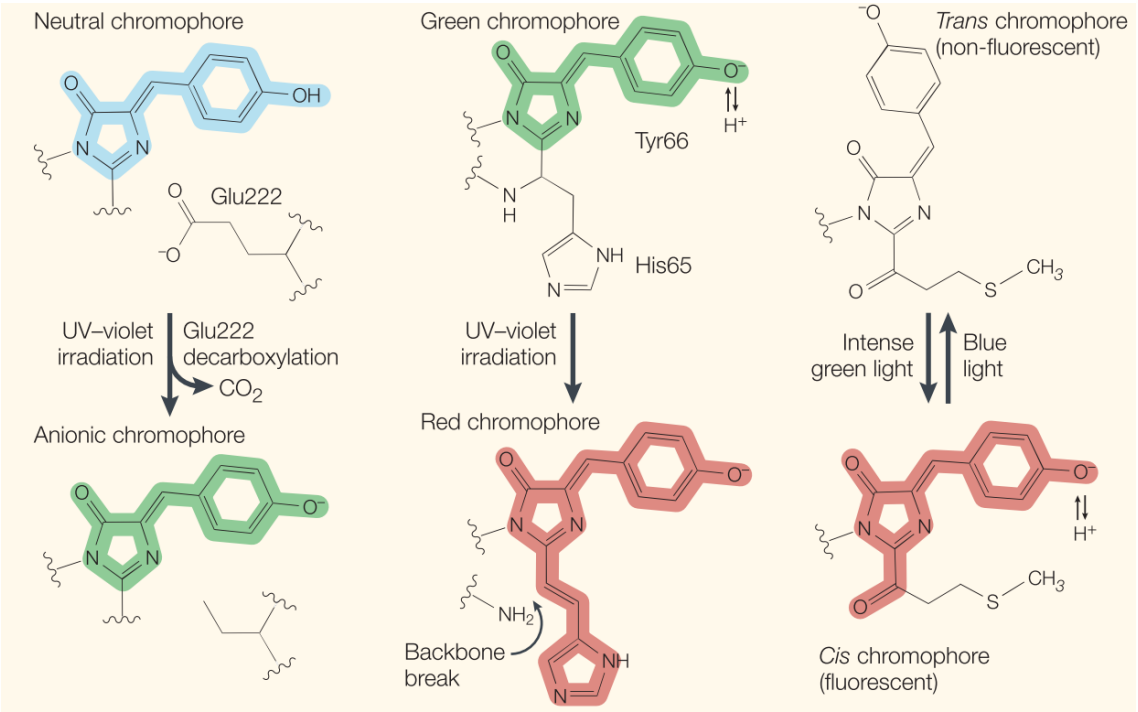

Figure 17. Chromophore photoconversion mechanisms for (from left to right) PA-GFP and PA-mCherry (decarboxylation of Glu222 followed by chromophore conversion from a neutral to anionic state), mEos2 (breakage of the polypeptide backbone and formation of an extra chromophore double bond), and KFP1 (trans–cis chromophore isomerization). Adopted from (Lukyanov et al., 2005) [112].

In contrast to fluorescent proteins, the organic fluorophores are initially emissive, and require high laser power and special buffer to be converted to the dark state. Under excitation, the fluorescent molecule absorbs one photon and enters its excited state from which it can return to the ground state by emitting a photon of lower energy or undergo the intersystem crossing and populate the triplet state (Figure 18). The probability of last event is very low, because this transition is forbidden by the selection rules. However, increasing the excitation laser power leads to numerous cycles of molecule excitation and relaxation, populating more and more the triplet state. The lifetime of the triplet state is in the microseconds range, but it can react with molecular oxygen to recover the singlet ground state. To achieve a dark state with a longer lifetime, the electron donors like thiols (e.g. β-mercaptoethylamine or MEA) are used to reduce the triplet state upon irradiation and create the radical anion of the fluorescent molecule. These radical anions are more stable to oxidation and display a lifetime in a milliseconds to seconds range in presence of molecular oxygen [114,115,116]. Using the oxygen

scavenging system to remove the molecular oxygen from a solution helps to increase the lifetime of the dark state up to several hours [117].

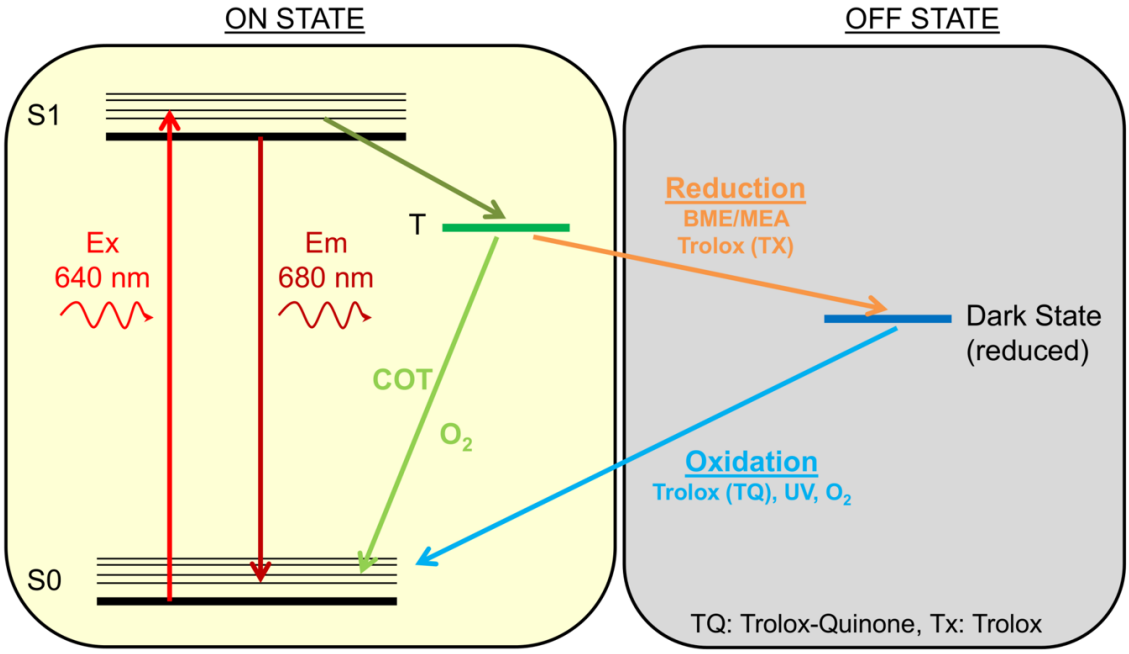

Figure 18. Switching mechanism of organic fluorophores (e.g. Alexa Fluor 647). Adopted from (Olivier et al., 2013) [118].

The molecule can return to the ground state upon oxidation by molecular oxygen and then be excited again. This process is stochastic but the transition rate from the bright to the dark state and vice versa can be controlled by the concentration of thiols, presence of an oxygen scavenger, excitation laser power and the use of UV laser to facilitate the recovery to the emissive state [117].

Buffer

While the photoactivable fluorescent proteins can transfer between the dark and bright states in a simple PBS buffer, the synthetic dyes, as it was discussed before, require a complex buffer with millimolar concentration of a reducing agent and oxygen scavenging system to produce a stable long-lived dark state. Heilemann et al. in the first article about dSTORM used a "switching buffer" composed of phosphate-buffered saline (PBS, pH 7.4), enzymatic oxygen scavenging system GLOX (0.5 mg/ml glucose oxidase, 40 µg/ml catalase, 10% w/v glucose) and 50 mM β-mercaptoethylamine [116]. The concentration of thiols (10 – 200 mM) differs with the respect to the organic fluorophore used during the experiment. In addition, the presence of oxygen scavengers depends on the family of organic dyes: cyanine fluorophores are far more easily oxidized than rhodamine or oxazine derivatives [119]. Olivier et al. demonstrated that adding the polyunsaturated hydrocarbon cyclooctatetraene (COT) to a switching buffer can

provide significantly increased photon yields of Alexa Fluor 647 and enhance its stability through direct quenching of the triplet state by energy transfer [118,120] (Figure 18). Trolox is another compound used to increase the stability of a dye. However, the mechanism of stabilization interfere with the redox reaction and formation of a long-lived dark state, thus preventing blinking of the dye [121]. Recently it was shown that the anti-fading mounting medium Vectashield can be also used to induce the blinking of organic fluorophores [122,123]. Unlike enzymatic scavenging system, that leads to buffer acidification (Figure 19) and as a result influences the blinking kinetics of organic fluorophore (especially the lifetime of a dark state) [124,125], the Vectashield medium does not change its pH and already prepared samples can be stored and used during several days. In terms of 3D imaging, the high refractive index of Vectashield provides better index-matching than water-based buffers, and thus reduce optical aberrations.

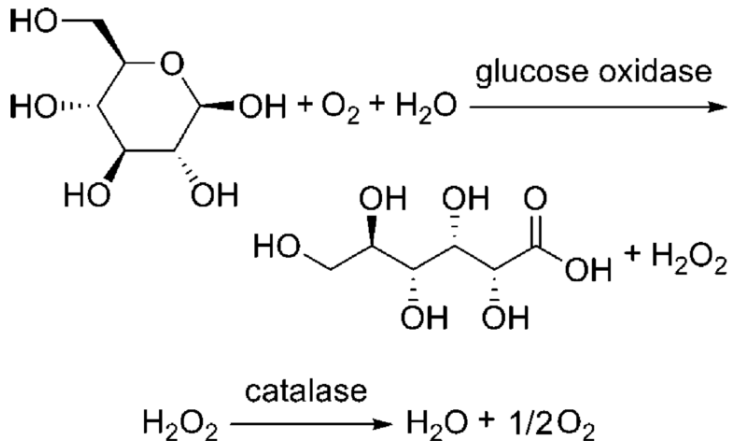

Figure 19. Enzymatic reaction involved in the oxygen scavenging system of glucose, glucose oxidase and catalase (GLOX). Adopted from (Shi et al., 2010) [124].

1.3.5. SOFI

The single-molecule localization techniques require very bright fluorescent emitters that can transfer between their fluorescent and non-fluorescent states. The time that the particle resides in the dark state should be much longer than in the bright state in order to avoid artifacts related to the detection of several particles within the same diffraction region. As the result, a slow acquisition rate together with high irradiation intensities and presence of chemical buffers (in STORM) reduce the potential of localization microscopy for a live-cell imaging.

Unlike PALM and STORM, the super-resolution optical fluctuation imaging (**SOFI**[126]) is a less demanding technique and can be used in conditions of low signal-to-noise ratio, high background and high labeling densities[127], when the latter often results in the overlapping of

diffraction patterns. SOFI is based on the high-order statistical analysis of images from the acquired stack. The image with improved resolution can be generated from the temporal correlation of each pixel intensity traces. The mixed signal coming from several fluorophores is less correlated than the fluctuations of a single emitter and this difference we basically observe on the SOFI image. Stochastic fluorescence fluctuations are still required for SOFI imaging, but not necessarily switching ON and OFF, it can be two states with different emission levels or even fluctuations caused by a change of polarization if these changes are detectable. For the second order autocorrelation function we get:

$$G_2(\boldsymbol{r},\tau) = \langle \delta F(\boldsymbol{r}, t+\tau) \cdot \delta F(\boldsymbol{r}, t) \rangle_t = \sum_k U^2(\boldsymbol{r} - \boldsymbol{r}_k) \cdot \varepsilon_k^2 \cdot \langle \delta s_k(t+\tau) \cdot \delta s_k(t) \rangle_t,$$

where $\delta F(\boldsymbol{r}, t)$ is a signal fluctuation, τ – time lag, $U(\boldsymbol{r} - \boldsymbol{r}_k)$ – point spread function, ε_k – constant molecular brightness, $s_k(t)$ – switching function and $\delta s_k(t)$ – its fluctuation. The G_2 defines the value for each pixel of a SOFI image. In this formula we assume that the signal fluctuation is dictated by the photophysics of the molecule and does not depend on the drift, nor on the optical aberrations, and that different particles do not fluctuate in a synchronous manner. As we can see from the above formula the value of G_2 is a sum of squared PSFs weighted by the molecular correlation function. This results in a new narrower PSF whose standard deviation (σ) is decreased by a factor of $\sqrt{2}$. Following this idea, we can calculate the correlations of higher orders and reduce the size of PSF even more. However, high-order correlation functions suffer from the cross-terms caused by lower-order correlation contributions, that is why cumulants are used instead. The general formula for n-th order cumulant is given below:

$$C_n(\boldsymbol{r}, \tau_1, \dots, \tau_{n-1}) = \sum_k U^n(\boldsymbol{r} - \boldsymbol{r}_k) \cdot \varepsilon_k^n \cdot w_k(\tau_1, \dots, \tau_{n-1}),$$

where $w_k(\tau_1, \dots, \tau_{n-1})$ is a correlation-based weighting function.

The resolution here is enhanced by a factor of $\sqrt{n}$. Another remarkable point is that the molecular brightness is also raised to the *n*-th power. This non-linear response results in diming of weaker fluorophores even more (see Figure 1). The problem has been overcome in the balanced (b)SOFI[128]. Here the molecular statistic (on-time ratio, brightness and concentration) extracted from several cumulant orders is accounted to compensate the nonlinear brightness response. In addition, the calculation of spatio-temporal cross-cumulants (the correlation of neighboring pixels' time traces) and post-process Fourier filtering result in even higher resolution: improvement by a factor of *n* for *n*-th order cross-cumulant[129,130].

In practice, the use of the photoswitchable fluorescent protein Dronpa with the second-order cumulant analysis of the acquired stack resulted in a factor-of-two improvement of resolution (about 120 nm)[131]. Higher-order cumulants can be applied to the intensity traces of quantum dots (QDs) that feature slower blinking kinetics and are longer because QDs are more photostable than fluorescent proteins. The resolution achieved in this case was 55 nm[126]. As a bonus, the uncorrelated noise and constant background signal are greatly reduced by cumulant analysis[126] (compare first image with other images in Figure 1).

Although SOFI does not match the resolution of the PALM, STORM or STED techniques, it allows a higher temporal resolution and is therefore more suitable for live-cell imaging.

As we could see in the Introduction, there is a variety of super-resolution techniques which differ in spatial and temporal resolution, way of sample preparation, complexity of imaging setups, required irradiation intensity, etc. Selection of one of these techniques is dictated by the biological system. Considering the fact that the structure of subnucleolar compartments cannot be resolved by a classical optical microscope, and that within the scope of this work we are interested more in the cellular distribution and relative localization of two proteins, we selected PALM [132] and dSTORM [116] techniques to address our questions. One of their main advantages relies on the simplicity of implementation and setup development.

1.3.6. Two-color imaging

With super-resolution localization microscopy, the co-localization of two proteins can be investigated in order to better understand their biological functions and possible interactions. While a single-color experiment is quite simple to perform, there are some important points in two-color imaging that are worth mentioning. The first one is the selection of a pair of photoswitchable dyes. A big choice of fluorescent labels results in a high number of different combinations: two organic fluorophores, two fluorescent proteins, or a combination of both. However, to achieve a minimal crosstalk between two channels, the spectral separation of the selected labels must be considered.

One of the first studies on the subject of multi-color imaging in localization microscopy was published in 2007 by Bates et al. [133] The authors used activator-reporter pairs of organic fluorophores (Cy2-Alexa Fluor 647 and Cy3-Alexa Fluor 647), as it was described in their previous works [134,135], and performed the co-imaging of microtubules and clathrin-coated pits (CCPs) within the same cells. Briefly, the principle of STORM technique relies on the

switching of a reporter dye (e.g. Alexa Fluor 647, Cy5, Cy5.5, Cy7) between the fluorescent and dark states using light of different wavelengths, where an activator dye (e.g. Cy2, Cy3, Alexa Fluor 405) is used to facilitate the transition of a reporter to the bright state. Indeed, the recovery rate depends critically on the close proximity of an activator. Certain buffer components are necessary for the efficient blinking: reducing agents (e.g. thiols) and oxygen scavenging system [134]. Using several such activator-reporter pairs and pulses of activation laser light with different wavelengths it is possible to obtain a two-color super-resolution image. This approach does not suffer from chromatic aberrations because the same dye is used as a reporter. However, the crosstalk between channels is possible, since a reporter can be activated spontaneously (thermal activation) or under the "wrong" activation pulse. Alternatively, the same activator can be used in combination with different reporter dyes, for example: Cy3-Cy5, Cy3-Cy5.5, and Cy3-Cy7 [133].

Two-color dSTORM may be performed as well after a careful selection of dyes and imaging buffer [136]. Among the best switching fluorophores are cyanine derivatives (Cy5, Alexa Fluor 647) and rhodamines (Alexa Fluor 488, Atto 488, Alexa Fluor 555). Unfortunately, these dyes require different buffers for optimal blinking. Whereas cyanine dyes work better in presence of oxygen scavenging system (high brightness and low duty cycle), the rhodamines don't blink properly in the absence of oxygen [137]. This limits the choices for multi-color imaging. After systematic characterization of the properties of most widely used organic fluorophores and their requirements for imaging buffer, Dempsey et al. in their study [137] selected four of them (Atto 488, Cy3B, Alexa Fluor 647, and DyLight 750) with a low crosstalk and performed four-color imaging of microtubule filaments and other cellular structures (ER, mitochondria). With multi-color dSTORM the color cross-talk can be reduced or eliminated, but we must deal with chromatic aberrations.

Another approach for chromatic aberration-free two-color imaging was proposed by Tam et al. [138], and is based on the sequential labelling and STORM imaging of the same region of interest (ROI) under identical imaging conditions (i.e. with the same fluorophore and imaging buffer). First, one of the proteins of interest was immunolabeled with primary and secondary (conjugated with Alexa Fluor 405-Alexa Fluor 647 pair) antibodies. After acquisition, the sample was removed from the microscope stage and unbleached fluorophores were quenched by adding a reducing agent. Then the second protein was labelled with an appropriate primary antibody derived from a different species, whereas the secondary antibody was again conjugated with Alexa Fluor 405-Alexa Fluor 647 pair. After locating the same ROI,

second protein was imaged. This approach is limited by the availability of specific primary antibodies derived from different species.

PALM technique, on the other hand, has several advantages over STORM and dSTORM: compatibility with live-cell imaging; minimum amount of staining and sample manipulation; it does not require complex buffers, fluorescent proteins are imaged in physiological media; because of proteins fusion and 1:1 tagging, the background caused by non-specific labeling is absent. Many studies were performed since 2007 in order to ameliorate the photophysical and photoswitching properties of fluorescent proteins and to find a pair of them for two-color PALM imaging. The problem is that the majority of photoswitchable proteins either emit in the same spectral region or, those that can change their emission wavelength under UV irradiation, cover almost the whole visible spectrum.

Shroff et al. used the reversible switching of Dronpa in combination with tdEos fluorescent protein to study the proteins involved in adhesion complexes [139]. In this case, the acquisition starts by tdEosFP, which is photoconverted with UV and excited with 561 nm laser until there is no more of tdEosFP molecules in a green form. Then the already activated by UV laser Dronpa molecules can be deactivated using intense 488 nm light and imaged under a combination of 405 nm and 488 nm lasers. However, Rosenbloom et al. discussed the problem of Dronpa photobleaching under a strong illumination by 488 nm laser, when molecules could no longer be reactivated or excited [140]. This can be explained by the additional photoactivation of Dronpa with 488 nm light. Spontaneous return to the fluorescent state was also observed, and it prevents the identification of single-molecule events and causes a high fluorescence background, particularly in densely labeled samples. To solve the mentioned above problems, the slow-switching Dronpa variant, rsKame was produced. The protein displays reduced photoactivation from the dark to the fluorescent state under excitation light. The rsKame protein in combination with PAmCherry1 was used in a two-color photoactivated localization microscopy to imagine inner and outer mitochondria membranes in mammalian cells [140].

Other Dronpa mutants (bsDronpa and Padron) with different blinking behavior can be used for chromatic aberration-free two color imaging [141]. Under irradiation with 405 nm laser bsDronpa goes to the bright state and Padron in the dark (non-fluorescent) state. The bsDronpa fluorescence is readout under irradiation with 405 nm laser. Then 496 nm laser switches bsDronpa into the dark state and Padron into the bright. Padron fluorescence emission is readout under 496 nm illumination.

Several other combinations were used in following years: PAmCherry1 with PA-GFP in (Subach et al., 2009) [142]; mGeos-M with PAmCherry1 in (Chang et al., 2012) [143]; mEos2-Dronpa, mEos2-PSCFP2 and PSCFP2-PAMCherry1 in (Annibale et al., 2012) [144]; EosFP*thermo* with mIrisGFP in (Brodehl et al., 2012) [145]. To be mentioned, PA-GFP has a relatively poor contrast ratio of 100 as compared to 1000 of PSCFP [146]. Existing disadvantages of PALM technique, like the effect of overexpression and the impact of large fluorescent proteins on the function and localization of the protein of interest, must be taken into account.

Sometimes, depending on the biological problem, there is a need in combination of PALM and STORM techniques. Bock et al. used the reversibly switchable fluorescent protein rsFastLime (cys-trans isomerization of a chromophore, variant of Dronpa) and the organic fluorophore Cy5 with PALMIRA strategy (PALM **i**ndependently **r**unning **a**cquisitions [147]) to record two-color nanoscale images inside whole cells [148]. Both labels were added exogenously, after cells fixation, permeabilization and indirect immunolabeling (biotinylated anti-mouse antibody for fluorescent protein).

The popular combination of tdEosFP with Alexa Fluor 647 was used in (Izeddin et al., 2011) [149] for dynamic imaging of dendritic spines under reducing buffer conditions (PBS, pH 7.4, containing 10% glucose, 50 mM β-mercaptoethylamine, 0.5 mg/ml glucose oxidase and 40 mg/ml catalase). This approach was later used in works of Sillibourne et al. [150] in order to localize centrosomal proteins. In the latter case, however, the dimeric version of Eos was substituted by the monomeric variant mEos2 [113].

Besides the selection of fluorescent labels, additional steps in multi-color super-resolution imaging must be performed in order to correct instrumental errors and achieve an accurate result. The long acquisition time often results in the lateral or axial sample drift, or both of them. Several strategies have been shown and used for drift correction [132,151,152,153]. Some of them will be discussed later in more details. Then, if two channels are imaged with different cameras the perfect manual alignment in nanometer range is a complicated task. In addition, chromatic aberrations deform one image with respect to the other one. The process of image registration, alignment of several images of the same scene, is used to deal with the problem. There are already existing algorithms that calculate a deformation field and transition matrix that can be applied on final images. The referent stack required for calculations can be obtained by a scanning procedure with isolated fluorescent beads visible in both channels (e.g. Tetraspeck beads from Invitrogen – 100 nm diameter microsphere, stained with four different

fluorescent dyes simultaneously: blue (365/430 nm), green (505/ 515 nm), orange (560/580 nm) and dark red (660/680 nm)) [144,154]. With an appropriate photon statistic and after a careful correction of all errors due to the optical/chromatic aberrations and mechanical shifts the position of the corresponding molecule can be determined with a localization accuracy down to $\Delta x < 1\ nm$, the limits depending on the photon emission statistics.

1.3.7. 3D imaging

For accurate study of cellular organization, the imaging in all three dimensions is required. Although it is possible to acquire a 3D image with techniques like STED, SIM and 4Pi, here we will focus on the single-molecule localization microscopy approaches: biplane detection [155], astigmatic imaging [153], double-helix (DH) PSF [156,157,158,159]. They were selected because require minor modifications of a standard microscope and can be easily implemented in any laboratory.

In **biplane (BP) FPALM** method (Juette et al., **2008**) the modifications in detection path are made to enable simultaneous detection from two axially separated object planes. To this end, a 50:50 beam splitter cube divides the focused light in front of the camera into a transmitted and a reflected path, which is redirected toward the camera (Figure 20A). The signal from the two recorded regions of interest can be therefore combined into a 3D raw data stack consisting of two planes. The experimentally obtained 3D PSF (by z-scan of a small fluorescent bead) is fit to each dataset to determine *x*, *y*, and *z* coordinates. BP FPALM is capable of 3D imaging of volumes ≤ 1 μm thickness with a lateral resolution of 30 nm and an axial resolution of 75nm. To image structures over a depth of several micrometers, BP FPALM data was recorded at different *z* positions of the sample stage and combined later to achieve a final image.

In the **astigmatism imaging** method (Huang et al. **2008**), introducing of a cylindrical lens or adaptive optics in the imaging path leads to the formation of two slightly different focal planes for the *x* and *y* axis (Figure 20B). As a result, the PSF acquires the shape of an ellipse with its orientation and ratio between two axis that depends on z-position of the fluorophore. Recording a stack of localizations of individual fluorophores, each one with different PSF, it is possible to obtain a three-dimensional super-resolution image without scanning the sample. By fitting localizations with 2D gaussian function, the (*x*,*y*) position of a fluorophore is obtained from the center of fit, whereas the peak widths w_x and w_y allow to localize the fluorophore along the z axis by using a calibration curve. To obtain this curve, an isolated

fluorescent particle is scanned in z-dimension (about 1 µm thick layer) and then the values of w_x and w_y are plotted as a function of z-coordinate. Using this approach, it is possible to achieve a lateral resolution of 20 nm and 50 nm in the axial direction.

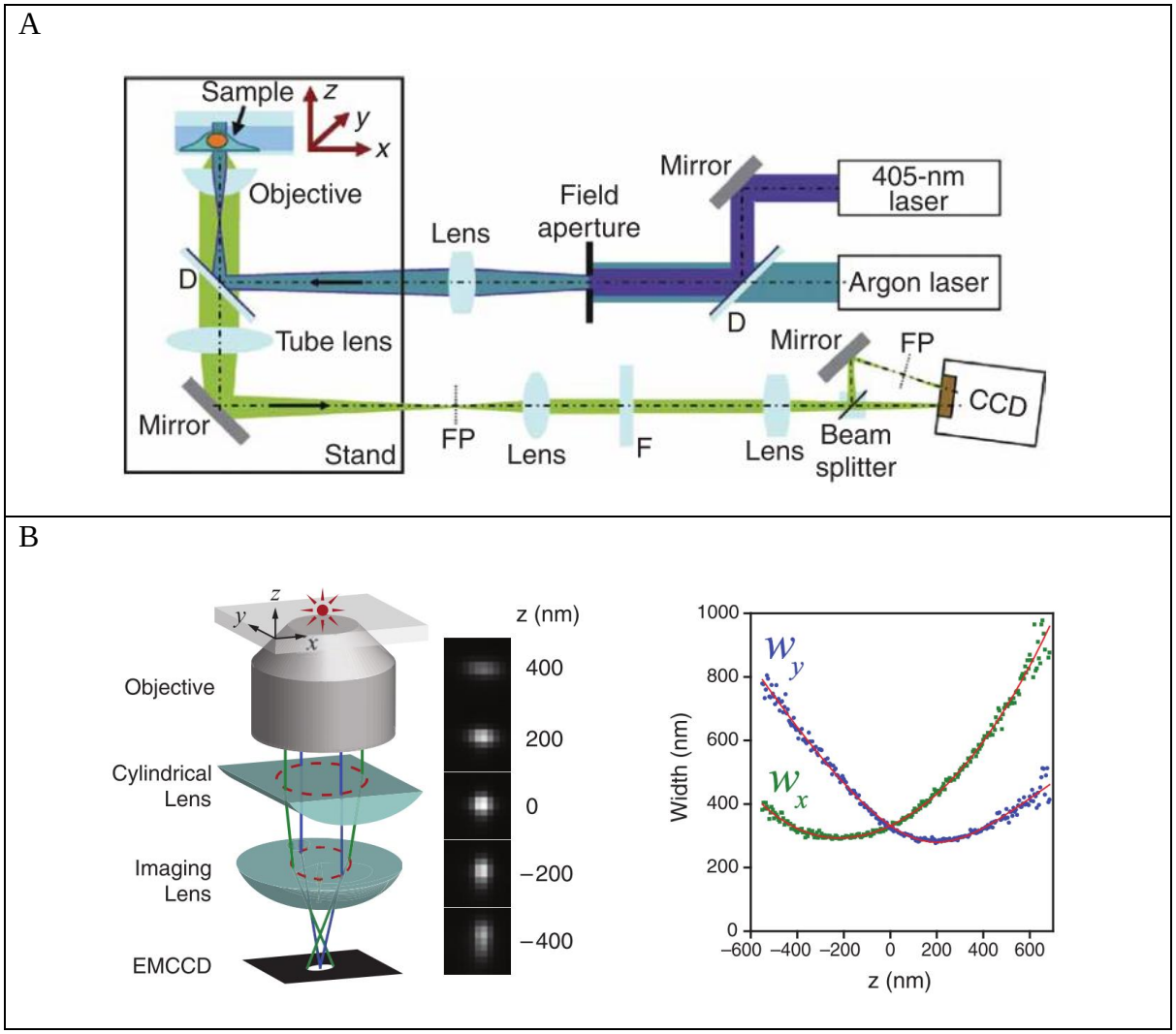

Figure 20. (A) BP FPALM setup. Adopted from (Juette et al., 2008) [155] *(B) The simplified optical diagram illustrates the principle of astigmatism imaging method. The images of a fluorophore at various z positions show the changes of PSF ellipticity. The right panel represents the calibration curve which is required for decoding of single emitter z-coordinate. Adopted from (Huang et al., 2008)* [153].

In **double helix** approach (Pavani et al., **2009**) the point spread function of the microscope is engineered to have two lobes that can rotate with respect to the center of the line which connects them (Figure 21). The angular orientation depends on a z-position of a single emitter [159]. As it was described in previous techniques, to obtain a z-coordinate of a fluorophore the raw data must be decoded with a help of the calibration curve, which can be acquired by a simple scanning procedure. This method enables a 3D imaging of thick samples (> 2 µm) with a resolution similar to the astigmatism imaging. The use of photoswitchable fluorophores with high brightness is required for a good signal to noise ratio, because of the PSF splitting and

losses associated with additional optical elements (a spatial light modulator with a phase-mask).

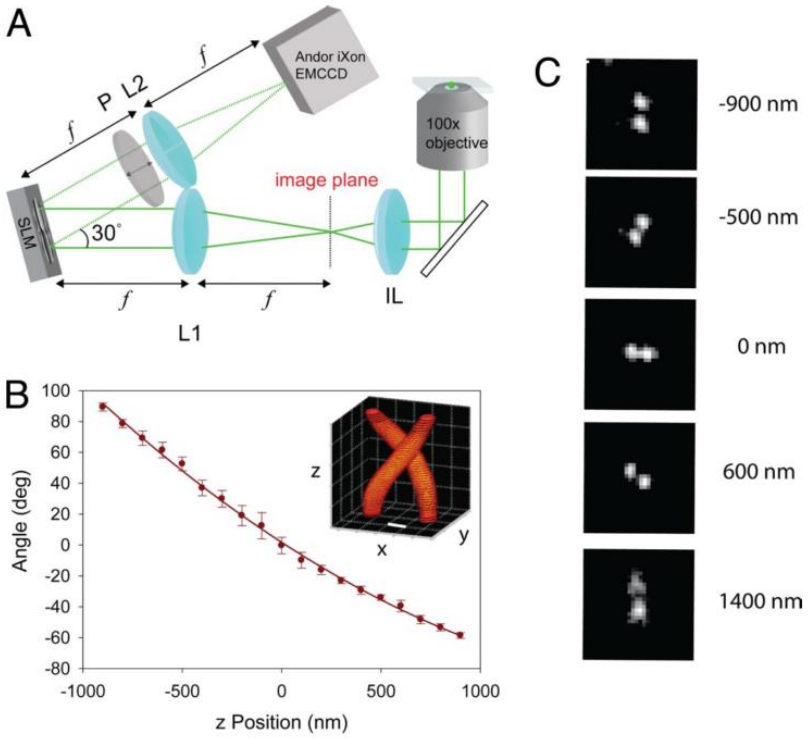

Figure 21. DH-PSF imaging system and z-calibration. SLM – spatial light modulator. Adopter from (Pavani et al., 2009) [159].

It worth to mention one more 3D technique, the interferometric PALM (iPALM) [157], which combines the photoactivated localization microscopy with single-photon simultaneous multiphase interferometry. Much more complicated arrangements of the optical setup are necessary in this case. Although iPALM provides an excellent axial resolution in sub-20-nm range, it only operates over a 200 nm range.

Research objectives

NC protein is an interesting target for the antiretroviral therapy. It has a highly conserved structure and sequence (zing-fingers and hydrophobic plateau). Therefore, by targeting NC, we target different viral strains of HIV. There are many studies looking for NC inhibitors. Some of these inhibitors, like zing ejectors, may damage health cells, because of their non-specificity. Knowing the protein functions and roles at each step of the viral life cycle, and by identifying its cellular partners, it is possible to design more efficient and less toxic inhibitors. To summarize what was presented above, NC localizes to the nucleolus – subnuclear structure, which is divided in three components associated to specific steps of the ribosome biogenesis. In addition to the formation of ribosomal subunits, the nucleolus plays important roles in stress response, proliferation and cell cycle regulation. Proteins responsible for these functions have specific localization in the nucleolus. Revealing the precise localization of NC protein in this multifunctional subnuclear compartment may shed some light on its role in the nucleolus during the virus replication cycle.

To achieve efficient viral replication and infection, HIV protein associations play essential roles (e.g., cleavage, inhibition, and activation) in the HIV life cycle. Each HIV protein collaborates with another viral protein to accomplish specific activities that precisely take place at the proper stages of the HIV life cycle. In 2012 the results of a huge study on HIV cellular partners were published. It was shown that NC interacts with twelve cellular proteins, and among them with the nucleolar protein NoL12 [160] (the results of experiments performed in our laboratory show this interaction *in-vivo*). Viral RNA with two other HIV proteins, Rev and Tat, also localize in the nucleolus [89,161,88]. Previously, it was demonstrated (*in-vitro*) that NC interacts with Tat and induces its degradation via the proteasome pathway [40]. NC also interacts with ribosomal proteins RPL26 [66] and RPL7 [162].

Although there are many evidences of nucleolar localization of NC protein, it is still not clear why NC localizes in this subnuclear compartment – is it due to the chaperoning role of NC in vDNA integration, passive diffusion due to the high affinity to cellular RNAs or an interaction with nucleolar and/or ribosomal proteins? And what is the role of NC in the nucleolus? Answers to these questions will fundamentally enhance our understanding of the HIV-1 replication cycle and will provide essential information to exploiting the nucleolar localization of NC as targets for therapeutic intervention.

Chapter 2. Materials and Methods

2.1. Plasmid constructs

The peGFP-NPM construct was kindly provided by Xin Wang (17578, Addgene).

The mEos2 constructs were obtained by replacing the eGFP ORF (open reading frame) in the peGFP-C1-GW vector corresponding to the Gateway® cloning version of peGFP-C1 (Clontech) by the mEos2 ORF in order to obtain the vector pmEos2-C1-GW. To do so, the mEos2 cDNA was PCR amplified from the pRSETa mEOs 2 plasmid (Addgene #20341) and was inserted between NheI and XhoI restriction sites of the digested and dephosphorylated peGFP-C1-GW vector in order to obtain the pmEos2-C1-GW vector. The cDNAs coding for NPM, Fib or RPA were PCR amplified from plasmids obtained at Addgene (plasmids # 17578, 26673 and 17660 respectively) with primers harboring the attB recombination sequences. hNol12 ORF was amplified from the pET52-hNoL12 plasmid which was a generous gift from Dr. Oeffinger Marlene (Institut de recherches cliniques de Montréal). The PCR products were purified (Macherey Nagel Nucleospin Gel and PCR Clean-up kit) and cloned into pmEos2-C1-GW using the Gateway technology to obtain the constructs pmEos2-NPM, pmEos2-Fib and pmEos2-RPA respectively.

pPAeGFP and pPAmCherry plasmids were obtained from Addgene (#11910 and 31929 respectively). To create fusion proteins, PAeGFP and PAmCherry ORFs were PCR amplified from plasmids obtained at Addgene (#11910 and 31929 respectively) using specific forward and reverse primers harboring NheI and KpnI restriction sites respectively. After purification, the PCR products were digested and inserted in a NheI/KpnI digested and dephosphorylated peGFP-C1-GW plasmid in order to obtain pPAeGFP-C1-GW and pPAmCherry-C1-GW plasmids. As before the ORFs coding NPM, Fib and RPA were inserted by the Gateway technology into this plasmid.

mEos2 ORF was PCR amplified from the pRSETa mEOs 2 plasmid (Addgene #20341) with specific primers harboring XhoI and XbaI restriction sites. After purification, the PCR product was digested with XhoI and XbaI restriction enzyme and inserted into a pcDNA3.1 Zeo(+) vector digested by XhoI/XbaI and dephosphorylated to give pmEos2-pcDNA3.1 Zeo plasmid. The NCp7 ORF was PCR amplified with primers harboring EcoRI and XhoI restriction sites. The PCR product was purified and digested by EcoRI and XhoI and inserted in fusion to mEos2 in the corresponding cloning sites of pmEos2-pcDNA3.1 Zeo to give pNCp7-mEos2-pcDNA3.1 Zeo plasmid.

The ffDronpa (fast folding Dronpa) ORF was digested from pffDronpa from Peter Dedecker (University of Leuven, Belgium) using BamHI and EcoRI restriction enzymes and inserted into a pcDNA3.1 Zeo(+) previously digested by the same enzymes and dephosphorylated to give pffDronpa-pcDNA3.1 Zeo plasmid. This construct was thus digested by BamHI and dephosphorylated. In parallel the NCp7 ORF was PCR amplified, the PCR product purified and digested by the restriction enzyme BamHI and inserted into pffDronpa-pcDNA3.1 Zeo to give pNCp7-ffDronpa-pcDNA3.1 Zeo.

The 3XFlag-Ncp7_pcI-neo construct was obtained by PCR amplification of the HIV-1 NCp7 ORF with primers harboring the attB recombination sequences on both sides. After purification the PCR product was cloned using the Gateway cloning strategy into a pcI-neo vector modified to contain the coding sequence of the 3XFlag tag followed by a Gateway cloning cassette (pcI-neo-GW).

NCp7-mCherry construct was obtained from Dr H. de Rocquigny and consists of the HIV-1 NCp7 ORF in frame with the mCherry ORF both coding sequences being separated by the linker GGDVASL and inserted into a pcDNA3.1 vector.

The integrity of all plasmid constructs was assessed by DNA sequencing (GATC Biotech, Germany).

2.2. Cell culture and transfection

HeLa cells (ATCC reference CCL-2; p7 – p20) were cultured in DMEM (1 g/l D-Glucose, [-] Phenol Red; Gibco by LifeTechnologies) supplemented with 10% Fetal Bovine Serum (S1810-500, Dutscher), 1% of Pen-Strep solution (100 units of Potassium Penicillin and 100 µg of Streptomycin Sulfate per 1 ml of culture media – final concentration; DE17-602E, Lonza, BioWhitaker) and 1% L-Glutamine (2 mM; BE17-605E, Lonza, BioWhitaker) in T75 flasks at 37 ºC with 5% CO_2.

Cells were seeded on round cover-glasses 18 mm in diameter (VWR) at a density of 75000 cells per well of a 12-well plate (ClearLine). Prior to seeding, cover-glasses were washed once with 70% ethanol and then three times with PBS 1x (Buffered Saline 0.0095 M (PO_4), [-] Ca, [-] Mg; Lonza, BioWhitaker). Cells were transiently transfected with different plasmids on the next day after seeding using jetPEI transfection reagent (PolyPlus Transfection) following the supplier's protocol (https://www.polyplus-transfection.com/resources/product-literature/) – 2 µl of jetPEI for 1 µg of plasmid DNA. Plasmids were stored at -20ºC.

2.3. Immunofluorescent labelling

1. Cells fixation:
    - the old medium was removed;
    - cells were washed quickly with PBS 1x (1 ml for 12-well plate);
    - 1 ml of freshly prepared 4% PFA was added to each well. The 16% PFA stock (15710, Electron Microscopy Science) was diluted in PBS1x and preheated in water bath to 37ºC. For a detailed protocol of samples preparation see the reference: Whelan and Bell (2015) [163]. Note that cell blebbing (Figure 22B) induced by chemical fixation can be removed by adding 0.02% Triton. It is required if transfected cells just need to be fixed before imaging, otherwise the step "Permeabilization" during the immunolabeling gives the same result. Reduced concentration of PFA as described in Zeng et al. (2012) [164] didn't work for us.
    - the plate was left in the incubator at 37ºC for 12 min;
    - cells were washed 3 times with PBS 1x; each time the plate was placed on a shaking machine for 5 min.
2. Permeabilization:
    - PBS was removed;
    - 1 ml of 0.2% Triton X-100 (X100-500ML, Sigma) (diluted in PBS 1x) was added to each well;
    - the plate was placed on a shaking machine for 10 min;
    - cells were washed 3 times with PBS 1x; each time the plate was placed on a shaking machine for 5 min.
3. Blocking:
    - PBS was removed;
    - 1 ml of 1% BSA (bovine serum albumin - sc-2323, ChemCruz) (diluted in PBS 1x) was added to each well;
    - the plate was left at room temperature for 1 h.

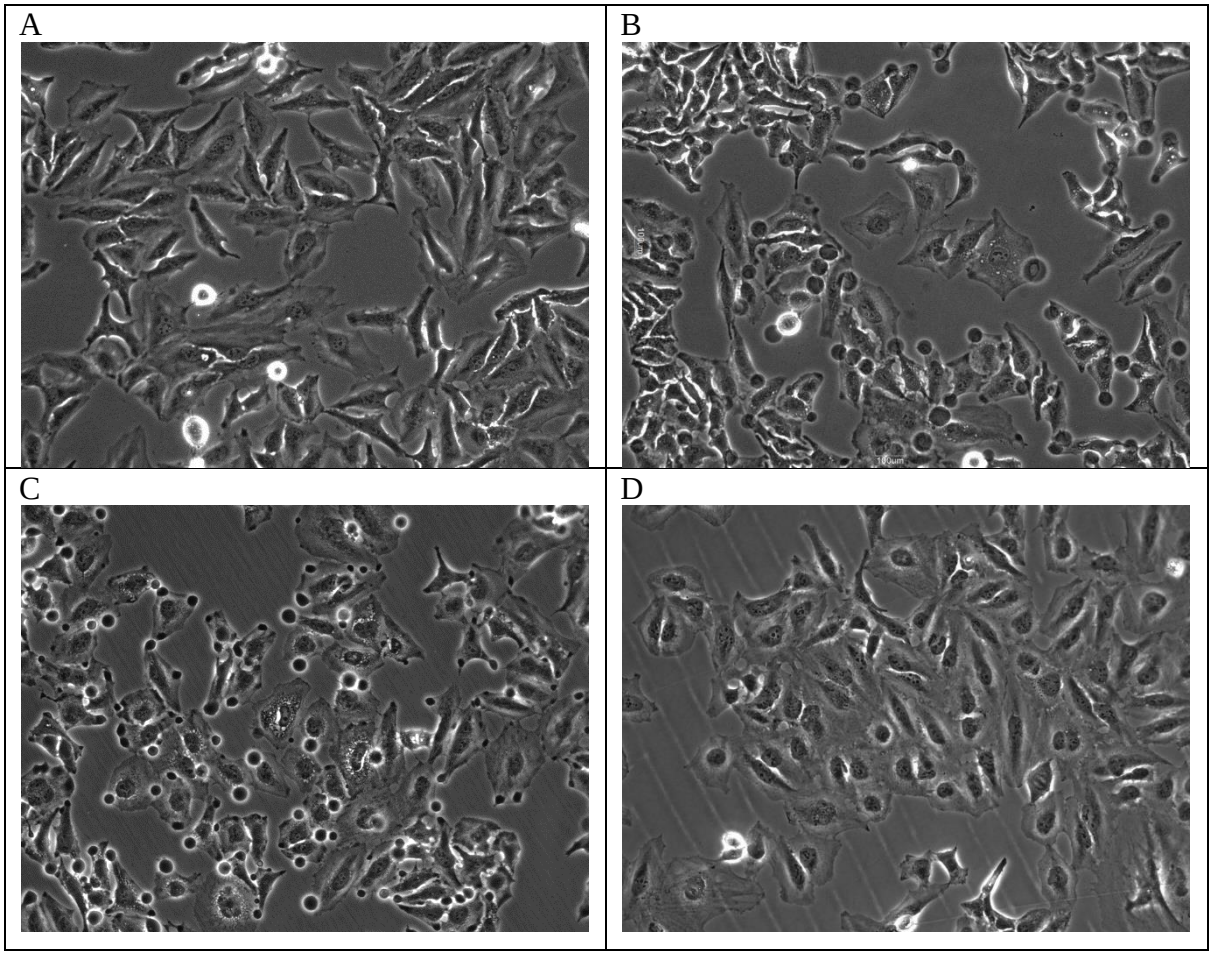

Figure 22. Effect of chemical fixation on cell blebbibg. (A) Living HeLa cells. (B) After fixation in 4% PFA for12 min. (C) After fixation in 1% PFA for12 min. (D) After fixation in 4% PFA + 0.02% Triton-X100 for 12 min.

4. Labeling with primary antibody:
    - primary antibodies were diluted in 1% BSA (for dilutions see Table 1);
    - drops of 50 µl were deposited on a parafilm and then cover-glasses were placed on the top of these drops (to save the stock of antibodies). Hint: cover-glasses were kept in a Petri dish covered with aluminum foil to prevent an accidental damage of samples.
    - Petri dish was left at room temperature for 1 h;
    - cover-glasses were placed back in a 12-well plate with a help of a tweezer and a needle;
    - cells were washed again (5 min) three times with PBS 1x.
5. Labeling with secondary antibody:
    - secondary antibodies were diluted in 1% BSA (for dilutions see Table 1);
    - QDs (Qdot 655 Streptavidin Conjugate - Q10121MP, Invitrogen) were added into the solution with antibodies at 2 pM concentration. The QDs are used to correct for the sample drift that occurs during a long acquisition.
    - cover-glasses were deposited on a parafilm and cells were incubated with secondary antibody at room temperature for 45 min;

- after cover-glasses were placed back in a 12-well plate and washed 3 times with PBS 1x, the plate was covered with aluminum foil and stored in cold room at +4ºC (one week maximum).

Table 1. List of primary and secondary antibodies used in this work. Dilutions are mentioned for each antibody.

Primary antibodies		
@NPM1 (7H10B9) (mouse)	NBP1-47354, Novus biological	1/750
@Fibrillarin (38F3) (mouse)	MA3-16771, Invitrogen	1/500
@RPA194 (F-6) (mouse)	sc-46699, Santa Cruz	1/50
@Flag M2 (mouse)	F1804, Sigma	1/500
@α-tubulin (mouse)	T9026, Sigma	1/500
@NPM(3A9F1)-A647 (mouse)	ab202578, Abcam	1/100
@Fib[EPR10823(B)]-A555 (rabbit)	ab203410, Abcam	1/100
@NCp7(goat)	from Gorelick	1/500
Secondary antibodies		
goat @mouse-A488	A11001, Invitrogen	1/500 – 1/1000
goat @mouse-A555	A21424, Invitrogen	1/500 – 1/1000
goat @rabbit-A555	A21429, Invitrogen	1/500 – 1/1000
F(ab′)2-goat @mouse-A647	A21237, Invitrogen	1/500 – 1/1000
F(ab')2-goat @rabbit-A647	A21246, Invitrogen	1/500 – 1/1000
donkey @goat-A647	ab150131, Abcam	1/500 – 1/1000

* “A” means “Alexa Fluor”

2.4. Buffers

The standard switching medium for organic fluorophores is composed of TN buffer (50 mM Tris (pH 8.0) and 10 mM NaCl), an oxygen scavenging system (0.5 mg/ml glucose oxidase (G7141-50KU, Sigma), 40 µg/ml catalase (C40-500MG, Sigma), 10% (w/v) glucose) and 100 mM β-mercaptoethylamine (MEA; 30070-10G, Sigma). Buffer was freshly prepared on the day of the experiment. All the modifications in composition of this buffer (e.g. substitution of MEA by BME, changes in the concentration of thiols, absence of an oxygen scavenging system or addition of triplet state quenchers like COT) will be mentioned in the text of the Results section.

The second buffer was prepared by mixing Vectashield (H-1000, Vector Laboratories) in TRIS-Glycerol (5% v/v TRIS 1 M pH 8 in Glycerol) to achieve a final concentration of 20% Vectashield (as described in Olivier et al., 2013 [123]). A 10 µl drop of this solution was deposited on a microscope slide, then a cover-glass (our sample) was rinsed in MilliQ water to remove salts and placed on a top of that drop. After 10 min at room temperature, enough to evaporate water from the surface of the cover-glass, the sample was sealed with a dental cement (Picodent). The sample is ready for imaging and can be stored at +4°C for several days and reused again later.

2.5. Confocal imaging

Confocal microscopy imaging was performed on inverted microscope Leica DMI 4000 with confocal head Leica SPE 2. Microscope is equipped with 63x 1.4 NA oil immersion objective and lasers with excitation wavelengths of 405, 488, 561 and 635 nm. The fluorescent labels were excited at 635 nm (Alexa Fluor 647), 561 nm (Alexa Fluor 555) and 488 nm (eGFP) and their emission was collected (650-750 nm; 570-630 nm, 500-555 nm) by a PMT detector.

2.6. Optical setup and super-resolution imaging

Super-resolution localization microscopy imaging was performed on a home-built setup based on the Nikon Eclipse Ti microscope (Figure 23A) equipped with 100x 1.49 NA oil immersion objective. The laser lines of different wavelengths, used for excitation and photoactivation of fluorescent labels (Table 2), were co-aligned into a single beam using single-band dichroic mirrors (Semrock). Two mirrors, placed after each laser, served for beam alignment. Z-fold configuration enables the first mirror to get the desired vertical and horizontal position of the beam on a target, and the second one to compensate for the angles. The half-wave plates (λ/2) were used to turn the polarization plane and align it with the optical axis of AOTF crystal.

Table 2. Laser lines

Laser	Used for	Intensity
405 nm	photoactivation of mEos2, Dronpa, PA-GFP, PA-mCherry1	1÷120 W/cm^2
488 nm	ATTO488, A488, mEos2 (green form), PA-GFP, Dronpa	1÷2 kW/cm^2
561 nm	A555, mEos2 (red form), PA-mCherry1	1÷2 kW/cm^2
642 nm	A647	2÷3 kW/cm^2

* "A" means "Alexa Fluor"
** diameter of illumination profile – 55 µm; area – 2.38*10^{-5} cm^2

An acousto-optic tunable filter (AOTFnC-400.650; Opto-Electronic) helped to switch between lasers (shutter) and to change the laser power. Here the vibrations of piezoelectric transducer create a sound wave in a crystal of Tellurium dioxide (TeO_2). The acoustic wave, in turn, induces a slight change of the refractive index distributed periodically in a crystal that now acts like a diffraction grating. Diffracted light has maxima at angles Θ_m: $d \sin \Theta_m = m\lambda$, where d is a distance between the centers of two adjacent slits, m – diffraction order, and λ – wavelength. Changing the radio frequency (RF) applied on the AOTF (changes d in the formula) and observing the transmitted light of the same order and at the same angle, we can change the wavelength of this light. Whereas the RF amplitude level applied on the transducer allows to adjust the laser power.

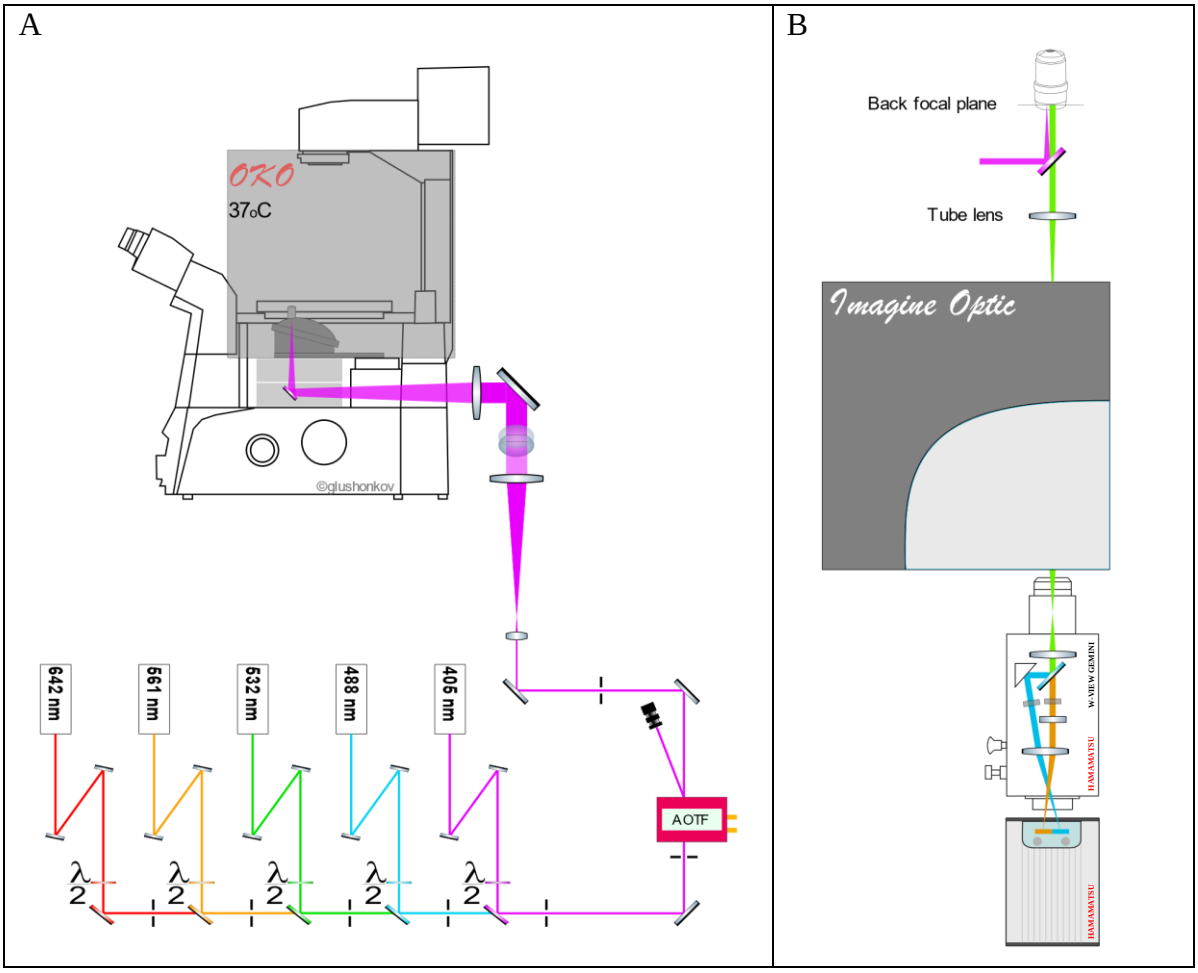

Figure 23. Optical setup based on a Nikon Eclipse Ti microscope. (A) Excitation path. (B) Emission/detection path. AOTF – acousto-optic tunable filter.

The laser beam was expanded with a help of the telescope system (6x magnification) and then focused by 300 mm lens to the back focal plane of the objective. The sample was illuminated in HILO mode (highly inclined and laminated optical sheet microscopy) [165] to minimize the background while imaging nucleoli (Figure 24B). Unlike HILO mode, in TIRF

the evanescent wave propagates over 200 nm within the cell, significantly limiting the observable region (Figure 24A).

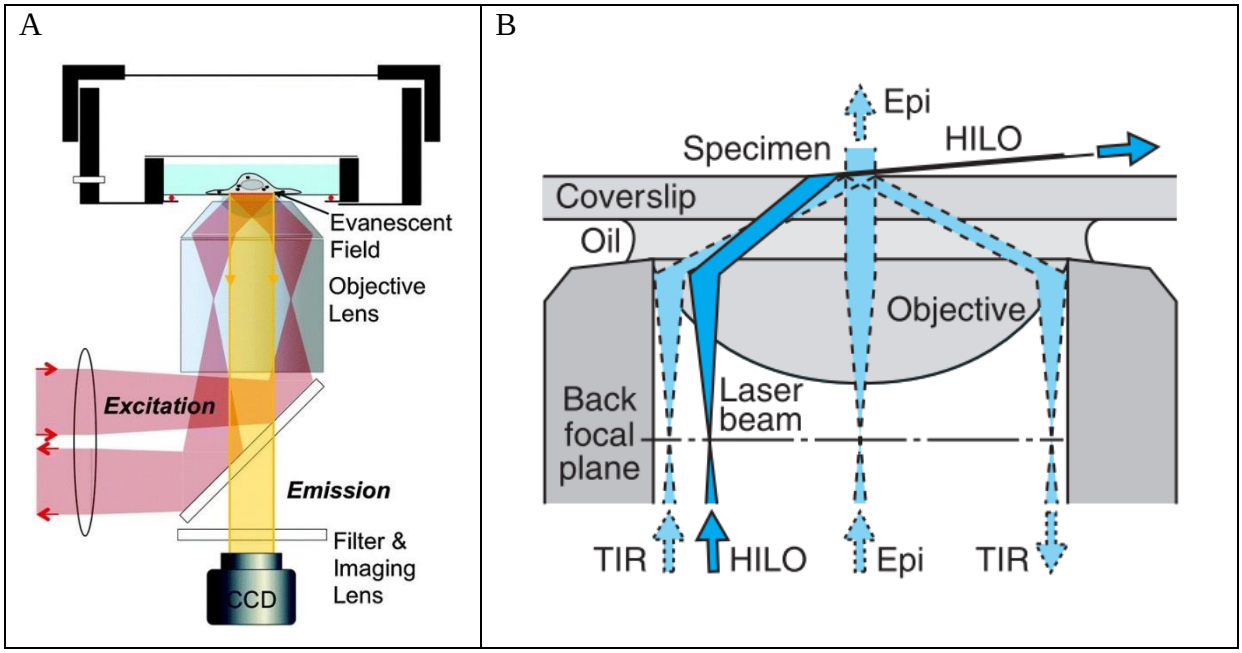

Figure 24. TIRF and HILO excitation modes. Adopted from (Park et al., 2015) [166] and (Tokunaga et al., 2008) [165].

Emission from the sample was spectrally filtered with the help of a multi-band dichroic mirror (405/488/561/635 nm). In addition, notch filters were used in order to attenuate the scattered laser light (see Table 3).

Table 3. Dichroics and filters configurations for different dye combinations

Turret 1	Dichroic 405/488/561/635	Di03-R405/488/561/635-t1-25x36, Semrock
	Notch 561	NF03-561E-25, Semrock

488+561 (Dronpa+mEos2; PA-GFP+PA-mCherry1)

Turret 2	Notch 488	NF03-488E-25, Semrock
Gemini	Dichroic 560	FF560-FDi01-25x36, Semrock
	BP 525/50	FF03-525/50-25, Semrock
	LP 561	BLP02-561R-25, Semrock

561+642 (mEos2+A647; A555+A647)

Turret 2	Notch 642	NF03-642E-25, Semrock
Gemini	Dichroic 640	FF640-FDi01-25x36, Semrock
	LP 561	BLP02-561R-25, Semrock
	LP 647	BLP01-647R-25, Semrock

The adaptive optics device (MicAO, Imagine Optic) contains a wavefront sensor and a deformable mirror that enables correction of various types of aberrations including those

induced by the optical elements inside the microscope and by the biological sample itself. MicAO optimizes the PSF of the microscope and consequently improves the lateral localization precision. For two-color experiments, the signal on the camera chip was split into two channels using a dual view system (Gemini, Hamamatsu) with a dichroic mirror (Figure 23B). For single color experiments, Gemini was used in Bypass mode. For the information about dichroic mirrors and filters that were mounted in a splitting system see Table 3. Finally, the emission was collected with an EM-CCD camera from Hamamatsu (ImagEM). Additional lens was used to obtain a final magnification of 150x corresponding to a pixel size of 106.67 nm. The OKO chamber was used to maintain a 37°C temperature for live-cells experiments.

The sample with 100 nm TetraSpek bead[167] (see the preparation protocol in Appendix) was used before each experiment to perform the PSF optimization and minimize the residual aberrations (with a help of adaptive optics). The reference image was acquired to correct for the lateral chromatic aberration using the image registration process performed by UnwarpJ plugin, ImageJ. To this end, a field of view with a single TetraSpek bead was selected to perform a raster scan by translating the microscope stage (for the Beanshell script see Appendix). The axial focus stability was ensured by the perfect focus system (PFS, Nikon Eclipse Ti) of the microscope. Here the same distance between the objective and the cover-glass is maintained during the long-term experiments (time-lapse overnight measurements) using the near-infrared 870 nm LED and CCD line sensor.

2.7. PSF optimization with Micao

The microscope objective is a complex system composed of multiple lenses with different properties in order to minimize optical aberrations. A short introduction to main optical aberrations is presented below.

Spherical aberration occurs when the light which is passing through the periphery of a lens is refracted more than the light passing through the center of a lens resulting in a different focus for peripheral and paraxial rays. Although microscope objectives are produced to be free of spherical aberration, this artifact may be introduced by utilizing the wrong mounting medium (results in the refractive index mismatches) or cover-glasses of different thickness.

Coma aberration is similar to spherical, but it appears only with off-axis objects and is most severe when the microscope is out of alignment. The comet-like image of a point source

is a result of refraction differences for light rays passing through the various lens zones as the incident angle increases.

Astigmatism aberration appears when rays that propagate in two perpendicular planes are brought together at different foci; this defect strongly depends on the angle of the light beam with respect to the optical axis. The image of a point source appears to be elliptical, with orientation that depends on the angle of the off-axis rays entering the lens. It worth to mention that there are two types of astigmatism aberration, or rather the origin of this aberration may be different. First occurs in a perfectly symmetrical optical system for objects away from the optical axis, whereas the second one occurs in the optical system without the axial symmetry (e.g. misalignment or use of a cylindrical lens). In later case, astigmatism is observed even for paraxial rays and this idea is used in 3D astigmatism imaging method.

The following procedure was performed with a help of adaptive optics in order to minimize aberrations that affect the shape of PSF and decrease localization precision.

Protocol of PSF optimization

1. The sample with 100 nm TetraSpek beads (T7279) was used for this optimization. The square region of interest (ROI) with only one bead was selected and cropped for further proceedings.
2. High exposure time (300 ms) and low camera gain (between 4 and 50) were selected in order to increase the signal to noise ratio.
3. Low laser power at 561 nm (~3 mW that corresponds to 125 W/cm^2) was used to prevent bleaching of the selected bead; still it should be high enough to have a good signal for correction procedure. Important: the signal of a bead should not be higher than ~75% of camera dynamic range, because after PSF optimization the signal will increase and can lead to the saturation.
4. Micro-Manager 1.4.22 was used for images acquisition. Parameters in the “Multi-Dimensional Acquisition” window: saving format - “Separate image files”, number of frames - “10000 images”, directory root - “tiff_temp” folder.
5. After the start of acquisition, following parameters were changed in the “Micao” application. In the “Image & Z-position” tab of the “Advanced setup” window (Figure 25, green ROI) the “directory to find TIFF files” was selected to be the one where we were saving recorded images: D:\tiff_temp\Image_1\Pos0.
6. “Diagnostics” window may be opened for the visualization of optimization process.

7. Next, the correction of aberrations (focus, astigmatism, coma, 3rd order spherical aberration and trefoil) was performed in the "Optimization" tab (Figure 25, right panel). Search limit was set to 0.050.
8. At the end of optimization, new contrast must be higher than the initial one. A small advice: changing the focus manually may give an idea about the PSF symmetry and residual aberrations. If the optimization was good new parameters were confirmed by clicking "OK" button and the mirror shape was saved by clicking on the "Save" icon. Note: individual aberration can be selected, and the search limit can be changed in case when the standard optimization protocol does not give a good result.

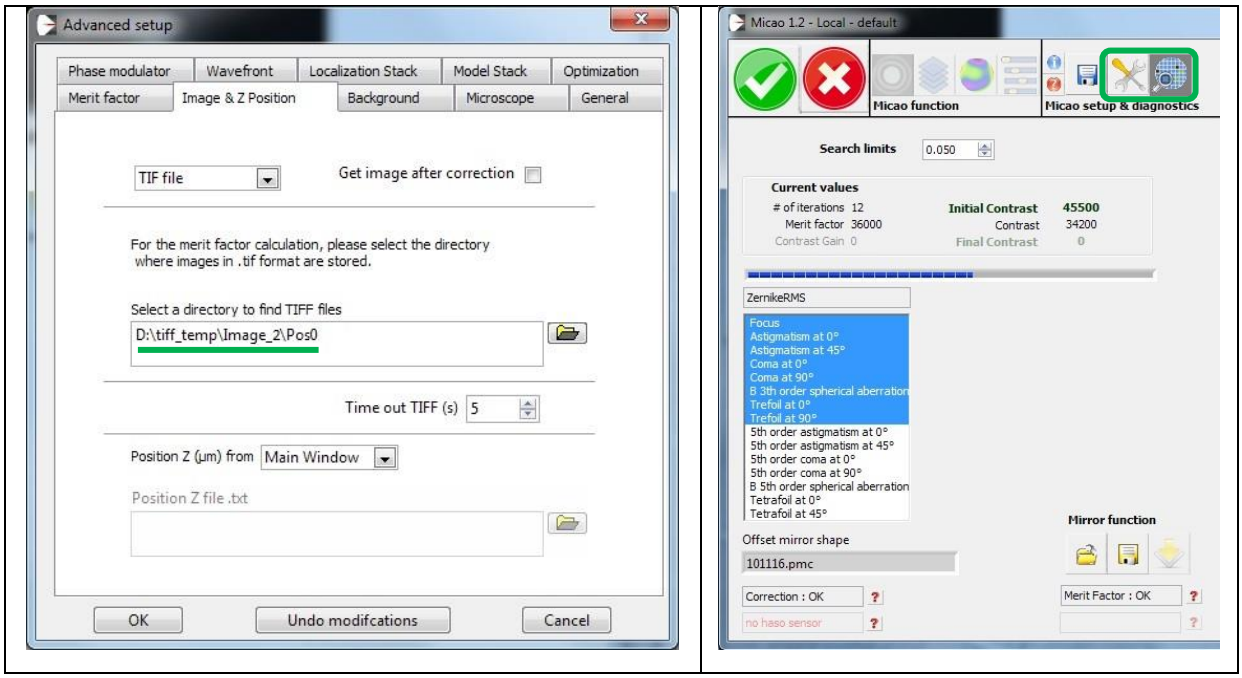

Figure 25. Screenshot of Micao software

2.8. Data analysis

A stack of 10000-20000 images of 512*256 pixels (two channels together) was analyzed with the Thunder STORM plugin in ImageJ [168]. The following parameters were used to find and fit the signal of each particle: image filtering – Difference-of-Gaussians filter (sigma1 = 1.0 and sigma2 = 1.6); approximate localization of molecules – Local maximum (peak intensity threshold: std(Wave.F1), connectivity: 8-neighbourhood); sub-pixel localization of molecules – Integrated Gaussian (fitting radius: 4 px, fitting method: Least squares, initial sigma: 1.3 px). Results were filtered by sigma and localization precision values: 120 nm < sigma < 180 nm, precision < 25 nm. Drift correction: with fiducial markers Max distance – 100 nm, Min marker visibility ratio – 0.15, Trajectory smoothing – 0.03. Reference images with TetraSpek beads were analyzed with the UnwarpJ plugin of ImageJ in order to

calculate the elastic deformations and create the transformation matrix, which will be applied to rendered images for correction of chromatic aberration.

2.9. Microinjection

Microinjection refers to the process of using a glass micro-needle to insert substances such as nucleic acids, proteins or fluorescent organic molecules into a single cell. It is a simple mechanical process in which a needle of 1µm in diameter penetrates inside the cytoplasm or nucleus. The desired contents are then injected into the subcellular compartment and needle is removed. Microinjection was performed on HeLa cells seeded on round cover-glasses with a diameter of 18 mm. Before loading into the micro-needle, the solution of 10 µM Rh-labeled NC 1-55 peptide was centrifuged for 20 min at 4ºC, to remove any protein aggregates or other big structures that can block the capillary. Microinjection was performed using a micromanipulator (Eppendorf Injectman NI 2) coupled to inverted microscope Leica DM IRE2, equipped with 100x 1.4 NA oil immersion objective. Emission was detected with Leica DC 350 FX digital camera.

Chapter 3. Results

The results of this thesis are organized in two parts. The first one describes the imaging protocol optimizations (fiducial markers for sample drift correction, chromatic aberration correction) and selection of the optimal conditions for two-color imaging (pair of fluorescent labels, buffer). These results are summarized in the article "Optimized protocol for combined PALM-dSTORM imaging" published in Scientific Reports. The second part is focused on a biological question: investigation of NC protein cellular distribution, in particular its nucleolar localization.

3.1. Sample drift (lateral and axial)

If we compare the localization microscopy with other super-resolution techniques or confocal microscopy, one of the biggest differences is the acquisition time. While taking one image on a confocal microscope takes only a second, the stack of ten thousand images for PALM or dSTORM is usually recorded within 5 to 10 min at a frame rate of 30 to 15 frames per second (fps). With the help of brighter fluorophores, it is possible to decrease the exposure and acquisition time. One of the drawbacks of a long acquisition time is the sample drift, which can be in the order of several hundreds of nanometers over the acquisition. Different factors, as temperature change, mechanical relaxation or external vibrations, can affect the position of a sample. Therefore, it is essential to control and correct this drift in order to improve the spatial resolution of the reconstructed image.

Axial focus stability

The perfect focus system (PFS) built in the microscope body (Nikon Eclipse Ti-E) was used to avoid fluctuations of the position along the axial direction. The reflection of a near-infrared 870 nm LED is detected by a CCD line sensor in order to track the change of the distance between the cover-glass and the objective. The objective is moved in real time to compensate the mechanical drift along the optical axis. This is particularly important for time-lapse experiments. In order to test the PFS of our microscope, the sample with TetraSpek beads immobilized on the glass coverslip was imaged over eleven hours.

Figure 26 represents the position of TetraSpek beads at the beginning of acquisition and at three following time points. The effect of photobleaching cannot be observed because the brightness and contrast were adjusted for each individual image. Even after eleven hours of imaging, the beads were still in focus.

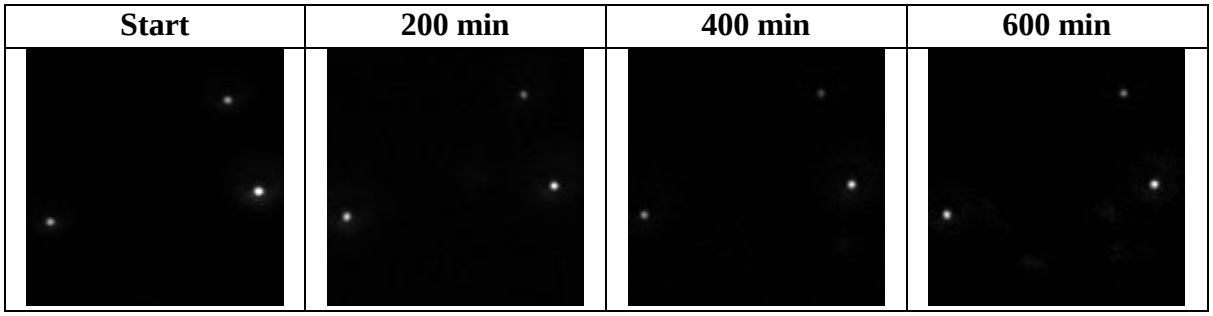

Figure 26. The axial focus stability. TetraSpek beads fixed on a cover-glass were imaged over eleven hours. All three beads are still in the focus at the end of acquisition. The brightness and contrast were adjusted for each individual image in order to correct for the intensity decrease caused by the photobleaching.

Each localization event was fitted with a 2D gaussian function to determine the value of standard deviation (sigma). Because this value depends on the emission wavelength, numerical aperture of the objective (both are constant during the imaging), and whether the emitting particle is in focus, we can track the focus fluctuation by monitoring the sigma value. In Figure 27 the sigma value of three presented particles is plotted for each frame. As we can see during the acquisition time this value is constant within a 10 nm error interval, which is in the range of statistical error of sigma determination that was obtained with seven beads in the FoV at each step of a z-scan (Figure S5 in the publication's SI). The spike in the middle of acquisition and the return to the initial sigma value demonstrate the efficiency of the PFS.

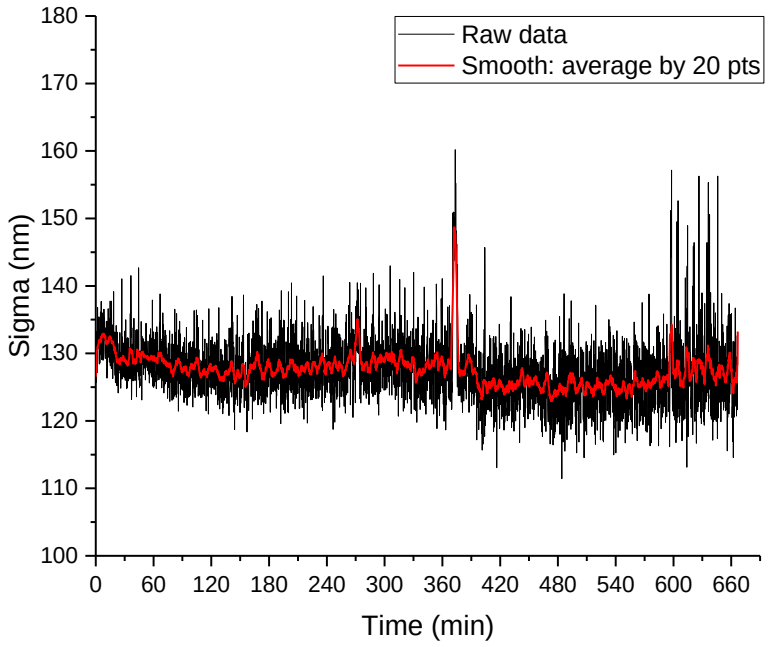

Figure 27. The size of PSF was measured over a time frame of 11 hours demonstrating the axial focus stability provided by the perfect focus system (PFS) of the microscope. The peak at 360 min reflects the change of the focus, after which the sigma returned to its initial value thanks to PFS of the microscope.

Lateral drift correction

To estimate the lateral sample drift on our setup a stack of 20000 images was recorded at a frame rate of 33 fps using the sample with immobilized TetraSpek beads. Here a low laser power (3 mW that corresponds to 125 W/cm^2) was used to prevent the photobleaching. The results are presented in Figure 28. On the left panel, the three beads are moving in the same direction demonstrating a good fixation of beads between cover-glass and microscope slide (see the protocol in Appendix). The displacement of these beads is about 700 nm during 10 min of acquisition.

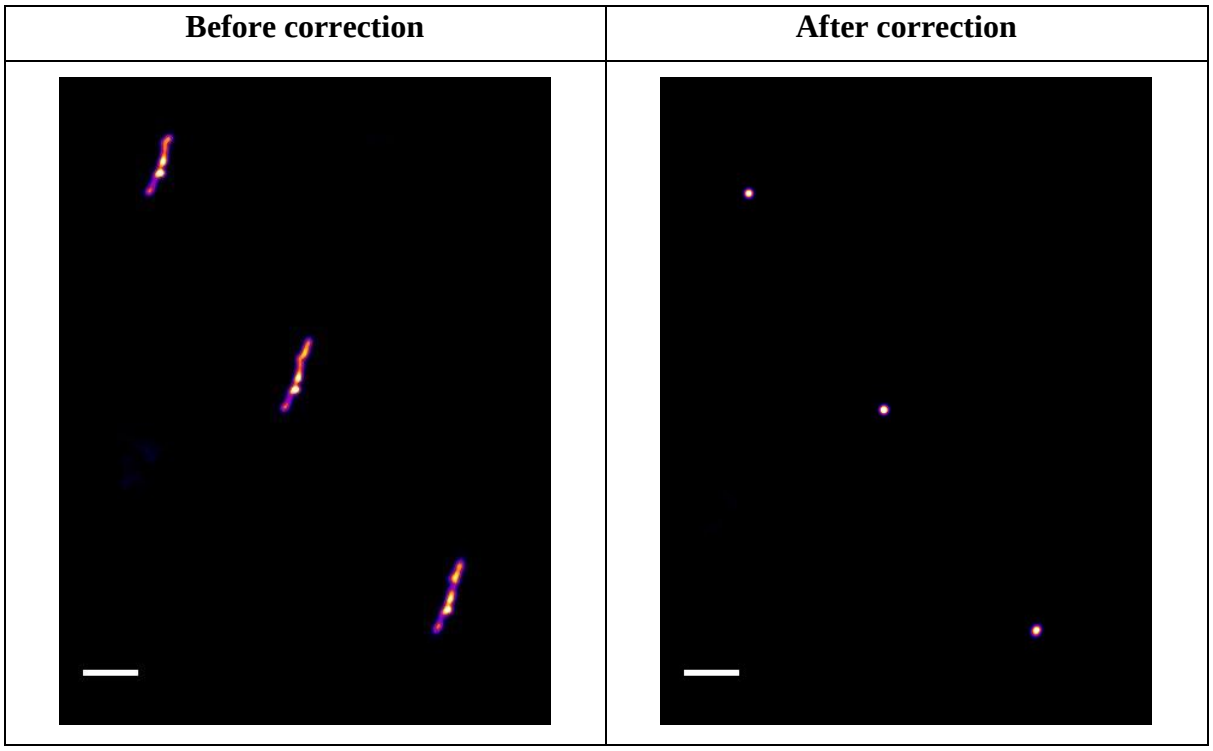

Figure 28. Sample drift represented by three TetraSpek beads that are moving in the same direction. The drift of over 700 nm was corrected using the ThunderSTORM plugin. Scale bar: 500 nm.

The ThunderSTORM plugin in ImageJ was used to correct for sample drift. After correction, the localizations of the same bead were spread just over 10 nm (see Figure 28), the value in a range of localization precision.

Fiducial markers for drift correction

While TetraSpek beads are good for control and test experiments, they are very bright compare to single fluorophores like Alexa Fluor 647 or fluorescent proteins. When employed as a fiducial marker in cells, the high laser power (60 mW) used for super-resolution imaging results in a saturation of the camera (Figure 29). The camera gain and exposure time were adjusted in this case to minimize the noise and cover the whole camera dynamic range for

imaging of single emitters Alexa Fluor 647 and mEos2. Because of this saturation, the position of TetraSpek beads cannot be determined precisely.

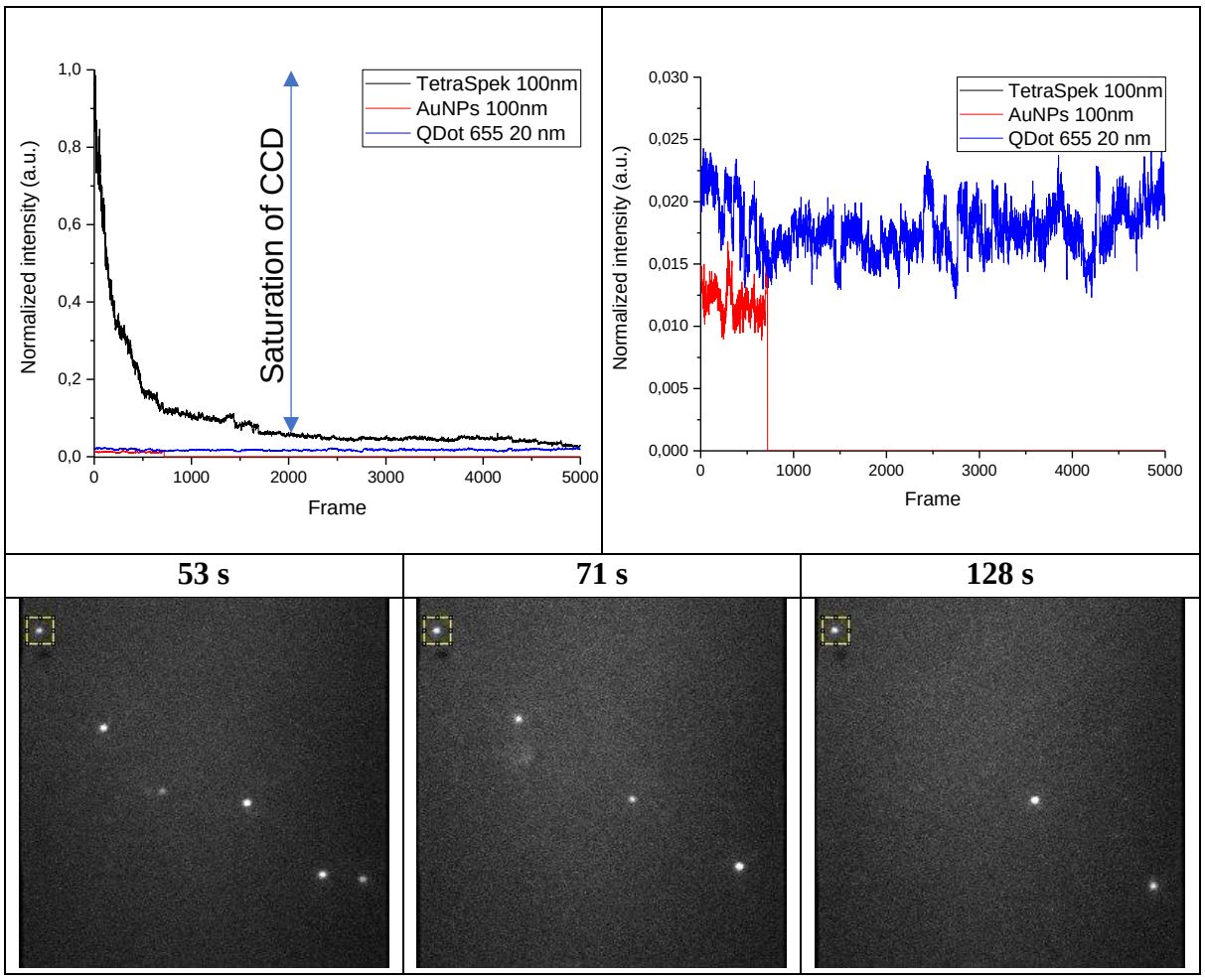

Figure 29. Comparison of fiducial markers. In the top panel, the intensity variation over time is presented for three most widely used types of fiducial markers: TetraSpek beads, gold nanoparticles (Au NPs) and quantum dots (QDs). At high laser power that is common for localization microscopy techniques, TetraSpek beads display very high intensity leading to the saturation of the camera. In addition, under such high excitation regime, TetraSpek are prone to photobleach. In the lower panel, a QD (yellow box, ROI) fixed on a surface of a HeLa cell was imaged with Alexa Fluor 647. Here the brightness of QD is comparable with the one of a fluorophore.

Gold nanoparticles and quantum dots were also reported to be good fiducial markers (for more details see "Drift correction" sub-section in the publication). Their brightness is comparable with the brightness of a single emitter (e.g. mEos2 or Alexa Fluor 647) which allows the simultaneous imaging and solves the problem of saturation (Figure 29). Unlike gold nanoparticles that are continuously losing their brightness over time (or suddenly disappear during the imaging), quantum dots are visible during the whole acquisition and can be used for the drift correction (Figure 30). Intensity of each type of fiducial markers was determined by fitting the individual PSFs with ThunderSTORM plugin. Sudden decrease of the intensity trace for Au NP means that the plugin was not able to detect this particle anymore.

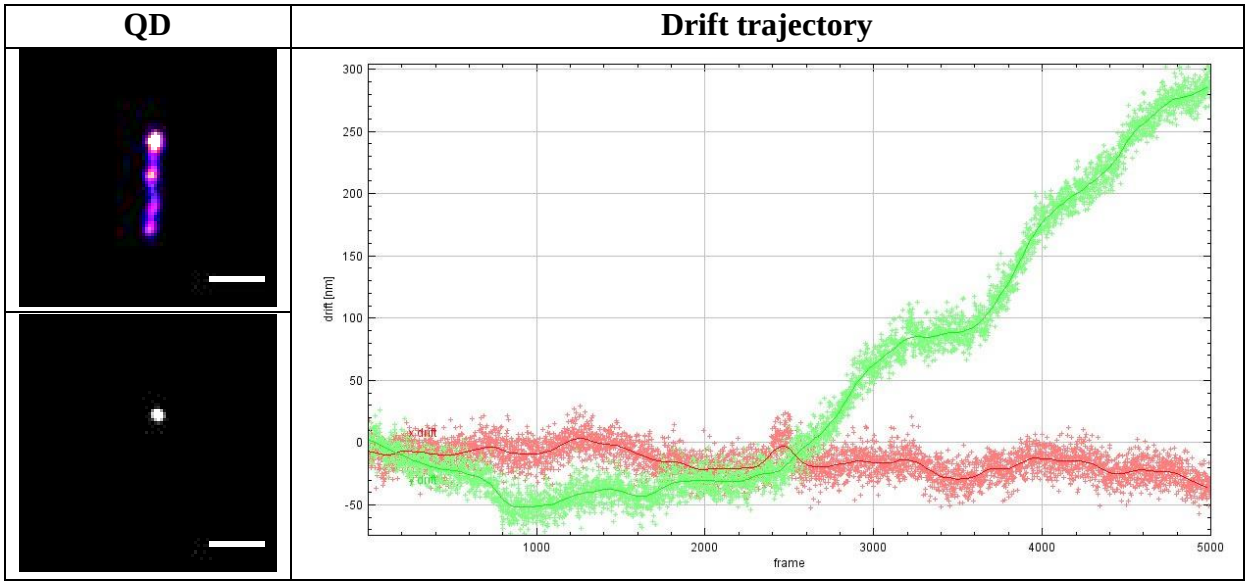

Figure 30. Quantum dot used as a fiducial marker in biological samples to correct for a drift. Scale bar: 200 nm.

Another method used for drift correction is a cross-correlation image analysis [152,153]. In this case, the final stack is divided to several smaller stacks, which are then reconstructed to obtain intermediate images. These images are used to track the sample drift and correct it. While there is no need in fiducial markers, this method requires a high number of localizations through the whole stack and it is not as precise as using fiducial markers.

3.2. Characterization of spatial resolution

The resolution in single molecule imaging is often determined as the precision of localization or as the smallest resolvable distance between two detected particles. In the Figure 31 a distance as small as 18 nm was measured between two TetraSpek beads localized on different frames during the raster scan with a localization precision of 5 nm.

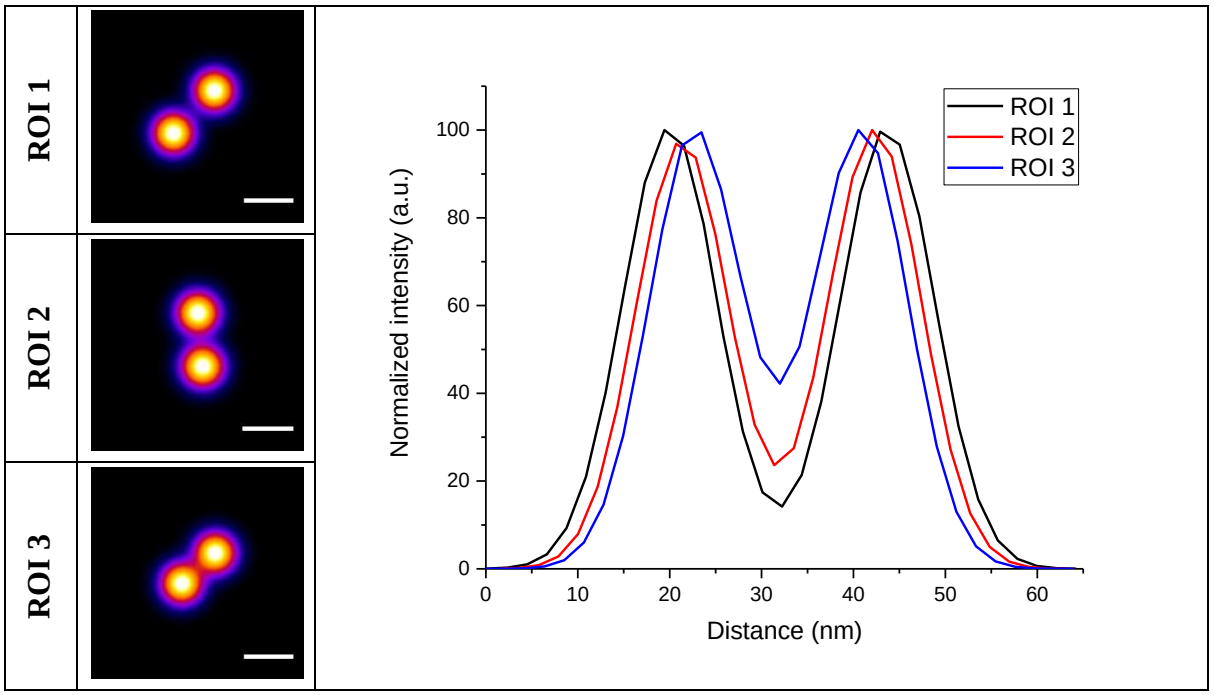

Figure 31. Minimal distance between two particles that still can be resolved. TetraSpek beads were used during the raster scan of the field of view. Two particles presented on each of three images were detected at different time points (different frames) with localization precision of 5 nm (blur radius used for rendering). The cross-section profiles for each ROI are represented on the graph. The distance between peaks' maxima is 24 nm for ROI 1, 21 nm for ROI 2, and 18 nm for ROI 3.

Another way to determine the resolving power of the microscope is using the GATTA-PAINT nanorulers (DNA origami from GATTAquant) labeled with ATTO 655 fluorophores. The reconstructed image of a sample with 1 μm^{-2} density of nanorulers is presented in Figure 32. The distance between maxima was measured to be 85 nm which, with a 5 nm localization uncertainty, corresponds to the 80 nm mark-to-mark distance given by the manufacturer.

However, during the imaging of complex biological structures represented by a large number of proteins, the labeling density plays also important role in determination of the final image resolution. The high localization precision in a range of several nanometers but with a small number of detected particles does not allow to obtain a continuous structure on the reconstructed image. In this case, spatial information is missing and affect the final spatial resolution. Fourier rings correlation method is used here to determine the effective resolution of a reconstructed image [109,169]. FRC evaluates the similarity/correlation of two statistically

independent subsets of detected localizations at different spatial frequencies in Fourier space. For low spatial frequencies that represent coarse details, the correlation between two images is observed; but for high spatial frequencies, where noise dominates the data and fine details cannot be resolved anymore, the FRC decays to zero (Figure 33).

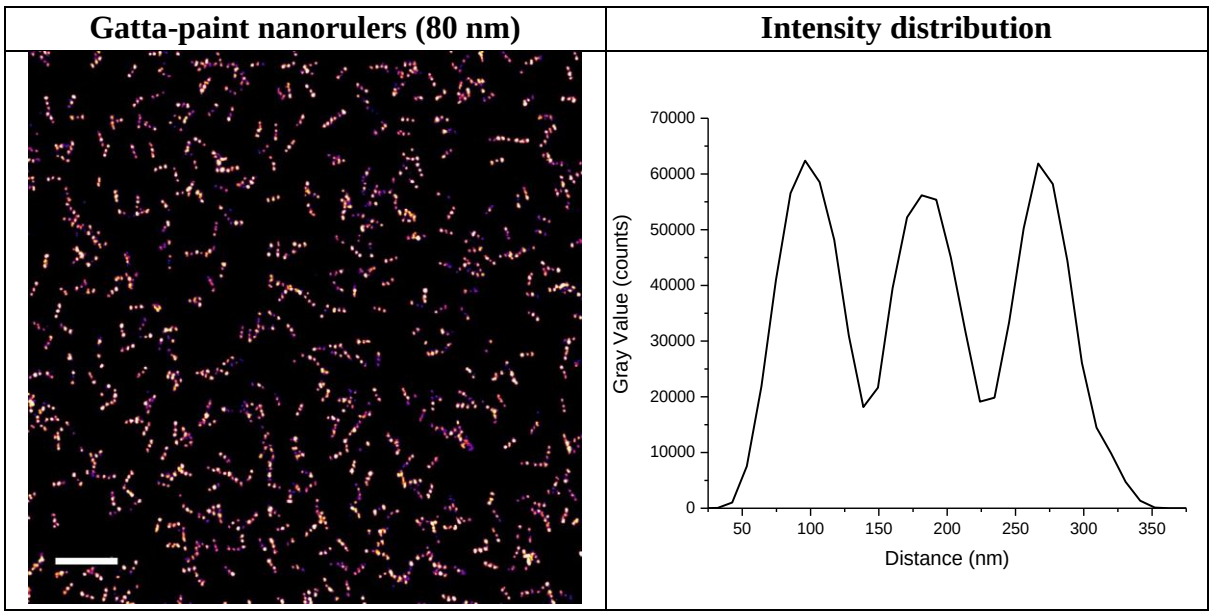

Figure 32. Gatta-paint nanorulers, labeled with ATTO 655 fluorophore, were imaged during 5 min to obtain a stack of 10000 frames. After the reconstruction the cross-section profiles of individual rulers were plotted and the distance between maxima was measured to be 85 nm. Scale bar 1 µm.

In Figure 33, microtubule network is observed by imaging α-tubulin labeled with Alexa Fluor 555 in 20% Vectashield buffer (will be discussed later). Using the 1.7 threshold criteria according to Nieuwenhuizen et al. (2013), the resolution of presented image was determined to be 46 nm (in GDSC SMLM plugin by Dr. Alex Herbert), which is of course bigger that 18 nm obtained by imaging the ultra-bright TetraSpek beads where the density of their localizations is not so important.

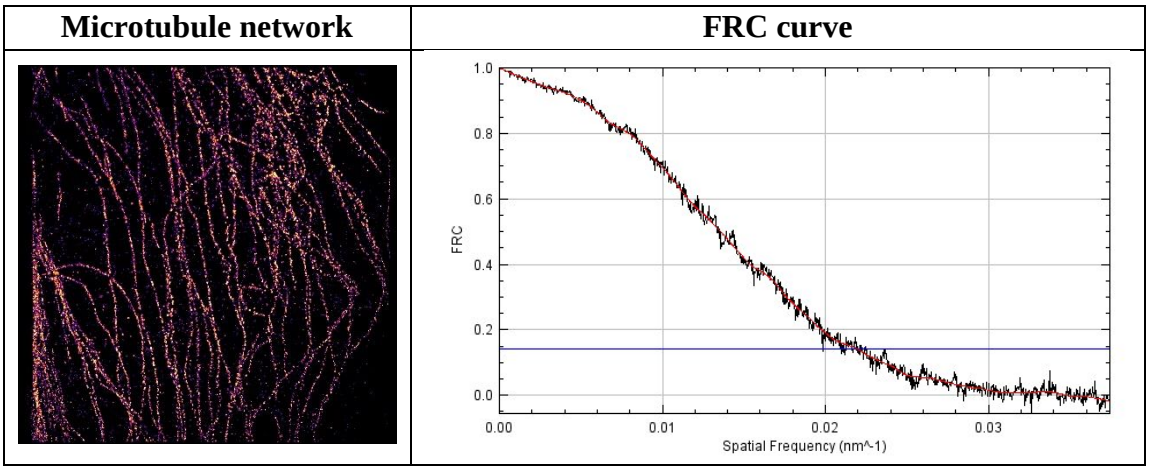

Figure 33. The microtubule network was reconstructed by imaging Alexa Fluor 555-labeled α-tubulin. The effective image resolution determined by FRC is equal to 46 nm (using 1/7 ≈ 0.143 threshold criterium).

3.3. Single-color super-resolution imaging of NC and nucleolar markers

After setting the protocol for drift correction and measuring the resolving power of the setup, the nucleolar markers and nucleocapsid protein (NC) were imaged in HeLa cells (Figure 34 and Figure 35). To label these proteins two different approaches were used: fusion with photoactivable fluorescent protein mEos2 and indirect immunolabeling using secondary antibodies labeled with Alexa Fluor 647. These labels were selected because they are ones of the best in their classes. mEos2 has high brightness (extinction coefficient of the red form of mEos2: 46000 $M^{-1}cm^{-1}$, quantum yield: 0.66) and photostability, unlike mEosFP it maturates successfully at 37°C, and its monomeric form does not alter the localization of fused proteins (which is not the case for dimeric and tetrameric form of EosFP) [113]. Alexa Fluor 647, on the other hand, is brighter than mEos2 (extinction coefficient: 239000 $M^{-1}cm^{-1}$, quantum yield: 0.33) improving thus the localization precision, demonstrates many switching cycles before bleaching, and has a low duty cycle (the fraction of time fluorophore resides in the bright state). The longer fluorophore resides in the bright state, the higher is the probability to detect another molecule within the same diffraction limited area, creating thus artefacts during the analysis or decreasing the number of localizations in the result table. However, Alexa Fluor 647 requires an appropriate buffer containing a millimolar concentration of thiols and an oxygen scavenging system to induce blinking of the dye and to regulate blinking kinetics, whereas mEos2 can be imaged in a simple PBS or TRIS buffer.

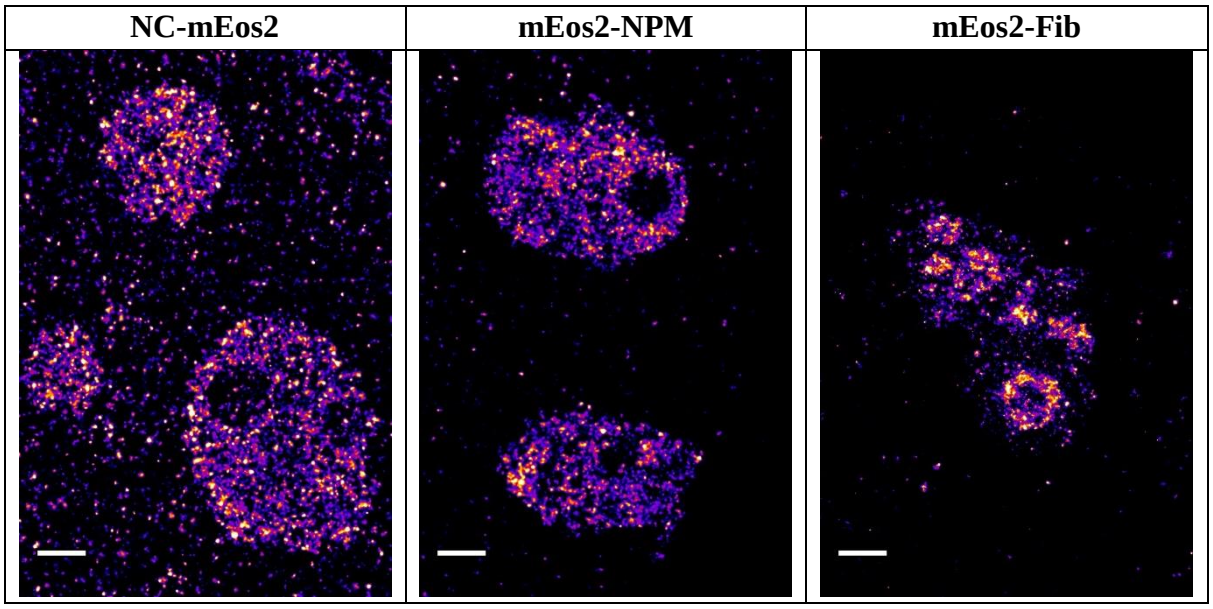

Figure 34. PALM images of NC protein and markers of nucleolar sub-domains NPM (granular component) and Fib (dense fibrillar centers). Protein of interest were fused to fluorescent protein mEos2 for imaging. Scale bar: 1 µm.

The nucleolar localization of NPM and Fib are similar to the localization of the granular and dense fibrillar components of the nucleolus obtained with electron microscopy and presented in the Introduction. We can see that the size of nucleolus may differ from one cell to another depending on how active this cell is in the protein synthesis. Bigger nucleolus results in higher production of ribosomes, which in turn produce more proteins. By comparing Figure 34 and Figure 35 (NPM), it is possible to observe that the number and the size of fibrillar centers may also vary. The images with Fib localization show typical ring-like structure of dense fibrillar component. Super-resolution images presented here demonstrate the gain in terms of spatial resolution and reveal more details of the nucleolar structure than confocal images. Localization precision measured for mEos2 fluorescent protein varies between 18 and 22 nm, while being 8-9 nm for Alexa Fluor 647.

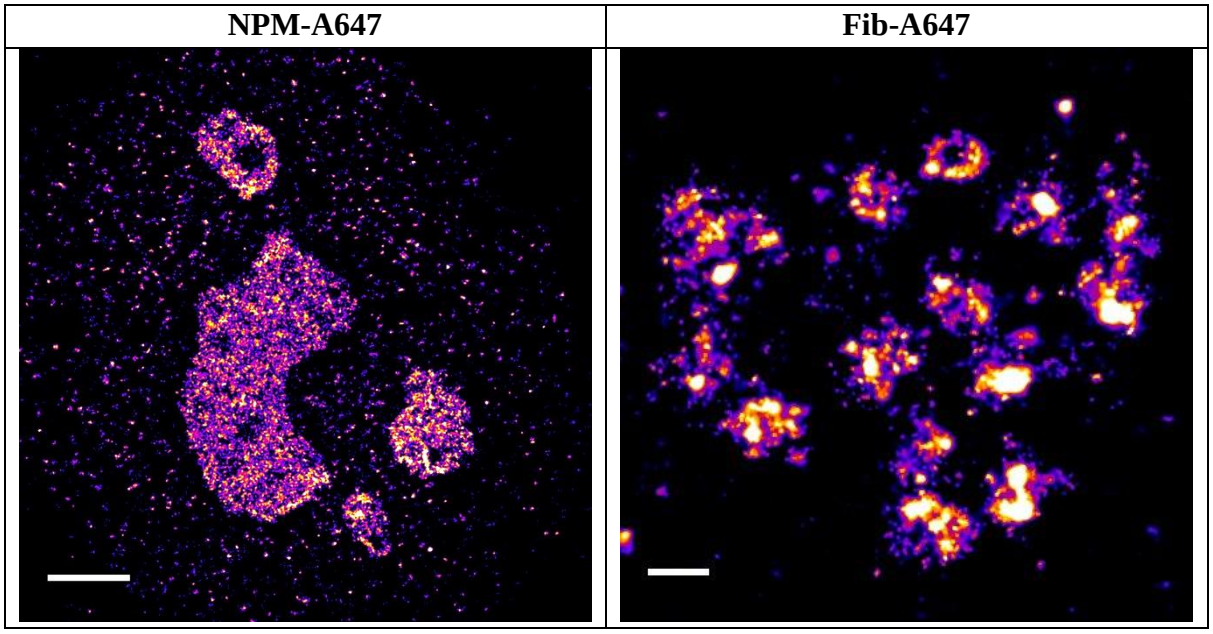

Figure 35. dSTORM images of granular and dense fibrillar components of the nucleolus represented by NPM and Fib proteins respectively. The proteins were immunolabeled with primary and secondary antibodies, where later was conjugated to Alexa Fluor 647 organic fluorophore. Scale bar: 1 µm (500 nm for Fib).

By comparing the localization of NC and NPM proteins in the Figure 34, we can see that proteins distribution is almost identical suggesting a preferential localization of NC in the granular component of the nucleolus. To prove this hypothesis, two-color labeling and imaging of both proteins within the same cell is required and will be presented in the following sections.

3.4. Selection of a pair of photoswitchable labels

The first challenge of two-color imaging is the selection of a pair of fluorescent labels and appropriate conditions for imaging (e.g. buffer, laser power, sequential or simultaneous imaging, etc.). Emission bands of these labels should be spectrally separated to avoid crosstalk between two imaging channels. Their brightness should be high enough to achieve a good localization precision and preferably similar for both fluorophores to avoid the saturation of one channel during the simultaneous imaging. And of course, the buffer used for one of the labels should not affect the photophysical properties of the second label. Many different pairs of photoactivable/ photoswitchable fluorescent proteins and organic fluorophores have been reported to work in two-color super-resolution imaging. Some of them were tested during the project and are described in the following section.

mEos2 + Dronpa

As proposed by Shroff et al., the photoswitching protein Dronpa can be used in combination with mEos2 in two-color imaging [139]. Because the green form of mEos2 can be excited with 488 nm laser and thus prevent imaging of Dronpa, the acquisition starts by converting mEos2 to the red form using a 405 nm laser and then, under excitation with 561 nm laser, the emission of the red form is readout by a camera. Almost all mEos2 molecules must be photoconverted and imaged to reduce the background in the green channel. After the first part of acquisition, a majority of Dronpa molecules resides in the bright state, because of the photoactivation with UV laser (Figure 36). Now using a high laser power at 488 nm, the residual mEos2 molecules are bleached, Dronpa return to the dark state and is ready to be imaged.

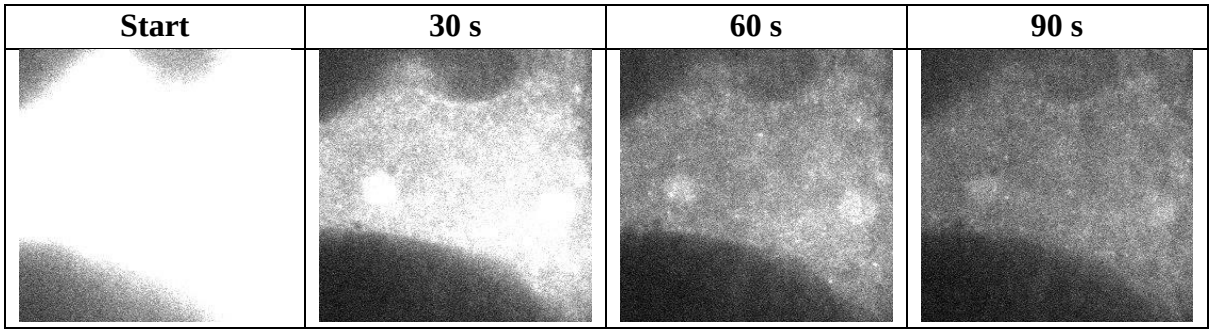

Figure 36. Imaging of Dronpa molecules after mEos2 fluorescent protein. Brightness and contrast were set to be the same for all images.

However, with our experimental conditions, after irradiation with 488 nm laser Dronpa molecules were not only transferred to the dark state, but also bleached. This leads to a strong

decrease in the number of localizations in the reconstructed image and thus to a lower spatial resolution. The same behavior was described by Rosenbloom et al. in 2014 [140], where it was explained by the additional photoactivation of Dronpa with 488 nm light. This behavior of Dronpa molecules results in a high background in the dense-labeled regions (e.g. nucleolus) preventing single molecule detections. Although this pair of fluorescent proteins sometimes result in good two-color images, it was not selected for our studies because of the above-mentioned problems and the low chances to achieve high enough number of localizations in the Dronpa channel (Figure 37 top and low panels respectively).

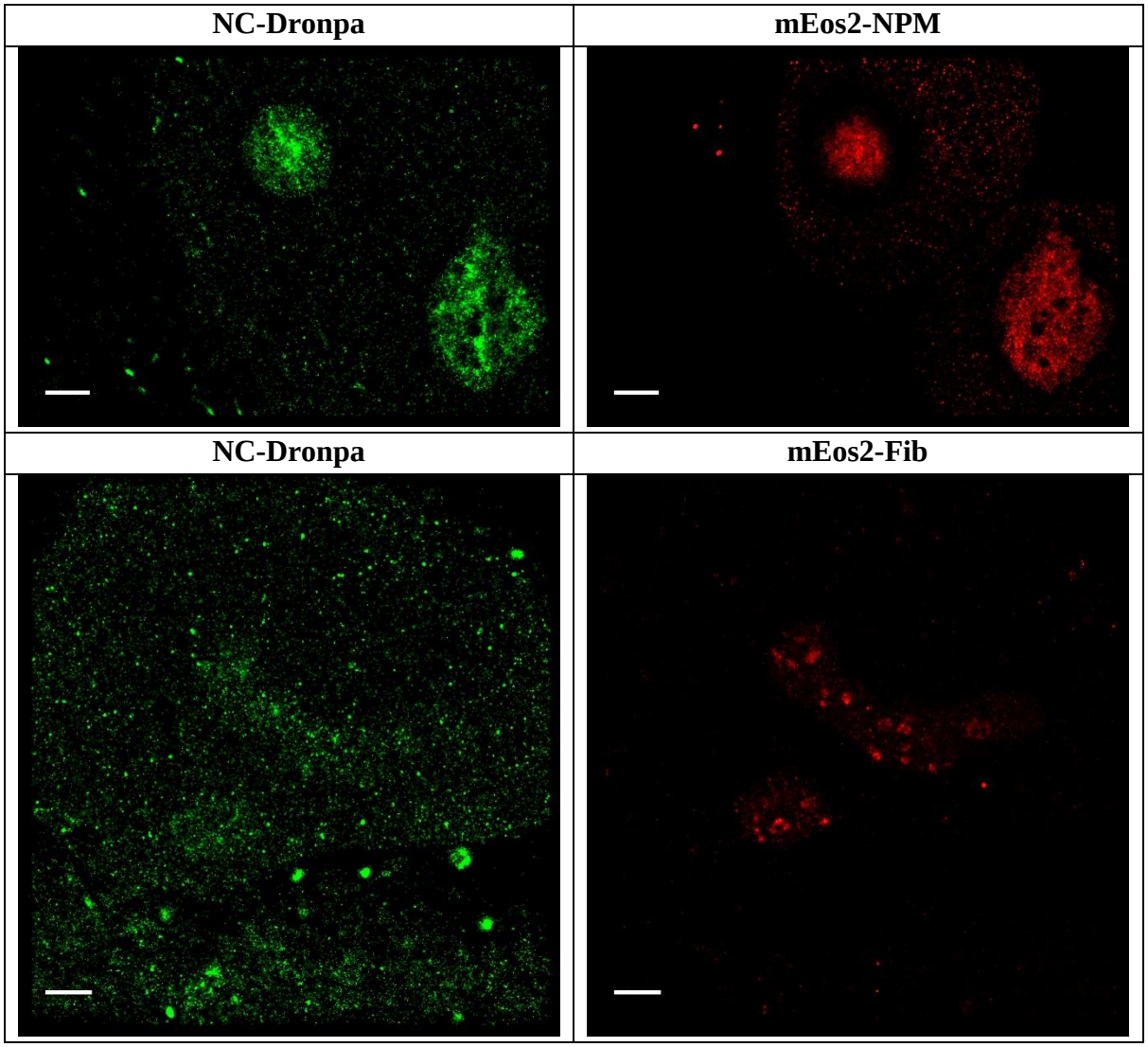

Figure 37. Super-resolution images of NC protein with nucleolar markers NPM and Fib. Because of the bleaching of Dronpa molecules with 488 nm laser before imaging, the total number of localizations is often not sufficient for a good reconstruction (lower panel). However, in rare case it is possible to collect enough localizations for the reconstruction (top panel). Localization precision of Dronpa molecules was 25 nm. Scale bar: 2µm.

mEos2 + Alexa Fluor 647 (in MEA+GLOX buffer)

Another possibility for two-color imaging relies in the combination of mEos2 fluorescent protein with Alexa Fluor 647 [149,150]. When imaged individually both labels demonstrate an excellent brightness and contrast between the bright and dark states resulting thus in high-resolution images as it has been already demonstrated on the examples of NC and nucleolar markers. But these two labels have different requirements in terms of imaging buffer. Whereas mEos2 protein can be imaged in PBS or TRIS at pH7.4, appropriate blinking of Alexa Fluor 647 cannot be obtained in these conditions. The millimolar concentration of thiols is required for the photoreduction of organic dye and formation of long-lived dark state. In addition, the presence of an oxygen scavenging system, usually the combination of glucose with enzymes glucose oxidase and catalase, prevents the oxidation of dye molecules and their return to the ground state.

To test the efficiency of the imaging protocol presented above, Hela cells were transfected with a plasmid coding for mEos2-NPM and immunolabeled with an antibody against the fibrillarin protein. Imaging of NPM fused to mEos2 was done sequentially after the acquisition of Fib labeled with Alexa Fluor 647 in a buffer containing 50 mM of β-mercaptoethylamin (MEA). A decrease in the mEos2 contrast was observed, especially in the dense labeled regions, which results in the lower localization precision (Figure 38).

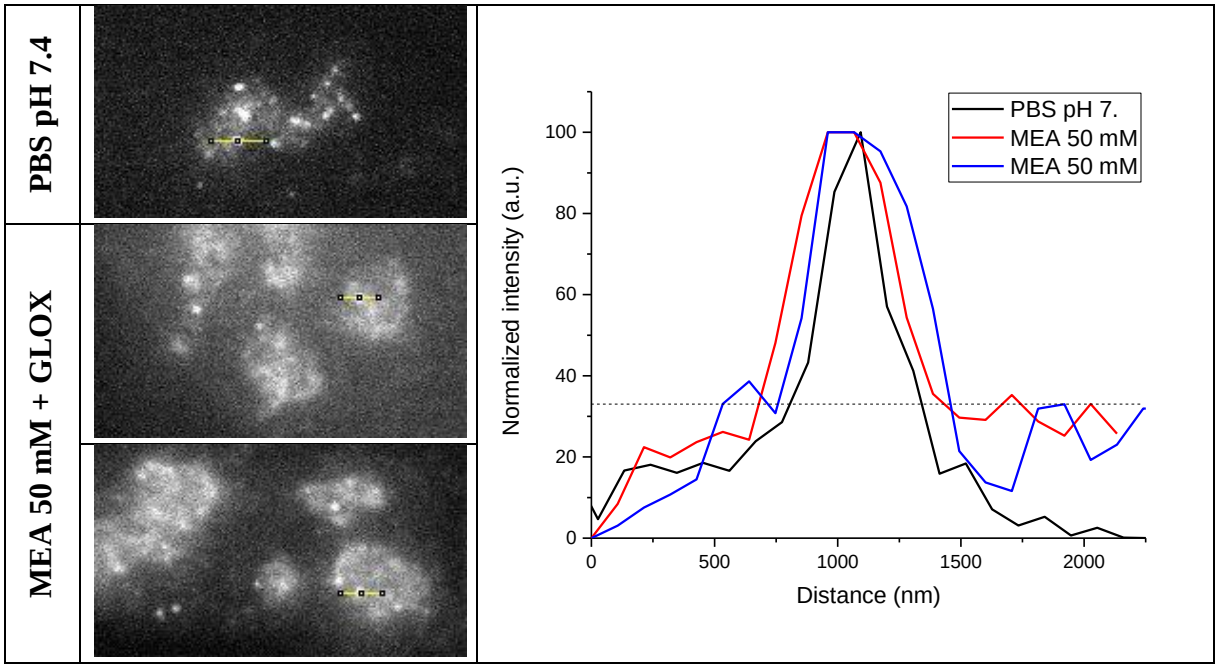

Figure 38. The effect of dSTORM buffer on the contrast of mEos2 protein during the sequential imaging. Raw images of two different acquisitions were compared to the image of mEos2 in PBS buffer at pH 7.4.

In order to find whether the dSTORM buffer can change the photophysical properties of the fluorescent protein mEos2 when it is imaged alone, the following experiments were performed. First, mEos2 fused to NPM was overexpressed in HeLa cells. Without further immunolabeling with Alexa Fluor 647, cells were imaged in three different buffers: PSB pH 7.4, TRIS pH 7.5 and dSTORM buffer (20 mM TRIS pH 7.5, 100 mM MEA pH 8.0, 0.5 mg/ml catalase, 40 µg/ml catalase, 10% glucose). The protein's brightness and contrast remain the same in all three conditions (laser power and camera parameters were identical for all acquisitions) (Figure 39). Imaging in these buffers resulted in high number of localizations and allowed to obtain super-resolution images of the nucleolar granular component (see the lower panel).

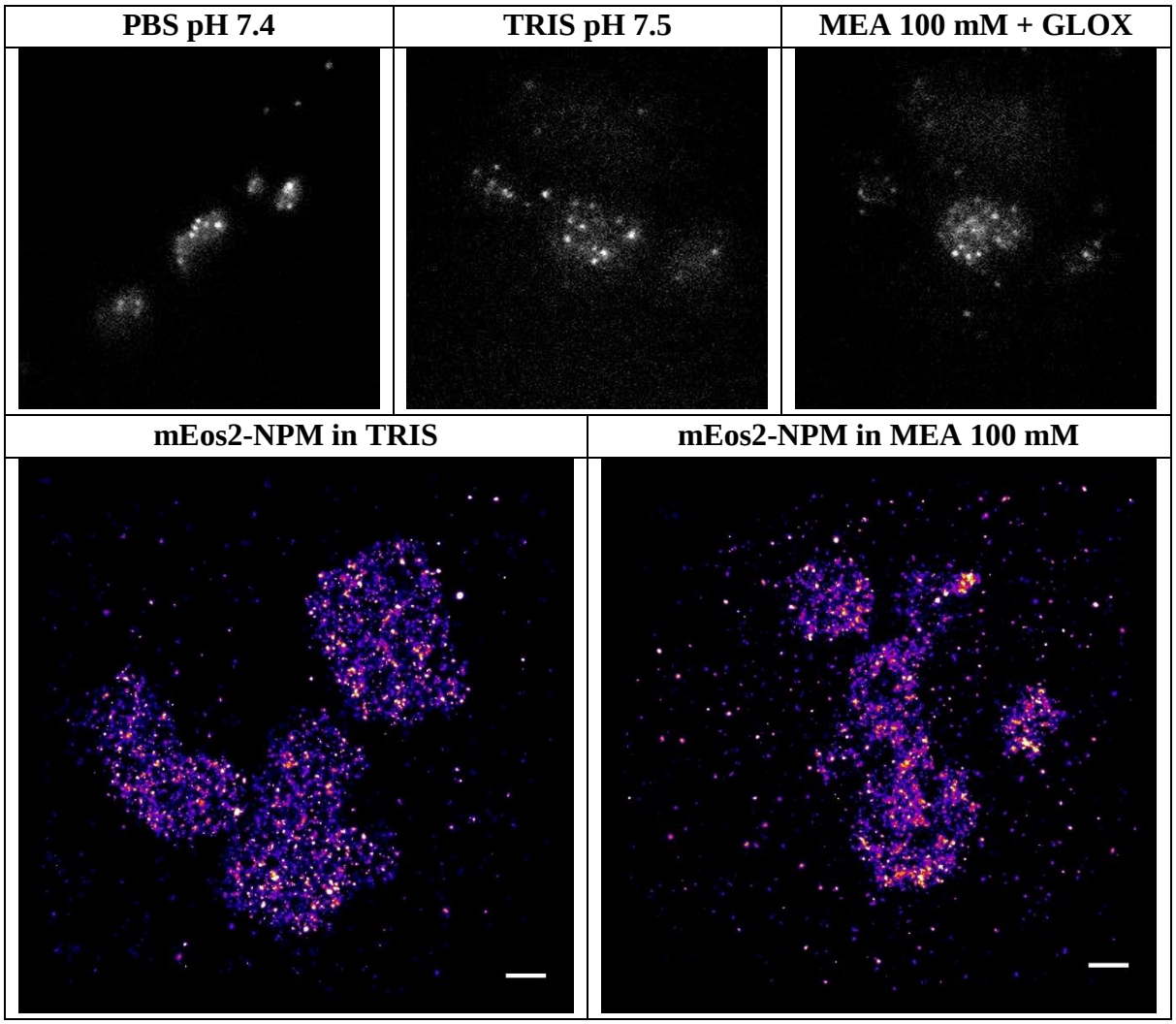

Figure 39. Super-resolution imaging of NPM protein fused to mEos2 after the overexpression in HeLa cells (single color labeling). The acquisitions were performed in three different imaging buffers. No changes were observed when comparing these conditions: contrast and brightness of mEos2 remained the same. Scale bar: 1 µm

Next, mEos2 protein alone without any fusions was overexpressed in HeLa cells. Here its photoconversion properties were observed at three different time points after adding

dSTORM buffer (MEA 50 mM). We observed that thiols did not modify the photoconversion rate nor the brightness of mEos2. The same results were obtained while imaging single mEos2 proteins deposited on the surface of LabTek chamber, where together with time-dependent measurements three concentrations of MEA (20, 50 and 90 mM) were tested (Appendix, Figure 61).

The reconstructed images of mEos2 cellular localization, presented in the figure below, demonstrate the homogeneous distribution of the fluorescent protein through all the cell, without any preferential localization (Figure 40 lower panel). This result serves as a control experiment suggesting that the fluorescent label should not affect the localization of the fusion protein.

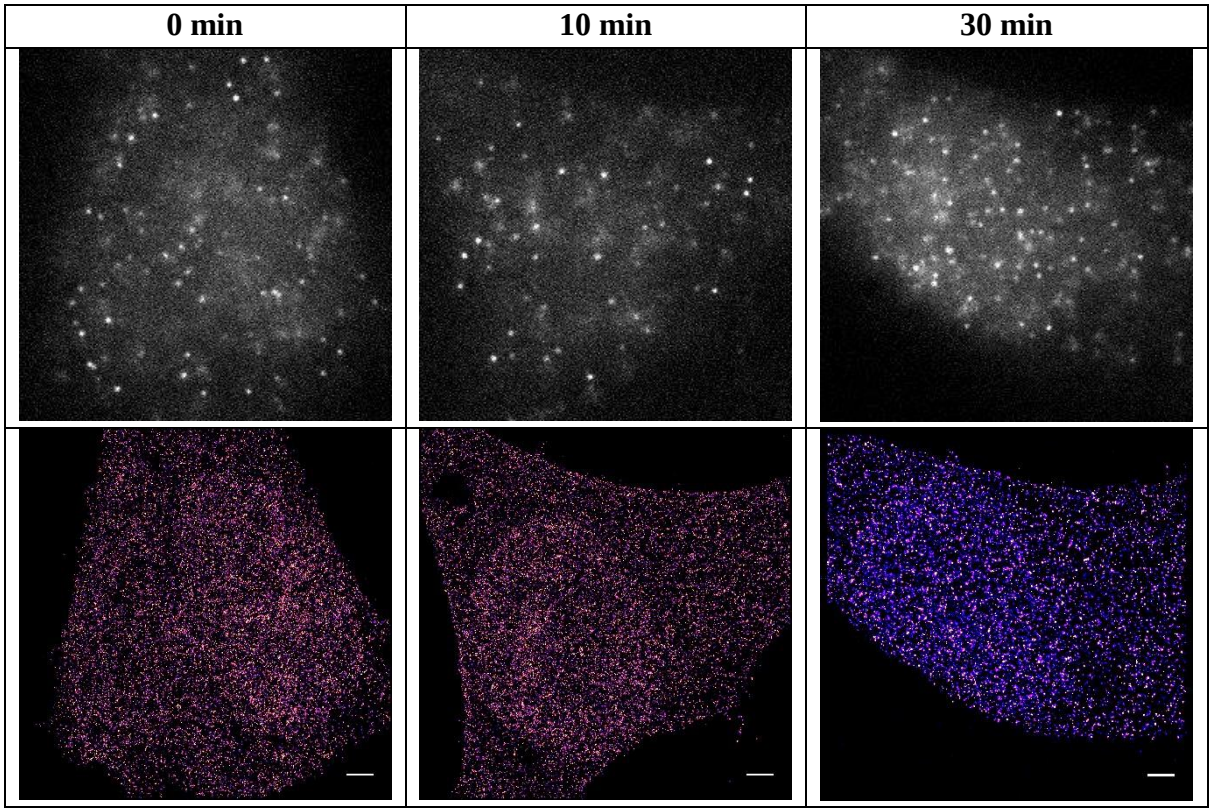

Figure 40. mEos2 overexpressed in HeLa cells (single color labeling) and imaged in MEA 50 mM + GLOX buffer at different time points after adding MEA. Scale bar: 2 µm

To conclude, when mEos2 protein was imaged in dSTORM buffer its conversion rate and brightness remained the same in comparison to PBS or TRIS buffers. However, when the fluorescent protein was imaged in presence of Alexa Fluor 647 organic fluorophore, in two-color experiments, the contrast has decreased. Further experiments have also revealed a decrease of mEos2 photoactivation rate in presence of Alexa Fluor 647 that leads to a lower number of detected proteins (see publication manuscript). Both changes have negative effect

on the final resolution. A possible explanation of this phenomenon may be the effect of the dye radical anion and thiyl radical on the photophysical properties of mEos2. These radicals are formed during the photoreduction process of the organic fluorophore in presence of thiols.

As an alternative to the conventional thiol-containing buffers, we tested the Vectashield medium that is used in microscopy as an antifading mounting medium and that has been recently shown to induce blinking of organic fluorophores [123]. The pair of organic fluorophores Alexa Fluor 555 and Alexa Fluor 647 was selected by authors of the publication for two-color imaging. In our tests, we tried to use 20% Vectashield medium as a substitution of MEA-containing buffer. When mEos2 protein was imaged after Alexa Fluor 647, as described previously, the brightness of mEos2 increased as well as localization precision (Figure 41). More details on the use of Vectashield buffer in two-color experiments can be found in the publication manuscript.

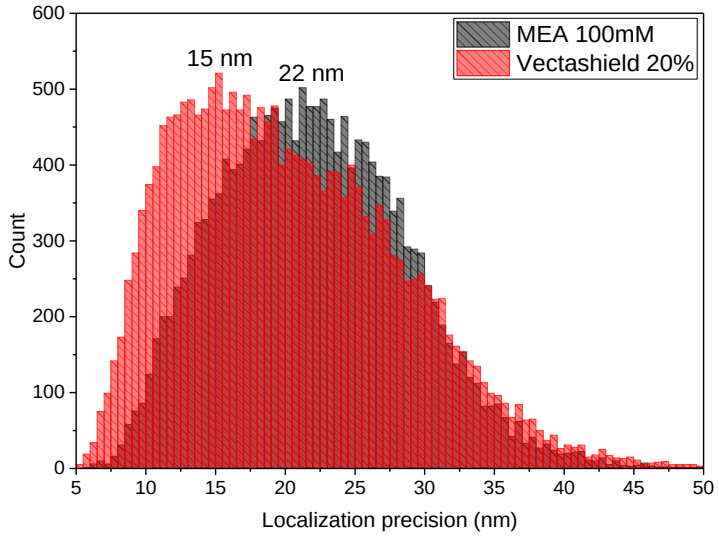

Figure 41. Localization precision of mEos2 protein imaged either in MEA 100 mM or 20% Vectashield medium.

3.5. Two-color imaging of microtubules and NPM

In order to demonstrate the effect of chromatic aberrations on the quality of the final two-color image, the microtubule network was imaged by labeling α-tubulin protein with primary antibody and two secondary antibodies labeled with Alexa Fluor 555 and Alexa Fluor 647 fluorophores. Imaging the same primary antibody with two different labels should results in almost perfect colocalization. However, because of chromatic aberration one of the channels appear to be shifted and distorted with respect to the other channel. In Figure 42 this effect is visible when the field of view was scanned with a single TetraSpek bead. The emission of two fluorophores embedded in the bead was split in two spatially separated spectral channels using Gemini system and then detected with the EMCCD camera.

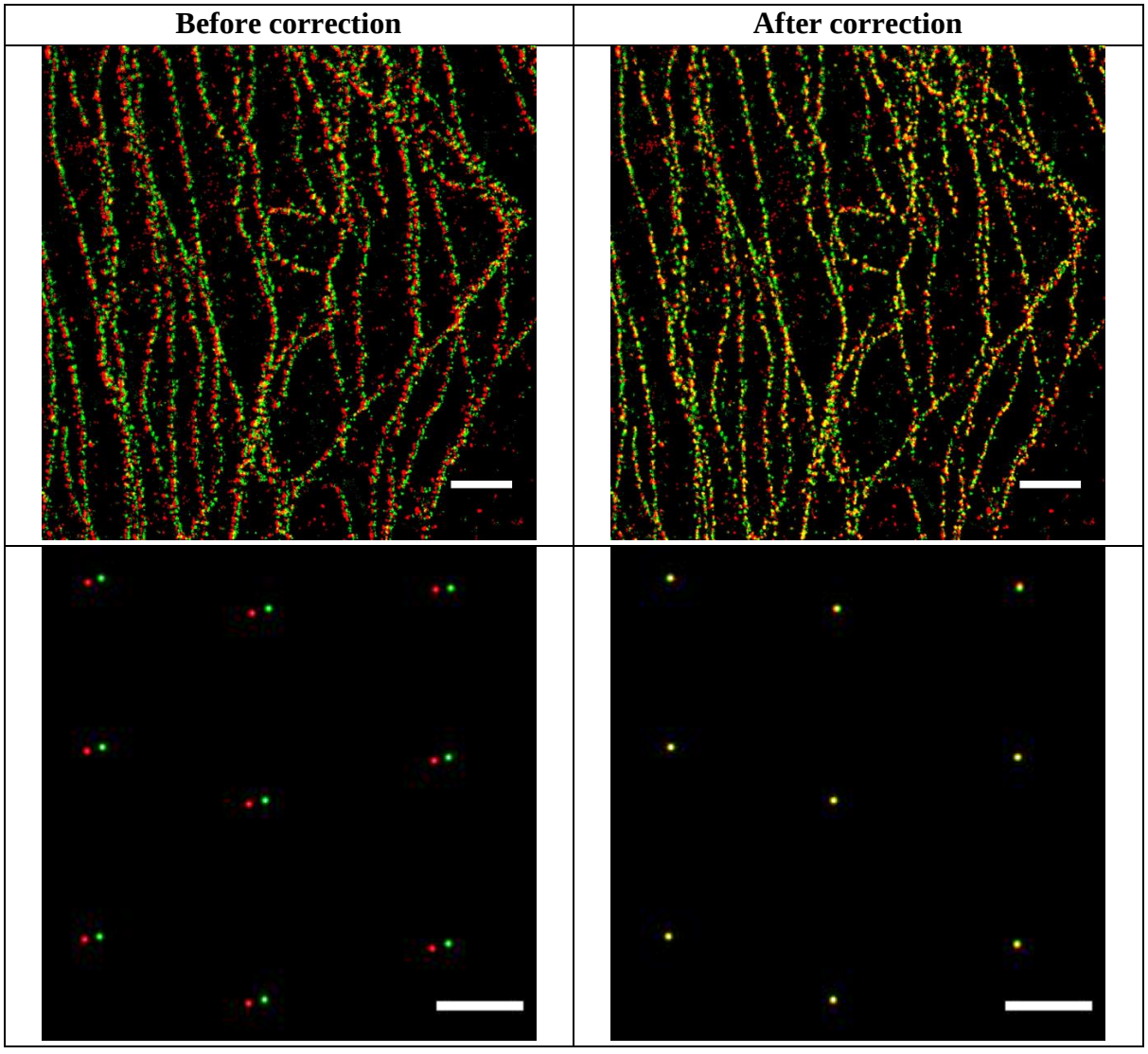

Figure 42. Primary @ α-tubulin antibody tagged with two different secondary antibodies conjugated with Alexa 555 and Alexa 647 dyes respectively. Left images correspond to the merge of two channels directly after the reconstruction, whereas right images were plotted after the process of image registration. Scale bar: 2 µm (tubulin) and 500 nm (TetraSpek).

Because the shift between two channels depends also on the alignment of Gemini system and only a small region of the field of view is cropped, all particles in the red channel appear to be shifted in the same direction with the respect to the green channel. Using the protocol for the correction of chromatic aberrations presented in Materials and Methods section, it was possible to correct this shift and to obtain a perfect colocalization between two channels.

More images are presented in the Figure 43 to further demonstrate the efficiency of correction protocols. The samples with Alexa 555 (emission spectrum is similar to the red form of mEos2, see Figure 60) and Alexa 647 dyes were imaged in 20% Vectashield medium.

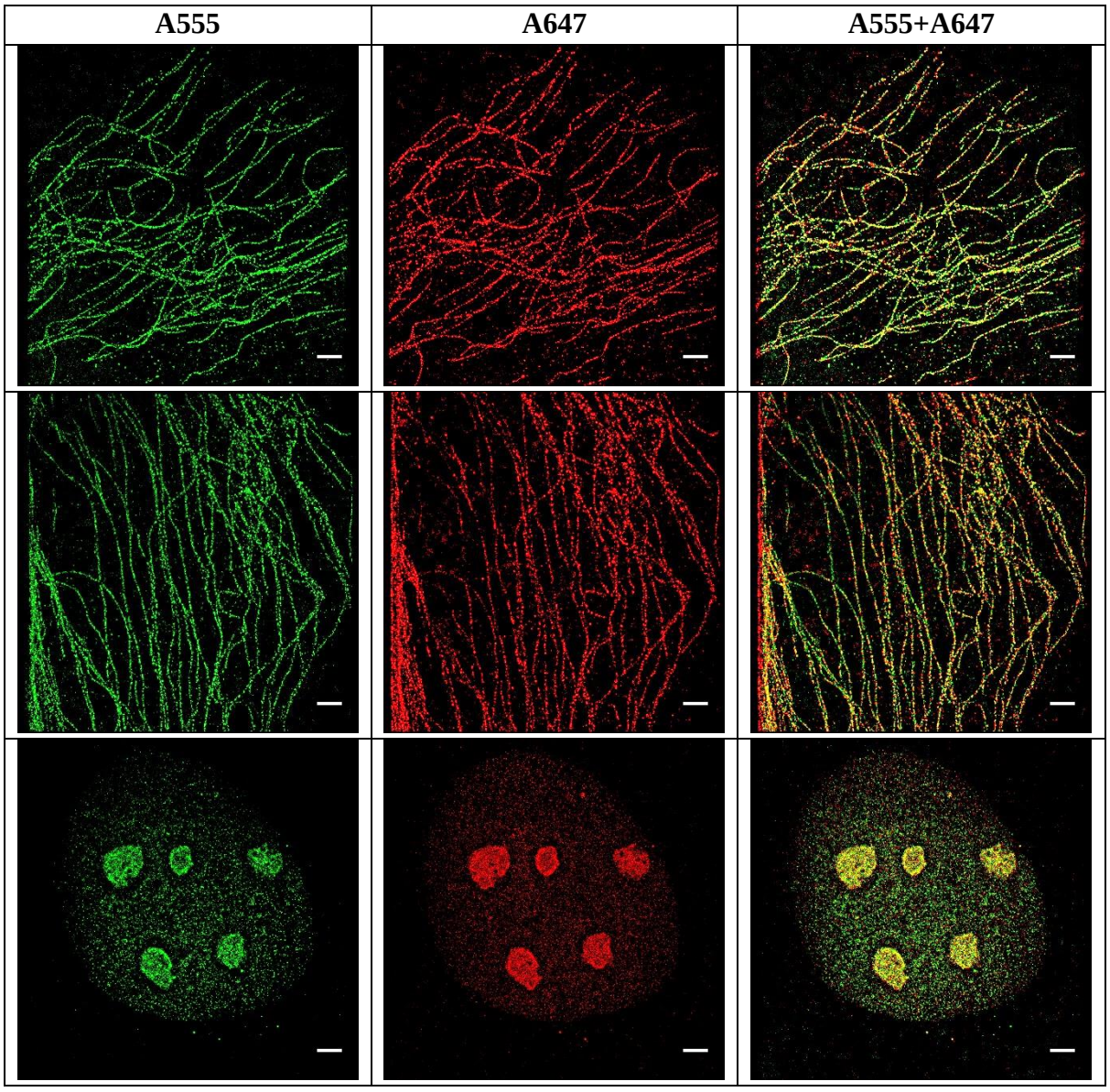

Figure 43. Primary antibodies against either α-tubulin or NPM proteins were tagged with two different secondary antibodies conjugated with Alexa 555 and Alexa 647 dyes respectively. The merge of two super-resolution images demonstrate the efficiency of drift and chromatic aberration corrections. Scale bar: 2 μm.

It is necessary to mention that the selection of immersion oil for two-color imaging is essential in order to reduce the axial chromatic aberration. The refractive index and dispersion of immersion oil produced by a microscope manufacturer are designed to match the values of glass optics (lenses in the objective). The results of a sample z-scan (TetraSpek beads) using two immersion oils with a different dispersion are presented in the Figure 44. Here we clearly see the advantage of Nikon immersion oil over Fluka when used on Nikon Eclipse Ti-E microscope with 100x 1.49 NA Nikon objective. Later the immersion oil Nikon Type F was tested and demonstrated even better results that Type NF (data not shown).

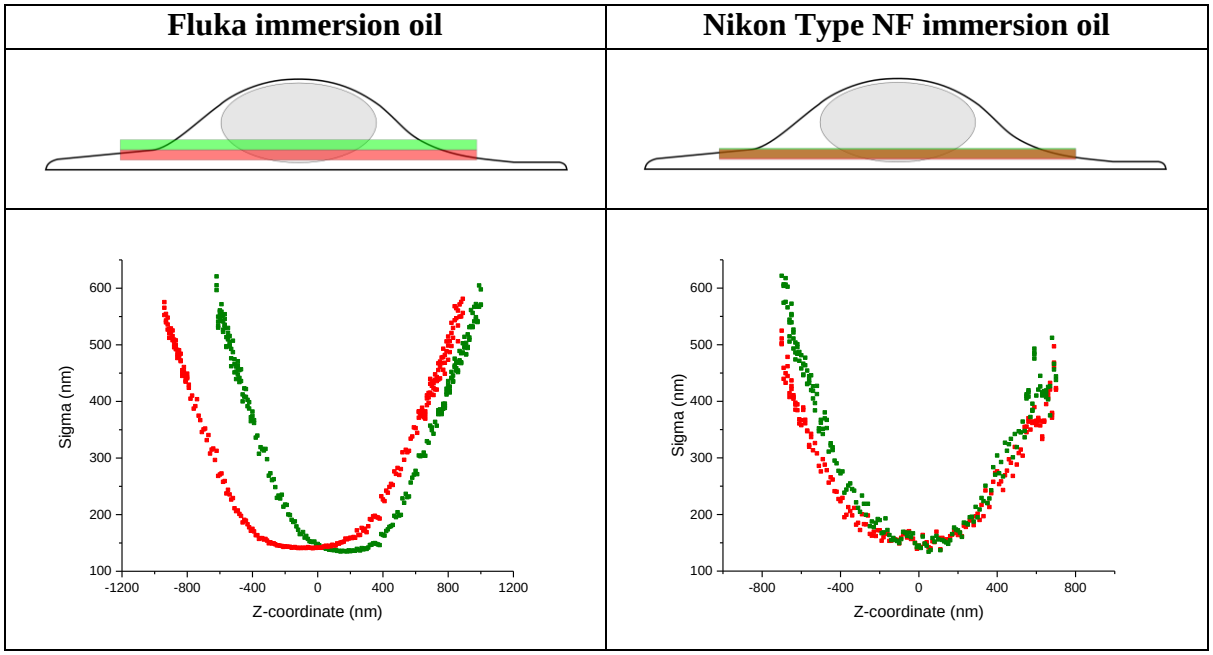

Figure 44. The effect of immersion oil with different dispersion on the axial chromatic aberration/ axial shift between two channels.

3.6. Summary of the first publication

In this work, we present a simplified protocol for super-resolution localization microscopy and, which is more important, a way to combine the PALM and dSTORM techniques that operate with different types of labels, fluorescent proteins and organic fluorophores. This can provide a higher degree of freedom to scientists who designs their experiment. These super-resolution fluorescence microscopy techniques are extensively used in cell biology.

The aim of our work was to optimize the conditions and existing protocols for sample preparation in order to combine PALM and STORM super-resolution techniques. This issue was recently brought up by M. Georgieva et. al. in their paper "Nanometer resolved single-molecule colocalization of nuclear factors by two-color super resolution microscopy imaging", *Methods*, 2016.

We found that the Vectashield buffer (Vector Laboratories) improves the photophysical properties of fluorescent protein and, at the same time, does not alter those of organic fluorophore. The number of emitted photons by mEos2 protein increased when the standard for the STORM technique buffer, 100 mM MEA in combination with enzymes oxygen scavenging system, was replaced by Vectashield. A further advantage is that Vectashield is much simpler to use than the mixture of enzymes, and, unlike them, does not change its pH, which enabled us to store samples at +4 °C for several days. Implementation of our new protocols allowed us to perform 3D two-color imaging and, for the first time to our knowledge, resolve all three components of the nucleolus using fluorescence microscopy.

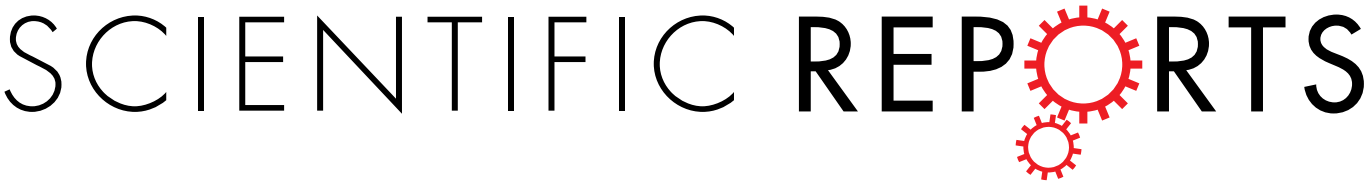

OPEN

Optimized protocol for combined PALM-dSTORM imaging

O. Glushonkov, E. Réal, E. Boutant, Y. Mély & P. Didier

Received: 24 January 2018
Accepted: 24 May 2018
Published online: 08 June 2018

Multi-colour super-resolution localization microscopy is an efficient technique to study a variety of intracellular processes, including protein-protein interactions. This technique requires specific labels that display transition between fluorescent and non-fluorescent states under given conditions. For the most commonly used label types, photoactivatable fluorescent proteins and organic fluorophores, these conditions are different, making experiments that combine both labels difficult. Here, we demonstrate that changing the standard imaging buffer of thiols/oxygen scavenging system, used for organic fluorophores, to the commercial mounting medium Vectashield increased the number of photons emitted by the fluorescent protein mEos2 and enhanced the photoconversion rate between its green and red forms. In addition, the photophysical properties of organic fluorophores remained unaltered with respect to the standard imaging buffer. The use of Vectashield together with our optimized protocol for correction of sample drift and chromatic aberrations enabled us to perform two-colour 3D super-resolution imaging of the nucleolus and resolve its three compartments.

Fluorescence microscopy has become an invaluable tool for cellular studies, both on structural and functional levels. A large number of labelling methods enable the specific attachment of fluorophores and fluorescent reporters to structures of interest in fixed and living cells[1]. Moreover, this non-invasive approach allows spatiotemporal observation of living specimens making optical far-field fluorescence microscopy a method of choice for imaging a large range of biological processes. In addition, the use of different fluorophores offers the possibility to visualize simultaneously different structures and to quantitatively characterize protein-protein interactions with the help of approaches such as Förster Resonance Energy Transfer coupled to Fluorescence Lifetime Imaging Microscopy (FRET-FLIM)[2] or Fluorescence Cross Correlation Spectroscopy (FCCS)[3]. However, in their conventional implementations, these methods are restricted by the diffraction phenomenon that limits their spatial resolution to about 200 nm in the lateral plane and 500 nm along the axial direction.

A breakthrough has been achieved by the development of high-resolution microscopy, that provides sub-diffraction resolution and introduces the extremely promising era of "nanoscopy"[4]. Both scanning and wide-field nanoscopy approaches were developed[5]. In the case of scanning imaging, point spread function (PSF) engineering methods allow to reduce the size of the emitting fluorescent volume. On the other hand, individual emitters are localized with high precision in wide-field nanoscopy techniques. Random switching schemes are exploited to determine the position of a single emitter much more precisely than the optical resolution of the instrument. The schemes are generally based on photoswitchable fluorescent proteins (PALM, photoactivation localization microscopy)[6,7] or organic dyes[8,9] (dSTORM, direct stochastic optical reconstruction microscopy; GSDIM, ground-state depletion followed by individual molecule return).

Under appropriate irradiance flux density, one-colour experiments are quite simple to perform[10,11]. In the case of two-colour experiments, one has first to determine the appropriate fluorophore pairs that can stain the system of interest while minimizing the spectral overlap. Photoactivable fluorescent proteins (PA-FP) and fluorescently labelled antibodies (F-Ab) can be used to perform two-colour super-resolution experiments. PA-FPs allow imaging overexpressed proteins (plasmid transfection) or modified endogenous proteins (CRISPR/Cas9) with a non-invasive one-to-one tagging but display a limited brightness compared to F-Ab that can target endogenous proteins. As two-colour super-resolution experiments with two PA-FPs are not straightforward to implement because of the limited number of available PA-FP pairs[12,13], a PA-FP can be combined with a F-Ab to demonstrate the co-localisation of two proteins with an improved spatial resolution. However, implementing such a two-colour super-resolution experiment is challenging due to the different parameters that need to be controlled simultaneously: (I) two lasers are required to control the ON-OFF conversion (for PA-FP) and generate the highest photon count rate within the shortest time interval; (II) appropriate imaging buffer composition is needed to

Laboratoire de Bioimagerie et Pathologies, UMR 7021 CNRS, Université de Strasbourg, 67000, Strasbourg, France. Correspondence and requests for materials should be addressed to P.D. (email: pascal.didier@unistra.fr)

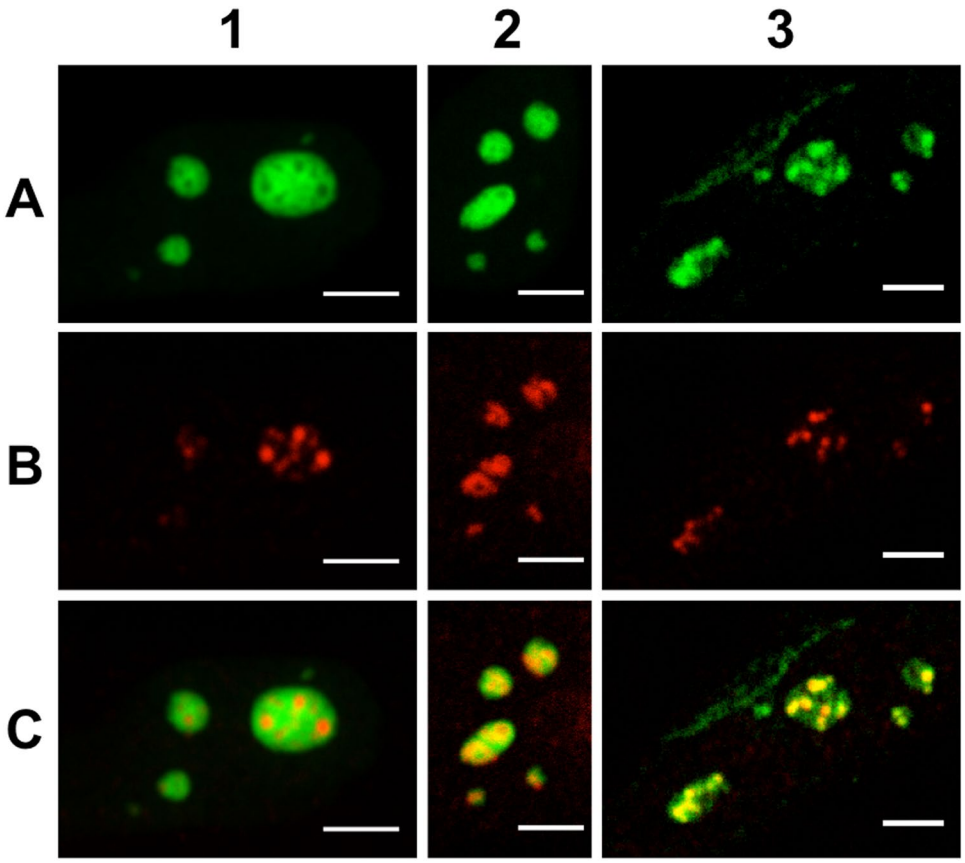

Figure 1. Confocal microscopy imaging of nucleolar sub-domains in HeLa cells. Column 1: NPM protein fused to the fluorescent protein eGFP was overexpressed after cell transient transfection in order to image the nucleoli granular component (**A1**). Endogenous RPA was immunolabelled with A647-Ab (**B1**). The merged images evidenced the specificity of the labelling strategy (**C1**). Column 2: eGFP-NPM localization is displayed in panel A2. Endogenous Fib was immunolabelled with A647-Ab (**B2**). The merged images evidenced the spatial overlap between the two domains (**C2**). Column 3: Endogenous Fib was immunolabelled with A555-Ab (**A3**). Endogenous RPA was immunolabelled with A647-Ab (**B3**). The merged images evidenced the spatial overlap between the two domains (**C3**). Scale bar: 5 µm.

ensure proper ON-OFF transition rate for both labels; (III) mechanical drift and chromatic aberrations between two channels need to be quantified and corrected.

In this work, we optimized all these parameters to perform 2D and 3D two-colour super-resolution experiments using a photoswitchable FP (mEos2)[14] in combination with an Ab labelled with Alexa Fluor 647 (A647-Ab). The nucleolus was chosen as a model system to apply this optimized protocol. This non enveloped nuclear compartment is subdivided into three sub-domains that are all associated with specific steps of ribosome biogenesis: fibrillar centres (FCs) – transcription of rDNA; dense fibrillar component (DFC) – pre-rRNA processing and modification (methylation, pseudouridylation); and granular component (GC) – assembly of ribosomal subunits[15]. These sub-domains have been spatially resolved by means of electron microscopy[15], but not with classical optical imaging. To resolve these sub-nucleolar domains by high resolution PALM/dSTORM microscopy, we used fibrillarin (Fib), nucleophosmin (NPM) and RPA (RPA194 – the largest subunit of RNA-polymerase-I) proteins as specific markers of the DFC, GC and FC subdomains, respectively[16]. These proteins were either overexpressed in fusion to the protein mEos2 or their endogenous forms were immunostained with specific A647 labelled antibodies. Two imaging buffers were compared to determine the most suitable one for simultaneous use of mEos2-FP and A647-Ab. The localization precision and the number of detected single emitters per frame were used as a benchmark to compare the two buffers. To obtain a perfect reconstruction, we also optimized the drift correction method by using quantum dots as fiducial markers to allow correction in both channels. Finally, we applied a procedure to minimize and correct the chromatic aberrations inherent to any optical microscope in order to generate 2D and 3D images of the nucleoli.

Results and Discussion

Confocal imaging. Confocal imaging was first used to assess our labelling strategies and in particular the immunostaining specificity. In order to visualize the nucleolar sub-domains, HeLa cells were transiently transfected to express the eGFP-NPM fusion protein and were simultaneously immunostained with A647 (or Alexa Fluor 555, A555)-labelled antibodies targeting Fib or RPA proteins. As depicted in the first column of Fig. 1,

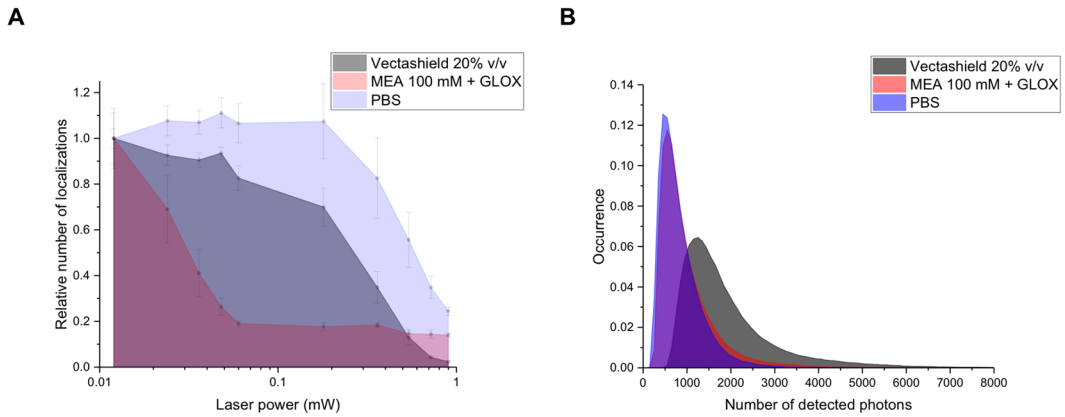

Figure 2. Comparison of the photophysical properties of overexpressed mEos2 in aqueous buffer (PBS), in the standard imaging buffer of thiols with oxygen scavenging system (MEA 100 mM + GLOX) and in the Vectashield mounting medium. (**A**) Relative number of localizations as a function of the UV laser power. A single cell was first imaged for 30 s with the 561 nm laser to bleach already activated mEos2. The same cell was then imaged using the 405 and 561 nm lasers for 30 s. Each point corresponds to number of detected localizations over 30 s for different UV laser power. All the points were normalized by the number of localizations measured during the first 30 s. (**B**) Number of detected photons per molecule per frame (integration time: 30 ms). The mode values are 500, 550 and 1250 photons for PBS, MEA + GLOX and Vectashield respectively. The median number of photons are 711, 793 and 1602 photons for PBS, MEA + GLOX and Vectashield respectively. These results (**A** and **B**) were obtained from the average of 5 different cells for each condition.

eGFP-NPM (A1) can be imaged simultaneously with RPA (A647, B1) and confocal imaging allows to clearly distinguish these two compartments. The absence of co-localisation in this case clearly supports the specificity of our labelling strategies. In experiments performed with eGFP-NPM (Fig. 1A2) and Fib (A647, Fig. 1B2) or with Fib (A555, Fig. 1A3) and RPA (A647, Fig. 1C3), there is a significant overlap between the two channels making impossible to spatially discriminate the two labelled domains with confocal microscopy. Nevertheless, the fluorescence intensities distributions differ for the three labelled proteins, strongly suggesting that as expected, the three proteins have different localizations in the nucleoli as it was evidenced by electron microscopy experiments[15]. The observed spatial overlaps between the fluorescence distributions (NPM/Fib and Fib/RPA) confirm that the diffraction-limited resolution of the confocal microscope is not sufficient to discriminate the different sub-domains. To overcome this limitation, we next performed super-resolution experiments with cells expressing a photoswitchable FP (mEos2) fused to NPM and immunostained with an A647-Ab targeting Fib or RPA.

Buffer selection. In a first series of experiments, a comparison between different imaging buffers was performed to determine the optimal conditions ensuring appropriate ON-OFF conversion for both labels (mEos2 and A647). To this aim, single colour imaging was performed with cells expressing a plasmid coding for mEos2. The standard imaging buffer of thiols/oxygen scavenging system[11] (i.e. MEA 100 mM + GLOX, see Buffers section in Materials and Methods) was found to generate a high ON-OFF switching rate of A647. In contrast, a decrease in the number of photoactivations of mEos2 was observed over time with this imaging buffer (Fig. 2A), likely as a result of a reaction between the thiols and the fluorescent protein chromophore. To reduce the effect of the imaging buffer on mEos2, it is possible to wash the sample with PBS buffer before starting a new acquisition. However, this step might modify the position of the sample on the microscope stage and damage the cells making this approach difficult to implement.

As an alternative to the conventional thiol-containing buffers, we tested the Vectashield medium that is used in microscopy as an antifading mounting medium and that has been recently shown to induce blinking of organic fluorophores[17]. The main advantage of this ready-to-use medium relies on its pH stability. In contrast, the pH of the standard imaging buffer is changing over time and might impact the photophysical properties of the fluorescent labels[18,19]. However, the Vectashield medium displays an absorption band in the UV range that generates some background with the high laser powers used in localization microscopy. Although this background limits the range of fluorophores that can be used to the orange-red range of the visible spectrum, it can be reduced by diluting Vectashield in glycerol. Several pairs of dyes, such as A555 with A647 were shown to work in two-colour experiments with Vectashield[17].

Figure 2A represents the relative number of localizations measured during 30 s for different UV laser powers in three different imaging buffers (PBS, thiol + oxygen scavenging system and Vectashield). As the concentration of the overexpressed proteins varies from cell to cell, modifying thus the absolute number of localizations per frame, we monitor the relative changes in the number of localizations between the three imaging buffers. To do so, the measurements were performed by using the following protocol: we first imaged a single cell during 30 s with the 561 nm laser to bleach the already activated mEos2 proteins. Then we imaged the sample with the 405 and 561 nm lasers for 30 s with a fixed UV laser power (0.012 mW). The measured number of localizations over 30 s gives thus the total number of localizations (N_1). The UV laser power was gradually increased and the total number of localizations (N_i)

was determined for the same ROI over 30 s after each change of UV laser power. The obtained number of localizations (which corresponds to the number of detected photoactivations for a 30 s time interval) for each UV laser power was normalized by N_1 (N_i/N_1) to give the relative changes of the number of localizations. This measurement was repeated on five cells for the three imaging buffers allowing to provide a more reliable comparison. Interestingly, the relative number of localizations (Fig. 2A) was lower for the thiols/oxygen scavenging buffer compared to Vectashield (except for power greater than 0.5 mW). Using appropriate UV laser power (in our case <0.5 mW) it will be possible to obtain an increased total number of localizations for the Vectashield medium. One can note that aqueous buffer (PBS) provides higher photoactivation rate compared to Vectashield and thiols/oxygen scavenging buffers. In addition, we determined the distributions of the number of blinks after photoactivation and ON time of mEos2 for the three imaging buffers. As reported in Fig. S1 the obtained results evidenced that the buffer composition has no noticeable effects on these parameters. Finally, we measured the brightness of mEos2 for the three imaging buffers (Fig. 2B). The results clearly indicate that, in the Vectashield medium, the number of photons emitted by mEos2 per frame (exposure time 30 ms) was twice higher than in the standard imaging buffer (and PBS) while the A647 brightness was similar for both imaging buffer (Fig. S2). We did not see any difference in the blinking rate of A647 with respect to the standard imaging buffer. As the localization precision depends, in first approximation, on the number of detected photons ($\Delta x \approx \frac{\sigma}{\sqrt{N}}$, where Δx is the localization precision, σ is the standard deviation of the Gaussian fit and N is the number of detected photons), mEos2 will thus be more accurately localized in the Vectashield medium[20]. Vectashield appears thus as an improved medium as compared to the standard imaging buffer to simultaneously monitor mEos2 and A647 localization.

Fluorescent proteins and organic fluorophores that are usually used in localization microscopy require different buffers for efficient blinking and high photon yield. Georgieva *et al.* show that the standard thiols/oxygen scavenging imaging buffer with a lower concentration of the reducing agent can be used for simultaneous use of these labels[21]. However, the main drawback of this multi-component buffer relies in the limited duration of the enzymatic oxygen scavenging reaction (one hour after mixing the components) which limits the duration of the experiment and results in buffer acidification[17,18].

Drift correction. In a next step, our aim was to optimize the corrections of the mechanical drift of the sample. These corrections are usually performed with fiducial markers, such as TetraSpek fluospheres, gold nanoparticles or quantum dots[6,8] or with the help of cross-correlation image analysis[22,23]. Two conditions need to be fulfilled to use fiducial emitters: (I) their brightness should be similar to that of fluorescent labels in order to work with the same exposure time and camera gain (to avoid saturation); and (II) they must be photostable during the acquisition time. Indeed, high and constant brightness throughout the acquisition of thousands of frames is required for high and constant localization precision.

TetraSpek fluospheres (T7279, Invitrogen, 100 nm) and gold nanoparticles (753688, Sigma-Aldrich, 100 nm) were added during cell growth and incorporated via endocytosis. They remained immobilized after cell fixation with 4% PFA. Despite being very bright, TetraSpek beads are prone to rapid photobleaching under high excitation power. In addition, the camera gain used for amplifying the signal of a single mEos2 protein or A647 dye leads to the saturation of the signal of the fluorescent beads, making challenging their use for drift correction. In the case of gold nanoparticles, the signal results from the scattering of the excitation beam by the nanoparticles allowing their use for multicolour imaging. Under our experimental conditions (excitation intensity: 2 kW/cm^2), the gold nanoparticle signal was suddenly disappearing before the end of the experiment. Moreover, the signal detected for the gold nanoparticles was not high enough to allow a precise correction of the mechanical drift. A similar behaviour was observed with gold nanoparticles incorporated after cell fixation.

Finally, we investigated the possibility to use quantum dots (QD, Qdot 655 Streptavidin Conjugate - Q10121MP, Invitrogen, 15–20 nm) in our experiments. When incorporated via endocytosis in living cells, we observed that their emission intensity was continuously decreasing, probably due to the low pH in endosomes. In contrast, when QDs were added directly after fixation during incubation with antibodies, the intensity of the emitted signal was constant over the entire acquisition. Moreover, the emitted intensity of a single QD was of the same order as that of mEos2 and A647 on the two detection channels. The drift correction was thus performed with the same precision for mEos2 and A647. Importantly, we did not observe any photobleaching of the intensity of the signal emitted by the QDs during the acquisition time in these conditions. However, QDs blink, so that among the stack of images, QDs disappear in some of them. Hence, an interpolation must be performed to retrieve the full trajectory. It is worth to note that the concentration of the QDs solution prepared in a 1.5 mL Eppendorf tube is changing over time (more than a month), even if the tube is sonicated and vortexed before the experiment. We recommend thus to prepare a fresh solution at least once in a month by diluting the purchased 1 µM stock solution of Qdot 655 in MilliQ water to achieve a final concentration of ~1 nM. Prepared solutions must be tested in cells at different dilutions to get the desired number of QDs per field of view. All super-resolution images displayed in this work were generated using QDs for drift correction. The properties of the fiducial markers measured in Vectashield are summarized in the following table. The measured intensities of the emitted signal obtained for a TetraSpek bead, a gold nanoparticle and a quantum dot are displayed in Fig. S3.

	Incorporated before fixation		Incorporated after fixation	
	Photostability	Brightness	Photostability	Brightness
TetraSpek	−	+++	−	+++
Gold Nanoparticle	−	−	−	−
QD	−	+	+	+

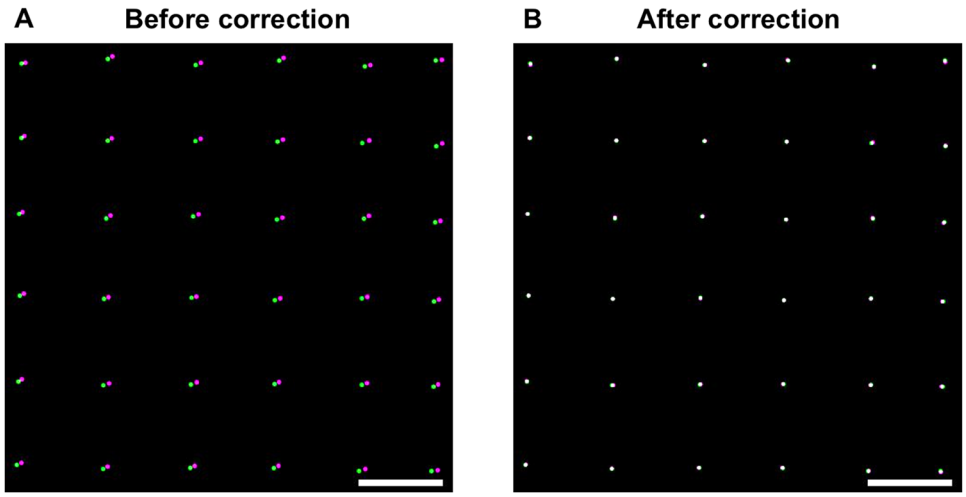

Figure 3. Correction of lateral chromatic aberrations. The images were obtained by performing a raster scan with a single TetraSpek bead (a detailed protocol is given in the SI). The final reconstructed image was obtained by localizing the bead on each individual frame with Thunder STORM ImageJ plugin for both channels (rendering with a PSF of 20 nm). The displayed images correspond to a zoom of one corner of the camera field of view ($27.3 \times 27.3\,\mu m^2$). (**A**) The largest distance between green and magenta spots is about 100 nm before correction. (**B**) Two-colour image obtained after correction with the UnwarpJ plugin. Scale bar: 1 µm.

Correction of chromatic aberration. An additional step is requested to correct for the residual chromatic aberration in our two-colour imaging experiments. The correction was performed with the previously mentioned TetraSpek fluospheres excited with a low laser power that does not induce any significant bleaching during measurements. The Gemini system from Hamamatsu was used to split the camera's chip in two spatially separated spectral windows. We first performed a raster scan of a single bead, using the microscope translation stage, to record a reference image and determined, for each frame, its localization with the help of Thunder Storm ImageJ plugin[24] (a detailed protocol for the acquisition of the reference image is given in the SI). The residual chromatic aberration, which results in a spatial shift between the two channels (100 nm at the edge of the field in Fig. 3A), was corrected using the UnwarpJ plugin[25]. The algorithm computes the correction matrix required for a perfect superposition of the two channels. In Fig. 3, we reported the colocalization image corresponding to the corner of the field of view ($27.3 \times 27.3\,\mu m^2$) before and after correction.

The residual chromatic aberration between the two channels will depend on the bandpass filters used for imaging. The emission spectra of the reference sample (TetraSpek beads) and the fluorophores used for imaging must then overlap. Axial chromatic aberration may also take place. To evaluate it, we performed a z-scan on a single TetraSpek bead and fitted the PSFs of both green and red channels with a 2D Gaussian function. By plotting the dependence of the standard deviation as a function of the z position, we obtained a curve with a minimum where beads are in focus. The minima for both channels must be at the same z-coordinate (Fig. S4) to have minimal axial aberration.

2D PALM/dSTORM imaging of nucleolar sub-domains. After having optimized our measurement conditions and corrections, we next imaged the labelled sub-domains of nucleoli. HeLa cells expressing mEos2-NPM fusion protein were immunostained with A647-Ab directed against Fib or RPA, stored at +4 °C and finally mounted on microscope slides on the day of imaging. Before mounting, the cells were washed with Milli-Q water to remove salts. Each time, we followed a pre-imaging routine, in which the Gemini system was adjusted in order to align the two channels by imaging in transmitted light the reference target provided with the Gemini system. Next, TetraSpek beads deposited on a glass coverslip were used to optimize the PSF with the help of adaptive optics[26] to minimize various aberrations (spherical, astigmatism, coma, trefoil) introduced by optical elements, and the refractive index mismatch between the objective and the immersion medium. This optimization is important because aberrations affect the quality of the PSF and reduce the number of detected photons, which results in lower localization precision and lower resolution. Finally, the same reference sample was used to perform a raster scan in order to generate the correction matrix required to correct the chromatic aberration between the two channels.

To image the sample, we performed a sequential acquisition. We first imaged the red channel (A647) to observe Fib and RPA localizations, then both 405 nm and 561 nm lasers were used for the acquisition of the green channel (to monitor the photoconverted form of mEos2-NPM). This sequential acquisition was needed because of the high staining efficiency with A647-Ab, which induces a saturation of the camera when exciting the sample with all laser sources simultaneously. Between five to ten thousand frames were recorded per channel. Thanks to the strong brightness of A647 and its fast ON-OFF transition, it was possible to reduce the exposure time to 16 ms, resulting in shorter acquisition times. For the fluorescent protein mEos2, the exposure time was set to 30 ms. Next, the data were treated and analysed with the Thunder Storm plugin of ImageJ (see parameters in Materials and Methods section). Rendered images (Fig. 4) were corrected for the drift (QDs) and then for the chromatic aberrations (reference sample of TetraSpek beads).

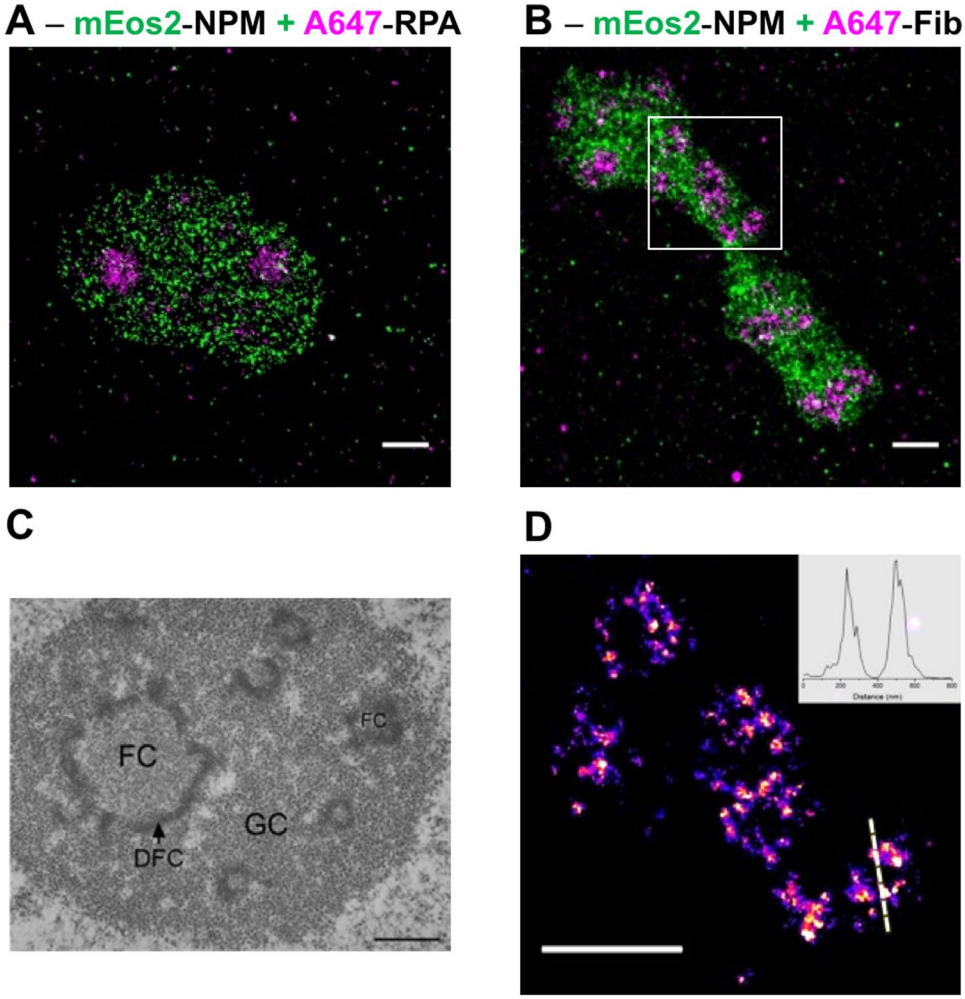

Figure 4. Two-colour super-resolution imaging of nucleolar sub-domains. (**A**) HeLa cells granular component (GC) was imaged with the help of NPM protein fused to mEos2 (green). The fibrillar centres (FCs) were imaged by immunostaining RPA proteins with A647-Ab (magenta). (**B**) HeLa cells GC was visualized together with the dense fibrillar component (DFC), by using mEos2-NPM in combination with Fib proteins immunostained by A647-Ab (magenta). (**C**) Nucleolar organization of human HeLa cell observed by electron microscopy. Reprinted with permission of the author and the editor (permission is granted to Macmillan Publishers Ltd, part of Springer Nature)[31]. (**D**) Ring-like structure of DFC revealed by super-resolution localization microscopy (zoom of the white ROI in **B**). The inner diameter (FWHM = 160 nm) and the thickness (FWHM = 75 nm) of the ring were measured from the cross section displayed in inset. All super-resolution images were obtained from a 20000 images stack as described in the main text. Scale bars: 1 µm.

In Fig. 4, we reported the two-colour super-resolution images of HeLa cells nucleoli. The granular component visualized through the emission of mEos2-NPM was co-imaged with the DFC (Fig. 4A) or FCs (Fig. 4B), immunostained with A647-Abs directed against Fib and RPA, respectively. The average localization precision was about 15 and 10 nm for the green and red channel, respectively. As observed by using confocal microscopy, the domains stained by NPM and RPA are mutually exclusive (Fig. 4A) confirming the specificity of our labelling strategy. In the case of GC and DFCs, the images (Fig. 4B) obtained using super-resolution microscopy did not show any colocalization confirming the gain in spatial resolution with respect to confocal imaging. Moreover, the ring like structures revealed by electron microscopy (Fig. 4C) could also be observed by super-resolution microscopy for some nucleoli (Fig. 4D). The improved spatial resolution of the images is further illustrated with the cross-section displayed in Fig. 4D from which it is possible to measure the inner diameter (FWHM = 160 nm) and the thickness (FWHM = 75 nm) of the ring-like domain.

3D imaging of nucleolus. While working in 2D, the spatial information along the z-axis is lost because of the projection onto the camera plane. As the size of the PSF does not change significantly over the depth of field (Fig. S5), different parts of the object that appear in focus may in fact localize at different depths within the sample. For instance, a hollow sphere will be visualized as a full disk if the diameter of this sphere is less than the depth of field (<400 nm). To obtain spatial information along the z-axis, we next used the 3D imaging capability on our setup, based on adaptive optics.

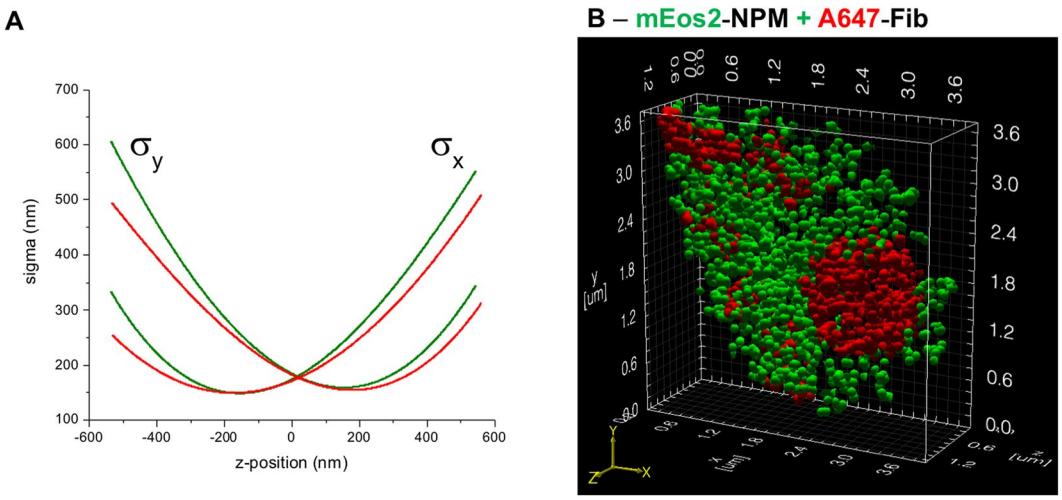

Figure 5. Two-colours 3D imaging of nucleolar sub-compartments. (**A**) The calibration curves for the green and red channels were obtained by performing a z-scan on a single TetraSpek bead. The sigma values (x and y) correspond to the width of the 2D Gaussian fit used to localize the bead position. The difference between the two sets of curves are higher for $|\Delta z| > 200$ **nm**. Therefore, the two channels must be treated individually. (**B**) Two-colour 3D image of the granular and dense fibrillar sub-domains visualized by using mEos2-NPM and A647-Ab directed against fibrillarin. Stacks (10000 images for each colour) were analysed with Thunder Storm to obtain the localization coordinates (x, y and z) from which it was possible to make a 3D surface rendering with the help of ViSP software.

Among the different methods allowing to perform 3D imaging[23,27,28], adaptive optics can be used to introduce astigmatism in order to create an asymmetric PSF with respect to the circle of least confusion. Therefore, the shape and orientation of this PSF depends on the z-position of the dye. By fitting the PSF with a two-dimensional Gaussian function, two sigma values are obtained from which the z-position of the fluorophore can be determined using a calibration curve (see Fig. 5A). To generate the calibration curve, TetraSpek beads were immobilized on a glass coverslip and we performed a z-scan over a 1.4 µm depth, while exciting with a 561 nm laser at low power. The analysis was done with the help of the Thunder STORM ImageJ plugin and the obtained calibration curves are reported in Fig. 5A.

Next, we performed two-colour imaging on cells expressing mEos2-NPM and immunostained with A647-Ab directed against Fib. The two channels were analysed individually using the Thunder STORM ImageJ plugin and the calibration curves to retrieve the x, y and z coordinates of each single emitter. A table containing the coordinates and the number of detected photons was next imported in the ViSP software in order to obtain a surface rendering for a better representation[29]. As depicted in Fig. 5B, it is possible to discriminate in 3D the granular and the dense fibrillar components with a lateral localization precision of 15 and 10 nm for the green and the red channels respectively. The axial localization precision depends on the number of detected photons and z-coordinate[30]. This value is high for $|\Delta z| > 50$ **nm**, where $\sigma_x \approx \sigma_y$ (including the error of σ determination) and decreases for higher z values. In our case, the highest axial localization precision was about 20 nm for both channels. Among the different modalities of electron microscopy[31], it is possible to obtain a 3D rendering, however the associated protocol is much more restrictive. Indeed, to generate 3D images, an ultramicrotome must be used to remove very thin layer (50–200 nm) on the fixed sample before the acquisition of the 2D image. This process is repeated until the whole sample volume is reconstructed. In addition, sample preparation and selection of fixation agent are critical for ultrastructural preservation and image acquisition. Finally, the contrast obtained in electron microscopy is less specific than the one obtained in fluorescence microscopy. Despite being less spatially resolved, 3D two-colour super-resolution imaging appears as an excellent alternative to 3D electron microscopy.

Conclusions

In this study, we demonstrated that the Vectashield mounting medium (Vector laboratories) does not only improve the photophysical properties of the fluorescent protein mEos2 but is also much easier to use than the standard imaging buffer of thiols/oxygen scavenging system. Indeed, one just needs to dilute the Vectashield in glycerol to reduce the background in the green channel caused by its autofluorescence. Later, buffer can be stored at +4 °C for several weeks and reused again for other super-resolution experiments. In addition, the number of photons emitted by mEos2 is increased while keeping constant the A647 brightness. The mounting medium Vectashield gives thus a higher level of freedom for the selection of labelling strategy, which is important to address various biological problems. The high refractive index of the buffer also provides a better index matching for 3D imaging than water-based buffers. A protocol for multicolour drift correction based on the use of quantum dots was also presented. The main advantage of these fiducial emitters relies on their brightness, which is similar to that of the fluorescent labels used for imaging under our excitation conditions. The drift correction is thus performed with a similar localization precision. Moreover, quantum dots allow the experimentalist to avoid detector saturation that is for instance observed with TetraSpek beads. The residual chromatic aberrations between the detection channels

was corrected *a posteriori* with the help of a reference image obtained with TetraSpek beads. All these optimizations allowed us to perform 2D and 3D two-colour super-resolution imaging of the nucleolar sub-domains that were spatially resolved for the first time, to our knowledge, with the help of fluorescence imaging.

Materials and Methods

Plasmid constructs. The peGFP-NPM construct was kindly provided by Xin Wang (plasmid # 17578, Addgene).

The mEos2-NPM construct was obtained by replacing the eGFP cDNA in the peGFP-C1-GW vector corresponding to the Gateway® cloning version of peGFP-C1 (Clontech) in order to obtain the vector pmEOs2-C1-GW. To do so, the mEos2 cDNA was inserted between NheI and XhoI restriction sites of a digested peGFP-C1 GW. The cDNA coding for NPM was thus PCR amplify with primers harbouring the attB recombination sequences and cloned using the Gateway technology in pmEOs2-C1-GW to obtain the fusion mEos2-NPM. The integrity of all plasmid constructs was assessed by DNA sequencing (GATC Biotech, Germany).

Cell culture and transfection. HeLa cells were cultured in DMEM (1 g/L D-Glucose, [−] Phenol Red; Gibco by LifeTechnologies) supplemented with 10% Foetal Bovine Serum (S1810–500, Dutscher), 1% of Pen-Strep solution (100 units of Potassium Penicillin and 100 µg of Streptomycin Sulfate per 1 mL of culture media – final concentration; DE17-602E, Lonza, BioWhitaker) and 1% L-Glutamine (2 mM; BE17-605E, Lonza, BioWhitaker) at 37 °C with 5% CO_2. Cells were transiently transfected with different plasmids on the next day after seeding using jetPEI transfection reagent (PolyPlus Transfection) following the supplier's protocol −2 µL of jetPEI for 1 µg of plasmid DNA.

Immunofluorescent labelling. Cells were seeded on round cover-glasses 18 mm in diameter (62407–063, VWR) at a density of 75000 cells per well of a 12-well plate (131024C, ClearLine). Prior to seeding, cover-glasses were washed once with 70% ethanol and then three times with DPBS (Buffered Saline 0.0095M (PO_4), Lonza, BioWhitaker). For imaging, cells were fixed in 4% PFA (15710, Electron Microscopy Science) (diluted in DPBS) for 12 min at 37 °C and then, permeabilized with 0.2% Triton X-100 (X100–500ML, Sigma) (diluted in DPBS) during 10 min at room temperature. These steps were followed by 3 washes with DPBS for 5 min. Non-specific sites were blocked using 1% BSA (sc-2323, ChemCruz) during 1 h. Primary antibodies @NPM (7H10B0) (NBP1-47354, Novus biological), @Fibrillarin (38F3) (MA3-16771, Invitrogen) and @RPA194 (F-6) (sc-46699, Santa Cruz) were diluted 500 and 50 times respectively in 1% BSA. To save the stock of antibodies, drops of 50 µL were deposited on a parafilm and then cover-glasses were placed on the top for 1 h. Cells were washed again three times with DPBS. The steps of dilution (750 to 1000 times for both), deposition and incubation were repeated with the secondary antibodies F(ab′)2-goat @mouse-A647 (A21237, Invitrogen) and goat @mouse-A555 (A21424, Invitrogen). QDs (Qdot 655 Streptavidin Conjugate - Q10121MP, Invitrogen) were added into the solution with antibodies at 2 pM. The QDs are used to correct for the sample drift that occurs during a long acquisition. Incubation with this mixture was done for 45 min at room temperature. After final washing, samples were covered with an aluminium foil and kept at +4 °C before imaging (one-week maximum).

Buffers. The standard switching medium for organic fluorophores is composed of TN buffer (50 mM Tris (pH 8.0) and 10 mM NaCl), an oxygen scavenging system (0.5 mg/mL glucose oxidase (G7141-50KU, Sigma), 40 µg/mL catalase (C40-500MG, Sigma) and 10% (w/v) glucose) and 100 mM β-mercaptoethylamine (MEA; 30070-10G, Sigma). Buffer was freshly prepared on the day of the experiment.

The second buffer was prepared by mixing Vectashield (H-1000, Vector Laboratories) in TRIS-Glycerol (5% v/v TRIS 1 M pH 8 in Glycerol) to achieve a final concentration of 20% Vectashield. A 10 µL drop of this solution was deposited on a microscope slide, then a cover-glass (our sample) was rinsed in MilliQ water to remove salts and placed on the top of that drop. After 10 min at room temperature, enough to evaporate water from the surface of the cover-glass, the sample was sealed with a dental cement (Picodent). The sample is ready for imaging and can be stored at +4 °C for several days and reused again later.

Setup and imaging. Confocal microscopy imaging was performed on a Leica SP2 microscope equipped with 63X oil-immersion objective (1.2 NA). For confocal imaging, Fib and RPA were immunolabeled with Abs labelled with Alexa Fluor 555 and Alexa Fluor 647, and NPM was expressed as a fusion protein with the fluorescent protein eGFP. The fluorescent labels were excited at 635 nm (Alexa Fluor 647), 561 nm (Alexa Fluor 555) and 488 nm (eGFP) and their emission was collected (650–750 nm; 570–630 nm, 500–540 nm) by a PMT detector.

Super-resolution localization microscopy imaging was performed on a home-built setup based on a Nikon Eclipse Ti microscope with 100x 1.49 NA oil-immersion objective. The laser lines at 488 nm, 561 nm and 642 nm (Oxxius) were used for excitation of mEos2, A555, A647, and the 405 nm laser was used for photoconversion of mEos2. Laser power during the experiments was set to 50 mW for 561 nm and 642 nm lasers, that results in 2 kW/cm^2 excitation intensity, and 0.5 to 120 W/cm^2 for 405 nm laser. Laser lines were co-aligned into a single beam using single-band dichroic mirrors (Semrock). An acousto-optic tunable filter (AOTF; Opto-Electronic) was used to switch between lasers (shutter) and change the laser power. Emission from the sample was spectrally filtered with the help of a multi-band dichroic mirror (405/488/561/635 nm, lasers BrightLine quad-edge super-resolution laser dichroic beamsplitter: Di03-R405/488/561/635-t1-25x36, Semrock) and notch filters (561 nm and 642 nm StopLine single-notch filters: NF03-561E-25 and NF03-642E-25, Semrock; in order to remove the scattered laser light), and then was imaged on an EM-CCD camera from Hamamatsu (ImagEM). An additional lens was used to obtain a final magnification of 150X corresponding to a pixel size of 106.67 nm. For two-colour experiments, the signal on the camera chip was split into two channels using an image splitting optics Gemini (Hamamatsu) with a dichroic mirror (640 nm edge BrightLine single-edge imaging-flat dichroic beamsplitter: FF640-FDi01-25x36, Semrock) and long-pass filters (561 nm and 647 nm EdgeBasic long-pass filters: BLP02-561R-25 and BLP01-647R-25) inside. Each time before imaging the sample, the point spread function was optimized, and residual

optical aberrations (spherical, coma, …) were minimized using adaptive optics (Imagine Optics) with the help of TetraSpek bead[32]. The reference image with TetraSpek beads (ThermoFischer) was acquired to correct the lateral shift and chromatic aberrations (UnwarpJ plugin, ImageJ) between the two channels. Z-stabilization was ensured by the perfect focus system (PFS, Nikon Eclipse Ti) on the microscope.

Data analysis. A stack of 10000–20000 images of 512 * 256 pixels (two channels together) was analysed with the Thunder STORM plugin in ImageJ. The following parameters were used to find and fit the signal of each particle: image filtering – Difference-of-Gaussians filter (sigma 1 = 1.0 and sigma 2 = 1.6); approximate localization of molecules – Local maximum (peak intensity threshold: std(Wave.F1), connectivity: 8-neighbourhood); sub-pixel localization of molecules – Integrated Gaussian (fitting radius: 4 px, fitting method: Least squares, initial sigma: 1.3 px). Results were filtered by sigma and localization precision values: 120 nm < sigma < 180 nm (see Fig. 4 in SI), precision < 25 nm. Drift correction: with fiducial markers Max distance – 100 nm, Min marker visibility ratio – 0.15, Trajectory smoothing – 0.03. Reference images with TetraSpek beads were analysed with the UnwarpJ plugin of ImageJ in order to calculate the elastic deformations and create the transformation matrix, which will be applied to rendered images for correction of chromatic aberration.

Data availability. The raw data of the results presented in the paper are available upon request to the corresponding author.

References

1. Dean, K. M. & Palmer, A. E. Advances in fluorescence labeling strategies for dynamic cellular imaging. *Nat. Chem. Biol.* **10**, 512–523 (2014).
2. Rinaldi, A. S. *et al*. The use of fluorescent intrabodies to detect endogenous gankyrin in living cancer cells. *Exp. Cell Res.* **319**, 838–849 (2013).
3. Anton, H. *et al*. Investigating the cellular distribution and interactions of HIV-1 nucleocapsid protein by quantitative fluorescence microscopy. *Plos One* **10**, 1–23 (2015).
4. Hell, S. W. Far-field optical nanoscopy. *2010 23rd Annu. Meet. IEEE Photonics Soc. Photinics 2010* **316**, 3–4 (2010).
5. Sahl, S. J., Hell, S. W. & Jakobs, S. Fluorescence nanoscopy in cell biology. *Nat. Rev. Mol. Cell Biol.* **18**, 685–701 (2017).
6. Betzig, E. *et al*. Imaging Intracellular Fluorescent Proteins at Nanometer Resolution. *Science (80-.).* **313**, 1642–1645 (2006).
7. Hess, S. T., Girirajan, T. P. K. & Mason, M. D. Ultra-High Resolution Imaging by Fluorescence Photoactivation Localization Microscopy. *Biophys. J.* **91**, 4258–4272 (2006).
8. Rust, M. J., Bates, M. & Zhuang, X. Sub-diffraction-limit imaging by stochastic optical reconstruction microscopy (STORM). *Nat. Methods* **3**, 793–796 (2006).
9. Heilemann, M. *et al*. Subdiffraction-resolution fluorescence imaging with conventional fluorescent probes. *Angew. Chemie - Int. Ed.* **47**, 6172–6176 (2008).
10. Gould, T. J., Verkhusha, V. V. & Hess, S. T. Imaging biological structures with fluorescence photoactivation localization microscopy. *Nat. Protoc.* **4**, 291–308 (2009).
11. van de Linde, S. *et al*. Direct stochastic optical reconstruction microscopy with standard fluorescent probes. *Nat. Protoc.* **6**, 991–1009 (2011).
12. Shroff, H. *et al*. Dual-color superresolution imaging of genetically expressed probes within individual adhesion complexes. *Proc. Natl. Acad. Sci.* **104**, 20308–20313 (2007).
13. Rosenbloom, A. B. *et al*. Optimized two-color super resolution imaging of Drp1 during mitochondrial fission with a slow-switching Dronpa variant. *Proc. Natl. Acad. Sci.* **111**, 13093–13098 (2014).
14. McKinney, S. A., Murphy, C. S., Hazelwood, K. L., Davidson, M. W. & Looger, L. L. A bright and photostable photoconvertible fluorescent protein. *Nat. Methods* **6**, 131–133 (2009).
15. Boisvert, F.-M., van Koningsbruggen, S., Navascués, J. & Lamond, A. I. The multifunctional nucleolus. *Nat. Rev. Mol. Cell Biol.* **8**, 574–585 (2007).
16. Olson, M. O. J. & Dundr, M. The moving parts of the nucleolus. *Histochem. Cell Biol.* **123**, 203–216 (2005).
17. Olivier, N., Keller, D., Rajan, V. S., Gönczy, P. & Manley, S. Simple buffers for 3D STORM microscopy. *Biomed. Opt. Express* **4**, 885 (2013).
18. Shi, X., Lim, J. & Ha, T. Acidification of the oxygen scavenging system in single-molecule fluorescence studies: *In situ* sensing with a ratiometric dual-emission probe. *Anal. Chem.* **82**, 6132–6138 (2010).
19. Vogelsang, J., Cordes, T. & Tinnefeld, P. Single-molecule photophysics of oxazines on DNA and its application in a FRET switch. *Photochem. Photobiol. Sci.* **8**, 486–496 (2009).
20. Thompson, R. E., Larson, D. R. & Webb, W. W. Precise nanometer localization analysis for individual fluorescent probes. *Biophys. J.* **82**, 2775–2783 (2002).
21. Georgieva, M. *et al*. Nanometer resolved single-molecule colocalization of nuclear factors by two-color super resolution microscopy imaging. *Methods* **105**, 44–55 (2016).
22. Schaffer, B., Grogger, W. & Kothleitner, G. Automated spatial drift correction for EFTEM image series. *Ultramicroscopy* **102**, 27–36 (2004).
23. Huang, B., Wang, W., Bates, M. & Zhuang, X. Three-Dimensional Super-Resolution Imaging by Stochastic Optical Reconstruction Microscopy. *Science (80-.).* **319**, 810–813 (2008).
24. Ovesný, M., Křížek, P., Borkovec, J., Švindrych, Z. & Hagen, G. M. ThunderSTORM: A comprehensive ImageJ plug-in for PALM and STORM data analysis and super-resolution imaging. *Bioinformatics* **30**, 2389–2390 (2014).
25. Sorzano, C. Ó. S., Thévenaz, P. & Unser, M. Elastic registration of biological images using vector-spline regularization. *IEEE Trans. Biomed. Eng.* **52**, 652–663 (2005).
26. Clouvel, G., Jasaitis, A. & Levecq, X. *Quasi-isotropic nanometric 3D resolution of PALM/STORM with the help of MicAO 3DSR. Imagine Optics* (2015).
27. Quirin, S., Pavani, S. R. P. & Piestun, R. Optimal 3D single-molecule localization for superresolution microscopy with aberrations and engineered point spread functions. *Proc. Natl. Acad. Sci.* **109**, 675–679 (2012).
28. Juette, M. F. *et al*. Three-dimensional sub-100 nm resolution fluorescence microscopy of thick samples. *Nat. Methods* **5**, 527–529 (2008).
29. El Beheiry, M. & Dahan, M. ViSP: Representing single-particle localizations in three dimensions. *Nat. Methods* **10**, 689–690 (2013).
30. DeSantis, M. C., Zareh, S. K., Li, X., Blankenship, R. E. & Wang, Y. M. Single-image axial localization precision analysis for individual fluorophores. *Opt. Express* **20**, 3057 (2012).
31. Olson, M. O. J. *The Nucleolus*. *Springer*, *Protein Reviews* (2011).
32. Izeddin, I. *et al*. PSF shaping using adaptive optics for three-dimensional single-molecule super-resolution imaging and tracking. *Opt. Express* **20**, 4957–4967 (2012).

Acknowledgements
We thank our colleagues Julien Godet, Frédéric Przybilla and Ludovic Richert for their help in writing the beanshell script for a raster scan, inspiring comments and fruitful discussions. O.G. was supported by the scholarship from French Ministry of Higher Education and Research.

Author Contributions
O.G. performed all the experiments and data analysis. E.R. and P.D. designed the experiments. E.R., E.B., Y.M. and P.D. contributed to materials and analysis. O.G. and P.D. wrote the manuscript.

Additional Information
Supplementary information accompanies this paper at https://doi.org/10.1038/s41598-018-27059-z.

Competing Interests: The authors declare no competing interests.

Publisher's note: Springer Nature remains neutral with regard to jurisdictional claims in published maps and institutional affiliations.

Supplementary Information

Optimized protocol for combined PALM-dSTORM imaging

Oleksandr Glushonkov, Eleonore Real, Emmanuel Boutant,
Yves Mely, Pascal Didier*

Laboratoire de Bioimagerie et Pathologies, UMR 7021 CNRS,
Université de Strasbourg, 67000 Strasbourg, France

**corresponding author: pascal.didier@unistra.fr*

Correction of the chromatic aberration.

In order to obtain a reference image for the correction of the chromatic aberration, we immobilized TetraSpek beads on a glass coverslip. The sample was next imaged under low excitation power at 561 nm to prevent photobleaching of the beads. By using this excitation wavelength, it was possible to excite two different dyes encapsulated in the bead. In that case, the single bead appears simultaneously in the green and red channel of the camera mounted after the Gemini module (Frame 0 on the scheme). As the chromatic aberration depends on the position in the field of view, we used the translation stage of the microscope to move the bead at specific positions in the field of view.

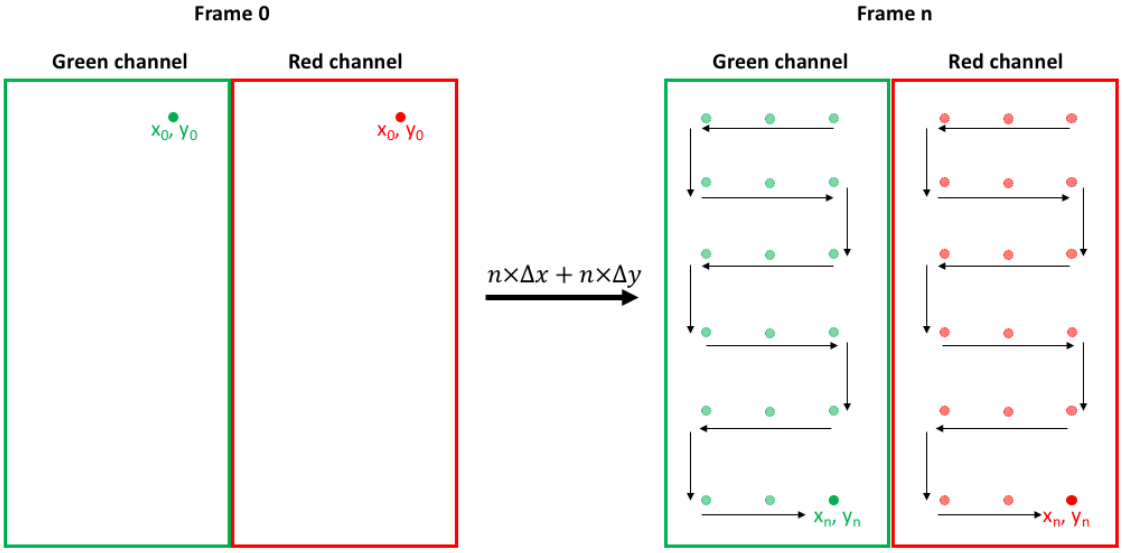

Thunder STORM plugin was then used to localize the position of the bead. For all positions we recorded an image with the bead appearing in both channels. By summing all the retrieved localization (with a PSF rendering of 20 nm), it was possible to obtain a reference image in which the same bead is placed in a periodic manner on different positions within the field of view (Frame n on the scheme). Without any chromatic aberration, a perfect superposition of the two channels could be obtained after cropping the green and the red channels. However, as depicted in Figure 3A such procedure does not allow to obtain a perfect superposition of the two channels because of the position depend chromatic aberration. Nevertheless, as the green and red spots originates from the same bead, an algorithm can be used to correct *a posteriori* the position depend chromatic aberration. To do so, we used the UnwarpJ plugin of ImageJ which is able to generate a field dependent deformation matrix by superposing the bead position on the green and the red channels. The obtained deformation matrix can be later used to correct the chromatic aberration on the images obtained with the biological sample. We recommend to record a reference image every day to account for the day to day change of the optical alignment.

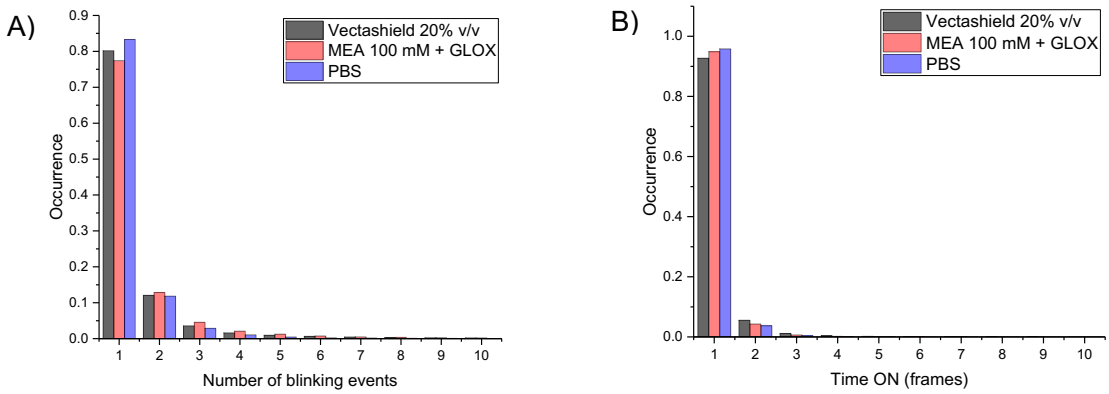

Figure S1. Comparison of the photophysical properties of overexpressed mEos2 in aqueous buffer (PBS), in the standard imaging buffer of thiols with oxygen scavenging system (MEA 100 mM + GLOX) and in the Vectashield mounting medium. A) Distributions of the number of blinks after photoactivation. B) Distributions of the ON time measured for mEos2 after photoactivation.

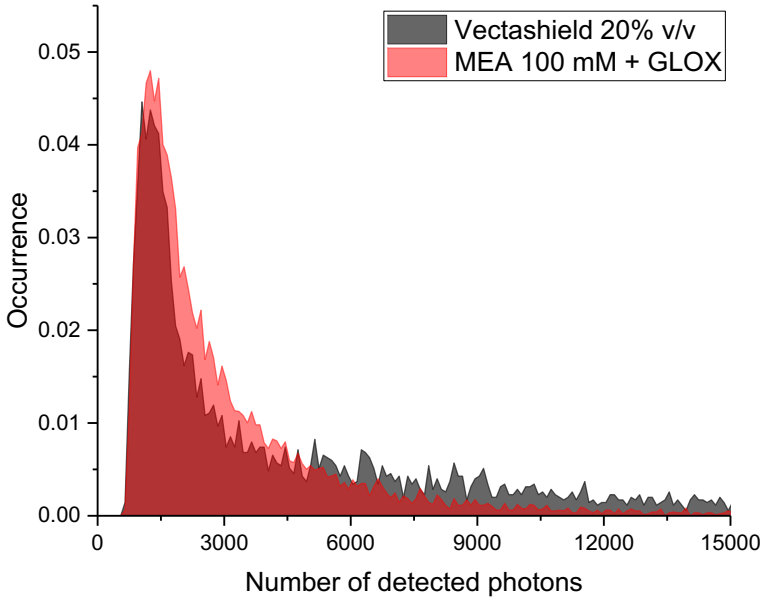

Figure S2. Photon number distributions of A647-Ab imaged in the standard Imaging buffer of thiols/oxygen scavenging system and in the Vectashield mounting medium (integration time: 16 ms). The mode values are 1240 and 1250 photons for MEA+GLOX and Vectashield respectively. The median number of photons values are 2079 and 2580 photons for MEA+GLOX and Vectashield respectively.

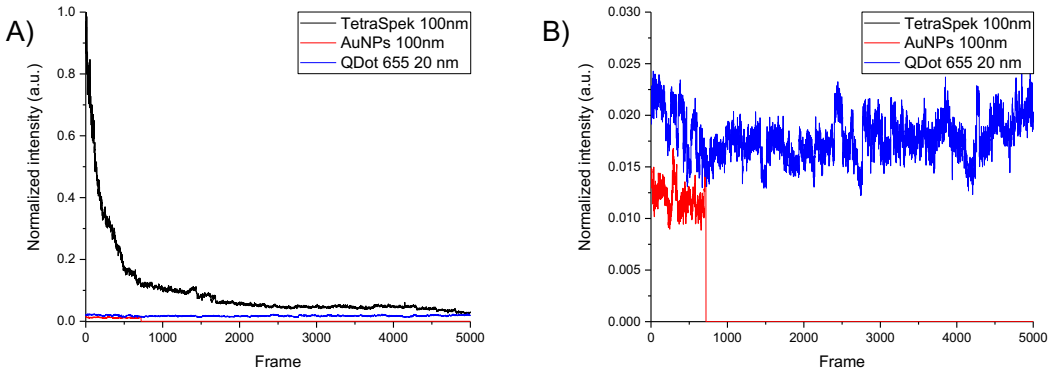

Figure S3. **Comparison of the intensities of the signal emitted by single fiducial markers**. The TetraSpek beads, gold nanoparticles (Au NPs) and quantum dots (QDs) were immobilized on a glass coverslip using Vectashield as mounting medium. At high laser power that is common for localization microscopy experiments, TetraSpek beads display very high intensity leading to the saturation of the camera with the EM gain used to maximize the number of detected photons per single fluorophore (panel A). In addition, under such high excitation regime, TetraSpek are prone to photobleach. Under our experimental conditions, the intensity of the signal emitted by single Au NP disappeared after few hundred images while the intensity of the signal emitted by the QD could be monitored over the entire acquisition (panel B).

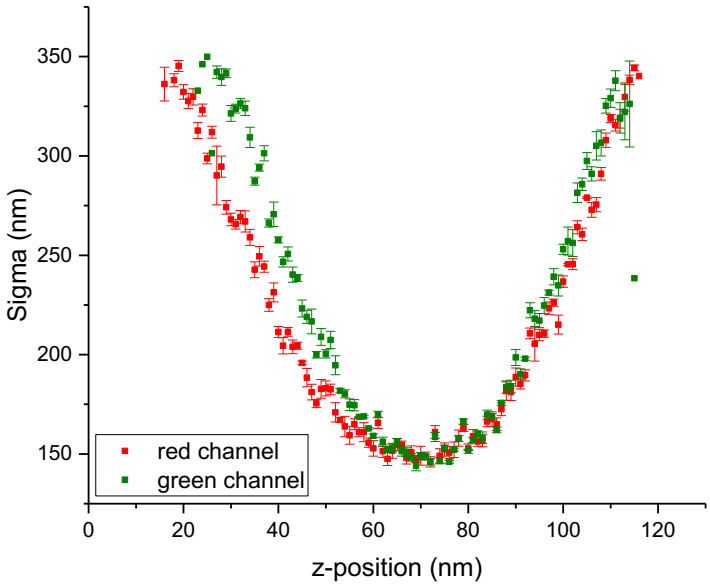

Figure S4. Axial chromatic aberration. A Z-scan of TetraSpek beads was performed with steps of 10 nm. The localizations of the beads in two different channels were fitted separately using a 2D Gaussian model. The standard deviation is reported as a function of the z-coordinate for each channel. The minima of both curves must co-localize to allow imaging of the same sample region in both channels.

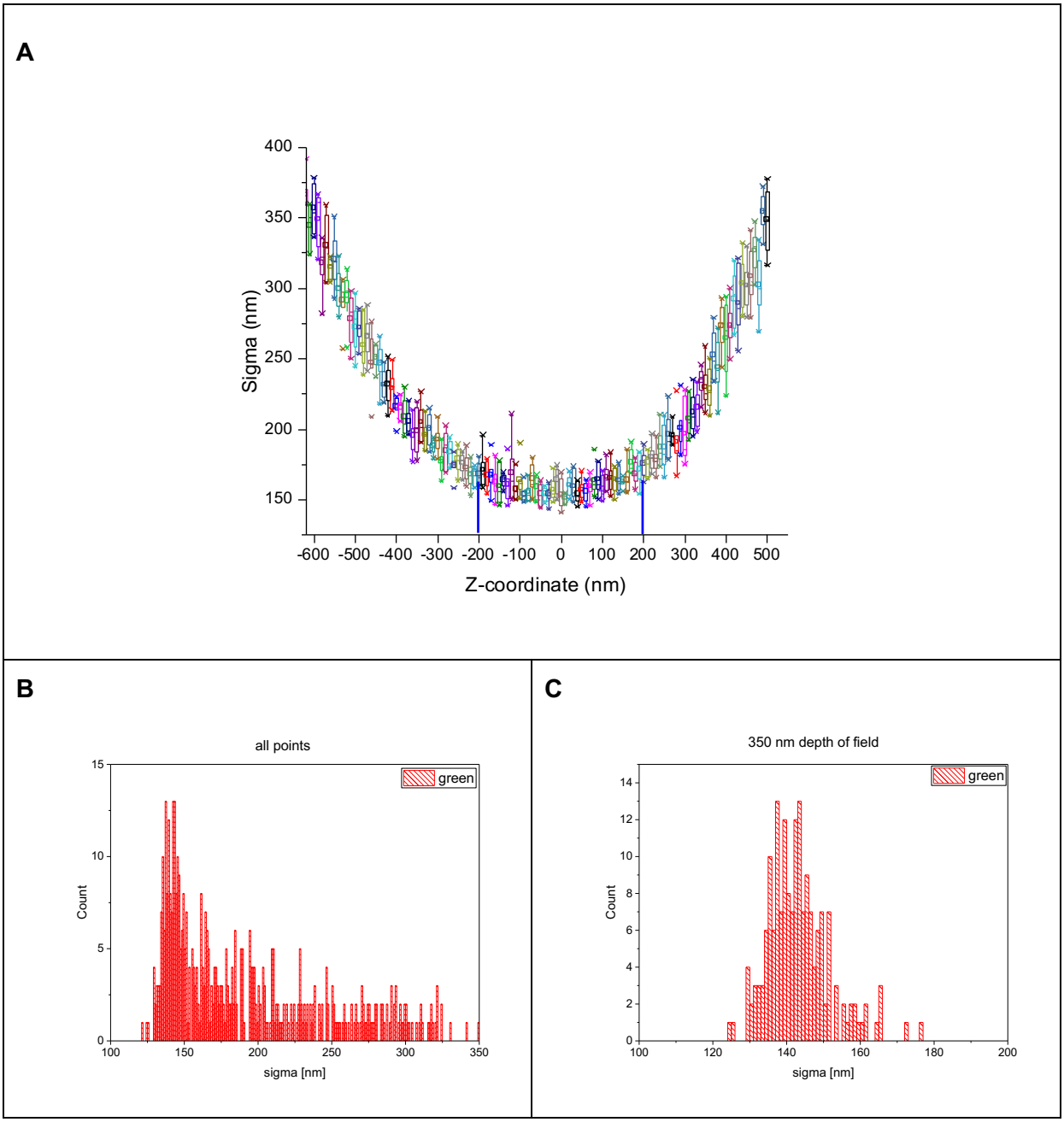

Figure S5. Measured sigma values as a function of the z position. (A) z-scan with 10 nm steps was performed on TetraSpek beads. At the minimum of the curve, where beads are in focus, the value of sigma (standard deviation of the Gaussian function) is around 150 nm. This value is almost constant over a range of 400 nm (blue bars). (B) Sigma values distribution obtained from the Gaussian fit of mEos2 localizations. The tail of the distribution (high sigma values) is associated to detection artefacts (e.g. two particles within diffraction-limited region or particles out of focus). (C) Sigma values distribution after filtering with a threshold: 120 nm < σ < 180 nm (150 nm ± 20%).

3.7. Microinjection

As it was mentioned in the introduction, several studies evidenced the nuclear localization of the nucleocapsid protein during the viral infection. While in the first experiment [65] the nuclear fraction, including the nucleolar proteins, was investigated by immunoprecipitation and western blot analysis, the immunofluorescence staining and imaging of NC distribution in H9 and PBMC cells during the second experiment [39] does not enable to define nucleoli because of signal saturation. Furthermore, the nucleolar localization of NC has been always observed in conditions of protein overexpression. To test whether this observation depends on the protein's concentration, we microinjected HeLa cells with NC 1-55 peptide conjugated to a rhodamine dye (Figure 45). Several concentrations were tested, and the lowest concentration at which the dye can still be detected by the camera was determined to be 10 µM. Assuming that the injected volume is about 100 fl (10^{-13} l), in that case the number of injected peptides will be: $N = c * V * N_A = 10 * 10^{-6} \frac{M}{l} * 10^{-13}\ l * 6.022 * 10^{23} = 6 * 10^5\ \frac{NC}{cell}$, which is not far from the estimated number during the real infection: $2 * 10^5\ \frac{NC}{cell}$, taking into account that around 100 virions infect a T-cell [170,171] with 2000 copies of NC protein per particle [172].

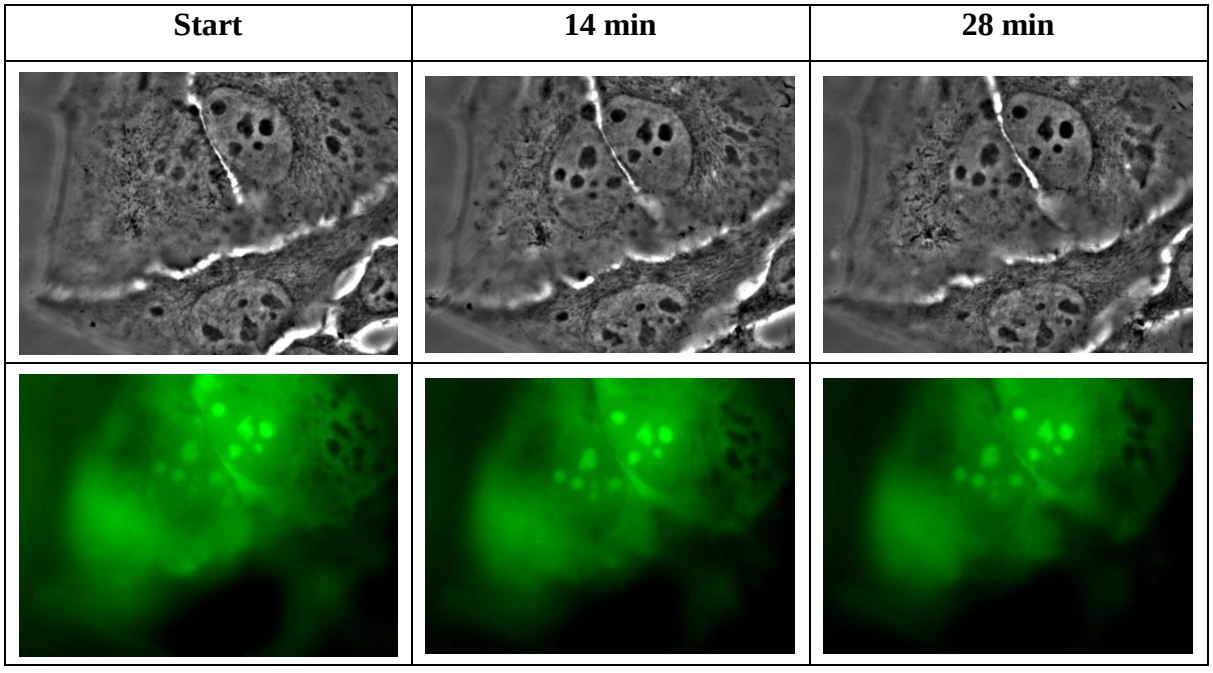

Figure 45. Microinjection of HeLa cells with 10 µM NC 1-55 labeled with Rh. Time-lapse experiment during 30 min after injection. Protein is highly concentrated in nucleoli. First row – phase contrast images, second row – fluorescence of rhodamine dye.

The control experiment was next performed using HeLa cells microinjected with rhodamine dye alone at the same concentration (10 µM, Figure 46). The results show that the

dye alone does not localize in nucleoli, preventing any label-dependent localization effects. Similar experiment has been previously performed by Sholokh et al., 2014, but with NC 11-55 peptide and at higher concentration: 100 µM [173].

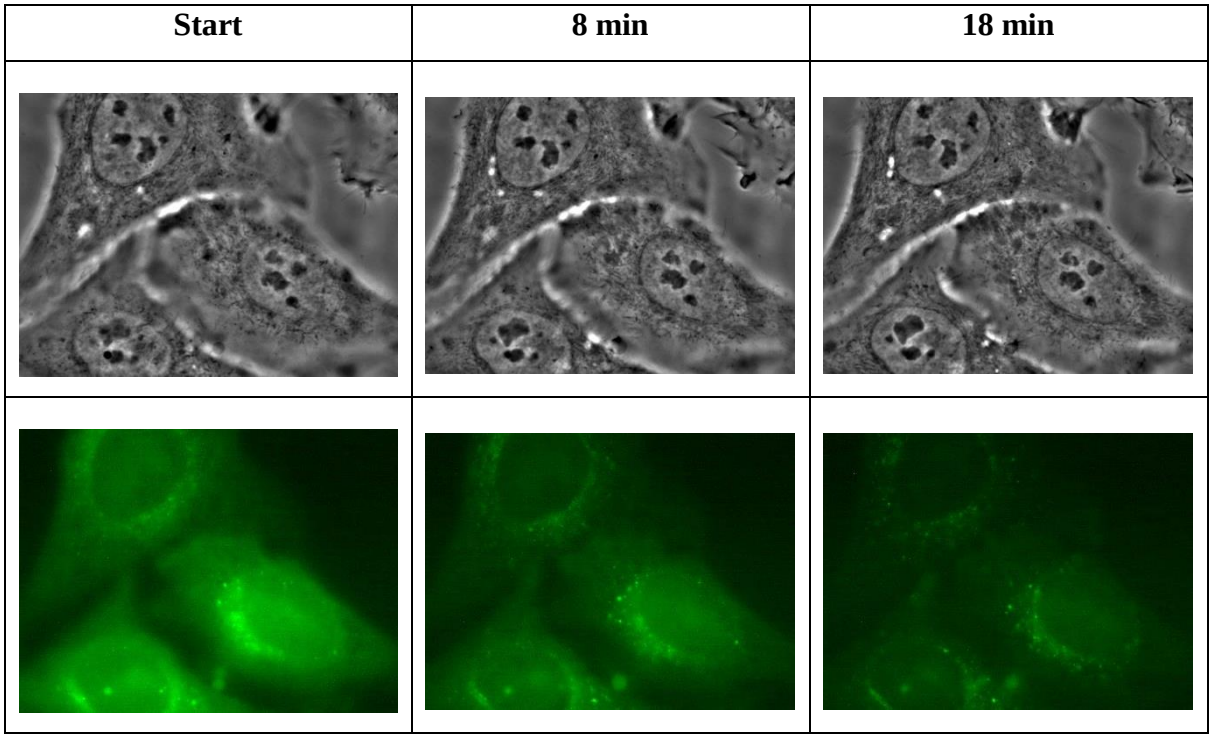

Figure 46. Control experiment. Microinjection of HeLa cells with Rh dye at 10 µM concentration. There is no specific localization, dye diffuses through the whole cell. In the top right corner, we can see a non-injected cell.

Our results demonstrate that NC localizes almost immediately in the nucleoli directly after microinjection and confirm that, in the case of NC, overexpression experiments can be used to investigate the nucleolar localization without introducing any bias.

3.8. Confocal imaging of NC

The localization of NC in fusion with fluorescent proteins mEos2 or eGFP, or indirectly immunostained with Alexa Fluor 647 (either NC of Flag-NC) will be discussed in this section. Comparison of fluorescent labels with different molecular weight is important, because the tags may affect the protein's localization. On the other hand, nonspecific labeling with primary antibody may also result in artefacts and lead to wrong conclusions.

For this experiment HeLa cells were transfected with plasmids coding for eGFP-NC, NC-mEos2 or Flag-NC (1 µg per well of a 12-well plate) using the transfection agent jetPEI. After 24 hours of incubation at 37°C cells were fixed in 4% PFA and immunolabeled with @GFP (Sc9996, SantaCruzBio) or @Flag antibody (the labeling with @NC will be discussed later). Cover-glasses were mounted then on microscope slides using mounting medium

Fluoromount G. On the next day samples were observed on the confocal microscope Leica SPE 2 equipped with 63x oil-immersion objective.

While nuclear localization of mEos2, eGFP and @Flag-A647 may vary from cell to cell, all three display a high concentration of NC in nucleoli (Figure 47). In contrast, by using antibodies @eGFP (1/250) with @mouse-A647 it was not possible to detect NC in the nucleolus, probably the primary antibody could not enter the tightly packed nucleolus.

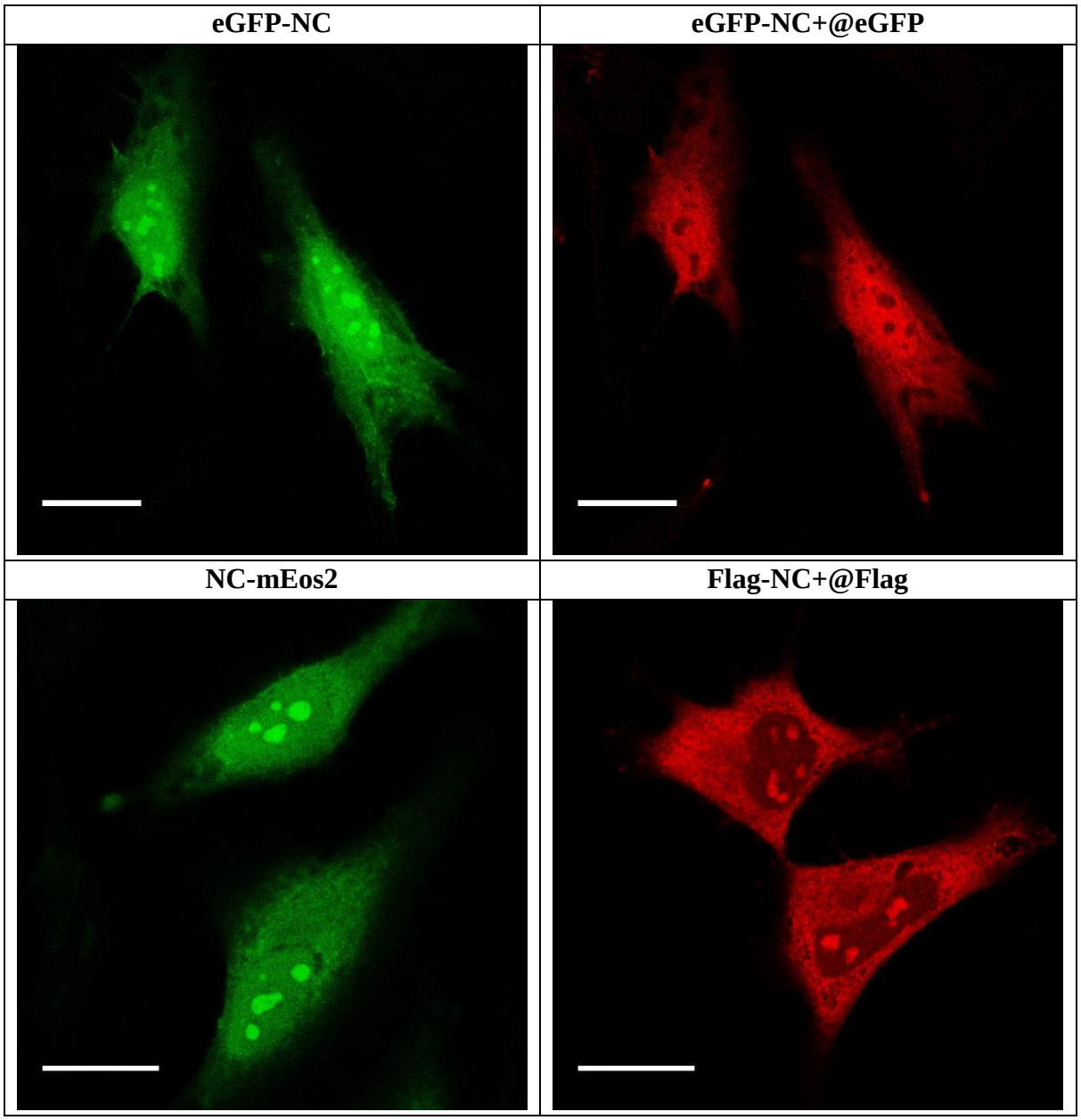

Figure 47. Confocal imaging of NC protein tagged with different fluorescent labels. Imaging parameters, excitation wavelength and spectral range from where emission was collected: eGFP-NC+@eGFP-A647 – 635 (650-700) and 488 (500-555); NC-mEos2 – 488 (500-600); Flag-NC+@Flag-A647 – 635 (645-750). Scale bar: 20 µm

In a second experiment, we tried to label overexpressed NC proteins with a primary anti-NC (kindly provided by the group of Goerlick) and secondary anti-goat-A647 antibodies.

Unfortunately, the staining was not specific (Figure 48 “NC+@NC”). Therefore, we repeated the immunolabeling experiment with cells overexpressing NC-mEos2 fusion protein and compared NC localization obtained by imaging mEos2 and Alexa Fluor 647 attached to the complex of two antibodies. From the images obtained in the red channel (A647) it was not possible to retrieve the characteristic nucleolar localization of NC (Figure 48 “NC-mEos2+@NC”). It is important to mention that one of the cells imaged with @NC antibody (yellow ROI) did not appear in the green channel, meaning that this cell was not transfected with NC-mEos2. This result demonstrates the nonspecific binding of the primary antibody.

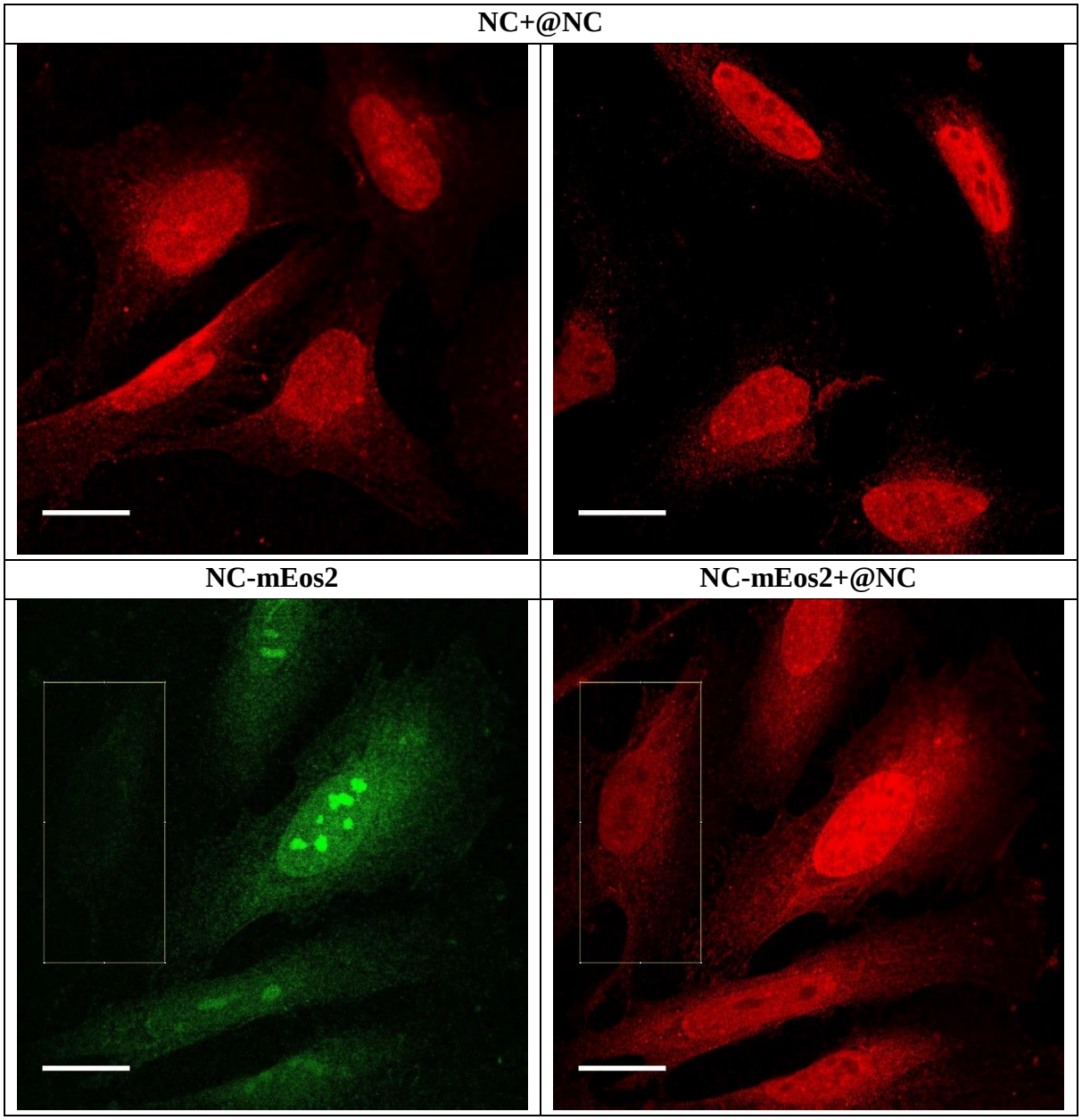

Figure 48. Confocal imaging of the overexpressed NC/NC-mEos2 protein immunolabeled with the primary @NC antibody and secondary Ab conjugated to Alexa Fluor 647. Imaging parameters, excitation wavelength and spectral range from where emission was collected: 635 (650-750) and 488 (500-600). Scale bar: 20 µm

PFA fixation and formation of crosslinks between proteins may hide the antibody's epitopes decreasing thus the efficiency of immunolabeling. Next, we tested the protocol of cells fixation in Methanol at -20°C for 10 min to avoid any detrimental effect of the fixating agent. The localization pattern appeared to be different, NC protein was again localized in nucleoli. However, when two antibodies were added to non-transfected cells, without overexpressed NC protein, the same images were obtained (Figure 49). Which leads to the conclusion that available antibody is not specific to NC.

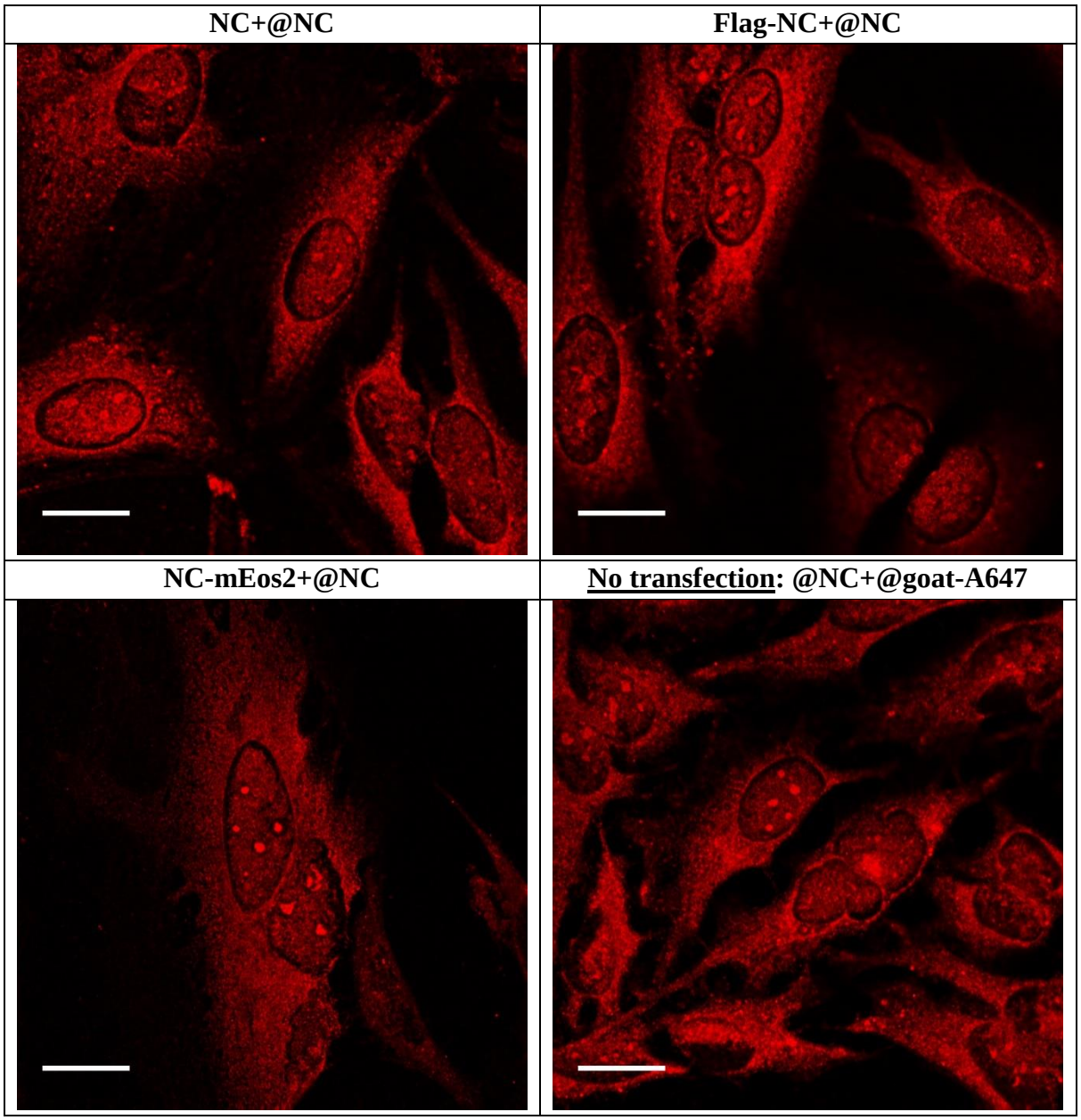

Figure 49. Confocal imaging of NC with different labels. After transfection, cells were fixed in Methanol at -20°C for 10 min. Imaging parameters: A647 was excited at 635 nm and emission from 650-750 nm range was collected with a detector. Scale bar: 20 µm

3.9. Western Blot

Some antibodies may be more efficient in western blot experiments and less efficient when used for immunostaining. Indeed, epitopes of folded and functional proteins can be hidden and not accessible for an antibody, whereas in western blot during the sample preparation the proteins are denaturated and unfolded, exposing thus their epitopes to the solvent. To check whether this is the case, we transfected HeLa cells with different NC constructs and labeled all of them with @NC antibody.

After first western blot experiment, we observed that while NC-mCherry and NC-eGFP fusion proteins were detected with @NC antibody, the rest of proteins showed much lower signal (Flag-NC, NC-mEos2) or were not detected at all (NC). The same experiment was repeated using, in parallel with jetPEI, another transfection agent jetPRIME, which displays higher transfection efficiency (Figure 50).

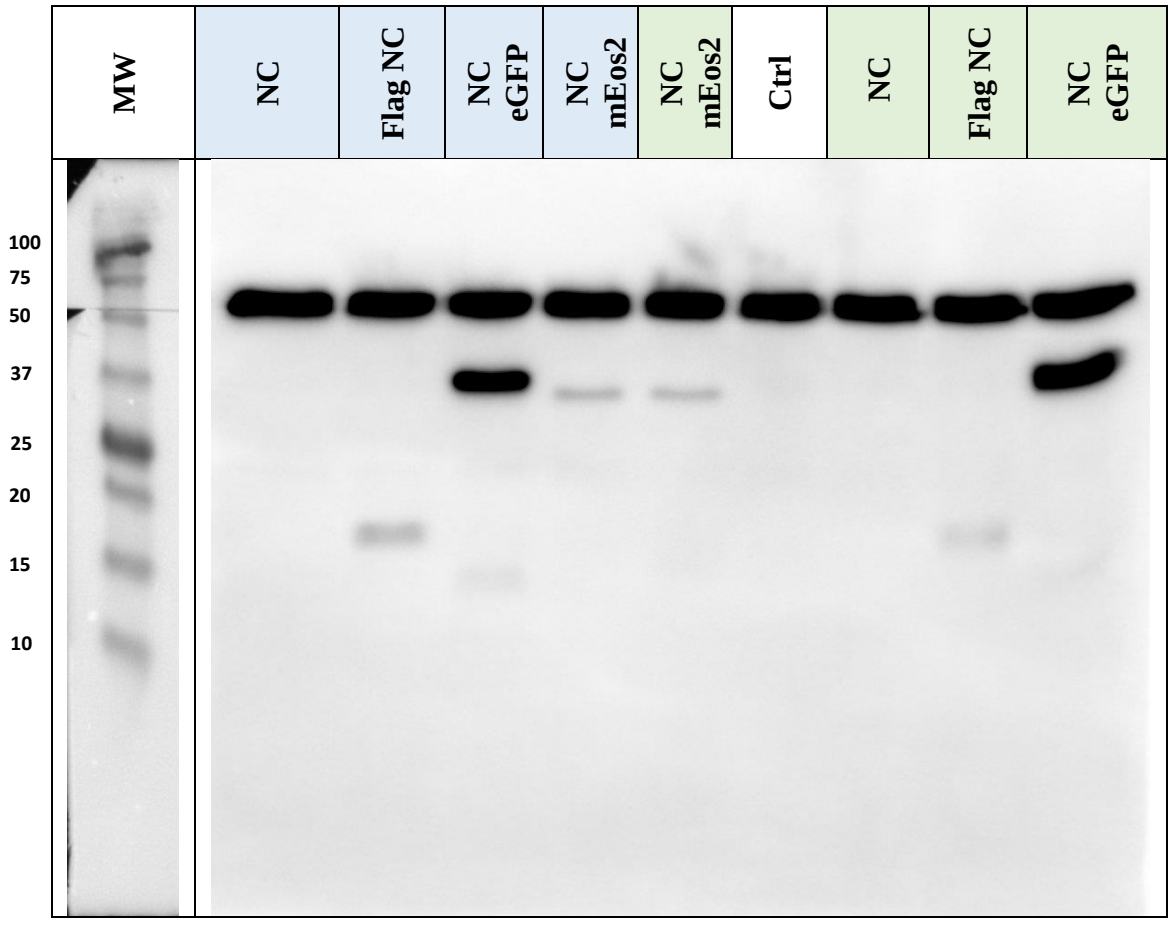

Figure 50. Western blot experiment. jetPEI (blue) vs jetPRIME (green) transfection agent: effect on the transfection efficiency. Primary antibody: @NC was diluted 3000 times; @α-tubulin was diluted 4000 times. Secondary antibody: @mouse-HRP was diluted 10000 times. Exposure time in LAS 4000 was 12s. MW of α-tubulin is 50 kDa. Labeled α-tubulin serves as a control of protein quantity in each condition.

From Figure 50 we can see that there is no significant effect of the transfection agent. These experiments confirmed the results obtained during immunostaining and confocal imaging: NC alone cannot be detected with available antibody. Unlike immunostaining assay, the western blot did not show any signal in the control sample likely because of the difference in Ab concentration. Taking into account that all other fusion proteins were detected with the same antibody, the problem can be related to the NC plasmid (bad expression), fast NC degradation in cells, non-specific binding of antibody to all other proteins.

To test the first hypothesis, a new plasmid was created where NC was inserted into the pCI-neo vector. And again, the obtained results were the same (Figure 51). But now plasmid-related problems can be excluded suggesting that NC-antibody binds nonspecifically to several proteins or NC quickly degrades when is not in fusion. To further study the problem more complex biological experiments are required and are beyond the scope of this work. We thus decided to label NC either with mEos2 fluorescent protein or Flag-NC with @Flag antibody.

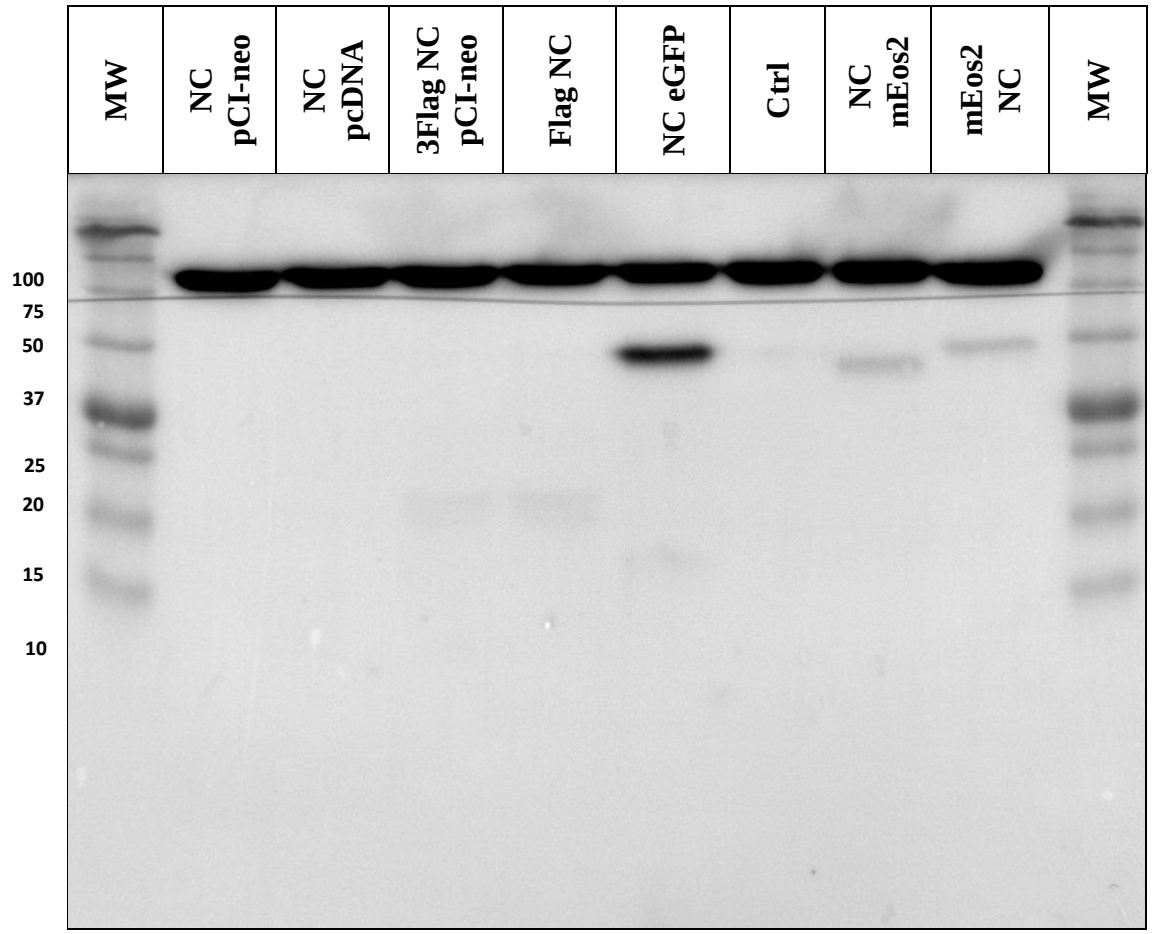

Figure 51. Western blot experiment with new NC plasmids (in pCI-neo vector). Primary antibody: @NC was diluted 3000 times; @α-tubulin was diluted 4000 times. Secondary antibody: @mouse-HRP was diluted 10000 times. Exposure time in LAS 4000 was 10s. MW of α-tubulin is 50 kDa. Labeled α-tubulin serves as a control of protein quantity in each condition.

3.10. Confocal imaging of NC with different nucleolar markers

Before the acquisition of two-color super-resolution images, HeLa cells, transfected with NC-mEos2 construct and immunolabeled with either @NPM or @Fib antibodies, were imaged on the confocal microscope. The obtained results demonstrate the nucleolar localization of NC-mEos2 together with the distribution of nucleolar markers. Using diffraction-limited methods, we observed that NC was homogeneously distributed in the whole nucleolus, in contrast to single-color super-resolution images of NC-mEos2, and subsequently, colocalized with both markers (Figure 52).

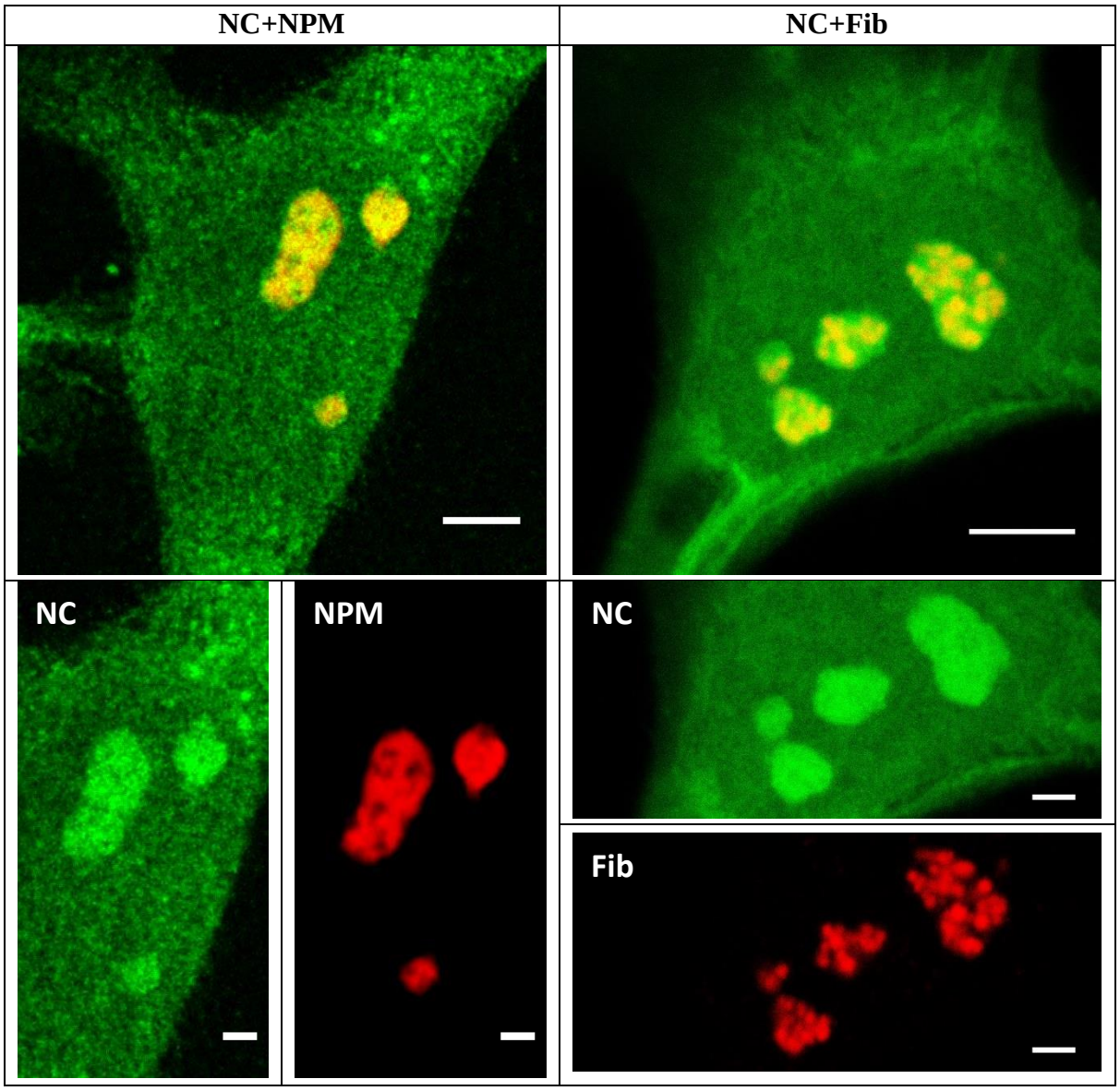

Figure 52. Two-color confocal imaging of NC-mEos2 with nucleolar markers Imaging parameters, excitation wavelength and bandpass for emission collection: A647 – 635 (650-750); mEos2 – 488 (500-600). Scale bar: 5 µm (2 µm for single channel).

3.11. Super-resolution co-imaging of NC with nucleolar markers

As was previously shown in the publication manuscript, the resolution of confocal microscopy is not sufficient to clearly separate nucleolar subdomains. For this reason, NC and nucleolar markers were labeled with photoswitchable fluorescent probes in order to perform super-resolution localization microscopy experiments. All the optimizations of imaging protocol and corrections for drift and chromatic aberrations were used during the data acquisition and analysis. Cells were imaged in 20% Vectashield medium with quantum dots used as fiducial markers for drift correction. The results are presented in the Figures 53-55.

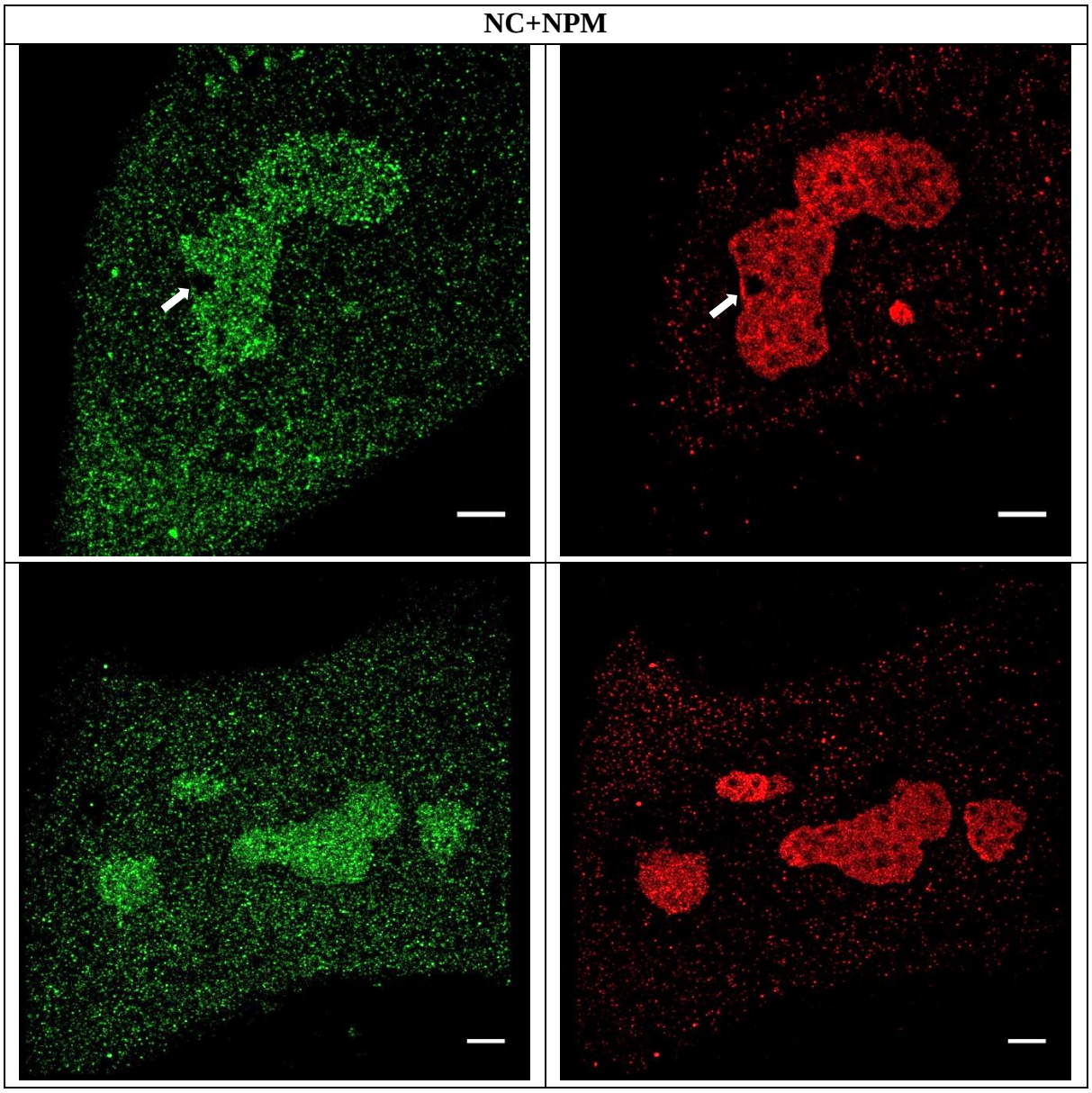

Figure 53. Super-resolution images of HeLa cells co-labeled with NC and NPM, marker of the granular component. White arrow highlights the expected localization of fibrillar center that appear on both images. Scale bar: 2 µm.

While some acquisitions result in good quality images of both channels (more than 10^5 localizations with the localization precision of 13 nm and 6 nm for mEos2 and Alexa Fluor 647 respectively) (Figure 53), there are others where the total number of NC-mEos2 localizations is low. For example, only 3×10^4 NC-mEos2 molecules were detected in the entire cell in case of co-imaging with Fib (Figure 54). However, the same number of detected Fib results in much higher density of localizations (DFC component is much smaller than entire cell), which in turn provides a better resolution. The provided number of detected proteins is far from the estimated one: $\sim 3 \times 10^6$ NC-eGFP proteins localize in HeLa cell in conditions of overexpression (calculated from FSC measurements). This number depends on the protein expression level, but longer acquisition time may also help to collect more data. By comparing obtained images, we can see that NC is mainly localized in the granular component of the nucleolus. There are several reasons for this localization that include an interaction with nucleolar and ribosomal proteins. All hypotheses will be discussed in the section "Discussion and perspectives".

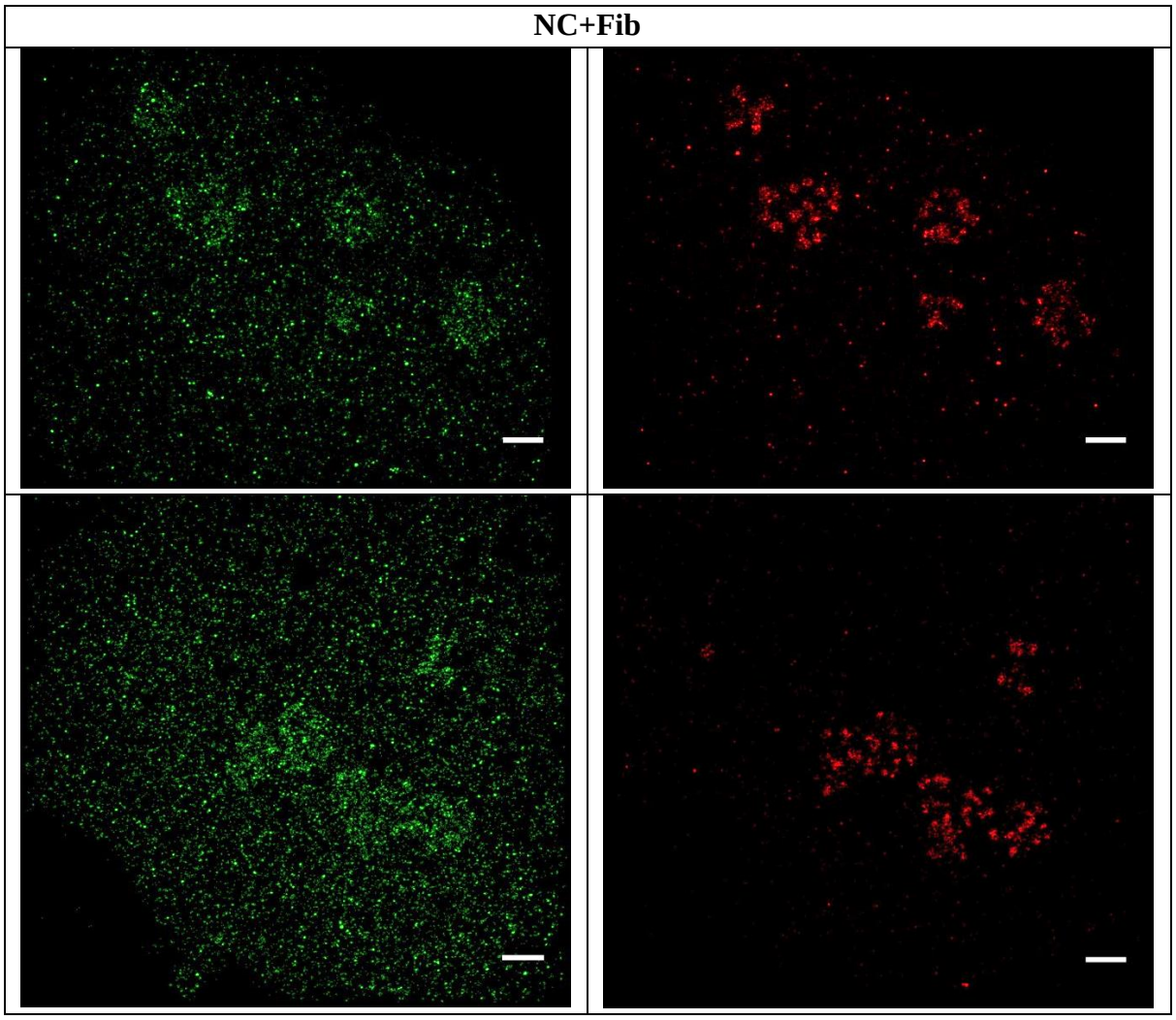

Figure 54. Super-resolution images of HeLa cells co-labeled with NC and Fib, marker of the dense fibrillar component. Scale bar: 2 µm

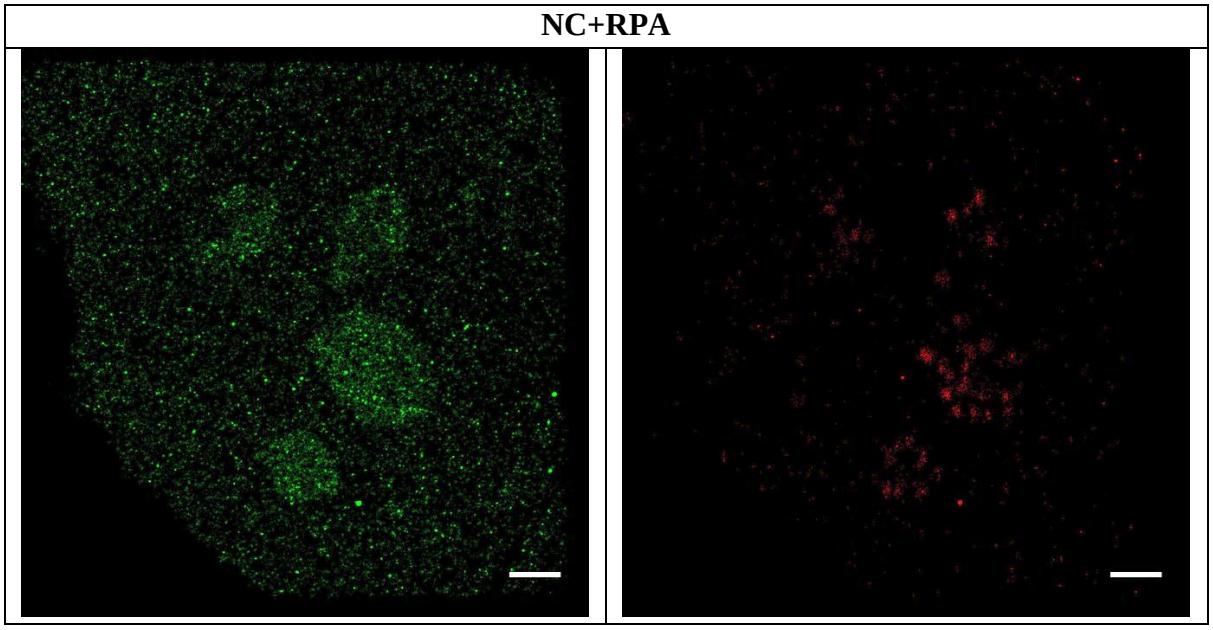

Figure 55. Super-resolution images of HeLa cell co-labeled with NC and RPA, marker of fibrillar centers. Scale bar: 2 µm

For better analysis of protein's nucleolar localization, the statistical data must be collected and analyzed quantitatively. While this analysis is well established for conventional fluorescence microscopy it cannot be directly applied to localization-based images because the former works with pixels and not localization coordinates, affecting thus the final results. Instead of calculation of a cross-correlation function using pixel intensities, it is more accurate to calculate a point-point correlation by representing localizations with Dirac functions or normal distributions, taking into account the localization precision [174]. The correlation function in this case is another set of coordinates that represents pair-distance distribution between two sets of proteins' localizations. The comparison of pair-distance distributions for our three conditions, when NC is imaged either with NPM, Fib or RPA, will help to determine more precisely the nucleolar localization of NC. For the moment of writing the manuscript, this type of analysis has not been done yet.

3.12. Single particle tracking (SPT)

Another possible approach to confirm proteins interaction lies in dual-color particle tracking experiments that can be used to identify simultaneous diffusion of a doubly labeled complex. The general idea of the single particle tracking in densely-labeled samples is similar to the super-resolution localization microscopy techniques. The photoswitchable nature of fluorescent proteins and organic fluorophores, used for labeling, is exploited in order to resolve and track individual proteins of interest. However, a lower laser power is used to prevent phototoxicity effects in living cells. In the case of fluorescent proteins, a lower laser power prevents fast bleaching of the label and results in longer trajectories. Depending on the dynamics of the system, a higher acquisition frame rate may be required, which means a lower exposure time and lower number of collected photons. In this case the precision of protein localization decreases and at some point, the labeled protein cannot be detected anymore. That is why it is important to find a compromise between the laser power and exposure time.

When the acquisition is finished, the trajectories of individual proteins can be plotted by simply connecting the protein's localizations on consecutive frames. The mean square displacement (MDS) can be calculated from the list of localizations and is used to characterize the diffusion process and proteins microenvironment [175,176] (Figure 56). In the case of free Brownian motion, the MSD varies linearly with the observation time. However, in the crowded environment of the cell, the protein can experience more complicated diffusion process. To account for all possible types of transport, we used a general model to fit the measured MSD: $< (r^2) > = 4D\Delta t^{\alpha}$, where α is a diffusive exponent and D – an apparent diffusion coefficient [176]. If α = 1, diffusion is Brownian; if α < 1 – particle adopts a confined motion due to the presence of small microdomains in the cell; if $1 < \alpha \leq 2$ – particle is transported by active forces (e.g. molecular motors or pulled by other proteins), leading to a displacement in one particular direction; the case when α = 0 corresponds to immobilized particles.

To define the optimal conditions for proteins tracking, we started with a single-color labeling. In our experiments, living cells expressing mEos2-NC fusion protein were imaged by simultaneously illuminating the sample with 405 nm (~1-100 W/cm^2 to maintain the same density of localizations) and 561 nm (~500 W/cm^2) lasers. Typically, 2000 images were recorded with an integration time of 25 to 50 ms and the trajectories of individual proteins were obtained and fitted using the Particle Tracking Analyzer (PTA) plugin under ImageJ.

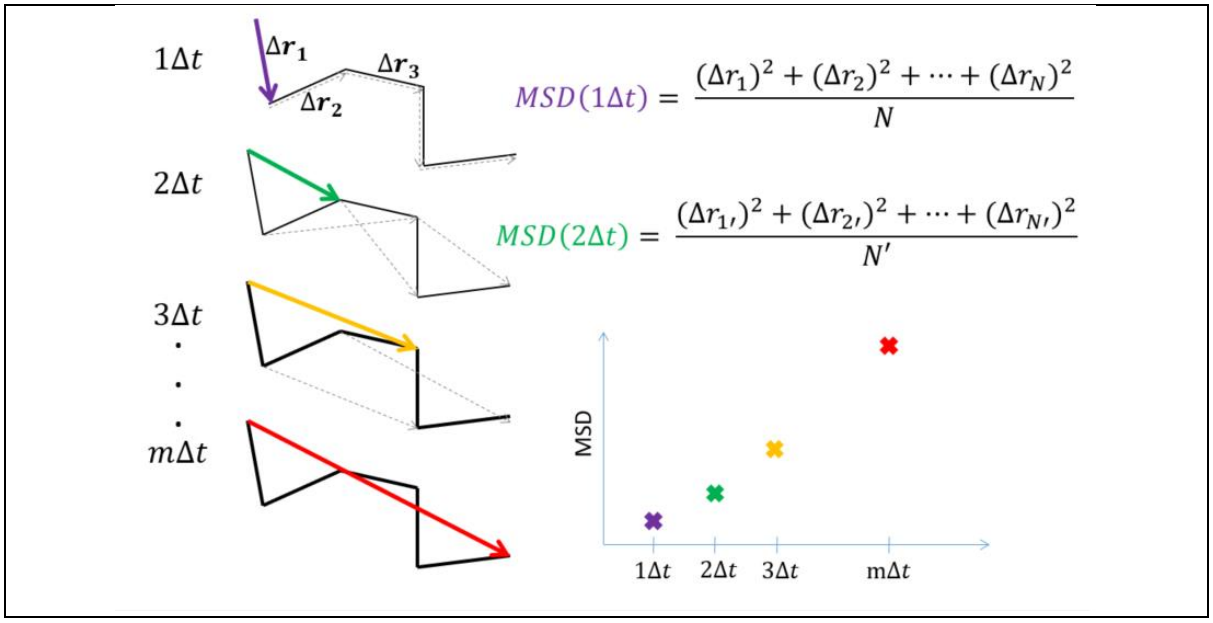

Figure 56. Determination of a mean square displacement (MSD) from protein's trajectory. The average MSD is calculated for different time intervals according to the given formula. These values are then plotted on a graph and fitted with a power function ($< (r^2) > = 4D\Delta t^{\alpha}$) in order to characterize the type of motion and determine the diffusion constant.

From the recorded data we calculated the values of a mean square displacement (MSD) for different time intervals. One of the trajectories and the corresponding plot MSD (Δt) is represented in Figure 57. A statistical analysis of more than two hundred trajectories was performed to determine the distribution of diffusive exponent (Figure 58). The obtained distribution of the diffusive exponent α is broad and centered around 1.25±0.1, meaning that most of the detected NCp7 proteins undergo a super diffusive motion that is likely driven by two types of forces: energy consuming (active) and thermally mediated.

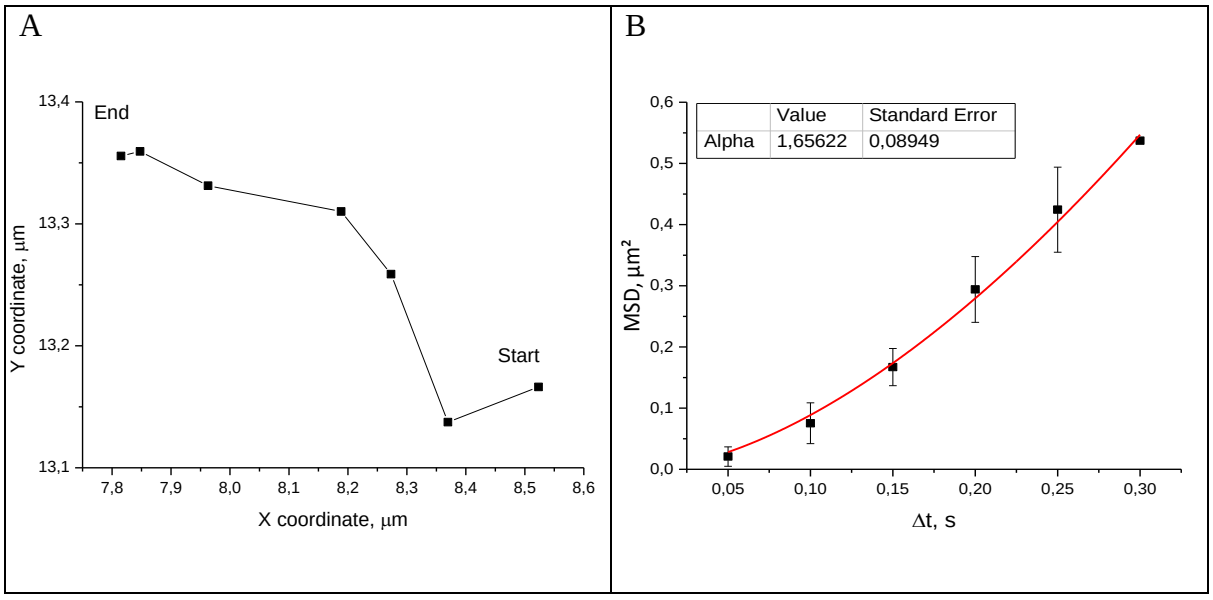

Figure 57. (A) Trajectory of protein movement. Protein was detected on seven consecutive frames. (B) The dependence of an average mean square displacement over time intervals was fitted with a power function ($< (r^2) > = 4D\Delta t^{\alpha}$) in order to determine α and therefore the type of protein's motion.

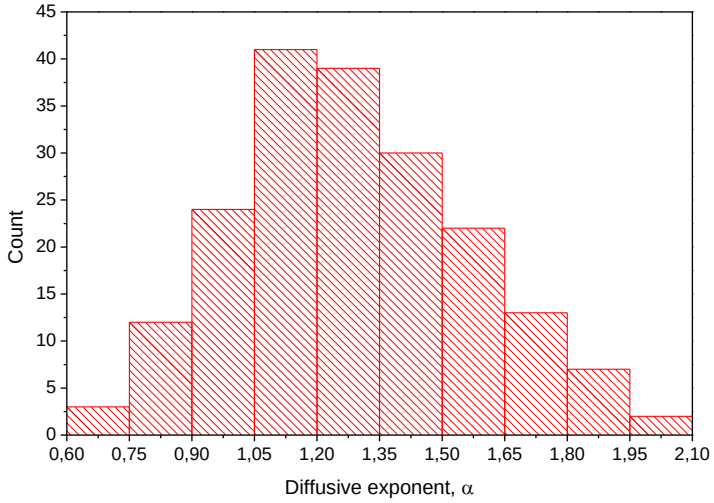

Figure 58. Distribution of the diffusive exponent (α).

There are several possibilities for a such behavior: transfer by molecular motors, by NC's interacting partner, or flows. The activity of molecular motors in the nucleus has already been demonstrated on the example of capsid protein of the herpes simplex virus 1 (HSV-1) [177]. Its directed movement is temperature and energy-dependent, and sensitive to a myosin inhibitor. Knowing that molecular motors are ATP-dependent, their role in NC transfer can be investigated with a help of SPT experiments under ATP depletion. Regarding the transport by other proteins, nucleolar protein NPM having a shuttling activity was found to be implicated in the transfer of HIV-1 Rev protein from the cytoplasm to the nucleus [88]. In addition, a recent study [178] has shown an interaction between the nucleocapsid protein of porcine epidemic diarrhea virus (PEDV) and NPM. It may be hypothesized that after the virus entry and uncoating, NC protein interacts with NPM in the cytoplasm and is transferred by the last one into the nucleus or nucleolus. Two-color SPT can be used in order to answer this question, as well to study the interaction of NC with its cellular partners.

Discussion and perspectives

As it was shown with super-resolution microscopy, NC protein displays a preferential localization in the granular component (GC) of the nucleolus. The GC is mostly known as the place where ribosomal subunits are assembled. However, a large number of proteins that localize in GC is implicated in other nontraditional functions of the nucleolus, like cell cycle regulation and stress response [79]. To understand better the reason of the nucleolar localization of NC and its impact on the virus replication cycle, it is important to identify cellular proteins that interact with NC in this compartment. It has been previously shown in our laboratory that NC interacts with two proteins of the large ribosomal subunit, RPL7 and RPL26 [179]. These interactions were confirmed by confocal imaging and FRET-FLIM experiments; in the case of RPL7 two additional experiments were performed: double-hybrid assay in yeast and co-immunoprecipitation. These experiments evidenced that both mature form of NC and NC domain of Gag protein interact with RPL7.

As it was mentioned before, the nucleolar activity plays role in the regulation of stress response and cell cycle arrest through p53 pathway [79,180]. Under normal conditions p53 is short-lived protein that is present at a barely detectable level. Exposure to different kind of stress (e.g. viral infection) stabilizes p53 and leads to either cell cycle arrest or apoptosis. It has been proposed that nucleolar sequestration of MDM2 protein relieve nucleoplasmic p53 from MDM2-mediated degradation [75,180]. In addition to this pathway, when the ribosome biogenesis is inhibited by the nucleolar stress or other stress factors, the released ribosomal proteins were observed to enter the nucleoplasm and block MDM2-mediated p53 degradation by interacting with MDM2 protein [181]. RPL26 in this case enhances the translation rate of p53 mRNA [182], which all together lead again to p53-dependent cell cycle arrest or apoptosis. By binding to RPL26, RPL7 and potentially other ribosomal proteins, NC may decrease p53 expression, restore MDM2-mediated p53 depletion and thus extent the cell survival. By simply binding to ribosomal proteins (e.g. RPL7 and RPL26) NC may decrease the formation of ribosomal subunits and consequently affect the process of protein expression. Alternatively, NC may recruit ribosomes for translation of viral RNA as it was proposed for coronavirus nucleoproteins [82].

Another potential interacting partner of NC in the nucleolus is the NoL12 protein as it was shown by Jager et al in their study published in 2012 [160]. One of the projects in our laboratory focusing on the characterization of NC/ NoL12 interaction was based on these

findings. The interaction between two proteins was confirmed by multiple experiments: double-hybrid assay in yeast, co-immunoprecipitation, confocal imaging and FRET-FLIM experiments. It is worth to mention that no interaction was observed with the NC domain of Gag neither by co-IP nor by FRET-FLIM experiments, making NoL12 a specific partner of the mature form of NC. Because NoL12 and NC are both RNA binding proteins, their interaction is likely RNA-mediated. This hypothesis was confirmed, when the interaction was lost after RNase treatment of the cell lysate in co-IP experiments. Two models of RNA-mediated interaction were proposed [183]: non-correlated binding of both proteins to the same RNA or specific interaction, when one protein first binds to RNA and change its conformation in order to facilitate the interaction with the second protein. FRET-FLIM experiments support more the second model, because this type of energy transfer occurs when proteins' labels localize within ten nanometers range. We may speculate that while in the first model both proteins bind RNA and the interaction can be detected in co-IP experiment, the binding may occur at different positions and the distance between proteins is big enough to not allow energy transfer in FRET-FLIM experiments. The second model can be also confirmed by super-resolution localization-microscopy when NC and NoL12 are labeled with photoswitchable fluorescent probes. Furthermore, it was shown that the knock-down of NoL12 by siRNA decrease the level of infection (data not published). Having exonuclease activity [184], NoL12 is responsible for the rRNA maturation. Interaction with NC could alter the activity of NoL12, for example by decreasing the number of ribosomal subunits and therefore affecting the protein expression; otherwise, NC could use the exonuclease activity of NoL12 to cleave HIV-1 RNA which was shown to localize in the nucleolus [89].

Another nucleolar protein, NPM, that we used in this study as a marker of the GC, can be also considered as a potential partner of NC. NPM is a shuttle protein that can move between cytoplasm and nucleoplasm and plays role in the transport of pre-ribosomal particles and in the process of ribosomal biogenesis. NPM is involved in the apoptotic response to stress and, together with previously mentioned ribosomal proteins, it can modulate the activity and stability of tumor-suppressor proteins such as p53 [185]. It is known that NPM interacts with two other HIV proteins Rev [88] and Tat [186]. Rev is involved in the export of unspliced or partially spliced HIV mRNA (intron-containing mRNA) from the nucleus to the cytoplasm. It was shown by Fankhauser that NPM participates in the Rev transfer from cytoplasm to the nucleus [88] for further rounds of mRNA export, which may be also the answer to how NC enters the nucleus and nucleolus. Furthermore, a direct interaction between Tat and NPM is

responsible for proper nucleolar localization of Tat [186]. Infection with HIV induces the acetylation of NPM, which is critical for nuclear localization of Tat and therefore transcription activation [187]. In addition, NPM was shown to interact with the nucleocapsid protein of porcine epidemic diarrhea virus (PEDV) in the nucleolus [178]. The knockdown of NPM in this case suppressed virus growth. Here NC binding could protect NPM from proteolytic degradation by caspase-3. It is possible that NC of HIV is using the same strategy for the regulation of cell survival, promoting higher viral burst (more released particles). Preliminary results of co-IP experiment performed in our laboratory showed the interaction between these two proteins (NC and NPM).

It would be of great interest to see whether NC plays a role in the regulation of translation process (protein expression) through the interaction with ribosomal proteins; or whether it plays a role in the process of stress response, preventing apoptosis, increasing cell survival and therefore number of released virions. Super-resolution microscopy can be used in future studies as additional tool to demonstrate proteins' co-localization and possible interaction. However, co-tracking of NC with one of the mentioned nucleolar partners on a single-molecule level will be a more reliable measure of proteins interaction. In addition, this approach can characterize the underlying mechanism associated to transport of studied proteins within the cellular microenvironment.

Conclusions

For biological studies on a subcellular level, the spatial resolution of conventional microscopy techniques becomes insufficient. For that reason, several super-resolution fluorescent microscopy techniques were developed starting from 90s and have been constantly improved till nowadays. Resolution down to several nanometers allow to define the shape of cellular structures, study the co-localization between proteins, and track the protein's movement in living cells.

While it is quite straightforward to perform the localization microscopy experiment with one probe, it much more challenging in multi-color imaging. Different factors as sample drift, chromatic aberration, optical and chemical properties of fluorescent probes need to be taken into account. In this work, we demonstrated that the performance of PALM-dSTORM experiments can be increased using commercially available Vectashield buffer instead of a combination of thiols with oxygen scavenging system. The results of the imaging protocol optimizations were published in the journal Scientific Reports. Implementation of this protocol enabled us to resolve optically the three nucleolar components in 2D (for the first time to our knowledge) and to perform 3D two-colors imaging of NPM with Fib proteins.

In the second part of Results section different labeling strategies were compared and used to investigate the nucleolar localization of the HIV-1 NC protein. In particular we showed that fusion of NC with fluorescent proteins and immunostaining of Flag-NC with Alexa Fluor 647 allow to observe the high nucleolar localization of HIV-1 nucleocapsid protein. To further support this observation, microinjection experiments were performed using much lower NC concentration and have shown that within two minutes NC was already accumulated in the nucleolus. In order to open the way to experiments with infected cells, we investigated the possibility to use an antibody directed against NC. All the experiments (immunostaining and western blot) shown that this antibody is not specific and cannot be used to detect non-labeled NC in cells. Therefore, mEos2 photoactivable fluorescent protein was used in combination with Alexa Fluor 647 organic dye in order to image NC with nucleolar markers.

The results obtained with two-color imaging suggest that NC mainly localizes in the granular component of nucleolus. However, more data and quantitative analysis are required for a definite conclusion. Previous studies from our laboratory [183,179] demonstrated the interaction of NC protein with nucleolar protein NoL12 (first presented by Jäger et al. in 2012 [160]) and ribosomal proteins 26 (RPL 26) [66] and RPL7 [162] by means of co-

immunoprecipitation, FCS and FLIM experiments. All three mentioned proteins localize in the nucleolus. Considering the multifunctional nature of nucleolus, the interaction of viral nucleocapsid protein with nucleolar or ribosomal proteins may have an impact on the production of ribosomal sub-units, favor the synthesis of other viral proteins and even change a cell cycle. In perspectives, co-tracking experiment of NC with its cellular partners can be performed in living cells to proof the proteins' interaction.

In order to perform a dual-color tracking, a second label is required. In this type of experiment, we are working with living cells, all the protocols that include cells fixation cannot be used, in particular immunostaining (with only exception: immunolabeling of a membrane protein). The simplest solution would be co-transfection with two photoswitchable fluorescent proteins. However, as it was already discussed, for the moment it is difficult to select a pair of proteins with appropriate photostability and brightness. The growing interest in super-resolution microscopy and the development of new fluorescent labels with better photophysical characteristics may soon resolve the mentioned problem. Alternatively, the small size of NC (55 amino acids) allows to synthesize fluorescently labeled peptide by using solid state synthesis. The final product can be introduced inside living cells at least by two different ways: microinjection and electroporation. In the first case, different concentration of NC may be injected in individual cells. The possibility to control the amount of NC (with respect to overexpression) allows to approach the conditions of a real viral infection. On the other hand, a higher number of cells may be labeled during the electroporation. Using one of these approaches, NC peptide may be introduced to living cells previously transfected with a plasmid coding for NC's potential partner fused to mEos2. Then two-color single particle tracking experiment could be performed in order to determine whether the interaction between two mentioned proteins exists.

Résumé en français

Le virus de l'immunodéficience humaine de type 1 (VIH-1) a été isolé pour la première fois à l'Institut Pasteur, à Paris en 1983 et les auteurs ont ensuite démontré que ce nouveau rétrovirus humain est en fait la cause du SIDA [1]. Depuis, des recherches intenses sur le virus lui-même, sa pathogenèse, ainsi que les approches pour tester, traiter et prévenir l'infection du VIH ont été menées. Après plus de trois décennies de recherche, le VIH est l'un des virus les mieux caractérisés. Les progrès dans le développement de médicaments (généralement des inhibiteurs d'enzymes virales) et le traitement ont permis de réduire la mortalité et d'augmenter l'espérance de vie.

L'efficacité du traitement antiviral permet de maîtriser la charge virale sans pour autant l'éradiquer, principalement à cause des mutations qui apparaissent lors de la réplication virale. L'une des manières de contourner le problème réside dans la recherche d'une cible conservée parmi les différentes souches virales. La protéine de la nucléocapside virale (NC) pourrait être un bon candidat [57]. Elle a une structure hautement conservée et joue un rôle clé dans les étapes précoces et tardives du cycle viral. En effet, la forme mature de la NC a des activités chaperonnes sur l'ARN et l'ADN du VIH-1, et est impliquée dans le processus de transcription inverse. Au sein de la polyprotéine Gag, le domaine NC reconnaît la séquence «packaging signal» de l'ARN viral, la dimérise et l'encapside dans la particule virale. En outre, il a déjà été démontré qu'une mutation ponctuelle de la NC conduit à la formation de virus non infectieux, faisant ainsi de la NC une cible thérapeutique de choix [57].

La distribution de la NC dans la cellule hôte et ses interactions avec ses partenaires cellulaires sont à l'heure actuelle mal connues. Des études antérieures ont révélé une forte accumulation cytoplasmique et nucléolaire de la protéine [66,67]. Gallay et al. ont démontré que la NC mature du VIH-1 peut migrer du cytoplasme vers le noyau et s'y accumuler 8h après l'infection [65]. Plus tard, Lochman et al. ont mis en évidence la localisation nucléolaire de la NC, en utilisant une protéine de fusion de la NC avec la protéine fluorescente YFP. Cette localisation est possible grâce à deux régions dans la séquence de la NC; aa 10-11 (Kyung Lee Yu et al. précisent que la région de N-terminale n'a pas d'importance [67]) et aa 32-34 [68]. Un modèle a été proposé récemment (Mirambeau G. et S. Lyonnais) dans lequel, en raison de sa plus faible affinité pour l'ADN double brin par rapport à l'ADN simple brin et l'ARN viral, une grande fraction de la NC est libérée dans le cytoplasme au cours du processus de la transcription inverse, alors qu'une petite fraction de la NC reste associée au PIC [63,64].

Cependant, on ne sait pas pourquoi la NC se localise dans le nucléole – est-ce dû aux fonctions chaperonnes de la NC dans l'intégration de l'ADN virale, la diffusion passive en raison de la forte affinité pour les ARNs cellulaires ou à une interaction avec les protéines nucléolaires et/ou ribosomales ? C'est dans ce contexte que j'ai caractérisé la distribution spatiale de la NC dans le nucléole afin d'obtenir des informations sur son rôle dans ce compartiment cellulaire.

Le nucléole, qui est le site de la biogenèse des ribosomes, est connu pour être ciblé par de nombreux virus afin de promouvoir leur réplication [84]. En plus de la production des particules ribosomales, le nucléole joue un rôle dans d'autres processus cellulaires tels que la régulation de la mitose, la croissance et la prolifération cellulaire et la réponse au stress [79]. En raison du rôle multifonctionnel du nucléole, plusieurs activités pourraient être ciblées, y compris la transcription cellulaire, la transcription du virus, la traduction de virus ou la division cellulaire. Le nucléole possède une structure complexe qui a été révélée par microscopie électronique. Les trois principaux domaines nucléolaires, correspondant aux différentes étapes de la biogenèse des ribosomes, ont été identifiés : les centres fibrillaires (FCs) – où a lieu la transcription de l'ADNr; le compartiment fibrillaire dense (DFC) – qui est le siège de la maturation et de la modification des pré-ARNr (méthylation, pseudouridylation); le compartiment granulaire (GC) – qui permet l'assemblage de sous-unités ribosomales [70]. Ainsi, la possibilité de localiser précisément la NCp7 dans le nucléole permettra de mieux comprendre les fonctions de la protéine et son rôle dans cet organite.

La microscopie optique, avec les techniques de marquage fluorescentes très spécifiques, est l'un des outils d'imagerie les plus puissants et polyvalents en biologie cellulaire moderne. Malheureusement, même avec des lentilles parfaites, un alignement optimal, et une grande ouverture numérique, la résolution spatiale du microscope optique est limitée par la diffraction à des dimensions de l'ordre de 200 nm dans le plan de l'échantillon. Plusieurs techniques de super-résolution ont été mises au point au cours des deux dernières décennies afin de franchir cette limite et ont permis d'atteindre des résolutions de l'ordre de quelques dizaines de nanomètres.

Dans la mesure où la structure des compartiments sub-nucléolaires et leur co-localisation avec la NC ne peuvent être résolues par microscopie optique classique, les techniques de microscopie de localisation de type PALM [132] (PhotoActivable Localization Microscopy) et STORM [116] (Stochastic Optical Reconstruction Microscopy) ont été sélectionnées. En séparant temporellement l'émission des fluorophores, il est possible d'obtenir

une situation dans laquelle un seul fluorophore est détecté dans une région limitée par la diffraction. La position de chaque fluorophore peut alors être déterminée en ajustant leur distribution d'intensité dans le plan de visualisation (point spread function - PSF) avec une fonction gaussienne en 2D. La précision de la localisation dépend, en première approximation, du nombre de photons détectés. L'avantage de ces techniques repose sur la simplicité de mise en œuvre par rapport à d'autres approches qui requièrent de mettre en forme le faisceau d'excitation (STED, SIM).

La première étape de ce projet était de caractériser le montage à l'aide de billes TetraSpek - particules de taille 100 nm, contenant quatre colorants différents. Le profil d'illumination, la taille du faisceau laser (section transversale) et la PSF ont été caractérisés avant d'entreprendre les expériences en milieu cellulaire.

La distribution précise (avec une résolution de l'ordre de 40 nm) de la NC dans le nucléole peut être déterminée en étudiant sa co-localisation avec les marqueurs des trois compartiments nucléolaires. Les protéines Fibrillarin, Nucleophosmine et RPA ont été utilisées pour identifier respectivement le DFC, le GC et le FC. Ces différentes protéines ont été marquées avec la protéine fluorescente photoactivable mEos2, en raison de sa brillance, sa photostabilité, l'absence de sensibilité à la température (repliement efficace à 37 ° C) et sa structure monomérique [113]. Les cellules HeLa ont été transfectées de manière transitoire avec des plasmides d'ADN, codant pour la protéine de fusion. Après 24 heures d'incubation, l'efficacité de la transfection a été vérifiée par microscopie confocal et à épifluorescence.

Les expériences de microscopie à haute résolution réalisées à une couleur montrent que la localisation de la NC est similaire à celle de la NPM. Cela suggère une localisation de la protéine NC dans le compartiment granulaire du nucléole. Afin de confirmer cette observation j'ai entrepris des expériences de co-localisation. Un deuxième fluorophore est donc nécessaire pour visualiser les marqueurs nucléolaires et la NC fusionnée à mEos2. Ce fluorophore doit présenter plusieurs propriétés : 1) absence de transfert d'excitation (FRET) et de fuite spectrale entre les deux canaux, les spectres d'excitation et d'émission de deux colorants doivent être bien séparés ; 2) ils doivent tous les deux être excitables et commutables dans les mêmes conditions, c'est-à-dire dans le même tampon (pH, piège à oxygène, cysteamine) et en présence du laser UV qui permet la photoactivation de mEos2. Tous ces critères font de la recherche du deuxième fluorophore une tâche complexe. Deux paires de colorants qui donnent les meilleurs résultats dans le tampon Vectashield [123] ont été sélectionnées après les essais de différentes

combinaisons : la protéine fluorescente mEos2 avec le fluorophore organique Alexa 647 ou Alexa 555 en présence de l'Alexa 647.

Afin d'obtenir des images à haute résolution en deux couleurs il a été nécessaire d'optimiser la préparation des échantillons et les protocoles d'imagerie. J'ai notamment pu montrer que les boites quantiques QD 655 permettent de corriger plus efficacement la dérive mécanique que d'autres émetteurs ponctuels (nanoparticules d'or ou billes TetraSpek que nous avions utilisée précédemment). Leur brillance (dans nos conditions d'excitation et de détection) est comparable à celle des fluorophores organiques Alexa 555 et Alexa 647. Pour accélérer et automatiser l'acquisition et l'analyse des données plusieurs scripts ont été écrits sur Java Bean Shell ainsi que des macros dans ImageJ.

Le tampon Vectashield qui a été sélectionné pour nos expériences à deux couleurs apparaît comme un milieu coloré en violet, et est donc autofluorescent [123]. En raison de la grande puissance laser utilisée lors de l'imagerie à haute résolution, cela génère un bruit de fond élevé et un faible rapport signal/bruit. Différentes dilutions du Vectashield dans le glycérol ont été testées pour trouver les conditions optimales. En outre, certains paramètres comme le nombre de photons émis par molécule, le rapport signal/bruit, la précision de la localisation, etc. ont été mesurés et comparés pour Alexa 555, Alexa 647 et mEos2 dans les différents tampons.

Au cours de mes expériences, j'ai surexprimé la NC en utilisant la transfection. Est-ce que cette surexpression de la protéine modifie sa distribution cellulaire ? Il existe au moins deux manières de répondre à cette question. La première repose sur l'infection de cellules HeLa avec des pseudo-particules virales visualisées par immunomarquage fluorescent indirect. Cependant, les anticorps, que nous avons au laboratoire, ne permettaient même pas de détecter la protéine NC dans des conditions de surexpression. C'est pourquoi une expérience du western blot a été réalisée en utilisant des cellules HeLa transfectées avec les différentes constructions de la NC. Les résultats montrent que l'anticorps peut reconnaître la protéine NC quand elle est fusionnée aux marqueurs fluorescents volumineux (comme mEos2); lorsque le «tag» devient plus petit (i.e. Flag tag), l'intensité de la bande diminue; et avec la protéine NC elle-même (deux plasmides différents ont été testés) il n'y avait pas de détection. La deuxième manière de caractériser la distribution cellulaire de la NC dans des conditions plus proche du contexte viral (en terme de concentration de protéines) est de microinjecter un peptide fluorescent de la NC. Le peptide NC 1-55 marqué avec de la rhodamine a été micro-injecté dans des cellules HeLa à

la concentration la plus faible que notre caméra pouvait détecter. J'ai pu montrer qu'en quelques minutes - temps entre l'injection du peptide dans les cellules et le moment où commence l'acquisition - le peptide NC était déjà concentré dans les nucléoles.

La microscopie à haute résolution à deux couleurs a permis de visualiser pour la première fois les différents compartiments nucléolaires (Figure 59). Ces résultats confirment l'efficacité de nos marqueurs et de notre technique en général. J'ai également implémenté une approche qui permet d'obtenir des images à haute résolution en trois dimensions et de s'affranchir des artefacts liés à la projection du volume de l'échantillon sur un seul plan (profondeur de champ).

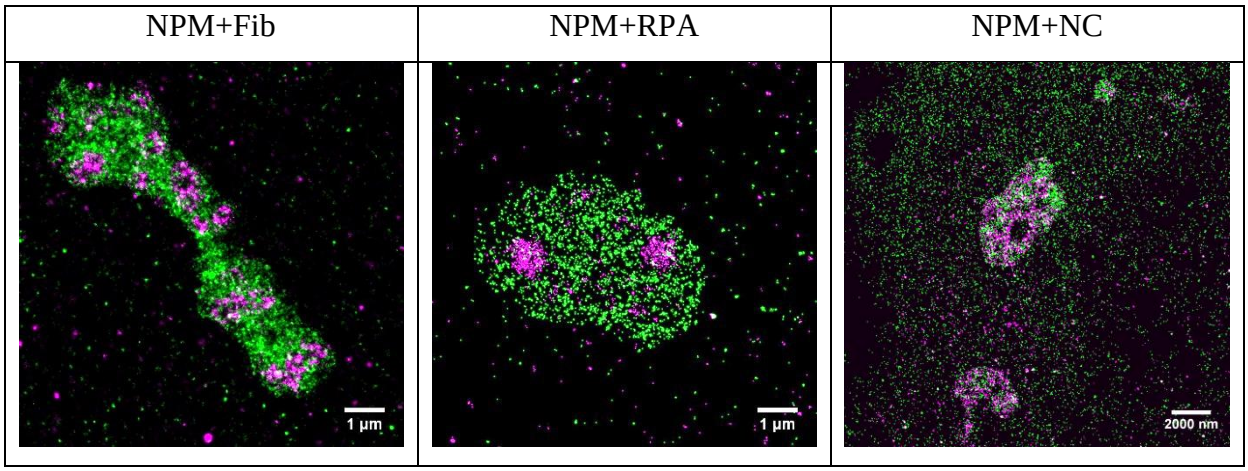

Figure 59. Les images à haute résolution en deux couleurs des compartiments nucléolaires et de la co-localisation de NCp7 avec le marqueur du composant granulaire.

Finalement, les expériences préliminaires avec des cellules vivantes ont permis de mettre en évidence que la NC fusionnée à mEos2 est transportée de manière active dans le noyau. D'autres études de localisation et de suivi de particules individuelles seront effectuées pour étudier l'interaction de NC avec certains partenaires nucléaires.

List of publication, posters and oral presentations:

Articles:

O. Glushonkov, E. Réal, E. Boutant, Y. Mély, P. Didier, "Optimized protocol for combined PALM-dSTORM imaging", Sci. Rep. **8**, 8749 (2018)

Potential second article about the nucleolar localization of HIV-1 protein NCp7.

V. Kilin, **O. Glushonkov**, L. Herdly, A. Klymchenko, L. Richert, and Y. Mely, "Fluorescence lifetime imaging of membrane lipid order with a ratiometric fluorescent probe," Biophys. J. **108**, 10 (2015)

Posters:

MAF 2015 – **O. Glushonkov**, E. Réal, P. Didier, Y. Mély. Localization of HIV-1 protein NCp7 in the nucleolus investigated by super-resolution microscopy. Würzburg, Germany, 13-16 September 2015

JCI 2016 – **O. Glushonkov**, E. Réal, Y. Mély, P. Didier. Localization and movement of HIV-1 protein NCp7 in the nucleolus investigated by Super-Resolution microscopy. Journées du Campus d'Illkirch 2016, Illkirch, France, 21-22 April 2016

NC congres 2016 - **O. Glushonkov**, E. Réal, P. Didier, Y. Mély. Cellular distribution of HIV-1 protein NCp7 investigated by super-resolution microscopy. Montpellier, France, 18-21 September 2016

Oral presentations:

MAF 2017 – **O. Glushonkov**, E. Réal, Y. Mély, P. Didier. Nucleolar localization of HIV-1 protein NCp7 investigated with super-resolution microscopy. Bruges, Belgium, 10-13 September 2017

Appendix

Western blot

Protein isolation and quantification

1. **Cells seeding (24 h)**

   HeLa cells (ATCC, CCL-2 Amp) were seeded in a 6-well plate (150000 cells/well); two wells for each condition. Cells were cultured in the same medium that was presented in Materials and Methods section.

2. **Transfection (24 h)**

   After 24 hours of cell seeding, cells were transiently transfected using the jetPEI transfection reagent (from PolyPlus) following the supplier's protocol (2 µg of plasmid DNA/ 4 µl of JetPEI/ 200 µl of NaCl 150 mM).

3. **Trypsinization**

   After 24 hours, the old medium was removed, and cells were washed with 1 ml of PBS 1x to increase the efficiency of Trypsin; after that 500 µl of Trypsin was added to each well, the plate was left in the incubator for 2-3 min; cells were rinsed with a fresh medium (1 ml per well), then collected in 15 ml Falcon tubes and placed on ice.

4. **Centrifugation**

   After centrifugation at 1500 rpm for 5 min at 4°C, the supernatant was discarded, cells were resuspended in 1 ml of PBS 1x and centrifuged one more time at 1500 rpm for 3 min at 4°C. Meanwhile, **Cell Lysis Buffer** was prepared.

Lysis buffer composition	**Volume**	**Final concentration**
Tris HCl 0.5M pH 7.5	1 ml	10 mM
NaCl 1.0M	1.5 ml	150 mM
EDTA 50mM	200 µl	1 mM
NP40	100 µl	1%
H_2O	7.2 ml	
Protease inhibitors (PI)	1 tablet	

5. **Lysis**

   The pellet was resuspended in 200 µl of fresh ice-cold Cell Lysis Buffer. Cell lysate was collected in Eppendorf tubes and incubated on ice for 30 min (vortexing gently after each 5 min).

6. **Centrifugation**

   Eppendorf tubes were centrifuged at 14000 g for 25 min at 4°C to get the proteins in a supernatant solution leaving cell debris at the bottom of the tubes. Two sets of Eppendorf tubes were prepared and labeled for the following steps.
7. The supernatant was collected in new Eppendorf tubes already placed on ice.
8. Each sample (5 µl) was diluted in TRIS-buffered Saline pH7.5 (95 µl), vortexed gently, and kept on ice.
9. 20 µl of BSA 1x was also diluted in TRIS-buffered Saline pH7.5 (180 µl) and kept on ice. BSA solution was prepared by dissolving 144 mg of BSA in 1 ml of water. Then this stock was diluted 100 times in TRIS to obtain the final concentration of 1.44 µg/µl.
10. 96-well plate was prepared for **Bradford test** and labeled as described below.

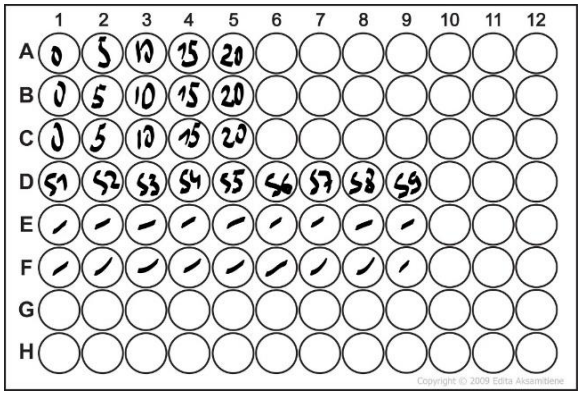

11. The Bradford solution was prepared by adding 2.5 ml of Bradford (from BioRad) to 10 ml of MilliQ water, and then it was kept on ice.
12. The mixture of either proteins or BSA in Bradford solution was added into the labeled wells. Note: before taking a solution with a pipette, each Eppendorf tube must be vortex briefly.

BSA (µl)	Bradford (µl)	Samples
0	200	10 µl of sample + 190 µl of Bradford solution
5	195	
10	190	
15	185	
20	180	

13. In order to calculate the protein concentration, the absorbance of each mixture was measured on a PlateReader Xenius (SAFAS, Monaco) at λ = 595 nm.

14. After protein quantification, samples were prepared for gel electrophoresis. Knowing the proteins concentration, the volume X can be calculated to have 30 µg of protein in each sample.

Protein (µl)	DTT (µl)	Laemmli 4X (µl)	Water (µl)
X	4	10	26-X

15. Samples were heated at 95°C for 5 min (heat shock) and were spin briefly after that. Now samples can be stored at -20°C.

Loading and running the gel

1. The plates were washed with a detergent, water, Milli-Q and Ethanol 70%.
2. A gel cassette was assembled and fixed in a holder. After adding water, the system was checked for a leakage.
3. 20 ml of **Resolving Gel 15%** was prepared following the protocol (see the composition below). First, MilliQ water was mixed with bis-acrylamide, TRIS and SDS. AMPS and TEMED were added at the end, because they catalyze a polymerization reaction.
4. Resolving Gel was loaded carefully into a cassette using a P1000 pipette, trying to avoid the formation of bubbles. After adding isopropanol (helps to remove bubbles) this cassette was left at room temperature for 10 min – the time for gel polymerization.
5. **Stacking Gel 4%** was prepared by mixing components listed below, following the same principle: AMPS and TEMED were added at the end.

Resolving Gel 15%		**Stacking Gel 4%**	
H_2O (milliQ)	3.55 ml	H_2O (milliQ)	5.1 ml
40% Acrylamide	3.75 ml	40% Acrylamide	0.8 ml
Tris 1.5 M pH 8.8	2.5 ml	Tris 0.5 M pH 6.8	2.0 ml
20% SDS	50 µl	20% SDS	40 µl
10% AMPS	100 µl	10% AMPS	40 µl
TEMED	10 µl	TEMED	10 µl

6. Isopropanol was removed and then Stacking Gel was loaded into a cassette. Combs were used to form the lanes for samples loading. Gel was left to polymerize at room temperature for 25 min.
7. **Migration Buffer 10x** was prepared by mixing TRIS (15.14 g), Glycine (72.06 g) and 20% SDS (25 ml) in MilliQ water to a final volume of 500 ml. Then this solution was diluted ten times in MilliQ to obtain Migration Buffer 1x.

8. Gel cassette was fixed in the system for gel electrophoresis. The system's components, Tank and Chamber, were washed before assembling.
9. Migration Buffer 1x was added into the Tank (between two chambers), and system was checked for a leakage.
10. Protein samples, that were already placed on ice for thawing, now were heated at 95°C for 3 min and spin briefly.
11. Samples (40 µl) were loaded on the gel along with Molecular Weight marker (6µl).
12. Tank, with a magnet stirrer at a bottom, was closed with a lid, the electrodes of a Power Source were connected to the system, and voltage was set to 150 V before launching the migration.
13. Ice was placed around the apparatus to avoid the degradation of gel and proteins. After 70-80 min the protein migration was completed, and the system was disassembled.

Transfer, immunolabeling and visualization

1. The following materials were prepared for the process of **Transfer:**
   a. **Transfer Buffer 10x** was prepared by mixing Tris (15.14 g) and Glycine (72.05 g) in MilliQ water to a final volume of 500 ml. The solution was diluted ten times by mixing 100 ml Transfer Buffer 10x with 700 ml MilliQ and 200 ml ethanol.
   b. the filter paper and blotting membrane
   c. new Cassette, new Tank and sponges were washed before assembling
2. Blotting membrane was activated by the absolute ethanol.
3. Cassette was assembled (sponge, 2 pieces of filter paper, gel, activated membrane, again 2 pieces of filter paper and a sponge were placed on the black side of a Cassette and covered with a white side) and fixed in a Tank. After adding the Transfer Buffer and ice packs into the Tank, the system was launched for the next 3 hours to transfer the proteins from gel to membrane.
4. After the transfer, membrane was blocked with the 3% blocking reagent (15-20 ml) by placing on rotor for 1 hour at room temperature.
5. Primary antibody diluted in the 3% blocking reagent (e.g. 3000 times for NC antibody) was added to the Falcon tube and was placed on a rotor at 4 °C for overnight incubation.
6. On the next day the membrane was washed 3 times with TBST (Tris-buffered saline with 0.1% of Tween 20) washing buffer (each time with fresh 10 ml buffer and placed on a rotor for 10 min).

7. Secondary antibody (anti-mouse HRP conjugate; W402B, Promega) diluted 10000 times in the 3% blocking reagent was added to the Falcon tube. Tube was placed on a rotor for 1 hour.
8. The membrane was washed with TBST buffer 3 times for 10 min each time.
9. After keeping in Clarity™ Western ECL Substrate (1705061, Bio-Rad) for 1 min, the digital images of a membrane were taken with a help of a camera system ImageQuant™ LAS 4000 (GE Healthcare).

Plasmid Amplification

Step I – Transformation

1. Agar plates were taken out form the fridge and left at room temperature.
2. Eppendorf tubes with bacteria (DH5α) were placed on ice for thawing (10-15 min).
3. Plasmid was diluted 10 times (9 µl of MilliQ water + 1 µl of plasmid), then 30 µl of bacteria was added into 10 µl of plasmid DNA and mixed by tapping gently the bottom of a tube.
4. Plasmid/ bacteria mixture was placed on ice for 30 min. During this time DNA covers bacteria.
5. Heat shock the mixture at 42°C for 45 s. Initiation of DNA uptake by bacteria.
6. Plasmid/ bacteria mixture was placed on ice for 5 min.
7. The tube with 500 µl of LB medium without antibiotic was left in the incubator at 37C for 1 h. Bacteria first grow in a good environment. Meanwhile, agar plates were placed in the incubator at 37°C as well.
8. Sterile glass beads were added to agar plates for streaking the bacteria over agar. Next, bacteria were spread over agar by shaking the plate with beads in different directions. 500 µl of bacteria suspension was split between two agar plates (100 µl and 400 µl). This gives the best chance of getting single colonies.
9. Beads were then removed from agar plates. Plates were placed upside-down in the incubator at 37°C for overnight.

STEP II – Pre-culture

1. Selection of the antibiotic to which plasmid is resistant (Ampicillin or Kanamycin)
2. 5-7 ml of LB medium was added into the 15 ml tube (close to the fire).
3. Then the selected antibiotic was added to LB medium. For example:
   Ampicillin 500X -> 6 ml (medium) -> 12 µl (antibiotic)
   Kanamycin 1000X -> 7 ml (medium) -> 7 µl (antibiotic)

4. One isolated colony (different colonies may have different DNA sequences) of bacteria was added to the small tube.
5. The tube was placed in the incubator at 37°C for 6-8 h.

STEP III – Maxi-culture

1. 200ml of LB medium with antibiotic was poured inside a conical flask.
2. Pre-culture from the small tube was mixed with LB medium that was just prepared in a conical flask and placed in the incubator at 37C overnight.

STEP IV – Plasmid DNA purification

NucleoBond® Xtra Midi Plus kit (Macherey-Nagel) was used for plasmid DNA purification. The purification was performed following the supplier's protocol for high-copy plasmids (http://www.mn-net.com). After purification, the concentration of each plasmid construct was measured on NanoDrop™ One/OneC (ThermoFisher).

Protein expression

Following the protocol from Supplementary Information to (McKinney et al., 2009) [113] for mEos2 protein expression in E. coli. plasmid was transformed into BL21(DE3)pLysS E. coli cells(Novagen) and cells plated on LB media agar (10 g/l Tryptone, 5 g/l Yeast Extract, 5 g/l NaCl, 10 g/l agar) supplemented with chloramphenicol (50 μg/ml) and ampicillin (100 μg/ml). A single colony was picked and grown to 0.6 OD_{600nm} in 400 ml LB growth media supplemented as above under shaking 200 rpm at 37°C. Cultures were then induced with 1mM IPTG and moved to room temperature for 24 hrs under constant shaking (200 rpm). Cells were collected by centrifugation at 3500 rpm for 30 min at 4°C and cell pellets harvested and flash frozen in liquid nitrogen before to be stored at -80°C.

Pellets were resuspended in buffer A (100mM sodium phosphate buffer pH 7.4, 500 mM NaCl) with 1mg/ml lysozyme (Sigma Aldrich) and incubated on ice for at least 30 min. The suspension was sonicated 7-8 times on ice for 10-15 sec with 30s on ice between each sonication. The supernatant was collected by centrifugation at 8000g for 10 minutes at 4°C. Aliquots of 200 μl were kept at -80°C. No further purification was necessary for our emission spectra measurements keeping in mind that other proteins or protein aggregates may affect the measurements of absorption spectra.

Steady-state fluorescence spectroscopy

After mEos2 overexpression, absorption spectrum of the protein solution was measured on Cary 4000 UV-Vis spectrophotometer (Agilent Technologies) in order to find protein's concentration. Knowing the extinction coefficient of mEos2 (56000 $M^{-1}cm^{-1}$) it is possible to calculate the concentration (C = 4.522 µM).

Fluorescence spectra were recorded in quartz cuvettes using Fluoromax 4 spectrofluorometer (Horiba Jobin Yvon) equipped with a thermostated cell compartment. In quartz cuvettes, the spectra were corrected for buffer fluorescence, lamp fluctuations and instrumental wavelength-dependent response of the detector. The particular excitation and emission wavelengths are mentioned below in the description of the different assays. In all cases the temperature was fixed at 20°C.

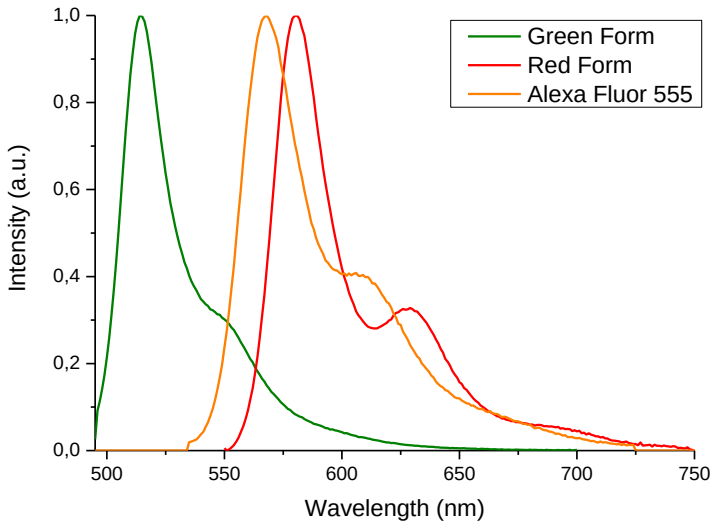

Figure 60. Normalized emission spectra of green and red form of mEos2 protein. The emission spectrum of Alexa Fluor 555 dye is presented in the same graph to demonstrate the similarity with the red form of mEos2 which result in the same chromatic aberration when imaged with Alexa Fluor 647.

Protein concentration 133 nM (30 µl of stock in 990 µl PBS 1x); green form: λ_{ex} = 485 nm, slits: 2 and 3 nm; red form: λ_{ex} = 540 nm, slits: 5 and 5 nm.

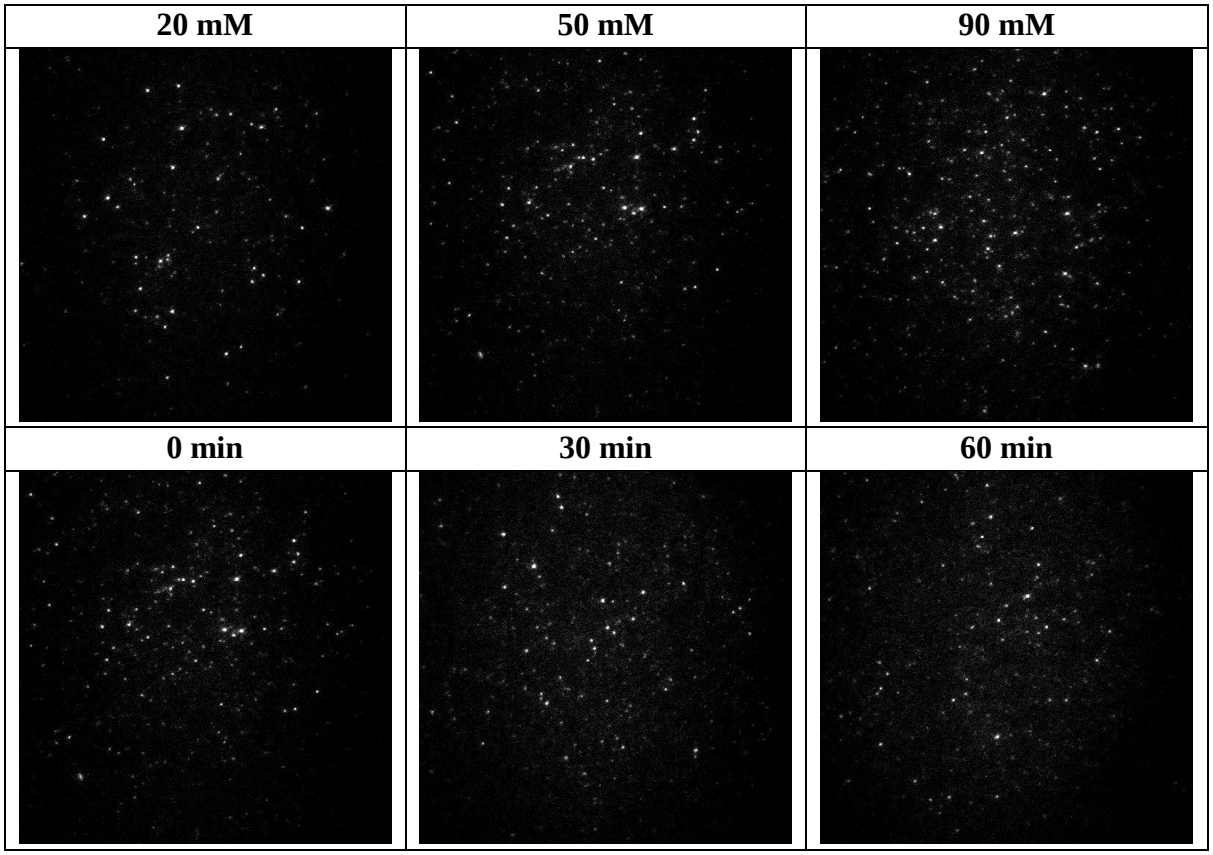

Figure 61. Single molecule behavior of mEos2 protein deposited on the surface of LabTek chamber. Three different concentrations were tested, as well time-dependent changes of photophysical properties. In later case three stacks were recorded immediately/ 30 min/ 60 min after adding dSTORM buffer at 50 mM concentration of MEA.

Sample with TetraSpek beads for PSF optimization

1. Fibronectin (stock of 1 mg/ml) was diluted under the hood in cold PBS 1x (or DPBS) to the final concentration of 5 µg/ml. Cold PBS is used to prevent the polymerization of the protein in a Falcon tube.
2. The stock of TetraSpek beads (T7279, Invitrogen) at the concentration of 1.8×10^{11}particles/ml was first diluted 100 times in MilliQ water and then again 100 times in Fibronectin solution.
3. Round cover-glasses (18 mm precision cover-glasses - Marienfeld, cat. no. 0117580) were placed in 12-well plate, washed once with 70% ethanol and trice with PBS 1x, and 1 ml of fibronectin solution with TetraSpek beads was added to each well.
4. After 2 hours of incubation at 37°C, sample were fixed in PFA 4% for 15 min, then washed trice with PBS 1x. Fluoromount G (0100-01, SouthernBiotech) was used to mount the cover-glasses on a microscope slide.
5. After overnight incubation at room temperature, cover-glasses were sealed on a microscope slide with a nail polish.

Beanshell script for raster scan

```
// Import required libraries

import java.io.*;
import org.micromanager.api.ScriptInterface;
import ij.process.*;
import ij.ImagePlus;
import ij.io.FileSaver;
import ij.IJ.*;

//parameters

stepSize = 1;           // ~2 µm
stepNmbre = (int)28/stepSize;
nbImagePerStep =1;      // number of images per position
waitTime=300;           // waitTime after the movement
pathname=ij.IJ.getDirectory("Choose a Directory");

int framenum = -1;
xStart = mmc.getXPosition("XYStage"); //read position X
yStart = mmc.getYPosition("XYStage"); //read position Y

x = xStart;
y = yStart;

displayImage = true;
ij.IJ.log("----------------------------------------");
ij.IJ.log("xStart = "+xStart +" , yStart = "+yStart);

print("------------------");
nbim = stepNmbre * stepNmbre;
ligne = -1;

mmc.setShutterOpen(false);

for (i=0; i<nbim; i++)
    {
        res = i % (stepNmbre);
        if(res==0) ligne++;
            x = xStart + (double)ligne * stepSize;

        if(ligne%2 == 0)
            {
                y = yStart + res * stepSize;
            }
        else
            {
                y = yStart + ((stepNmbre - 1) - res)* stepSize;
            }
        ij.IJ.log("i = "+ i + "  ligne = "+ ligne +"  xpos = "+ x + "  ypos = " + y);
        mmc.setXYPosition("XYStage", x, y);
        mmc.waitForSystem();
        mmc.setShutterOpen(true);
        mmc.sleep(waitTime);
        for (j=0; j<nbImagePerStep; j++)
            {
                // Snap a picture
                mmc.snapImage();
                Object img = mmc.getImage();
                // Process it
                ImageProcessor processor =
                new ShortProcessor((int) mmc.getImageWidth(), (int) mmc.getImageHeight());
                processor.setPixels(img);
                ImagePlus Imp = new ImagePlus("", processor);
                // Display it
                if(displayImage)
                    {
                        gui.displayImage(img);
                    }
                // Save the picture
                FileSaver Fs = new FileSaver(Imp);
                framenum ++;

                String Path = pathname +framenum+".tif";
                Fs.saveAsTiff(Path);
            }
    }
```

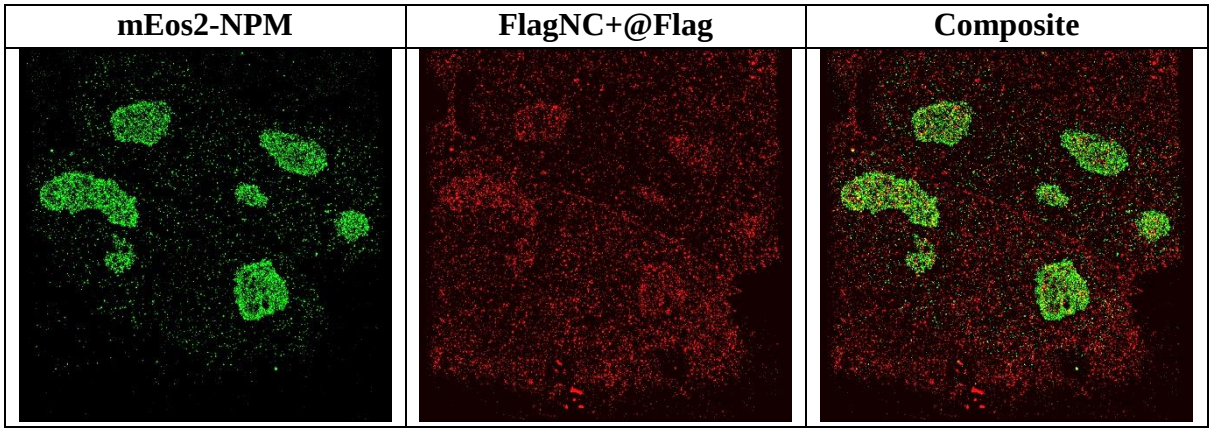

Figure 62. Two-color super-resolution imaging of Flag-NC immunostained with A647 and NPM fused to fluorescent protein mEos2.

Laser power loses

Table 4. Measured laser power loses along the excitation path (AOTF, lenses - reflections on the air-glass interface)

Laser (nm)	Before AOTF	After AOTF	Sample plane	Transmission
405	29.8 mW	20.6 mW	5.7 mW	19%
488	90.2 mW	60.7 mW	44.4 mW	49%
561	81.1 mW	73.4 mW	53.9 mW	67%
642	87.5 mW	71.3 mW	50.7 mW	58%

List of abbreviations

A555 or 647	Alexa Fluor 555 or 647
Ab	Antibody
AIDS	Acquired immunodeficiency syndrome
ALIX	ALG2-interacting protein X
AOTF	Acousto-optical tunable filter
ART	Antiretroviral therapy
ATP	Adenosine triphosphate
Au NPs	Gold nanoparticles
BME	β-mercaptoethanol
BP	Biplane
BSA	Bovine serum albumin
CA	Capsid protein
CCD	Charge-coupled device
CCPs	Clathrin-coated pits
CCR5	β-chemokine receptor type 5
co-IP	Co-immunoprecipitation
COT	Cyclooctatetraene
CXCR4	α-chemokine receptor type 4
Cy (e.g. Cy5)	Cyanine dye
DAPI	4',6-diamidino-2-phenylindole
DFC	Dense fibrillar component
DH	Double-helix
DIC	Differential interference contrast microscopy
DIS	Dimer initiation signal
DMEM	Dulbecco modified eagle medium
DNA	Deoxyribonucleic acid
ds	Double-stranded (about DNA and RNA)
dSTORM	Direct stochastic optical reconstruction microscopy
DTT	Dithiothreitol
eGFP	Enhanced green fluorescent protein
EM	Electron microscopy
EMCCD	Electron multiplying CCD
Env	Envelope protein
ESCRT	Endosomal sorting complex required for transport
FCs	Fibrillar centers
FCS	Fluorescence correlation spectroscopy
Fib	Fibrillarin
FITC	Fluorescein isothiocyanate
FLIM	Fluorescence-lifetime imaging microscopy
FOV	Field of view
FP	Fluorescent protein

FPALM	Fluorescence photoactivable localization microscopy
fps	Frames per second
FRC	Fourier rings correlation
FRET	Forster resonance energy transfer
FWHM	Full width at half maximum
Gag	Group specific antigen
GC	Granular component
GFP	Green fluorescent protein
GLOX	Oxygen scavenging system; composition: 0.5 mg/ml glucose oxidase, 40 µg/ml catalase and 10% w/v glucose
gp	Glycoprotein
gRNA	Genomic RNA
GSD	Ground state depletion
HILO	Highly inclined and laminated optical sheet microscopy
HIV	Human immunodeficiency virus
HRP	Horseradish peroxidase
Ig	Immunoglobulin
IN	Integrase
iPALM	Interferometric photoactivable localization microscopy
ISC	Intersystem crossing
LED	Light emitting diode
MA	Matrix protein
MEA	β-mercaptoethylamine
mRNA	Messenger RNA
MSD	Mean square displacement
MW	Molecular weight
NA	Numerical aperture
NC, NCp7	Nucleocapsid protein
Nef	Negative regulatory factor
NES	Nuclear export signal
NLS	Nuclear localization signal
NoL12	Nucleolar protein 12
NoLS	Nucleolar localization signal
NPM	Nucleophosmin
NSOM	Near-field scanning optical microscopy
OD	Optical density
ORF	Open reading frame
OTF	Optical transfer function
PA	Photoactivable
PALM	Photoactivable localization microscopy
PBMC	Peripheral blood mononuclear cell
PBS	Primer-binding site
PBS	Phosphate-buffered saline

PCR	Polymerase chain reaction
PEDV	Porcine epidemic diarrhea virus
PFA	Paraformaldehyde
PIC	Pre-integration complex
PM	Plasma membrane
PR	Protease
PS	Photoswitchable
PSF	Point spread function
QD	Quantum dot
rDNA	Ribosomal DNA
RESOLFT	Reversible saturable optical linear fluorescence transitions
Rev	Regulator of virion expression
Rh	Rhodamine dye
RNA	Ribonucleic acid
RNase	Ribonuclease
ROI	Region of interest
RP	Ribosomal protein
RPA	Replication protein A
RRE	Rev-response element
rRNA	Ribosomal RNA
RT	Reverse transcriptase
RTC	Reverse transcription complex
SD	Splice donor
SDS	Sodium dodecyl sulfate
SIM	Structured illumination microscopy
SIV	Simian immunodeficiency virus
SL	Stem-loop
SMLM	Single molecule localization microscopy
snoRNP	Small nucleolar ribonucleoprotein
SOFI	Super-resolution optical fluctuation imaging
SPT	Single particle tracking
ss	Single-stranded (about DNA and RNA)
Std	Standard deviation
STED	Stimulated emission depletion microscopy
STORM	Stochastic optical reconstruction microscopy
SU, gp120	Surface glycoprotein
TAR	Transactivation response element
Tat	Trans-activator of transcription
TBST	Tris-buffered saline with 0.1% Tween 20
td	Tandem dimer (about EosFP)
TEM	Transmitted electron microscopy
TIRF	Total internal reflection fluorescence microscopy
TM, gp41	Transmembrane glycoprotein

tRNA	Transfer RNA
TSG	Tumor susceptibility gene
UNAIDS	Joint United Nations Programme on HIV/AIDS
UTR	Untranslated region
Vif	Viral infectivity factor
VLP	Virus-like particle
Vpr	Viral protein R
Vpu	Viral protein U
vRNA	Viral RNA
YFP	Yellow fluorescent protein
ZFs	Zinc fingers

References

1. Barré-Sinoussi, F. *et al.* Isolation of a T-Lymphotropic Retrovirus from a Patient at Risk for Acquired Immune Deficiency Syndrome (AIDS). *Science (80-.).* **220,** 868–871 (1983).

2. Swanstrom, R. & Coffin, J. HIV-1 pathogenesis: The virus. *Cold Spring Harb. Perspect. Med.* **2,** (2012).

3. Stevenson, M. HIV-1 pathogenesis. *Nat. Med.* **9,** 853–860 (2003).

4. Barré-Sinoussi, F., Ross, A. L. & Delfraissy, J.-F. Past, present and future: 30 years of HIV research. *Nat. Rev. Microbiol.* **11,** 877–883 (2013).

5. Sharp, P. M. & Hahn, B. H. Origins of HIV and the AIDS Pandemic. 1–22 (2011). doi:10.1101/cshperspect.a006841

6. Gao, F. *et al.* Origin of HIV-1 in the chimpanzee Pan troglodytes troglodytes. *Nature* **397,** 436–441 (1999).

7. Keele, B. F. *et al.* Chimpanzee Reservoirs of Pandemic and Nonpandemic HIV-1 Chimpanzee Reservoirs of Pandemic and Nonpandemic HIV-1 Chimpanzee Reservoirs of Pandemic and Nonpandemic HIV-1. *Science (80-.).* **523,** 1–8 (2006).

8. Hirsch, V. M., Olmsted, R. A., Murphey-Corb, M., Purcell, R. H. & Johnson, P. R. An African primate lentivirus (SIVsmclosely related to HIV-2). *Nature* **339,** 389–392 (1989).

9. Gao, F. *et al.* Human infection by genetically diverse SIVSM-related HIV-2 in West Africa. *Nature* **358,** 495–499 (1992).

10. Faria, N. R. *et al.* The early spread and epidemic ignition of HIV-1 in human populations. *Science (80-.).* **346,** 56–61 (2014).

11. UNAIDS. Data 2017. *Jt. United Nations Program. HIV/AIDS* 1–248 (2017). doi:978-92-9173-945-5

12. Arts, E. J. & Hazuda, D. J. HIV-1 antiretroviral drug therapy. *Cold Spring Harb. Perspect. Med.* **2,** a007161 (2012).

13. UNAIDS. Ending AIDS: Progress Towards the 90-90-90 Targets. 6–21 (2017).

14. Tang, M. W. & Shafer, R. W. HIV-1 antiretroviral resistance: Scientific principles and clinical applications. *Drugs* **72,** 1–25 (2012).

15. Clutter, D. S., Jordan, M. R., Bertagnolio, S. & Shafer, R. W. HIV-1 drug resistance and resistance testing. *Infect. Genet. Evol.* **46,** 292–307 (2016).

16. Buzon, M. J. *et al.* HIV-1 persistence in CD4+ T cells with stem cell–like properties. *Nat. Med.* **20,** 139–142 (2014).

17. Chomont, N. *et al.* HIV reservoir size and persistence are driven by T cell survival and homeostatic proliferation. *Nat. Med.* **15,** 893–900 (2009).

18. Frankel, A. D. & Young, J. A. T. HIV-1: Fifteen Proteins and an RNA. *Annu. Rev. Biochem.* **67,** 1–25 (1998).

19. Sundquist, W. I. & Kräusslich, H. G. HIV-1 assembly, budding, and maturation. *Cold Spring Harb. Perspect. Med.* **2,** (2012).

20. Freed, E. O. HIV-1 Gag Proteins: Diverse Functions in the Virus Life Cycle. *Virology* **251,** 1–15 (1998).

21. Freed, E. O. HIV-1 assembly, release and maturation. *Nat. Rev. Microbiol.* **13,** 484–496 (2015).

22. Lu, K., Heng, X. & Summers, M. F. Structural determinants and mechanism of HIV-1 genome packaging. *J. Mol. Biol.* **410,** 609–633 (2011).

23. Bernacchi, S. *et al.* HIV-1 Pr55Gag binds genomic and spliced RNAs with different affinity and stoichiometry. *RNA Biol.* **14,** 90–103 (2017).

24. Mailler, E. *et al.* The life-cycle of the HIV-1 gag–RNA complex. *Viruses* **8,** 1–19 (2016).

25. Luciw, P. A. Human immunodeficiency viruses and their replication. in *Fields virology* 845–916 (Raven Press, 1996).

26. Wilen, C. B. *et al.* HIV : Cell Binding and Entry. *Cold Spring Harb. Perspect. Med.* **2,** 1–14 (2012).

27. Turner, B. G. & Summers, M. F. Structural biology of HIV. *J. Mol. Biol.* **285,** 1–32 (1999).

28. Robinson, H. L. Vaccines: New Hope for an Aids Vaccine. *Nat. Rev. Immunol.* **2,** 239–250 (2002).

29. Campbell, E. M. & Hope, T. J. HIV-1 capsid: The multifaceted key player in HIV-1 infection. *Nat. Rev. Microbiol.* **13,** 471–483 (2015).

30. Pornillos, O., Ganser-Pornillos, B. K. & Yeager, M. Atomic-level modelling of the HIV capsid. *Nature* **469,** 424–427 (2011).

31. Alfadhli, A. & Barklis, E. The roles of lipids and nucleic acids in HIV-1 assembly. *Front. Microbiol.* **5,** 1–11 (2014).

32. Tedbury, P. R., Novikova, M., Ablan, S. D. & Freed, E. O. Biochemical evidence of a role for matrix trimerization in HIV-1 envelope glycoprotein incorporation. *Proc. Natl. Acad. Sci.* **113,** E182–E190 (2016).

33. Darlix, J. L., de Rocquigny, H., Mauffret, O. & Mély, Y. Retrospective on the all-in-one retroviral nucleocapsid protein. *Virus Res.* **193,** 2–15 (2014).

34. Levin, J. G., Mitra, M., Mascarenhas, A. & Musier-Forsyth, K. Role of HIV-1 nucleocapsid protein in HIV-1 reverse transcription. *RNA Biol.* **7,** 754–774 (2010).

35. Wu, H. *et al.* Aromatic residue mutations reveal direct correlation between HIV-1 nucleocapsid protein's nucleic acid chaperone activity and retroviral replication. *Virus Res.* **171,** 263–277 (2013).

36. Kafaie, J., Song, R., Abrahamyan, L., Mouland, A. J. & Laughrea, M. Mapping of nucleocapsid residues important for HIV-1 genomic RNA dimerization and packaging. *Virology* **375,** 592–610 (2008).

37. Thomas, J. A. & Gorelick, R. J. Nucleocapsid protein function in early infection processes. *Virus Res.* **134,** 39–63 (2008).

38. Darlix, J. L. *et al.* Flexible nature and specific functions of the HIV-1 nucleocapsid protein. *J. Mol. Biol.* **410,** 565–581 (2011).

39. Zhang, J. & Crumpacker, C. S. Human Immunodeficiency Virus Type 1 Nucleocapsid Protein Nuclear Localization Mediates Early Viral mRNA Expression. *Society* **76,** 10444–10454 (2002).

40. Hong, H. W., Lee, S. W. & Myung, H. Induced degradation of tat by nucleocapsid (NC) via the proteasome pathway and its effect on HIV transcription. *Viruses* **5,** 1143–1152 (2013).

41. Cimarelli, A. & Darlix, J. L. HIV-1 reverse transcription. *Methods Mol. Biol.* **1087,** 55–70 (2014).

42. Craigie, R. & Bushman, F. D. HIV DNA integration. *Cold Spring Harb. Perspect. Med.* **2,** a006890 (2012).

43. Checkley, M. A., Luttge, B. G. & Freed, E. O. HIV-1 envelope glycoprotein biosynthesis, trafficking, and incorporation. *J. Mol. Biol.* **410,** 582–608 (2011).

44. Jeang, K. T., Xiao, H. & Rich, E. A. Multifaceted activities of the HIV-1 transactivator of transcription, Tat. *J. Biol. Chem.* **274,** 28837–28840 (1999).

45. Pollard, V. W. & Malim, M. H. The Hiv-1 Rev Protein. *Annu. Rev. Microbiol.* **52,** 491–532 (1998).

46. Sleiman, D. *et al.* Characterization of RNA binding and chaperoning activities of HIV-1 Vif protein Importance of the C-terminal unstructured tail. *RNA Biol.* **11,** 906–920 (2014).

47. Guenzel, C. A., Hérate, C. & Benichou, S. HIV-1 Vpr-a still "enigmatic multitasker." *Front. Microbiol.* **5,** 1–13 (2014).

48. González, M. E. Vpu protein: The viroporin encoded by HIV-1. *Viruses* **7,** 4352–4368 (2015).

49. Kestier, H. W. *et al.* Importance of the nef gene for maintenance of high virus loads and for development of AIDS. *Cell* **65,** 651–662 (1991).

50. Lama, J., Mangasarian, A. & Trono, D. Cell-surface expression of CD4 reduces HIV-1 infectivity by blocking Env incorporation in a Nef- and Vpu-inhibitable manner. *Curr. Biol.* **9,** 622–631 (1999).

51. Argañaraz, E. R., Schindler, M., Kirchhoff, F., Cortes, M. J. & Lama, J. Enhanced CD4 Down-modulation by Late Stage HIV-1 nef Alleles Is Associated with Increased Env Incorporation and Viral Replication. *J. Biol. Chem.* **278,** 33912–33919 (2003).

52. Isel, C. *et al.* Specific initiation and switch to elongation of human immunodeficiency virus type 1 reverse transcription require the post-transcriptional modifications of primer tRNA3Lys. *EMBO J.* **15,** 917–24 (1996).

53. Lanchy, J. M. *et al.* Contacts between reverse transcriptase and the primer strand govern the transition from initiation to elongation of HIV-1 reverse transcription. *J. Biol. Chem.* **273,** 24425–24432 (1998).

54. Balvay, L., Lastra, M. L., Sargueil, B., Darlix, J. L. & Ohlmann, T. Translational control of retroviruses. *Nat. Rev. Microbiol.* **5,** 128–140 (2007).

55. Karn, J. & Stoltzfus, C. M. Transcriptional and posttranscriptional regulation of HIV-1 gene expression. *Cold Spring Harb. Perspect. Med.* **2,** a006916 (2012).

56. D'Souza, V. & Summers, M. F. How retroviruses select their genomes. *Nat. Rev. Microbiol.* **3,** 643–655 (2005).

57. Ganser-Pornillos, B. K., Yeager, M. & Sundquist, W. I. The structural biology of HIV assembly. *Curr. Opin. Struct. Biol.* **18,** 203–217 (2008).

58. Briggs, J. A. G. *et al.* Structure and assembly of immature HIV. *Proc. Natl. Acad. Sci.* **106,** 11090–11095 (2009).

59. Goodsell, D. S. Illustrating the machinery of life: Viruses. *Biochem. Mol. Biol. Educ.* **40,** 291–296 (2012).

60. Mori, M. *et al.* Nucleocapsid protein: A desirable target for future therapies against HIV-1. *Curr. Top. Microbiol. Immunol.* **389,** 53–92 (2015).

61. Thomas, J. A. *et al.* Human immunodeficiency virus type 1 nucleocapsid zinc-finger mutations cause defects in reverse transcription and integration. *Virology* **353,** 41–51 (2006).

62. Buckman, J. S., Bosche, W. J. & Gorelick, R. J. Human immunodeficiency virus type 1 nucleocapsid zn(2+) fingers are required for efficient reverse transcription, initial integration processes, and protection of newly synthesized viral DNA. *J. Virol.* **77,** 1469–80 (2003).

63. Lyonnais, S. *et al.* A protein ballet around the viral genome orchestrated by HIV-1 reverse transcriptase leads to an architectural switch: From nucleocapsid-condensed RNA to Vpr-bridged DNA. *Virus Res.* **171,** 287–303 (2012).

64. Mirambeau, G. *et al.* HIV-1 protease and reverse transcriptase control the architecture of their nucleocapsid partner. *PLoS One* **2,** e669 (2007).

65. Gallay, P., Swingler, S., Song, J., Bushman, F. & Trono, D. HIV nuclear import is governed by the phosphotyrosine-mediated binding of matrix to the core domain of integrase. *Cell* **83,** 569–576 (1995).

66. Anton, H. *et al.* Investigating the cellular distribution and interactions of HIV-1 nucleocapsid protein by quantitative fluorescence microscopy. *PLoS One* **10,** 1–23 (2015).

67. Yu, K. L., Lee, S. H., Lee, E. S. & You, J. C. HIV-1 nucleocapsid protein localizes efficiently to the nucleus and nucleolus. *Virology* **492,** 204–212 (2016).

68. Lochmann, T. L. *et al.* NC-Mediated Nucleolar Localization of Retroviral Gag Proteins. *Virus Res.* **171,** 304–318 (2013).

69. Godet, J. *et al.* Comparative nucleic acid chaperone properties of the nucleocapsid protein NCp7 and Tat protein of HIV-1. *Virus Res.* **169,** 349–360 (2012).

70. Hernandez-Verdun, D. Nucleolus: From structure to dynamics. *Histochem. Cell Biol.* **125,** 127–137 (2006).

71. Olson, M. O. J. *The Nucleolus*. *Springer, Protein Reviews* (2011).

72. Raška, I., Shaw, P. J. & Cmarko, D. Structure and function of the nucleolus in the

spotlight. *Curr. Opin. Cell Biol.* **18,** 325–334 (2006).

73. Colau, G., Thiry, M., Leduc, V., Bordonné, R. & Lafontaine, D. L. J. The small nucle(ol)ar RNA cap trimethyltransferase is required for ribosome synthesis and intact nucleolar morphology. *Mol. Cell. Biol.* **24,** 7976–86 (2004).

74. Olson, M. O. J. & Dundr, M. The moving parts of the nucleolus. *Histochem. Cell Biol.* **123,** 203–216 (2005).

75. Visintin, R. & Amon, A. The nucleolus: the magician's hat for cell cycle tricks. *Curr. Opin. Cell Biol.* **12,** 372–377 (2000).

76. Emmott, E. *et al.* Viral nucleolar localisation signals determine dynamic trafficking within the nucleolus. *Virology* **380,** 191–202 (2008).

77. Salvetti, A. & Greco, A. Viruses and the nucleolus: The fatal attraction. *Biochim. Biophys. Acta - Mol. Basis Dis.* **1842,** 840–847 (2014).

78. Hiscox, J. A. RNA viruses: hijacking the dynamic nucleolus. *Nat. Rev. Microbiol.* **5,** 119–127 (2007).

79. Boisvert, F.-M., van Koningsbruggen, S., Navascués, J. & Lamond, A. I. The multifunctional nucleolus. *Nat. Rev. Mol. Cell Biol.* **8,** 574–585 (2007).

80. Puvion-Dutilleul, F. & Christensen, M. E. Alterations of fibrillarin distribution and nucleolar ultrastructure induced by adenovirus infection. *Eur. J. Cell Biol.* **61,** 168–176 (1993).

81. Matthews, D. Adenovirus protein V induces redistribution of nucleolin and B23 from nucleolus to cytoplasm. *J. Virol.* **75,** 1031–1038 (2001).

82. Hiscox, J. a *et al.* The Coronavirus Infectious Bronchitis Virus Nucleoprotein Localizes to the Nucleolus. *J. Virol.* **75,** 506–512 (2001).

83. Wurm, T. *et al.* Localization to the nucleolus is a common feature of coronavirus nucleoproteins, and the protein may disrupt host cell division. *J. Virol.* **75,** 9345–9356 (2001).

84. Hiscox, J. A. The nucleolus - A gateway to viral infection? *Arch. Virol.* **147,** 1077–1089 (2002).

85. Miyazaki, Y., Nosaka, T. & Hatanaka, M. The post-transcriptional regulator Rev of HIV: Implications for its interaction with the nucleolar protein B23. *Biochimie* **78,** 1081–1086 (1996).

86. Yoo, D., Wootton, S. K., Li, G., Song, C. & Rowland, R. R. Colocalization and interaction of the porcine arterivirus nucleocapsid protein with the small nucleolar RNA-associated protein fibrillarin. *J. Virol.* **77,** 12173–12183 (2003).

87. Daelemans, D. *et al.* In vivo HIV-1 Rev multimerization in the nucleolus and cytoplasm identified by fluorescence resonance energy transfer. *J. Biol. Chem.* **279,** 50167–50175 (2004).

88. Fankhauser, C., Izaurralde, E., Adachi, Y., Wingfield, P. & Laemmli, U. K. Specific complex of human immunodeficiency virus type 1 rev and nucleolar B23 proteins: dissociation by the Rev response element. *Mol. Cell. Biol.* **11,** 2567–75 (1991).

89. Michienzi, A., Cagnon, L., Bahner, I. & Rossi, J. J. Ribozyme-mediated inhibition of HIV 1 suggests nucleolar trafficking of HIV-1 RNA. *Proc. Natl. Acad. Sci. U. S. A.* **97,** 8955–60 (2000).

90. Pohl, D. W., Denk, W. & Lanz, M. Optical stethoscopy: Image recording with resolution λ/20. *Appl. Phys. Lett.* **44,** 651–653 (1984).

91. Lewis, A., Isaacson, M., Harootunian, A. & Muray, A. Development of a 500 Å spatial resolution light microscope. *Ultramicroscopy* **13,** 227–231 (1984).

92. Dürig, U., Pohl, D. W. & Rohner, F. Near-field optical-scanning microscopy. *J. Appl. Phys.* **59,** 3318–3327 (1986).

93. *Springer Handbook of Lasers and Optics*. (2012). doi:10.1007/978-3-642-19409-2

94. Hell, S. & Stelzer, E. H. K. Properties of a 4Pi confocal fluorescence microscope. *J. Opt. Soc. Am. A* **9,** 2159 (1992).

95. Hanninen, P. E., Hell, S. W., Salo, J., Soini, E. & Cremer, C. Two-photon excitation 4Pi confocal microscope: enhanced axial resolution microscope for biological research. *Appl. Phys. Lett.* **66,** 1698–1700 (1995).

96. Malik, T., Chauhan, G., Rath, G., Murthy, R. S. R. & Goyal, A. K. "Fusion and binding inhibition" key target for HIV-1 treatment and pre-exposure prophylaxis: Targets, drug delivery and nanotechnology approaches. *Drug Deliv.* **24,** 608–621 (2017).

97. Hell, S. W. & Wichmann, J. Breaking the diffraction resolution limit by stimulated emission: stimulated-emission-depletion fluorescence microscopy. *Opt. Lett.* **19,** 780 (1994).

98. Donnert, G. *et al.* Macromolecular-scale resolution in biological fluorescence microscopy. *Proc. Natl. Acad. Sci.* **103,** 11440–11445 (2006).

99. Hell, S. W. & Kroug, M. Ground-state-depletion fluorscence microscopy: A concept for breaking the diffraction resolution limit. *Appl. Phys. B Lasers Opt.* **60,** 495–497 (1995).

100. Bretschneider, S., Eggeling, C. & Hell, S. W. Breaking the Diffraction Barrier in Fluorescence Microscopy by Optical Shelving. *Phys. Rev. Lett.* **98,** 218103 (2007).

101. Hell, S. W. Far-field optical nanoscopy. *2010 23rd Annu. Meet. IEEE Photonics Soc. PHOTINICS 2010* **316,** 3–4 (2010).

102. Gustafsson, M. G. L. Surpassing the lateral resolution limit by a factor of two using structured illumination microscopy. *J. Microsc.* **198,** 82–87 (2000).

103. Frohn, J. T., Knapp, H. F. & Stemmer, A. True optical resolution beyond the Rayleigh limit achieved by standing wave illumination. *Proc. Natl. Acad. Sci.* **97,** 7232–7236 (2000).

104. Schermelleh, L., Heintzmann, R. & Leonhardt, H. A guide to super-resolution fluorescence microscopy. *J. Cell Biol.* **190,** 165–175 (2010).

105. Kner, P., Chhun, B. B., Griffis, E. R., Winoto, L. & Gustafsson, M. G. L. Super-resolution video microscopy of live cells by structured illumination. *Nat. Methods* **6,** 339–342 (2009).

106. Hirvonen, L. M., Wicker, K., Mandula, O. & Heintzmann, R. Structured illumination

microscopy of a living cell. *Eur. Biophys. J.* **38,** 807–812 (2009).

107. Gustafsson, M. G. L. Nonlinear structured-illumination microscopy: Wide-field fluorescence imaging with theoretically unlimited resolution. *Proc. Natl. Acad. Sci.* **102,** 13081–13086 (2005).

108. Thompson, R. E., Larson, D. R. & Webb, W. W. Precise nanometer localization analysis for individual fluorescent probes. *Biophys. J.* **82,** 2775–2783 (2002).

109. Nieuwenhuizen, R. P. J. *et al.* Measuring image resolution in optical nanoscopy. *Nat. Methods* **10,** 557–562 (2013).

110. Nyquist, H. Certain topics in telegraph transmission theory. *IEEE Proc.* **90,** 617–644 (1928).

111. Gould, T. J., Verkhusha, V. V & Hess, S. T. Imaging biological structures with fluorescence photoactivation localization microscopy. *Nat. Protoc.* **4,** 291–308 (2009).

112. Lukyanov, K. A., Chudakov, D. M., Lukyanov, S. & Verkhusha, V. V. Innovation: Photoactivatable fluorescent proteins. *Nat. Rev. Mol. Cell Biol.* **6,** 885–890 (2005).

113. McKinney, S. A., Murphy, C. S., Hazelwood, K. L., Davidson, M. W. & Looger, L. L. A bright and photostable photoconvertible fluorescent protein. *Nat. Methods* **6,** 131–133 (2009).

114. Heilemann, M., Van De Linde, S., Mukherjee, A. & Sauer, M. Super-resolution imaging with small organic fluorophores. *Angew. Chemie - Int. Ed.* **48,** 6903–6908 (2009).

115. Van De Linde, S., Kasper, R., Heilemann, M. & Sauer, M. Photoswitching microscopy with standard fluorophores. *Appl. Phys. B Lasers Opt.* **93,** 725–731 (2008).

116. Heilemann, M. *et al.* Subdiffraction-resolution fluorescence imaging with conventional fluorescent probes. *Angew. Chemie - Int. Ed.* **47,** 6172–6176 (2008).

117. Van de Linde, S. *et al.* Photoinduced formation of reversible dye radicals and their impact on super-resolution imaging. *Photochem. Photobiol. Sci.* **10,** 499–506 (2011).

118. Olivier, N., Keller, D., Gönczy, P. & Manley, S. Resolution Doubling in 3D-STORM Imaging through Improved Buffers. *PLoS One* **8,** 1–9 (2013).

119. Doose, S., Neuweiler, H. & Sauer, M. Fluorescence quenching by photoinduced electron transfer: A reporter for conformational dynamics of macromolecules. *ChemPhysChem* **10,** 1389–1398 (2009).

120. Zheng, Q. *et al.* On the mechanisms of cyanine fluorophore photostabilization. *J. Phys. Chem. Lett.* **3,** 2200–2203 (2012).

121. Cordes, T., Vogelsang, J. & Tinnefeld, P. On the mechanism of trolox as antiblinking and antibleaching reagent. *J. Am. Chem. Soc.* **131,** 5018–5019 (2009).

122. Cordes, T., Maiser, A., Steinhauer, C., Schermelleh, L. & Tinnefeld, P. Mechanisms and advancement of antifading agents for fluorescence microscopy and single-molecule spectroscopy. *Phys. Chem. Chem. Phys.* **13,** 6699 (2011).

123. Olivier, N., Keller, D., Rajan, V. S., Gönczy, P. & Manley, S. Simple buffers for 3D STORM microscopy. *Biomed. Opt. Express* **4,** 885 (2013).

124. Shi, X., Lim, J. & Ha, T. Acidification of the oxygen scavenging system in single-

molecule fluorescence studies: In situ sensing with a ratiometric dual-emission probe. *Anal. Chem.* **82,** 6132–6138 (2010).

125. Vogelsang, J., Cordes, T. & Tinnefeld, P. Single-molecule photophysics of oxazines on DNA and its application in a FRET switch. *Photochem. Photobiol. Sci.* **8,** 486–496 (2009).

126. Dertinger, T., Colyer, R., Iyer, G., Weiss, S. & Enderlein, J. Fast, background-free, 3D super-resolution optical fluctuation imaging (SOFI). *Proc. Natl. Acad. Sci.* **106,** 22287–22292 (2009).

127. Geissbuehler, S., Dellagiacoma, C. & Lasser, T. Comparison between SOFI and STORM. *Biomed. Opt. Express* **2,** 408 (2011).

128. Geissbuehler, S. *et al.* Mapping molecular statistics with balanced super-resolution optical fluctuation imaging (bSOFI). *Opt. Nanoscopy* **1,** 1–7 (2012).

129. Dertinger, T. *et al.* Advances in superresolution optical fluctuation imaging (SOFI). *Q. Rev. Biophys.* **46,** 210–221 (2013).

130. Dertinger, T., Colyer, R., Vogel, R., Enderlein, J. & Weiss, S. Achieving increased resolution and more pixels with Superresolution Optical Fluctuation Imaging (SOFI). *Opt. Express* **18,** 18875 (2010).

131. Dedecker, P., Mo, G. C. H., Dertinger, T. & Zhang, J. Widely accessible method for superresolution fluorescence imaging of living systems. *Proc. Natl. Acad. Sci.* **109,** 10909–10914 (2012).

132. Betzig, E. *et al.* Imaging Intracellular Fluorescent Proteins at Nanometer Resolution. *Science (80-.).* **313,** 1642–1645 (2006).

133. Bates, M., Huang, B., Dempsey, G. T. & Zhuang, X. Multicolor Super-Resolution Imaging with Photo-Switchable Fluorescent Probes. *Science (80-.).* **317,** 1749–1753 (2007).

134. Bates, M., Blosser, T. R. & Zhuang, X. Short-range spectroscopic ruler based on a single-molecule optical switch. *Phys. Rev. Lett.* **94,** 1–4 (2005).

135. Rust, M. J., Bates, M. & Zhuang, X. Stochastic optical reconstruction miscroscopy (STORM) provides sub-diffraction-limit image resolution. *Nat. Methods* **3,** 793–795 (2006).

136. Nahidiazar, L., Agronskaia, A. V., Broertjes, J., Van Broek, B. Den & Jalink, K. Optimizing imaging conditions for demanding multi-color super resolution localization microscopy. *PLoS One* **11,** 1–18 (2016).

137. Dempsey, G. T., Vaughan, J. C., Chen, K. H., Bates, M. & Zhuang, X. Evaluation of fluorophores for optimal performance in localization-based super-resolution imaging - Supplementary. *Nat. Methods* **8,** 1027–1036 (2011).

138. Tam, J., Cordier, G. A., Borbely, J. S., Álvarez, Á. S. & Lakadamyali, M. Cross-talk-free multi-color storm imaging using a single fluorophore. *PLoS One* **9,** e101772 (2014).

139. Shroff, H. *et al.* Dual-color superresolution imaging of genetically expressed probes within individual adhesion complexes. *Proc. Natl. Acad. Sci.* **104,** 20308–20313 (2007).

140. Rosenbloom, A. B. *et al.* Optimized two-color super resolution imaging of Drp1 during

mitochondrial fission with a slow-switching Dronpa variant. *Proc. Natl. Acad. Sci.* **111,** 13093–13098 (2014).

141. Andresen, M. *et al.* Photoswitchable fluorescent proteins enable monochromatic multilabel imaging and dual color fluorescence nanoscopy. *Nat. Biotechnol.* **26,** 1035–1040 (2008).

142. Subach, F. V *et al.* Erratum: Photoactivatable mCherry for high-resolution two-color fluorescence microscopy. *Nat. Methods* **6,** 311–311 (2009).

143. Chang, H. *et al.* A unique series of reversibly switchable fluorescent proteins with beneficial properties for various applications. *Proc. Natl. Acad. Sci.* **109,** 4455–4460 (2012).

144. Annibale, P., Scarselli, M., Greco, M. & Radenovic, A. Identification of the factors affecting co-localization precision for quantitative multicolor localization microscopy. *Opt. Nanoscopy* **1,** 9 (2012).

145. Brodehl, A. *et al.* Dual color photoactivation localization microscopy of cardiomyopathy- associated desmin mutants. *J. Biol. Chem.* **287,** 16047–16057 (2012).

146. Chudakov, D. M., Lukyanov, S. & Lukyanov, K. A. Tracking intracellular protein movements using photoswitchable fluorescent proteins PS-CFP2 and Dendra2. *Nat. Protoc.* **2,** 2024–2032 (2007).

147. Geisler, C. *et al.* Resolution of λ/10 in fluorescence microscopy using fast single molecule photo-switching. *Appl. Phys. A Mater. Sci. Process.* **88,** 223–226 (2007).

148. Bock, H. *et al.* Two-color far-field fluorescence nanoscopy based on photoswitchable emitters. *Appl. Phys. B Lasers Opt.* **88,** 161–165 (2007).

149. Izeddin, I. *et al.* Super-resolution dynamic imaging of dendritic spines using a low-affinity photoconvertible actin probe. *PLoS One* **6,** (2011).

150. Sillibourne, J. E. *et al.* Assessing the localization of centrosomal proteins by PALM/STORM nanoscopy. *Cytoskeleton* **68,** 619–627 (2011).

151. Rust, M. J., Bates, M. & Zhuang, X. Sub-diffraction-limit imaging by stochastic optical reconstruction microscopy (STORM). *Nat. Methods* **3,** 793–796 (2006).

152. Schaffer, B., Grogger, W. & Kothleitner, G. Automated spatial drift correction for EFTEM image series. *Ultramicroscopy* **102,** 27–36 (2004).

153. Huang, B., Wang, W., Bates, M. & Zhuang, X. Three-Dimensional Super-Resolution Imaging by Stochastic Optical Reconstruction Microscopy. *Science (80-.).* **319,** 810–813 (2008).

154. Georgieva, M. *et al.* Nanometer resolved single-molecule colocalization of nuclear factors by two-color super resolution microscopy imaging. *Methods* **105,** 44–55 (2016).

155. Juette, M. F. *et al.* Three-dimensional sub-100 nm resolution fluorescence microscopy of thick samples. *Nat. Methods* **5,** 527–529 (2008).

156. Pavani, S. R. P., DeLuca, J. G. & Piestun, R. Polarization sensitive, three-dimensional, single-molecule imaging of cells with a double-helix system. *Opt. Express* **17,** 19644–19655 (2009).

157. Shtengel, G. *et al.* Interferometric fluorescent super-resolution microscopy resolves 3D cellular ultrastructure. *Proc. Natl. Acad. Sci.* **106,** 3125–3130 (2009).

158. Pavani, S. R. P. & Piestun, R. High-efficiency rotating point spread functions. *Opt. Express* **16,** 3484 (2008).

159. Pavani, S. R. P. *et al.* Three-dimensional, single-molecule fluorescence imaging beyond the diffraction limit by using a double-helix point spread function - Supplementary. *Proc. Natl. Acad. Sci.* **106,** 2995–2999 (2009).

160. Jäger, S. *et al.* Global landscape of HIV-human protein complexes. *Nature* **481,** 365–370 (2012).

161. Siomi, H., Shida, H., Maki, M. & Hatanaka, M. Effects of a highly basic region of human immunodeficiency virus Tat protein on nucleolar localization. *J. Virol.* **64,** 1803–7 (1990).

162. El Mekdad, H. *et al.* Characterization of the interaction between the HIV-1 Gag structural polyprotein and the cellular ribosomal protein L7 and its implication in viral nucleic acid remodeling. *Retrovirology* **13,** (2016).

163. Whelan, D. R. & Bell, T. D. M. Image artifacts in Single Molecule Localization Microscopy: why optimization of sample preparation protocols matters. *Sci. Rep.* **5,** 7924 (2015).

164. Zeng, F., Yang, W., Huang, J., Chen, Y. & Chen, Y. Determination of the lowest concentrations of aldehyde fixatives for completely fixing various cellular structures by real-time imaging and quantification. *Histochem. Cell Biol.* 1–15 (2012). doi:10.1007/s00418-012-1058-5

165. Tokunaga, M., Imamoto, N. & Sakata-Sogawa, K. Highly inclined thin illumination enables clear single-molecule imaging in cells. *Nat. Methods* **5,** 159–161 (2008).

166. Park, Y. Il, Lee, K. T., Suh, Y. D. & Hyeon, T. Upconverting nanoparticles: a versatile platform for wide-field two-photon microscopy and multi-modal in vivo imaging. *Chem. Soc. Rev.* **44,** 1302–1317 (2015).

167. Izeddin, I. *et al.* PSF shaping using adaptive optics for three-dimensional single-molecule super-resolution imaging and tracking. *Opt. Express* **20,** 4957–4967 (2012).

168. Ovesný, M., Křížek, P., Borkovec, J., Švindrych, Z. & Hagen, G. M. ThunderSTORM: A comprehensive ImageJ plug-in for PALM and STORM data analysis and super-resolution imaging. *Bioinformatics* **30,** 2389–2390 (2014).

169. Banterle, N., Bui, K. H., Lemke, E. A. & Beck, M. Fourier ring correlation as a resolution criterion for super-resolution microscopy. *J. Struct. Biol.* **183,** 363–367 (2013).

170. Haase, A. T. *et al.* Quantitative image analysis of HIV-1 infection in lymphoid tissue. *Science (80-.).* **274,** 985–989 (1996).

171. de Boer, R. J., Ribeiro, R. M. & Perelson, A. S. Current estimates for HIV-1 production imply rapid viral clearance in lymphoid tissues. *PLoS Comput. Biol.* **6,** e1000906 (2010).

172. Darlix, J. L., Lapadat-Tapolsky, M., De Rocquigny, H. & Roques, B. P. First glimpses at structure-function relationships of the nucleocapsid protein of retroviruses. *J. Mol.*

Biol. **254,** 523–537 (1995).

173. Sholokh, M. *et al.* Fluorescent amino acid undergoing excited state intramolecular proton transfer for site-specific probing and imaging of peptide interactions. *J. Phys. Chem. B* **119,** 2585–2595 (2015).

174. Schnitzbauer, J. *et al.* A correlation analysis framework for localization-based super-resolution microscopy. 125005 (2017). doi:10.1101/125005

175. Manley, S. *et al.* High-density mapping of single-molecule trajectories with photoactivated localization microscopy. *Nat. Methods* **5,** 155–157 (2008).

176. Weihs, D., Mason, T. G. & Teitell, M. A. Bio-Microrheology: A Frontier in Microrheology. *Biophys. J.* **91,** 4296–4305 (2006).

177. Forest, T., Barnard, S. & Baines, J. D. Active intranuclear movement of herpesvirus capsids. *Nat. Cell Biol.* **7,** 429–431 (2005).

178. Shi, D. *et al.* Nucleocapsid Interacts with NPM1 and Protects it from Proteolytic Cleavage, Enhancing Cell Survival, and is Involved in PEDV Growth. *Sci. Rep.* **7,** 39700 (2017).

179. Mekdad, H. El. Caractérisation de l'interaction entre Gag(NCp7) et la protéine cellulaire RPL7 : aspects moléculaire et fonctionnel. (Université de Strasbourg, 2014).

180. Węsierska-Gądek, J. & Horky, M. How the Nucleolar Sequestration of p53 Protein or Its Interplayers Contributes to Its (Re)-Activation. *Ann. N. Y. Acad. Sci.* **1010,** 266–272 (2003).

181. Zhang, Y. & Lu, H. Signaling to p53: Ribosomal Proteins Find Their Way. *Cancer Cell* **16,** 369–377 (2009).

182. Chen, J., Guo, K. & Kastan, M. B. Interactions of nucleolin and ribosomal protein L26 (RPL26) in translational control of human p53 mRNA. *J. Biol. Chem.* **287,** 16467–16476 (2012).

183. Zgheib, S. Distribution cellulaire de la protéine de la nucléocapside NCp7 du VIH-1 et caractérisation de son interaction avec la protéine nucléolaire hNoL12. (Université de Strasbourg, 2015).

184. Sloan, K. E. *et al.* Both endonucleolytic and exonucleolytic cleavage mediate ITS1 removal during human ribosomal RNA processing. *J. Cell Biol.* **200,** 577–588 (2013).

185. Grisendi, S., Mecucci, C., Falini, B. & Pandolfi, P. P. Nucleophosmin and cancer. *Nat. Rev. Cancer* **6,** 493–505 (2006).

186. Li, Y. P. Protein B23 is an important human factor for the nucleolar localization of the human immunodeficiency virus protein Tat. *J. Virol.* **71,** 4098–102 (1997).

187. Gadad, S. S. *et al.* HIV-1 infection induces acetylation of NPM1 that facilitates tat localization and enhances viral transactivation. *J. Mol. Biol.* **410,** 997–1007 (2011).